The Pennsylvania State University

The Graduate School

Eberly College of Science

ULTRAFAST MOLECULAR ROTOR AND PROTON TRANSFER DYNAMICS IN SOLUTION

A Dissertation in
Chemistry
by
Jens Breffke

© 2014 Jens Breffke

Submitted in Partial Fulfillment
of the Requirements
for the Degree of

Doctor of Philosophy

December 2014

The dissertation of Jens Breffke was reviewed and approved* by the following:

Mark Maroncelli
Professor of Chemistry
Dissertation Adviser
Chair of Committee

John Asbury
Associate Professor of Chemistry

James B. Anderson
Professor of Chemistry
Evan Pugh Professor

John Golbeck
Professor of Biochemistry and Biophysics
Professor of Chemistry

Kenneth S. Feldman
Graduate Program Chair

*Signatures are on file in the Graduate School.

Abstract

Dynamic solvent effects on several charge transfer reactions in different molecular rotors and an excited state intramolecular proton-transfer reaction have been studied in a range of representative solvents. Combining broadband Kerr-gated emission spectroscopy and time-correlated single photon counting techniques enables determination of fluorescence lifetimes over femtosecond to nanosecond times. Using conventional solvents with well-known physical properties (viscosity, dielectric constant, solvation time, etc.) allows one to discern what types of solvent effects influence the solute's dynamics. When these experiments are complemented by quantum chemical calculations, a better understanding of reaction mechanisms and solvent dependencies can be gained. Three studies have are described in this dissertation to provide new information and insights.

The first study involves three naphthalene malononitrile derivatives which belong to the family of molecular rotors. Previous studies of other malononitriles remained inconclusive with respect to the fluorescence deactivating mechanism. By tuning the rotational barrier and inhibiting rotating degrees of freedom through structural design and by measuring in a series of eleven representative solvents new experimental and computational information supporting a deactivation mechanism consisting of an excited-state double bond isomerization contrary to the more accepted concept of a single bond rotation were provided.

The second study looks at Thioflavin T, a popular fluorescence sensor for fibrillization kinetics. In solution Thioflavin T has a viscosity dependent quantum yield. A recent publication indicates a fast auto-degradation which produces a fluorescent impurity which could have led to wrong conclusions about the photophysics. After intensive purification Thioflavin T has been measured here in 18 representative solvents and quantum mechanical calculations have been performed on the rotation dynamics. We find viscosity alone as insufficient to describe the fluorescence quenching but determined a solvation time dependence as well as a difference between protic (alcohols) and aprotic solvents.

The third study is the ultrafast excited-state intramolecular proton transfer (ESIPT) reaction of the 3-hydroxyflavone derivative DEAHF was studied. Recent literature suggested a proton-tunneling in the Frank-Condon state leading to prompt tautomer formation. However, solvent relaxation induces a reaction barrier which also results in a slow component to the tautomerization process. A binary mixture of acetonitrile and propylene carbonate provides a solvent system having constant polarity but solvation times which vary by a factor of ten between acetonitrile to propylene carbonate. Spectroscopic analysis confirms that the excited-state equilibrium does not change within this mixture series. Time-resolved measurements showed no evidence of a non-zero concentration of the tautomer form at time zero. However, our data clearly shows a slowing in the tautomer formation at early times with decreasing solvation time, suggesting a reaction barrier build-up upon solvation dynamics.

Contents

List of Figures **ix**

List of Tables **xiii**

List of Symbols **xiv**

Preface **xvi**

Acknowledgments **xvii**

1 Introduction **1**

1.1 Solvent Effects in Charge Transfer Reactions [1] 1

1.2 Molecular Rotors for Environmental Sensing 2

1.3 Light Induced Proton Transfer Reactions 4

1.4 Outline of this Dissertation 4

2 Theory **6**

2.1 Solvation 6

2.1.1 Equilibrium: Reaction Field Theory 6

2.1.2 Perturbation of the Equilibrium: Solvation Dynamics 7

3 Experimental and Data Analysis Methods **9**

3.1 Experimental Methods 9
3.2 Kerr Spectroscopy 9
3.2.1 Kerr Shutter Setup 11
3.2.2 Time Correlated Single Photon Counting (TCSPC) 20
3.2.3 Steady State Techniques 22
3.3 Analysis of KGE Data 23
3.3.1 Group Velocity Dispersion and Time Correction 23
3.3.2 Photometric Correction 26
3.3.3 IRF Deconvolution 27
3.3.4 Data Fitting 29

4 Malononitriles **35**
4.1 Abstract 35
4.2 Introduction 36
4.3 Experimental Section 41
4.4 Results 44
4.4.1 Electronic Structure Calculations 44
4.4.2 Steady-State Spectra and Solvatochromism 58
4.4.3 Transition Dipole Moments 70
4.4.4 Time-Resolved Emission 73
4.4.5 Potential Energy Surface and its Reaction Coordinate 79
4.5 Summary & Conclusion 80

5 Thioflavin T **88**
5.1 Abstract 88
5.2 Introduction 89
5.3 Experimental 94
5.4 Results 95

5.4.1 Quantum Mechanical Calculations 95
5.4.2 Thioflavin T Purity 99
5.4.3 Ion Pairing 104
5.4.4 Steady State Spectra 105
5.4.5 Time Resolved Emission 115
5.5 Summary 121

6 Solvation Dynamics and Proton Transfer in DEAHF 123
6.1 Abstract 123
6.2 Introduction 124
6.3 Experimental Section 131
6.4 Results and Discussion 133
6.4.1 Computational Section 133
6.4.2 Steady State Results 134
6.4.3 Time Resolved Results 140
6.5 Summary 145

Bibliography 149

A Theory of Light 157
A.1 Polarization of Light: Linear and Nonlinear 157
A.1.1 Polarization as a Wave 157
A.1.2 Higher Order Polarization 159
A.1.3 The *Kerr*-Effect as χ^3-Process 161
A.1.4 Local Coordinate System 161
A.1.5 Birefringence as a χ^3-Process 163
A.1.6 Orientation Distribution Functions 164

B Deconvolution Function 166

C Standard Operational Procedure (SOP) for Kerr-Gated Emission Spectroscopy 173

C.1 Introduction 173

C.2 Hazards 173

C.3 Controls 174

C.4 Operating Procedures - Startup 176

C.5 Operating Procedure Daily Tuning 178

C.6 Operating Procedure Shutdown 179

C.7 Training 180

C.8 Responsibilities 180

C.9 Miscellaneous 181

List of Figures

1.1 Solvation Dynamics Diagram 3
3.1 Principles of a Kerr-Shutter Setup 12
3.2 Kerr Shutter Setup 13
3.3 Laser System Enclosure 14
3.4 Schwarzschild Objective 15
3.5 IR image of temperature controlled flow cell 17
3.6 Micro Box Design for Kerr-Shutter Setup 18
3.7 Glan-laser polarizer 19
3.8 Kerr Cell 19
3.9 TCSPC Setup 30
3.10 Time Shifts due to Group Velocity Dispersion 31
3.11 Sigmoid Function and its Derivatives 31
3.12 Time Correction for Kerr Experiments 32
3.13 Photometric Correction for Kerr Experiments 33
3.14 Transient Solvent Raman Line of Ethanol as IRF 34
4.1 Studied Malononitrile Structures 37
4.2 Schematic Malononitrile Bond Rotation 40
4.3 B3LYP Absorption Calculation Comparison 50
4.4 TD-B3LYP Absorption Calculation Comparison 54
4.5 TD-CAM-B3LYP Absorption Calculation Comparison 55

4.6 CAM-B3LYP Absorption Calculation Comparison 56
4.7 Frontier Orbitals from B3LYP/6-31G(d,p) Calculations 59
4.8 CAM-B3LYP Absorption Calculation Comparison 61
4.9 Comparison of the Absorption Spectra of 2-MN and r2-MN 62
4.10 2-MN Lognormal Decomposition 63
4.11 Correlations of First-Moment Absorption Band Frequencies 71
4.12 Stokes Shift vs. Solvent Nuclear Polarizability 72
4.13 Transition Dipole Moments vs. Solvent Polarizability 74
4.14 Excitation Wavelength-Dependent Emission of 2-MN in n-Hexane 76
4.15 1-MN Data Analysis Progression 84
4.16 Decay Time Correlations 85
4.17 Correlation Times 86
4.18 Naphthalene Malononitrile S_1 Resonance Structure 87
4.19 Conical Intersection in Double Bond Torsion 87
5.1 ThT Structure 89
5.2 Comparison Experimental Absorption Spectrum vs. Calculated 96
5.3 Calculated φ_1 Torsion Profile 96
5.4 ThT Computational Structure 98
5.5 Bend vs. Twist Angle 100
5.6 Calculated τ_1 Torsion Profile 100
5.7 Calculated τ_1 Oscillator Strengths 101
5.8 Calculated τ_1 Transition Moments 101
5.9 Calculated τ_1 Dipole Moments 102
5.10 Calculated φ_2 Torsion Profile 102
5.11 ThT Purification and Impurity 103
5.12 ThT Ion Pairing Study 105
5.13 ThT SS Absorption Spectra 108

5.14 ThT SS Emission Spectra 109
5.15 ThT SS Absorption 1^{st} Moment Frequency vs. Dielectric Parameters 110
5.16 ThT SS Emission 1^{st} Moment Frequency vs. Dielectric Parameters 110
5.17 ThT SS Emission FWHM vs. Field Factors 111
5.18 ThT SS Emission FWHM vs. Solvation Time and Viscosity 111
5.19 ThT Experimental Transition Moments 112
5.20 ThT Data Analysis Progression 114
5.21 ThT Time Dependent Lognormal Parameters in Acetonitrile 118
5.22 ThT Time Dependent Lognormal Parameters in 1,2-Propylene Glycol . . . 119
5.23 ThT Peak Shift vs Viscosity, Lifetime and Solvation Time 120
5.24 ThT Emission Lifetime $\langle \tau_f \rangle$ vs. Solvation Time and Viscosity 122
5.25 ThT Isoemissive Point Reproduction 122
6.1 DEAHF Proton Transfer Cycle 126
6.2 DEAHF Steady State Spectra 127
6.3 DEAHF Potential Energy Surface (PES) 128
6.4 Extracted DEAHF Solvation and Reaction Times 129
6.5 DEAHF Synthesis Scheme 132
6.6 Calculated DEAHF Dipole Moment States 134
6.7 DEAHF Steady State Spectra in Binary Mixture Series 136
6.8 DEAHF Absorption Peak Frequency in Binary Mixture Series 136
6.9 DEAHF Steady State Principal Spectral Dissection 137
6.10 Conversion from Spectrum to Lineshape 137
6.11 DEAHF Steady State Emission Properties in Binary Mixture Series 138
6.12 DEAHF Data Analysis Progression 143
6.13 2D Contour Plot of DEAHF Spectral Evolution 144
6.14 DEAHF TR Lognormal Parameters ($x_{acn} = 0.2$) 146
6.16 Tautomer Rise Times 147

6.17 Average Tautomer Rise Times 147
6.15 DEAHF Dynamic Stokes Shift Times 148
C.1 SOP: Diagram of Laser Laboratory #411 174
C.2 SOP: Kerr Shutter Setup 175

List of Tables

3.1 Kerr Data Matrix Structure 26
3.2 Secondary Emission Standards 27
4.1 Calculated Ground State Properties 47
4.2 Excited-State and Transition Properties 47
4.3 Comparison of Calculated and X-Ray Structures of Benzylidene Malononitrile 49
4.4 Comparison of Calculated and X-Ray Structures of 1-MN 51
4.5 Comparison of Calculated and X-Ray Structures of r2-MN 52
4.6 Additional DFT Calculations 53
4.7 Orbital Compositions of the S_1 and S_2 States 58
4.8 Solvent-Dependent Photophysical Properties of 2-MN at 25°C 64
4.9 Solvent-Dependent Photophysical Properties of 1-MN at 25°C 65
4.10 Solvent-Dependent Photophysical Properties of r2-MN at 25°C 67
4.11 Solvent Properties (25°C) 68
4.12 Solvatochromic Regression Results 69
5.1 ThT Recrystallization Solutions 94
5.2 ThT Absorption and Emission Band Properties 113
6.1 Binary Mixture Preparation 133
6.2 DEAHF SS Emission Lognormal Parameters 139
6.3 Tautomer Rise Times in Binary Mixture Series 141
6.4 Dynamic Stokes Shift Times for DEAHF and C153 148

List of Symbols

c	Speed of light in a vacuum
$C153$	Coumarin 153
CW	Continuous Wave
$DEAHF$	4'-N,N-diethylamino-3-hydroxyflavone
$DPSS$	Diode-Pumped Solid-State (laser)
e	Euler Number
ϵ_0	Dielectric Constant
$ESIPT$	Excited State Intramolecular Proton Transfer
η	Viscosity
FQD	Fluorescence Quantum Distribution
$FWHM$	Full Width at Half Maximum
GVD	Group Velocity Dispersion
h	Plank constant
IL	Ionic Liquid
IRF	Instrument Response Function
λ	Wavelength
μ	Dipole Moment
n, n_D	Refractive index

ν	Frequency in Wavenumber (cm^{-1})
OD	Optical Density
OKE	Optical Kerr Effect
$OPSL$	Optically Pumped Semiconductor Laser
PES	Potential Energy Surface
PSF	Point Spread Function
S/N	Signal-to-Noise Ratio
SS	Steady State
$TCSPC$	Time Correlated Single Photon Counting
$TDDFT$	Time-Dependent Density Functional Theory
ThT	Thioflavin T
$TICT$	Twisted Intramolecular Charge transfer
TR	Time Resolved
$TRES$	Time Resolved Emission Spectrum
$TRANES$	Time Resolved Area Normalized Emission Spectra
vdW	van der Waals (radius)

Preface

This dissertation serves two purposes: First and foremost it provides new insights and knowledge for the scientific community, gained from work conducted during my graduate research in the group of Mark Maroncelli. Secondly, it provides a comprehensive description of the Kerr-shutter setup to enable new incoming students and postdoctoral researchers to understand the principles and key elements to this pump-probe technique. To the latter end the principles of the Optical Kerr Effect (OKE) will be summarized here as will the design of the Kerr-shutter which was developed in the group of Nikolaus P. Ernsting at the Humboldt-Universität zu Berlin in Germany as part of my German Diplom thesis. For new research group members who will start working on the Kerr system there are several theoretical parts provided in dept in appendix, e.g. the theory of light propagation and its polarization properties for a better understanding of how the Kerr effect works and the full derivation of the used deconvolution mathematics.

Acknowledgments

My gratitude goes to numerous people I had the pleasure to meet and work together with over the years. First and most of all I want to thank my adviser Mark Maroncelli for taking me into his group and giving me autonomy in my scientific work. Together with my committee members John Asbury, Jim Anderson, and John Golbeck I want to them for granting me the opportunity to receive a PhD degree from the Pennsylvania State University. My research involved extensive quantum mechanical calculations in which Andrew Sirjoosingh, Igor Schapiro, Jörg Kussmann and Chet Swalina took great part in. Sean McCarthy and Johannes Belmar have contributed to my projects significantly with their support for the synthesis and purifications of my chromophores. For my laser, data acquisition and data processing skills and for their continuing support over the years I want to thank Luis Lustres, Sergey Kovalenko, Alexander "Sasha" Dobryakov and Mohsen Sajaadi from the Humboldt-Universität zu Berlin Germany. But not everyone who was a great supporter took necessarily part in the actual research. My life was a little less painful thanks to Sabrina Glasgow by guiding me through the jungle of bureaucracy, budgeting, and administration where reason sometimes just doesn't apply. Larry Johns and his team were working with me on the facility challenges of the Chemistry Building, and their efforts are truly appreciated. Last but certainly not least I want to express my sincere gratitude to Rod Kreuter and Bob Crable in the Research Instrumentation Facility. Both have taught me a fundamental understanding and appreciation of electronics, machining and instrument maintenance, repair and design.

Chapter 1

Introduction

1.1 Solvent Effects in Charge Transfer Reactions [1]

Electron-transfer processes in solution are among the most important reactions in chemistry and living nature. One of the important questions in solution-phase chemical reaction dynamics is the influence of the solvent on the reaction rate. One distinguishes between static and dynamic solvent effects. Static effects refer to the stabilization of reactants, transition state, and products, i.e. how the solvent affects the free energies and the energy of activation. This interpretation of solvent effects on all kinds of chemical reactions is well established. A more recent development is the investigation of the influence of solvent dynamics on the rate of a reaction, accessible by ultrafast laser spectroscopy. The transfer of an electron is usually thought to be triggered by a fluctuation of the dielectric polarization in the surrounding solvent. This charge redistribution can result from chemical reaction, photo-excitation, vibrational excitation or other processes. Better knowledge about solvation dynamics is therefore key for a better understanding of reactions in condensed phases. In most conventional solvents solvation dynamics occurs on an ultrafast timescale, typically in the range of femtosecond to picoseconds. The dynamics of such fluctuations are determined by the finite response time of the orientational polarization of the solvent. Un-

der certain conditions this solvation response time can become the rate-determining factor of the reaction. Photo-excitation induced charge transfer using ultra-short laser pulses in combination with fluorescence emission is the method of choice to study solvation dynamics. Figure 1.1 illustrates the principle of time-resolved emission spectroscopy to study dynamic solvent effects.

1.2 Molecular Rotors for Environmental Sensing

Rotor probes are often used with the idea that they measure solvent friction. Friction in a dynamical solvent effect which is distinct from solvent dynamics and it needs to entail electrostatic solute - solvent coupling. That is, the friction associated with coupling to solvent viscosity can be exclusively due to a Lenard-Jones type interaction rather than to electrostatic i.e. "dielectric"' interactions.

A molecular rotor commonly describes a fluorescent molecule that can undergo an intramolecular twisting motion on the excited state potential energy surface (PES) upon charge transfer. This mechanism is commonly described as twisted intramolecualr charge transfer or TICT. Typically, a molecular rotor consists of three molecular elements. For the fluorescence charge transfer character it usually has (but not always required) an electron donor unit, an electron acceptor unit, and a π-electron bridge that can conduct charge transfer. This network brings the donor and acceptor units in conjugation, thus facilitating electron movement between this pair. At the same time this bridge holds the capability of rotating if not constrained but other ring-closing structures. Upon photo excitation a molecular rotor can relax to a nonplanar (twisted) state with a lower excited state energy. This relaxation can occur either with or without a barrier, affecting the reaction rate accordingly. Relaxation into the twisted state is associated with either a red-shifted fluorescence emission or non-fluorescent relaxation, depending on the molecular structure.

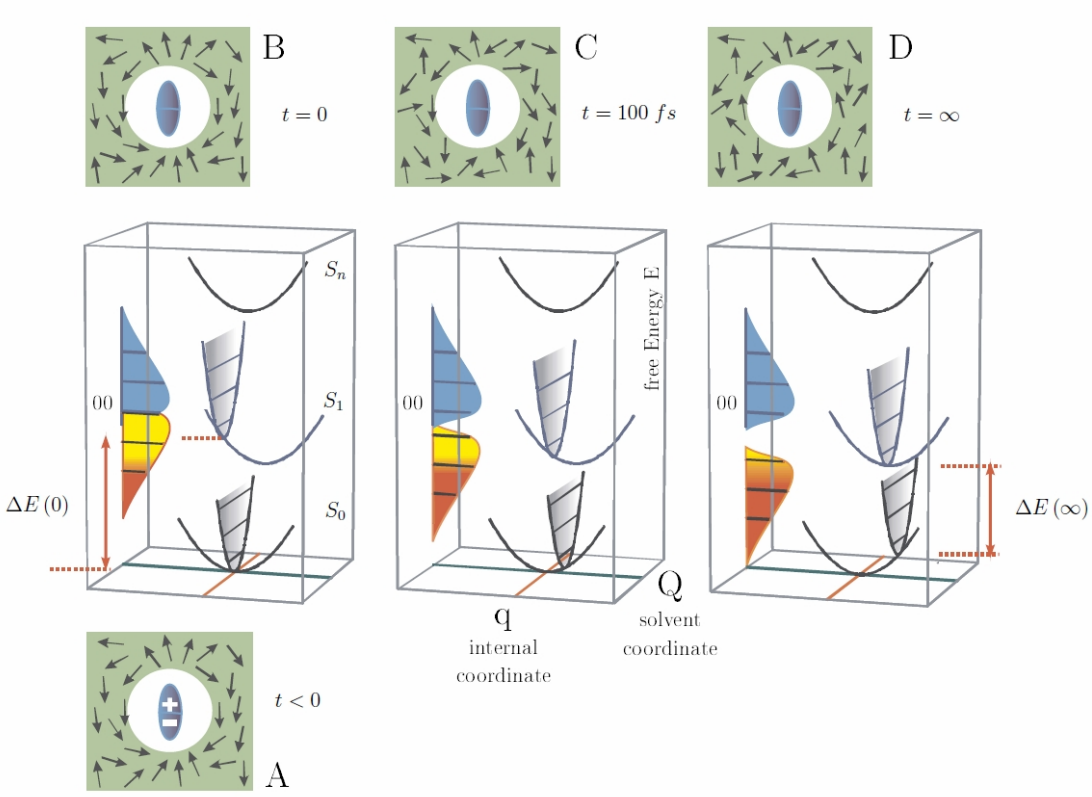

Figure 1.1: The dynamic Stokes shift of fluorescence (yellow-red band) reflects the relaxation of the surrounding solvent in the S_1 state of the solute. The solvent coordinate Q represents the configurational state of the environment and is treated classically. High-frequency motion along internal coordinate q for bond lengths and angles is quantized in vibrational states. Before femtosecond excitation (a) the solute is in the equilibrated ground state S_0 and the (blue) absorption band extends over a Franck-Condon progression for upward optical transitions. Immediately after excitation (b) the emission overlaps the absorption band at the electronic absorption origin 00. Partially relaxed $E_1(Q)$ (c) corresponds to solvent configurations that have raised $E_0(Q)$. The fluorescence therefore changes from yellow to red as solvation proceeds. After several picoseconds (d) a new equilibrium is reached for the S_1 state. A point dipole in a spherical polarizable cavity represents the solute, while a continuum with dielectric dispersion $\epsilon(\nu)$ represents the surrounding liquid.

Reprinted with permission from Reference [2]. Copyright 2005 John Wiley & Sons, Inc.

Hence a TICT state can be emissive or dark. [3, 4].

1.3 Light Induced Proton Transfer Reactions

In living nature, proton transfer (PT) reactions are ubiquitous and a vital chemical transformation. Despite their chemical simplicity, their reaction pathways are multifaceted, difficult to determine and consequently often complicated to understand. On the potential energy surface (PES) it can undergo quantum mechanical tunneling effects and have extremely high reaction rates making it appear like an equilibrium reaction. Such a transfer can occur intermolecular but also intramolecular between adjacent acidic and basic functional groups. In many cases, the proton affinities of these sites change upon photoexcitation, leading to excited-state proton transfer (ESPT). In particular, intramolecular ESPT with a well defined transfer distances can be triggered conveniently with recent advances in ultrafast laser technologies compared to rather diffusion limited intermolecular ESPT. Despite significant progress that has been made in understanding principle reaction pathways, not much is known about the effect of solvation dynamics on this type of chemical reaction.

1.4 Outline of this Dissertation

Common principle in the investigation of molecular rotors and excited state intramolecular proton transfer (ESIPT) with respect to their dependence on solvent effects is the use of ultrafast laser systems for time-resolved fluorescence spectroscopy. Static solvent effects can usually be determined by changes in stationary (steady state) absorption and emission spectra, but dynamic solvent effects can be determined usually only by time-dependent spectral changes on a femtosecond to picosecond timescale in conventional low viscosity solvents. These time-resolved experiments are performed using broadband Kerr-

gated emission (KGE) spectroscopy and time-correlated single photon counting (TCSPC)

A more detailed theoretical concept of solvation and solvent effects will be discussed in chapter 2, followed by a full-depth experimental description of some of extensive custom-build spectroscopy systems as well as the data processing necessary in broadband detection (chapter 3).

Chapter 4 and 5 will address molecular rotors for a better understanding of underlying molecular reaction mechanisms, their solvent dependencies (both static and dynamic), and the nature of the emitting state.

Chapter 6 presents a model system for ESIPT. Unlike for the studied molecular rotors we designed a solvent system that allows to look only at the dynamic solvent effect of the proton transfer reaction at virtually no change of the static solvent effect.

For comprehensive purposes and to assist future research group members of the Maroncelli Group at Penn State to get more familiar with the Kerr-gated emission system more laser principals and a full derivation of the data deconvolution theory is provided in the appendix.

Chapter 2

Theory

2.1 Solvation [5, 6]

2.1.1 Equilibrium: Reaction Field Theory

Onsager's model views the solvent environment as a continuous dielectric medium with the dielectric constant ϵ_0 [7]. The solvated molecule (solute) occupies a spherical cavity with a van der Waals (vdW) radius a [8] [1]. If the solute has a permanent dipole moment $\vec{\mu}$ it polarizes its environment and an electric moment is induced in the solvent molecules which is proportional to their electronic polarizabilities. Also, the permanent dipole moments of the solvent molecules are oriented with respect to the dipole moment of the solute. Both sources of polarization establish a new field at the solute dipole location which has same orientation as the solute dipole $\vec{\mu}$. This field is called by Liptay et al. the reaction field $\vec{R}$ [10]. Assuming $\vec{\mu}$ to be non-polarizable, we can write [7]:

$$\vec{R} = f \cdot \vec{\mu} \tag{2.1}$$

$$= \frac{2}{a^3} \cdot \frac{\epsilon_0 - 1}{2\,\epsilon_0 + 1} \cdot \vec{\mu} \tag{2.2}$$

[1] J.T. Edward provides here an empirical library for atoms and molecule groups to determination an approximate van-der-Waals radius with remarkable satisfying results [9]

We obtain the energy of an ideal point dipole in $\vec{R}$ by the work of displacing the solute from vacuum into its own reaction field $\vec{R} \leftarrow 0$. This work is:

$$U_{\vec{R}\leftarrow 0} = -\int_0^{\mu} \vec{R} \cdot d\vec{\mu} = -\frac{1}{2} f \left|\vec{\mu}\right|^2 \tag{2.3}$$

To describe an electronic transition, the energy difference from the ground state to the excited state in their equilibrium, $\vec{\mu}_e \leftarrow \vec{\mu}_g$, the integral has the value [11]

$$U_{\vec{\mu}_e \leftarrow \vec{\mu}_g} = -\int_{\mu_g}^{\mu_e} \vec{R} \cdot d\vec{\mu} = -\frac{1}{2} f \left(|\vec{\mu_e}|^2 - |\vec{\mu_g}|^2\right) \tag{2.4}$$

which represents the energy difference of the well minima $\Delta E = E(S_1) - E(S_0)$ in Figure 1.1.

As mentioned previously the reaction field consists of an electronic or optical (opt) polarization and an orientation polarization (or). For the proportionality in Eq. 2.4 we assume $f = f_{opt} + f_{or}$:

$$f_{opt} = \frac{2}{a^3} \cdot \frac{n^2 - 1}{2\, n^2 + 1} \tag{2.5}$$

$$f_{or} = \frac{2}{a^3} \cdot \left(\frac{\epsilon_0 - 1}{2\, \epsilon_0 + 1} - \frac{n^2 - 1}{2\, n^2 + 1}\right) \tag{2.6}$$

where n is the refractive index of the solvent.

In modeling electronic spectra we assume that the optical component of the solvent response $\vec{R}$ can occur instantaneously, but the orientation component stays unaltered during the solute transition.

2.1.2 Perturbation of the Equilibrium: Solvation Dynamics

The previous description of the simplified continuum theory we considered only the equilibrium case. We now expand these thoughts to a time-varying solute dipole as it occurs upon optical excitation in the Frank-Condon state. For simplicity we consider all possible

Fourier-components of the reaction field:

$$\vec{R}(\omega) = f(\omega) \cdot \vec{\mu}(\omega) \tag{2.7}$$

According to Eqs. 2.5 and 2.6 the proportionality factors become:

$$f_{opt}(\omega) = \frac{2}{a^3} \cdot \frac{n-1}{2\,n+1} \tag{2.8}$$

$$f_{or}(\omega) = \frac{2}{a^3} \cdot \left(\frac{\epsilon(\omega)-1}{2\,\epsilon(\omega)+1} - \frac{n-1}{2\,n+1} \right) \tag{2.9}$$

where it is assumed that ω is below the electronic frequencies of the solvent. $\epsilon(\omega)$ is the dielectric response of the solvent, which can be obtained from microwave and terrahertz spectroscopy. To connect to the time domain experiments studied here we use the solvation variable $z(t)$ defined by van der Zwan and Hynes [12]:

$$z(t) := \frac{\int_0^t f_{or}(\tau)\,d\tau}{\int_0^\infty f_{or}(t)\,d(t)} = \frac{1}{f_{or}} \int_0^t f_{or}(\tau)\,d\tau \tag{2.10}$$

where $f(t)$ is the *Fourier* transform of $f(\omega)$.
But the main parameter of interest in solvation dynamics is the normalized solvation relaxation function $S(t)$:

$$S(t) = \frac{\nu(t)-\nu(\infty)}{\nu(0)-\nu(\infty)} \tag{2.11}$$

Eq. 2.11 is the foundation of analyzing solvation dynamics and its frequencies will be obtained through the peak or weighted frequency parameter of a lognormal fit of the dynamic *Stokes* shift which will be applied accordingly in chapter 3.3. The observable solvation response function $S(t)$ is related to $\epsilon(\omega)$ via the simple expression [13]

$$S(t) = 1 - z(t) \tag{2.12}$$

Chapter 3

Experimental and Data Analysis Methods

3.1 Experimental Methods

Key technique in this work to study the effect of solvation on charge transfer reactions is the employment of a broadband optical Kerr-shutter described in Section 3.2.1. However, several different techniques have to be utilized to obtain information which can then be combined. In Section 3.2.2 the complementary technique of time-correlated single photon counting is described which covers a longer time range. Steady state UV-Vis and emission provide information about extinction coefficients, quantum yields and spectral shifts. In Section 3.3 the data preparation and analysis will be explained in detail.

3.2 Kerr Spectroscopy

Measuring processes like intramolecular electron or proton transfer comes with a price. This price is illustrated by a simple thought experiment: In order to measure an electron

that travels a few Angstroms from A to B within a single molecule you cannot use a copper cable where also an electron has to travel but feet of Angstroms instead (namely, from a detector to your computer). You have to utilize a technique that allows you to probe such an ultrafast process differently. This is the field of ultrafast spectroscopy, where very short but intense laser pulses are used to induce nonlinear optical effects in e.g. crystals or liquids. Generally, two of these ultrafast laser pulses are crossed in time and space in order to obtain time resolved information. These two-beam techniques are commonly described as pump-probe experiments. One of them is used exclusively in the work of this dissertation, a Kerr-shutter which utilizes the optical Kerr effect (OKE).

In a Kerr-shutter setup a sample is excited by the second harmonic of a laser pulse and the resulting fluorescence is collected with a combination of mirrors and focused on a Glan-polarizer to obtain polarized fluorescence light. It is then passed through a Kerr active medium (benzene in our case) and then through a second polarizer and finally focused into an optical multi-mode fiber connected to a broadband CCD detector. Figure 3.1 illustrates the following: The two polarizers are 90° rotated with respect to each other ("crossed") to ensure that under regular conditions no photons reach the detector. The thin benzene cell is perpendicular to the propagation direction so the refractive index has no effect on the fluorescence light. However, when excited by a strong laser pulse (the "gate pulse") it induces a temporal birefringence in the Kerr medium and causes the polarization of the passing fluorescence light to rotate. As a result, this fluorescence light with rotated polarization is able to pass the second, crossed polarizer and will be measured by the detector (see Figure 3.1). By delaying the gate pulse with respect to the excitation pulse it allows one to gate a thin slice of the fluorescence on a femtosecond time scale. The detection itself is not time resolved but the photons detected over a certain acquisition has the time information due to our controlled delay between the two pulses. Details of this gating process is explained in its theory in section A.1.3 and its experimental setup in section 3.2.1.

3.2.1 Kerr Shutter Setup

One of the most powerful techniques used to measured time resolved fluorescence is Kerr-gated emission (KGE) spectroscopy. It allows for measurement of broadband spectra with high time resolution and great performance with respect to the photometric accuracy of these spectra. This amount of information allows one to analyze peak shifts and lifetime decays with high data point density and without the need for spectral reconstruction.

In this section the Kerr-shutter setup will be described in detail due to its custom design and features. In Figure 3.2 the complete pump-probe setup is provided. Five elements shall be addressed in further detail *i*) the laser system, *ii*) the sample flow cell *iii*)the Schwarzschild objective, *iv*) the Glan-Laser polarizer, and *v*)the Kerr cell.

1. Pulsed Laser System

The laser system consists of an 18 W pump laser (Verdi G-18, Coherent, Inc.) which pumps with 30 % the oscillator (Mira 900, Coherent, Inc.), producing 130 fs pulses at 775 nm with 10 nm spectral bandwidth at a repetition rate of 76 MHz and an average power of 1 W. These pulses are stretched (Expander/Compressor 9100, Coherent, Inc.) and seeded into a regenerative amplifier (RegA 9050, Coherent, Inc.). The latter is pumped with the remaining 70 % of the pump power and reducing the repetition rate to 250 kHz using a cavity dumper. After compression (Expander/Compressor 9100, Coherent, Inc.) 130 fs pulses with 1.5 W average power (pulse energy: 6 μJ) are obtained.

Due to varying temperature and humidity in the lab, which compromises the stability of the laser system, the entire laser and Kerr spectroscopy system is enclosed (Figure 3.3)

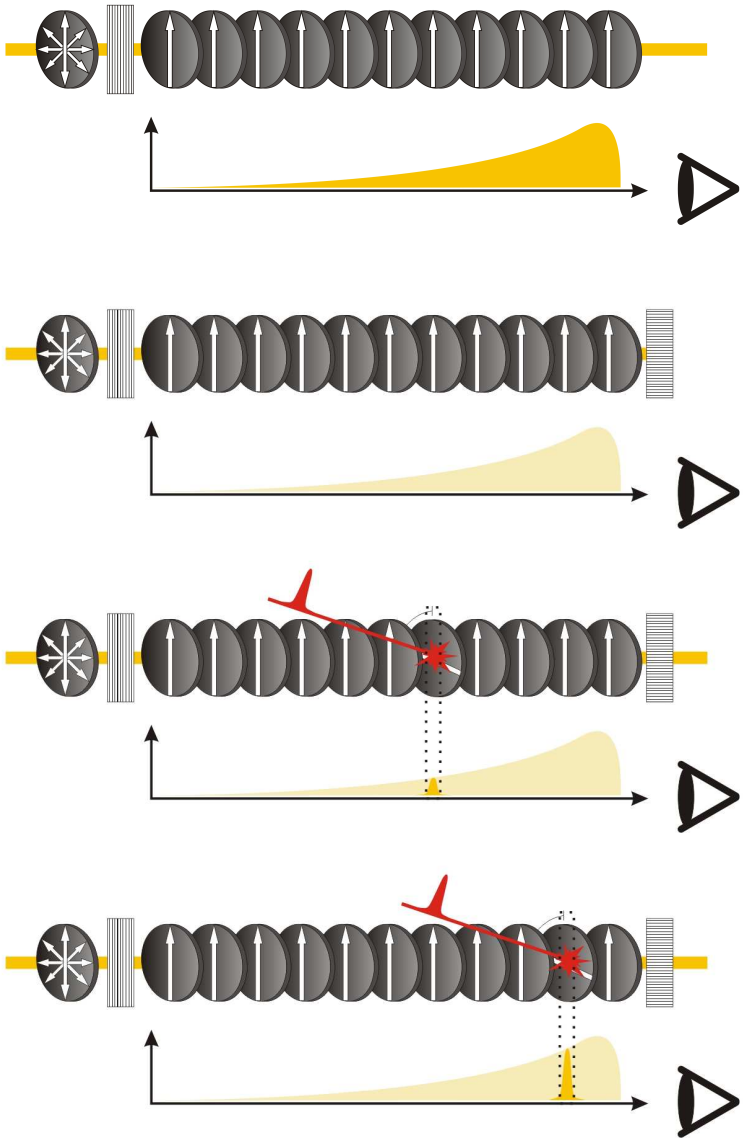

Figure 3.1: Kerr-shutter principle from top to bottom: 1. Full detection of fluorescence light after polarizer filter. The observer is able to detect the whole fluorescence decay. 2. Complete blockage by two crossed polarizers. 3. and 4. crossed polarizers but with additional *Kerr* medium excitation at different times. Within the synchronized birefringence the fluorescence polarization changes and can pass the crossed polarizer. The observer detects light from only a specific time window out of the entire fluorescence decay.
Reprinted with permission from Reference [6].

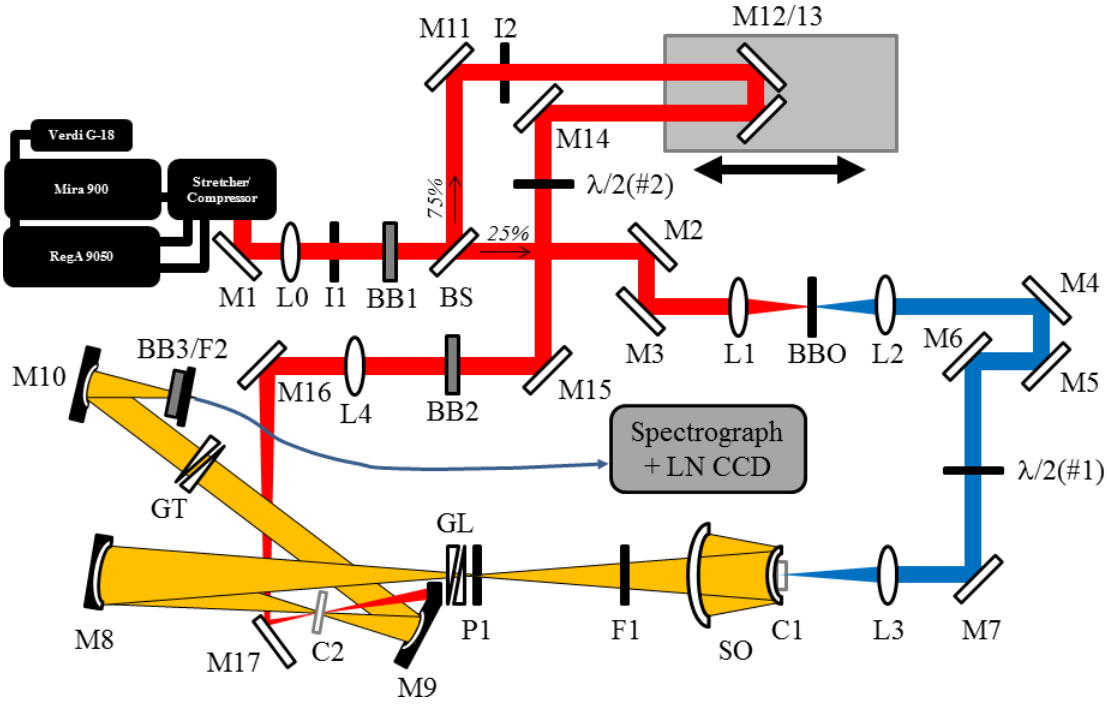

Figure 3.2: Kerr shutter setup: The black boxes represents the amplified Ti:Sapphire laser system. *M1* 45° high reflectivity (*HR*) mirror; *L0* 3000 mm focal length lens to collimate the laser; *I1,I2* irises for alignment purposes; *BB1* solenoid beam blocker #1; *BS* beam splitter (75 % reflectivity; 25% transmittance).
25% transmittance path: *L1,L2* 50 mm focal length lenses; *BBO* 0.2 mm BBO (*Inrad*, Type I); $\lambda/2$*(#1)* $\lambda/2$ retarder for magic angle excitation; *L3* 100 mm focal length lens; *C1* 0.5 mm sample flow cell, 0.2 mm / 1 mm suprasil window; *S0* on-axis Schwarzschild objective with 1:10 magnification; *F1* GG400 optical filter to remove excitation scattering; *P1* 300μm pinhole; *GL* Glan-Laser calcite polarizer (Halle); *M8* 250 mm focal length mirror; *C2* 0.65 mm *Kerr* flow cell (benzene), 0.2 mm / 0.2 mm suprasil window; *M9* 100 mm concave mirror to collimate beam; *GT* Glan-Taylor polarizer (1.5 in aperture); *M10* -100 mm focal length mirror; *BB3* UniBlitz® beam blocker; *F2* 0° dichroic mirror for 775nm to filter gate beam scattering; multimode optical fiber coupling directly into spectrograph (Acton SpectraPro-300i) with attached liquid nitrogen cooled CCD detector (Princeton Instrument, LN/CCD-1340/100-EB/1).
75 % transmittance path: *M12/M13* translation/delay stage (Newport ILS250PP), $\lambda/2$*(#2)* $\lambda/2$ plate for 45° polarization; *BB2* solenoid beam blocker #2; *L4* 500 mm focal length lens; *C2* 0.65 mm *Kerr* flow cell (benzene), 0.2 mm/0.2 mm suprasil window; *M9* holder serves as beam blocker.

and the air dried by circulating it through a 100 lbs industrial grade desiccant column (not shown).

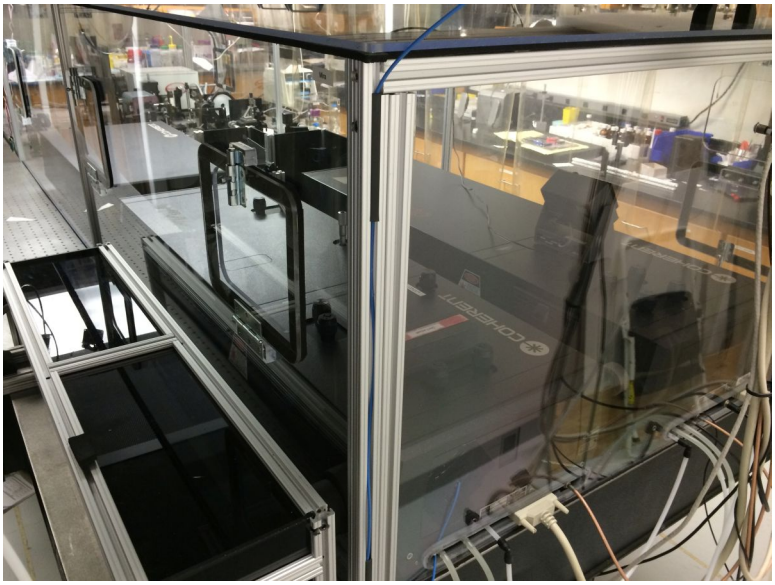

Figure 3.3: Enclosed laser and Kerr spectroscopy system in room 411 Chemistry Building.

2. Schwarzschild objective

Effectively collecting the emitted fluorescence after excitation is crucial for signal intensity hence signal-to-noise (S/N) ratio. The optical design used is a combination of concave + convex mirrors to achieve magnification originally designed by Karl Schwarzschild [14]. Because of group velocity dispersion, explained in section 3.3.1, it is desirable to minimize the amount of optical transparent materials (glasses) light has to propagate through to avoid chirping. Therefore the group of Niko Ernsting designed a pair of concave and convex mirrors to achieve a 1 : 10 magnification [15] with an integrated sample flow cell residing inside the center of one of them, as illustrated in Figure 3.4. It provides a very long focal length to minimize the numerical aperture in its focal point due to the limitation

of the Glan-Laser polarizer (see below) for high extinction ratio.The fluorescence spot is truncated by a 300μm pinhole in front of the Glan-laser polarizer to allow for only single pass collected light ($\rightarrow 1 \rightarrow 2 \rightarrow 3$). Multiple reflections between the two mirrors would introduce a time-offset and therefore distortion in the time information purity.

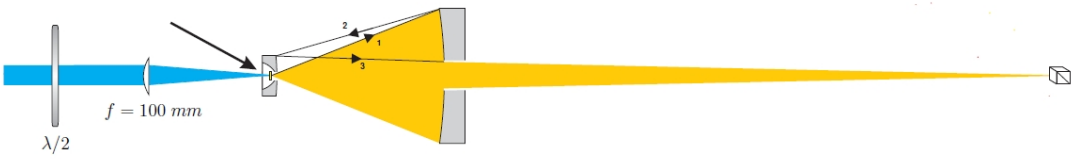

Figure 3.4: On-axis Schwarzschild objective with 1:10 magnification. The arrow points out the sample flow cell.

3. Sample flow cell

The flow cell in this Schwarzschild objective setup is custom machined from stainless steel and fits precisely inside the center of the hollow mirror from the backside as schematically illustrated in Figure 3.4. It is of conical shape with a 0.5 mm window on top. Inside the conical body it allows for a hollow screw with the complementary window on top to adjust the thickness of the cell it arises from. The cell thickness is adjusted here to ~1 mm. The tubing is integral part of the cell design and will both (in and out) be connected from the back of the cell.

A common occuring problem is that the probe can drop out of solution in a nonpolar solvent. It then happens the aggregated probe particles stick to the cell window and burn a spot onto the glass when in the laser focus spot. This circumstance causes scattering or in worst cases burning of the window. To prevent the deposition the window surfaces are coated with a fluoroalkylsilane (FAS) via the following procedure:

1. Immerse windows in 0.2 M NaOH/methanol solutions for 24 h in order to remove all organic contaminants;
2. Immerse windows in chromic acid for 24 h in order to get rid of all inorganic contaminants, including previous coatings;
3. Rinse windows with distilled water;
4. Air dry windows;
5. Immerse windows in 0.1 % tridecafluoro-1,1,2,2-tetrahydrooctyl)trichlorosilane (CAS 78560-45-9) in heptane solution for 10 min;
6. Immediately, immerse windows in heptane and sonicate for 1 h;
7. Air dry windows.

Typically, chromic acid was prepared by dissolving 1 g of potassium dichromate (CAS 7778-50-9) in 30 ml of concentrated sulfuric acid. However, washing by chromic acid is not necessary, when a new window is used. This step is important only if you want to coat a window again.

Important to all experiments carried out for dynamics measurements is temperature control. Taking advantage of the stainless steel body of the cell with significant heat capacity and heat transfer properties a copper tubing is attached on the back of the cell allowing for a rigorous heat exchange. Accounting for losses to the environment by tubing and other heat sink contacts in an empirical fashion the actual temperature at the cell was measured using a calibrated heat camera shown in Fig 3.5.

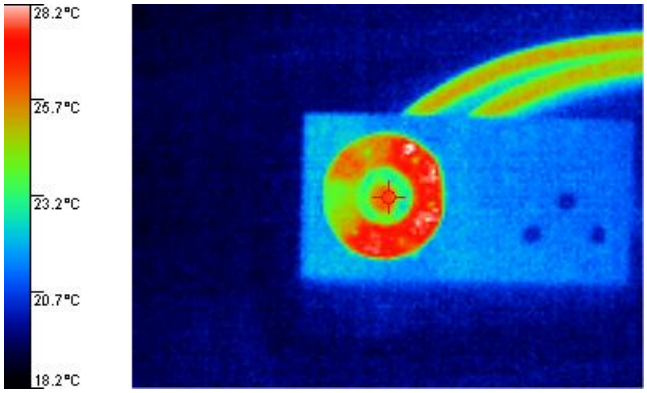

Figure 3.5: IR image of temperature controlled flow cell. Setting the water bath to 27.3°C provides constant temperature of 25.0°C at the flow cell accounting for all heat losses.

Some projects require a low humidity controlled environment to prevent hygroscopic samples from incorporating water. For this purpose a micro glove box which allows for a nitrogen flushed environment inside a temperature controlled heat block was constructed (see Figure 3.6).

4. Glan-laser polarizer

The performance of a Kerr-shutter depends on its ability to suppress ungated fluorescence leaking passed the pair of crossed polarizers (GL and GT in Figure 3.2). Niko Ernsting at the Humboldt-Universität zu Berlin designed a calcite Glan-type polarizer for ultrafast laser application (hence Glan-laser) which is patented in both Germany and the U.S. [1] [2]

[1] Ernsting, N.P. (Humboldt-Universität zu Berlin, Germany). Anordnung für ein optisches System für polarisationsabhängige Zeitaufgelöste optische Spektroskopie, optische Messsystem und Verfahren zum polarisationsabhängigen spektroskopischen Untersuchungen von Messlicht. German Patent Nr. 10 2006 039 425, August 23, 2006.

[2] Ernsting, N.P. (Humboldt-Universität zu Berlin, Germany). Arrangement for an Optical System for Polarization-Dependent, Time-Resolved Optical Spectroscopy, Optical Measurement System and Method for the Polarization-Dependent Spectroscopic Analysis of Measurement Light. U.S. Patent 7,920,259, April 5, 2011.

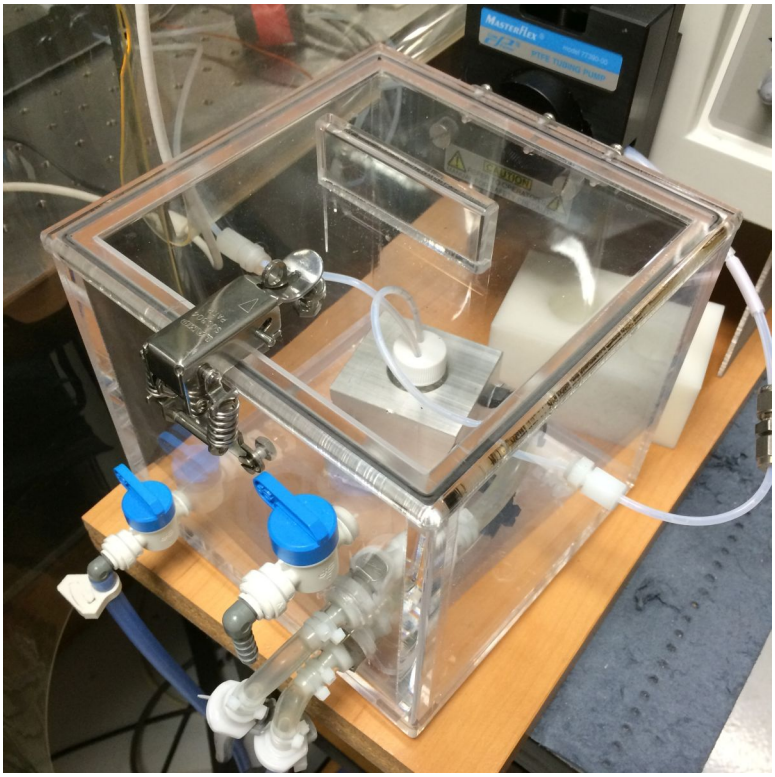

Figure 3.6: Micro glove box with connectors for nitrogen air line, water bath panel mount connectors and temperature controlled vial holder and peristaltic pump tubing in/out.

The high performance of this polarizer is limited by the small acceptance angle $\gamma \leq 3°$. The Schwarzschild objective is designed accordingly as described above and delivers $\gamma = 2.4°$ onto Glan-laser polarizer (GL of Figure 3.2). It is mounted on a X-Z stage so that the thickness of the polarizer can be adjusted to allow for a balance between extinction and chirping.

5. Kerr cell

The actual pump-probe spectroscopy takes place in the Kerr cell which transiently tilts the polarization. A practical problem is the alignment, i.e. overlapping the fluorescence and

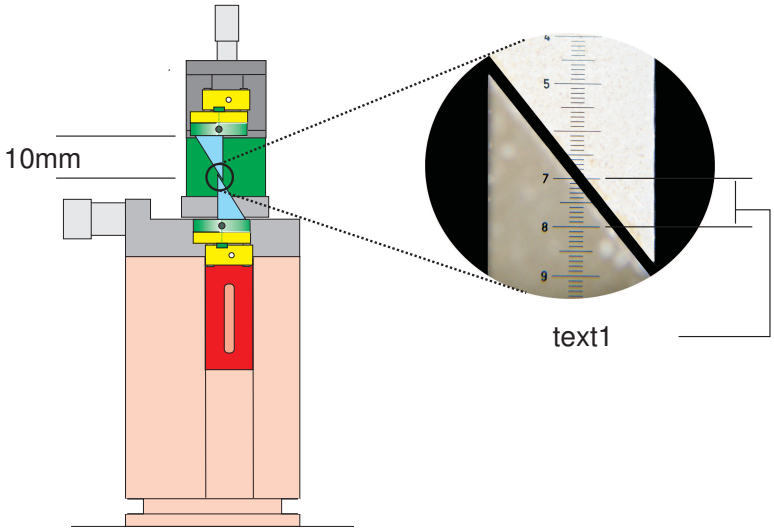

Figure 3.7: Glan-laser calciate polarizer with mount for adjustable thickness. Shown on the right is a microscope image of the actual overlap.

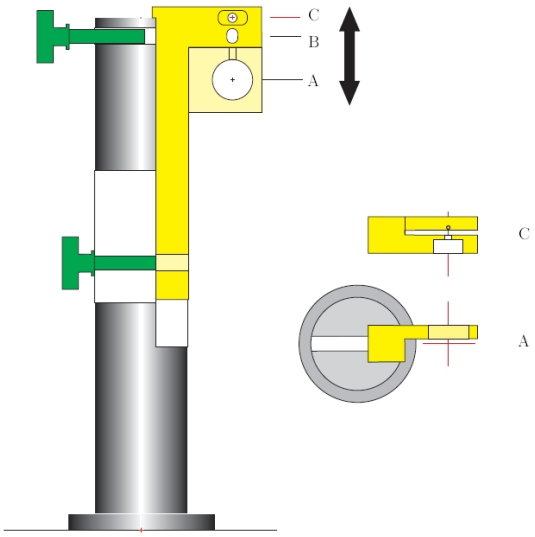

Figure 3.8: Kerr cell with mount. *A* Kerr media (benzene) flow cell, *B* white reflective surface, *C* pinhole

gate beams inside the cell. Since the focus spots are small and the flow cell is thin there is the practical problem of observing the spots in the cell. A custom designed holder shown

in Figure 3.8 offers a convenient alignment procedure. In addition to the cell itself (A), the holder supports a pinhole (C) and a reflection standard (B), all in the same plane.

The pinhole facilitates the first alignment step using just a white card behind it. Closing iris I2 in Figure 3.2 allows one to overlap both beams precisely on the white reflection standard. Inserting the Kerr cell now the alignment should be close enough so with minor gate movement a transient signal should be obtained.

Frequent maintenance is required for the purity of the benzene as Kerr-medium. Over time the mechanics of the gear pump, which continuously circulates the benzene to avoid excessive heating and boiling, produces particles which can get in the gate beam focus and burn on the window causing scattering. These particles are removed using in-line staged 10 μm and 2 μm filter elements.

The Kerr cell is constructed to allow adjustment of the cell thickness using spacer rings. The measurements presented in this work were all performed with a cell thickness of 0.75 mm. Spectroscopic grade benzene is used due to its high Kerr number (efficiency). [16] One characteristic of benzene as Kerr media that requires attention is a nuclear relaxation due to the large contribution of orientational polarizability to its nonlinear refractive index (birefringence). [17] This nuclear relaxation can be seen in the instrument response function (IRF) of a solvent blank Raman line (Figure 3.14). This transient decay profile makes a deconvolution fitting procedure necessary and will be derived in full detail in section 3.3.3.

3.2.2 Time Correlated Single Photon Counting (TCSPC)

A complementary technique to the Kerr-shutter which covers a longer time range $\gg$100ps is the time-correlated single photon counting (TCSPC) setup. It consists of a Ti:sapphire

oscillator (Mira 900, Coherent, Inc.) with extended cavity dumper (Pulse Switch, APE), pumped by a CW DPSS laser (Verdi V-5, Coherent, Inc.) at 532 nm. Output pulses have a pulse width of <200 fs at a variable repetition rate of 5.43 MHz or lower and a tunable wavelength range of 760-900 nm. The output pulses are frequency doubled in a BBO crystal (2 mm, Type I, Eksma). Beam intensity is attenuated by an adjustable $\lambda/2$ plate in front of a Glan-Thompson polarizer to provide vertical polarization with attenuated pulse energy to ensure single photon emission. The system allows for aligning the excitation beam with respect to either right angle detection or front face detection, as illustrated in Figure 3.9. Emission from the sample passes through an optical filter to remove excitation light scattering and a second Glan-Thompson polarizer for either magic angle (54.7°) or anisotropy measurements at 0° or 90° detection with respect to the excitation polarization. Finally, the emission is spectrally resolve using a 100 mm single grating monochromator (H-10, Instruments SA, Inc.) with 4 nm band pass prior detection with a 6 μm microchannel plate photomultiplier (R3809U, Hamamatsu). The MCP-PMT signal is amplified (HFAC-26, Becker & Hickl GmbH) prior to acquisition by the photon counting module (SPC-130, Becker & Hickl GmbH) on which the constant fraction discriminator (CFD), the time-to-amplitude converter (TAC), the analog-to-digital converter (ADC), the data processing logic, and the data memory are integrated. Photon counting acquisition is operated in a reversed start-stop mode where an emission photon triggers the TAC and a delayed reference signal from a photodiode (PD) (PD-30, Opto-Electronics) is used to synchronize a termination signal ("*Sync*" in Figure 3.9). The instrument response function determined by Rayleigh scattering is 25 ps FWHM. The experiments performed here utilized right angle detection from a 1 cm square cuvette with a Schott GG-400 optical filter at magic angle detection.

3.2.3 Steady State Techniques

Absorption Spectra and Extinction Coefficient

Our lab is equipped with two identical UV-Vis spectrophotometers (U-3010 UV/Vis, Hitachi). Samples for measuring the extinction coefficients are prepared from a concentrated 1,4-dioxane stock solution (∼0.01 M) and diluted at least 300-fold with the target solvent. At this level of dilution no distortion by the 1,4-dioxane with respect to spectral shapes, positions and lifetimes are observed. [18] Measurements were carried out in 1 cm quartz cuvettes at concentrations yielding ∼1 OD for absorption spectra to provide confidence due signal intensity. Lambert-Beer law allows one to calculate the extinction coefficient at a known concentration: [19, 20]

$$A = \epsilon L c \tag{3.1}$$

$$\Rightarrow \epsilon = \frac{A}{Lc} \tag{3.2}$$

where A is the absorbance, ϵ is the extinction coefficient, L is the cuvette path length, and c is the concentration of the dye.

Emission Spectra and Quantum Yield

For steady state emission measurements we employ two fluorimeters (SPEX Fluorolog FL2 and Fluorolog FL3, Horiba Jobyn Ivon, Inc.) which allow temperature controlled acquisition in right angle or front face geometries. Emission spectra were corrected with respect to spectral responsitivity using secondary emission standards. [21] For all emission spectra and quantum yield measurements sample concentrations were prepared for an absorbance of <0.1 OD at the excitation wavelength and for single photon counting experiments <0.3 OD. Temperature was set at 25°C ± 0.1 using a water chiller circulating fluid through sample holders unless reported otherwise. Fluorescence quantum yields were measured

relative to project-specific quantum yield standards, listed in each respective chapter, and calculated according to

$$\Phi_S = \Phi_R \left(\frac{n_S^2}{n_R^2}\right)\left(\frac{I_S}{I_R}\right)\left(\frac{1-10^{-0.5\cdot A_R}}{1-10^{-0.5\cdot A_S}}\right) \tag{3.3}$$

where the subscripts S and R are for sample and reference, respectively. Φ is the quantum yield, n the refractive index of the solvent, I is the integrated emission intensity and A is the absorbance at the excitation wavelength.

3.3 Analysis of KGE Data

The acquired data must be corrected and fit using the procedure described in this section. Only then it can provide accurate information.

3.3.1 Group Velocity Dispersion and Time Correction

Most common transparent media like air and glasses are normal dispersive. It means the phase velocity of a wave is frequency dependent. In particular, it is the refractive index n which is frequency dependent described by the simple relation

$$v = \frac{c}{n(\lambda)} \tag{3.4}$$

where v is the phase velocity, c the speed of light in vacuum and $n(\lambda)$ the refractive index. $n(\lambda)$ decreases with increasing wavelength λ: $n(\lambda_{blue}) > n(\lambda_{yellow}) < n(\lambda_{red})$. One common phenomenon which results from this dependence is the material dispersion when white light shines through a prism and a rainbow is created. More importantly for our acquired data is the temporal effect. Fluorescence traverses a umber of dispersive materials

before gating: The solvent the solute is dissolved in, the cell window, optical Schott filter (GG-400), the Glan-laser calcite polarizer and another cell window of the Kerr cell. The sum of the dispersion in these materials causes the time information within the broadband spectra to be "chirped" and have a λ-dependent origin. In principle, one can calculate the time shift across the spectrum if the frequency dependence of all elements is known. Each material's refractive index property is empirically described by the Sellmeier equation: [22]

$$n^2(\lambda) \quad = \quad A + \frac{B_1 \cdot \lambda^2}{\lambda^2 - C_1} + \frac{B_2 \cdot \lambda^2}{\lambda^2 - C_2} + \cdots \tag{3.5}$$

where A, $B_{1,2,..}$ and $C_{1,2,..}$ are material specific Sellmeier coefficients which can be found in optics databases.

Consequently, the sum of all time shifts at a specific wavelength obtained when using Eq. 3.4 with Eq. 3.5 times their individual path lengths (thickness) would equal the time delay. We approach this group velocity dispersion empirically by measuring C153 in cyclcohexane and observe the rise time at each wavelength. C153 in cyclohexane has no dynamics Stokes shift which would alter rise times across the spectra. We analyze the signal rise profile in the wavelength dependent time domain as shown in Figure 3.10.

At each wavelength time zero is considered the half-way point. To obtain these times across the spectrum, spectra of C153 in cyclohexane are measured between ± 3 ps and then each wavelength is fitted using a sigmoid function:

$$I\left(t\right) \quad = \quad \frac{A}{1 + \delta e^{-\beta t}} \tag{3.6}$$

where A is the amplitude, δ is a time offset (not the desired time zero) and β is the rise slope. With the first derivative

$$\frac{\partial I(t)}{\partial t} \quad = \quad \frac{A\beta\delta e^{-\beta t}}{\left(1 + \delta e^{-\beta t}\right)^2} \tag{3.7}$$

and the second derivative

$$\frac{\partial^2 I(t)}{\partial^2 t} = A\left(\frac{2\beta^2\delta^2 e^{-2\beta t}}{(1+\delta e^{-\beta t})^3} - \frac{\beta^2\delta e^{-\beta t}}{(1+\delta e^{-\beta t})^2}\right) \tag{3.8}$$

The intersection with the x-axis in the second derivative in Eq. 3.8 represents the half-way point of the original sigmoid function as illustrated in Figure 3.11 and defines our time zero for a particular wavelength. Solving the second derivative for zero give us

$$0 = \frac{\partial^2 I(t)}{\partial^2 t} \tag{3.9}$$

$$\Rightarrow t_0(\lambda) = \frac{ln(\delta)}{\beta} \tag{3.10}$$

In Figure 3.12 the result for our Kerr-shutter setup is shown. The high noise on the red edge is due to insufficient signal from C153. Fitting based on the data set between 410 - 600 nm with a Sellmeier equation (Eq. 3.5) provides our time correction function.

$$t_{0,fit}(\lambda) = 28.4186 + \frac{15.0536\lambda^2}{\lambda^2 - 11274.7} + \frac{15.0536\lambda^2}{\lambda^2 - 11548.7} \tag{3.11}$$

The data matrix structure is illustrated in Table 3.1. To apply the time correction the matrix is transposed so each column represents a wavelength. An individually shifted time column $t - t_{0,fit}$ (Eq. 3.11 is assigned for each wavelength. Finally, a cubic spline interpolation matches the corrected time spectra with respect to the original time steps.

1	time
λ	$\ddots$

Table 3.1: Kerr data matrix structure

3.3.2 Photometric Correction

The relative quantum efficiency (QE) of virtually any detector is wavelength depend, i.e. a sensor has λ-dependent efficiencies to detect the correct numbers of photons reaching the detector. For example, the human eye is less capable of detecting light in the UV and infrared regions compared to the "visible" range. For quantitatively correct results it is therefore necessary to know the quantum efficiency as a function of wavelength $QE(\lambda)$. Once this correction function has been found, we can obtain the 'true' emission spectra from those directly measured. Measured empirically it can also account for distortions due to optical filters like the Schott GG-400 and the dichroic mirror in front of the optical fiber which is visible in the severe structuring of TPB in Figure 3.13A. The function is obtained with well-known dyes by calculating the ratio between the known fluorescence quantum distribution (FQD) and the measured Kerr-gated spectrum (KG) which yields the correction function:

$$C_{photo} = \frac{FQD}{KG} \tag{3.12}$$

Gardecki et al. [21] published a list of secondary emission standards with FQD data intended primarily for steady state fluorimeter calibration. However, some of these dyes can also be employed for Kerr-gated emission correction because in their proposed solvent the

dynamic Stokes shift is either very fast or non-existent and the integral intensity (i.e. FQD) matches the long-time (≥100 ps) time-resolved emission spectra acquired with KGE. For our setup we use the dyes listed in Table 3.2, measured and averaged 64 times at +100 ps. The procedure to determine the correction function (Figure 3.13A→B) based on multiple emission standards is provided by Gardecki et al. [21] The data matrix illustrated already in Table 3.1 is corrected by simply multiplying each row (equals wavelength) with the corresponding correction factor from Figure 3.13B.

Probe	CAS	Solvent	Emission
TPB	1450-63-1	Cyclohexane	390-570
Coumarin 153	53518-18-6	Methanol	486-678
DCM	51325-91-8	Methanol	556-736

Table 3.2: Secondary emission standards suitable for photometric correction in Kerr-shutter system with respect to excitation (387 nm) and emission range. [21]

3.3.3 IRF Deconvolution

The instrument response function (IRF) dictates the time resolution of an instrument for time-resolved measurements. It can be obtained directly by measuring the Raman signal of a solvent blank. In Figure 3.14 the Raman transient observed in ethanol is shown. Benzene as Kerr medium has a ∼15 % broad nuclear relaxation component (vs. ∼85 % electronic) due to the contribution of orientational polarizability to its nonlinear refractive index (birefringence). [16, 17]. Because of this asymmetric IRF a deconvolution of our Kerr-gated emission is necessary to achieve accurate time information, especially at early time (<1 ps).

Any measured fluorescence signal represents a convoluted response of the sample emis-

sion and the instrument response. A general convolution of two functions is defined by

$$(f * g)(t) = \int_{-\infty}^{+\infty} f(t')g(t-t')dt' \tag{3.13}$$

$$= \int_{-\infty}^{+\infty} f(t-t')g(t')dt' \tag{3.14}$$

Our experimental data is a convolution of an ideal lifetime decay, assumed to be representable as a sum of exponentials and an IRF represented as a sum of Gaussian functions.

$$I(t) = \int_0^{\infty} \overbrace{R(t-t')}^{IRF}\overbrace{D(t')}^{Decay}\,dt' \tag{3.15}$$

I(t) will be composed of a sum of terms of the form

$$\therefore R(t) = \sum_{i=1}^{M} R_i(t) = \sum_{i=1}^{M} a_i \times e^{-\frac{(t-t_i)^2}{2\sigma_i^2}} \tag{3.16}$$

$$\therefore D(t) = \sum_{j=1}^{N} D_j(t) = \sum_{j=1}^{N} b_j \times e^{-\frac{t'}{\tau_j}} \tag{3.17}$$

$$\Longrightarrow I(t) = \sum_{i=1}^{M}\sum_{j=1}^{N} a_i b_j \int_0^{\infty} e^{-\frac{(t-t_i-t')^2}{2\sigma_i^2}} e^{-\frac{t'}{\tau_j}}\,dt' \tag{3.18}$$

where M is the number of Gaussians used to describe the instrument response function (IRF) and N is the number of exponentials to describe the fluorescence lifetime decay. t_i is an wavelength-dependent time shift which allows one to correct for a displacement of time zero since the experiment might not be exactly set to zero.

For a complete derivation of the deconvolution function based on the above listed elements please see Appendix B.

This fit function allows us to fit the data with respect to the IRF described by 3 Gaussian functions, a selectable number of exponentials describing the fluorescence lifetimes and

a time shift correction. We are using MathWorks^{TM}MatLab® nonlinear least-squares data fitting routine for processing. The Gaussian functions are allowed to vary by $\sim$ 15-20 % in width and time relative to each other to account for varying daily performance. As an additional boundary condition we restrict the time shifts t_i across the spectra to match a second polynomial function to account for minor deviations between the absolute time shift and the correction function measured as describes in section 3.3.1. As a result we obtain an idealized data matrix the effects of the IRF and time shift are removed.

3.3.4 Data Fitting

Ultimately, we want to obtain information about spectral shapes of absorption and emission. Those can typically fitted with a lognormal function:

$$F(\nu,t) \quad = \quad h \times exp\left\{ -ln2 \left[\frac{ln\left(1+\frac{2\gamma\,(\nu-\nu_p)}{\Delta}\right)}{\gamma} \right]^2 \right\} \tag{3.19}$$

where h is the intensity amplitude, ν_p the peak position (can be in frequency, wavenumber or wavelength), Δ the width parameter (in the unit chosen for ν_p), and γ is an asymmetry parameter. If you would have a symmetric shape then $\gamma = 0$ and Eq. 3.19 would simplify to a Gaussian function. When $\gamma \neq 0$, a lognormal function is a skewed Gaussian function.

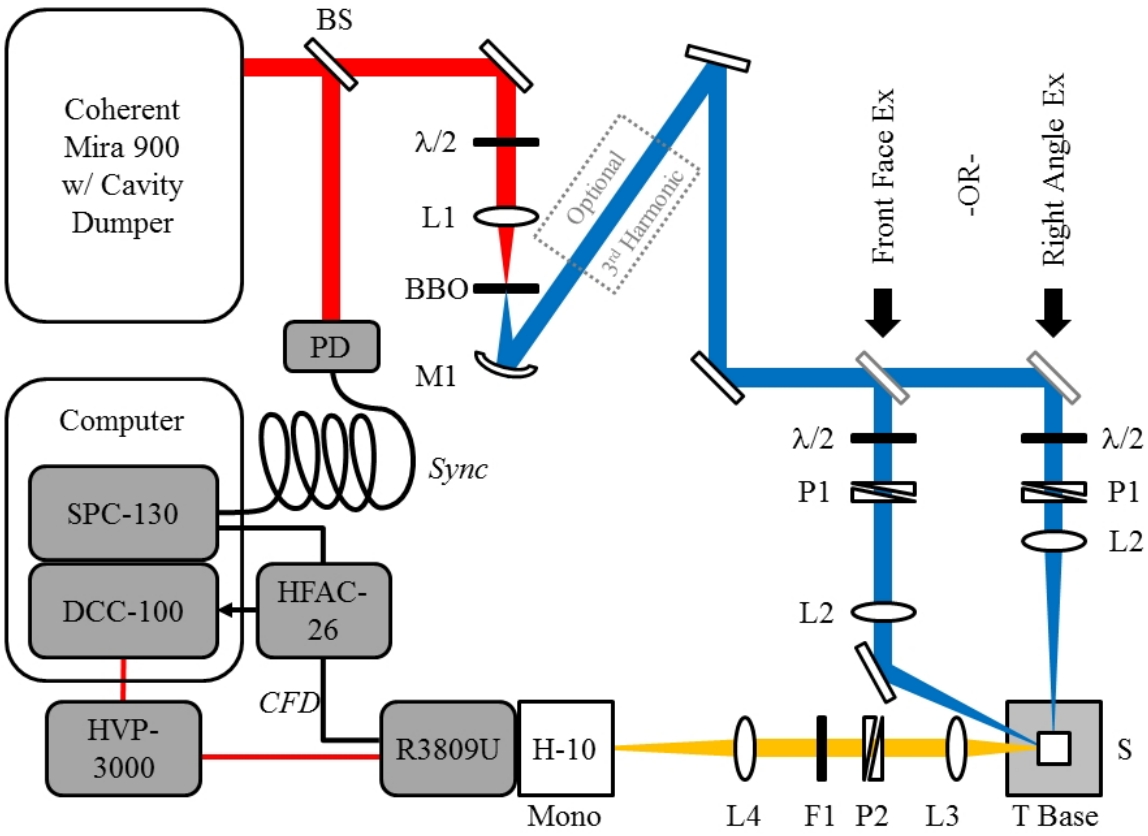

Figure 3.9: TCSPC Setup: *BS* beam splitter (5% reflectivity; 95% transmittance); *PD* Photo Diode (Opto-Electronics, PD-30); $\lambda/2$ plate to rotate the polarization from horizontal to vertical; *L1* 50 mm focal length lens; *BBO* 0.2 mm BBO (*Eksma*, 6x6x2 mm, $\theta = 29.2°$, $\phi = 90°$, Type I); *M1* 50 mm focal length 0° dichroic mirror; $\lambda/2$ retarder for pulse energy attenuation; *P1* Glan-Thompson polarizer for vertical excitation; *L2* 250 mm focal lens; *S* temperature controlled sample holder; *L3* 50 mm focal lens; *P1* motorized Glan-Thompson polarizer for variable emission polarization detection; *F1* GG-400 optical filter; *L4* 100 mm focal lens; *H-10* monochromator (H-10, Instruments SA, Inc.); *R3809U* 6 μm microchannel plate photomultiplier (Hamamatsu, R3809U). The single photon counting electronics are described in 3.2.2.

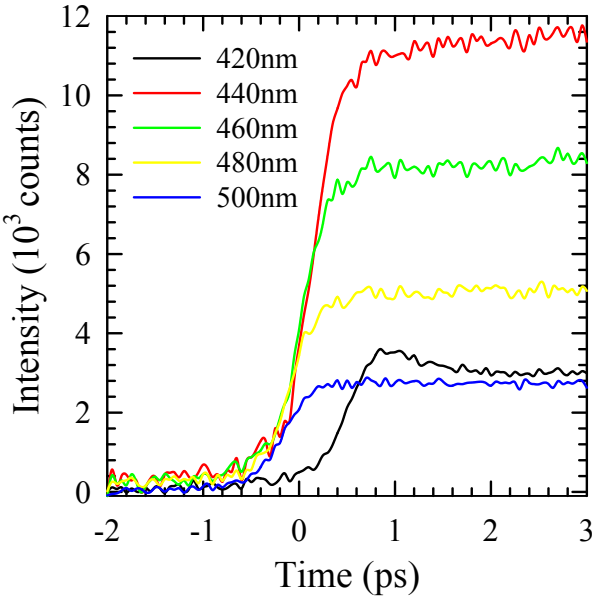

Figure 3.10: Time shifts due to group velocity dispersion using C153 in cyclohexane which has very little solvent dynamics that would otherwise perturb the rise time.

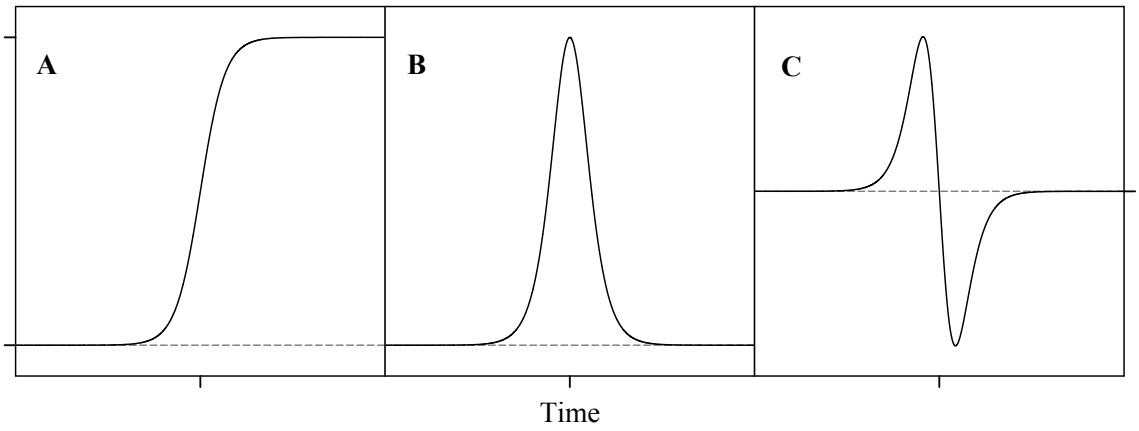

Figure 3.11: Sigmoid function (A) and its first (B) and second (C) derivative. The x-axis intersection provides the graphical description of the half-point.

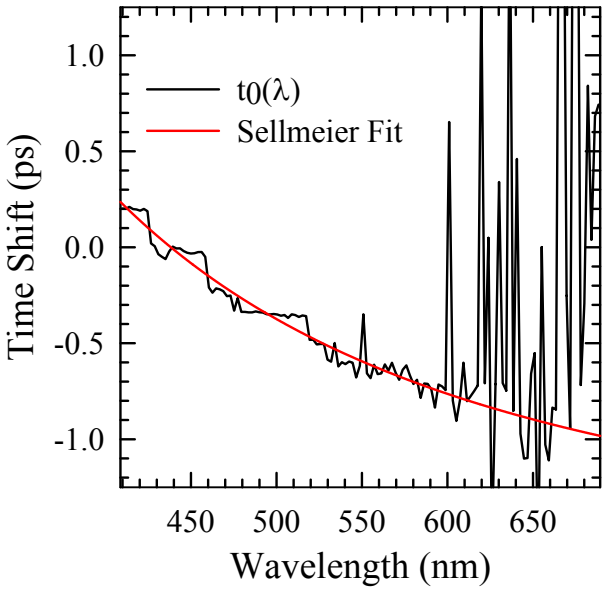

Figure 3.12: Measured time shift versus wavelength and fitted correction function (Eq. 3.11) for Kerr Experiments .

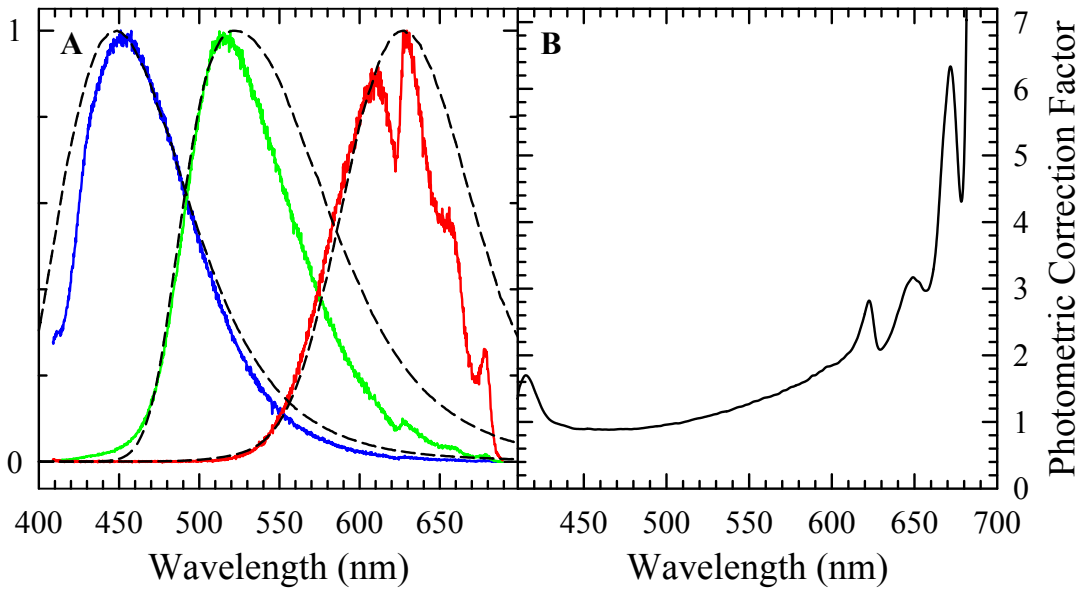

Figure 3.13: *Left*: Kerr-gated emission spectra at 100 ps (TPB blue, C153 green, DCM red) and their respective FQD emission spectra. The structure within the DCM signal is due to a 0° dichroic mirror in front of the optical fiber; *Right*: Resulting correction function C_{photo}

.

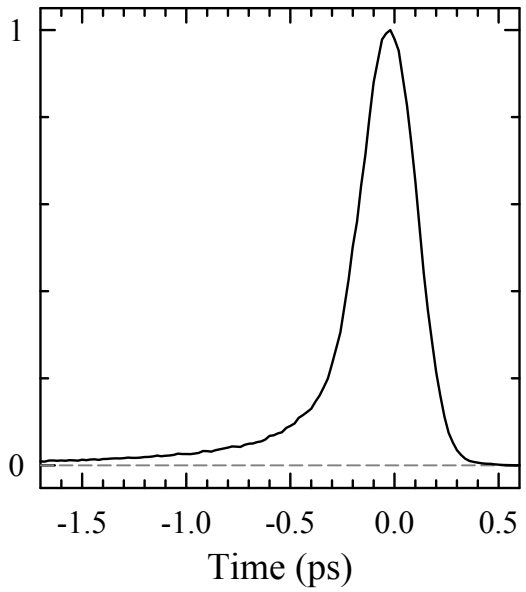

Figure 3.14: Transient solvent Raman line of ethanol at 436 nm as IRF measured with benzene as Kerr medium in our setup.

Chapter 4

Malononitriles

4.1 Abstract

The solvent dependence of the photophysical properties of three naphthylmethylene malononitriles, 1-(1-naphthalenylmethylene)-propanedinitrile (1-MN), 2-(2-naphthalenylmethylene)-propanedinitrile (2-MN), and 2-(3,4-dihydro-1(2H)-phenanthrenylidene)-propanedinitile (r2-MN), were studied in order to determine their potential utility as fluidity probes and to make comparisons to the better studied benzylidene malononitriles. Density functional calculations were used to understand conformational possibilities related to rotation about the vinyl - aromatic bond ("τ"). Absorption and emission frequencies, extinction coefficients, fluorescence quantum yields, and fluorescence lifetimes were measured in a collection of 11 representative solvents. Both the computational and experimental results indicate that the $S_0 \rightarrow S_1$ transitions of these molecules have substantial charge-transfer character and produce highly polar excited states. Emission appears to result from relaxed S_1 states which do not differ qualitatively from the Frank-Condon states reached by absorption. In 2-MN, time-resolved emission reveals the presence of two ground-state conformers ("a" and "b" differing by $\sim 180^\circ$ rotation about τ) coexisting in low-polarity solvents. In contrast, 1-MN appears to exist primarily as a single dominant ground-state conformer. Fluorescence

lifetimes vary from ∼1 ps in 1-MN to ∼200 ps in 2-MN(a) at room temperature. With the exception of 2-MN(a), the lifetimes vary systematically with solvent in a manner similar to what is observed in the benzylidene malononitriles. Both solvent polarity and fluidity appear to be important determinants of lifetime. The primary mechanism of fluorescence decay in naphthylmethylene malononitriles is likely to be the same as that of the benzylidene malononitriles - twisting about the double bond in S_1, which leads to rapid internal deactivation via a conical intersection with S_0.

4.2 Introduction

Benzylidenemalononitriles are a class of molecules that have long been studied for their biological activity [23, 24] and fluorescence sensing properties. [4, 18, 25] We have recently examined three such molecules, shown in the top row of Figure 4.1, in order to better understand the origins of their environmentally sensitive fluorescence. [18,26,27] DMN and JDMN have been widely used as local fluidity sensors in a variety of contexts since the pioneering work of Law and Loutfy in the early 1980s. [28, 29] In low viscosity solvents these molecules are weakly fluorescent, with fluorescence lifetimes in the few picosecond range, [18] whereas in high viscosity solvents [30] or polymers [31] their fluorescence yields and lifetimes increase markedly.

Some disagreement still exists concerning whether the mechanism responsible for this environmental sensitivity is a twisted intramolecular charge transfer (TICT) process [32] involving rotation about the benzene vinyl single bond (τ in Figure 4.1) or a (null) "isomerization" about the double bond (ω). Computational work by our group [26] and others [33,34] favors the isomerization mechanism, which leads to a conical intersection between S_1 and S_0 and rapid internal conversion. In the asymmetric variant CCVJ this mechanism can be verified experimentally because the isomerization leads to long-lived photoproducts. [27] (The potential presence of photoproducts resulting from this isomerization means

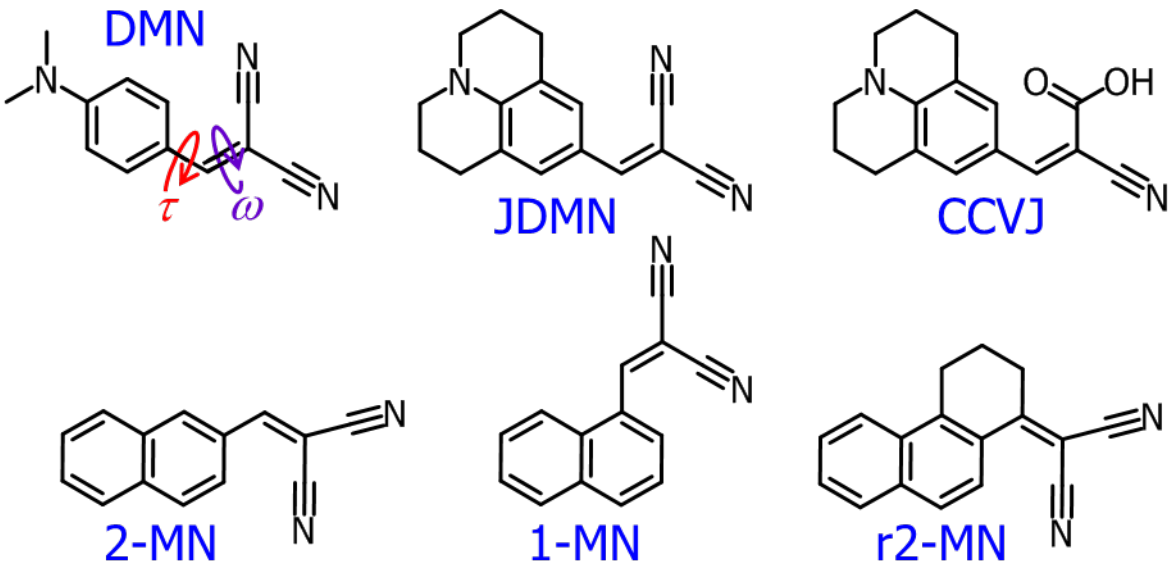

Figure 4.1: Scheme of previous malononitriles (top row) and currently investigated naphthalene malonitriles studied by our group.

that CCVJ and related molecules, which have overshadowed DMN and JDMN as biological "rotor probes", [3, 35] should be used with caution.) However, the question of mechanism is not completely settled. A recent study of JDMN by Gaffney and coworkers [36] has suggested that a long-lived TICT state may also be present in these molecules, at least when accessed with significant excess energy. Finally, recent work has made it clear that the fluorescence of DMN, JDMN, and CCVJ respond very similarly to environment, [18, 27, 37] with both friction and polarity playing important roles. [18] But, even in simple solvents, it remains unclear how one should interpret the often weak viscosity scaling and apparent polarity dependence of these "fluidity" sensors.

The present study seeks to provide additional perspective on such questions by exploring the photophysics and solvent sensitivity of several related molecules, depicted in the lower portion of Figure 4.1. In these naphthylmethylene malononitriles the dimethy-

laniline donor of the former probes is replaced by naphthalene. We anticipated that this change would significantly alter the details of the S_1 potential energy surface on which the reaction is expected to sensitively depend [26] while maintaining electronic spectra in an experimentally convenient range. The differences in electronic and steric interactions between the donor and acceptor groups in 1-MN versus 2-MN might also be expected to produce significantly different excited-state behavior in these two molecules. The conformational restrictions imposed in the variant r2-MN should eliminate the possibility of TICT state formation, providing additional perspective on the deactivation mechanism. In the present work we provide the first systematic look at the electronic structures and photophysical properties of these molecules in a selected collection of solvents and attempt to relate their behavior to those of DMN and JDMN.

Compared to the extensive work on benzylidene malononitriles, only limited and sporadic attention has been paid to vinyl malononitriles with other aromatic donors. Three papers have reported systematic studies of such systems. [38–40] In a brief note, Aihara et al. [38] measured the absorption frequencies and extinction coefficients of a collection of nine aromatic malononitriles (Ar-CH_2=$C(CN)_2$) in chloroform. They observed a clear correlation between the frequencies of the lowest absorption bands and the ionization potentials of the aromatic subsystem, indicating that the (Franck-Condon) S_1 states of these molecules are of intramolecular charge transfer (ICT) character.

The most extensive study to date was performed by Katritzky et al. [39] who measured absorption and emission spectra of five Ar-CH_2=$C(CN)_2$ molecules with Ar = benzene, naphthalene (1-MN), phenanthrene, anthracene, and pyrene in a collection of eight solvents. They found that whereas the absorption bands did not vary much with solvent polarity, the emission spectra did. They interpreted this observation as indicating that the emission comes from an ICT state which is distinct from the Franck-Condon state reached

by absorption. They also noted the fluorescence of these molecules is very weak (quantum yields typically less than 10^{-3}), which led them to suggest that this ICT state was likely to be a TICT state, achieved by a 90° rotation about the aryl-vinyl bond.

In the most recent study, Wang et al. [40] measured the emission spectra of 1-MN and the same anthracene and pyrene variants as the Katritzky study in poly(methylmethacrylate) at pressures of up to nearly 80 kbar. They reported emission of all three solutes to consist of two distinct bands, which they interpreted as emission from a locally excited (LE) state and an ICT state. With increasing pressure the intensity of the overall emission as well as the relative intensity of the ICT state increased dramatically. In the anthracene case, the main focus of their work, they observed the total emission intensity to increase ∼100-fold and the ICT intensity by ∼400-fold at 74 kbar relative to atmospheric pressure. Wang et al. analyzed this pressure dependence in terms of a model in which pressure affects the relative populations of two ground-state conformers which independently give rise to the LE and ICT emission, rather than to an LE→ICT reaction occurring in the excited state. However, we believe that this analysis and interpretation are incorrect because the authors neglected the fact that the 325 nm excitation used in their experiments excites into S_2. Based on the relative absorption and emission frequencies, it is clear that rather than LE and ICT emission, what was being observed was emission from S_2 and S_1, with this violation of Kasha's rule being allowed by the very weak character of the S_1 emission even in a polymer host at low pressures.

Two additional studies should also be mentioned relative to the present work. Liu and coworkers [41] measured the effect of irradiation on the absorption spectra of 2-MN and 1-MN in a 77 K glass, in ordered to provide evidence for the "hula-twist" mechanism of isomerization in rigid media. [42] In this mechanism isomerization about a double bond is accomplished by concerted motion of this bond and a neighboring bond in a manner that

minimizes the volume required. This mechanism has a higher intrinsic activation energy than direct rotation about the isomerizing bond but may be preferred in rigidified media. In the case of 2-MN and 1-MN the hula-twist mechanism converts an extended conformer into a more compact conformer (**a**→**b** in Figure 4.2). Liu and coworkers reported changes to the absorption spectra upon irradiation consistent with the hula-twist mechanism occurring in 1-MN. In 2-MN, either the change did not occur or the spectroscopic changes produced were too small to observe.

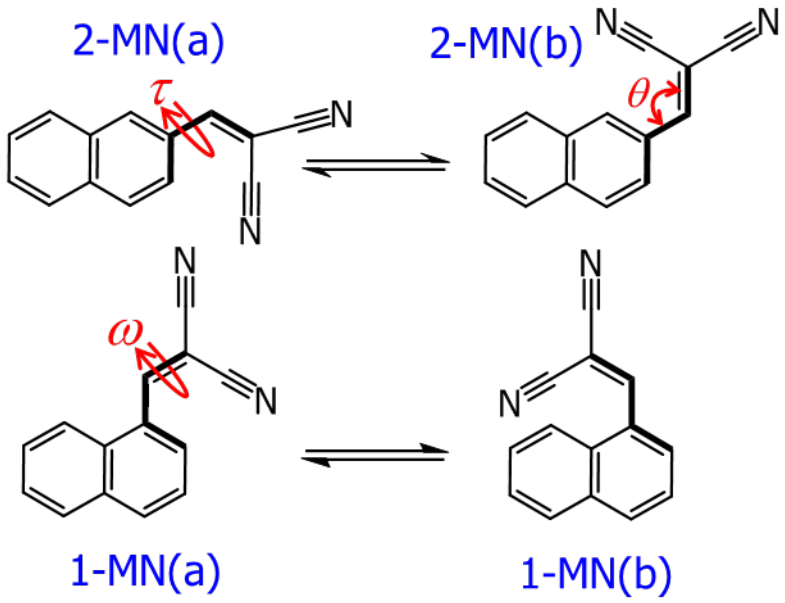

Figure 4.2: Defined naphthalene malononitrile bond rotations and their confomers.

Finally, we note that the present work was initiated partly as a follow-up to a survey of the solvent dependence of the absorption and emission spectra of 2-MN and r2-MN by Donovan [43] under the guidance of one of us (BW). This earlier study examined the solvatochromism of both of solutes, and some of these prior results are comparable to what we report herein. However, based on the present work, we now believe that the

r2-MN emission data reported by Donovan are incorrect due to the presence of low-levels of a fluorescent impurity which dominated the very weak fluorescence of r2-MN. All of the results reported here have been collected subsequent to this earlier work and with independently synthesized solutes.

4.3 Experimental Section

Solutes: *1-(1-naphthalenylmethylene)-propanedinitrile* (1-MN, CAS 2972-83-0) was synthesized by Knoevenagel condensation [44, 45] as follows. 1-Naphthalenecarboxaldehyde (4.81 g; 30.8 mmol), propanedinitrile (2.16 g; 32.6 mmol) and zinc chloride (4.51 g; 33.1 mmol) were mixed and ground together. The ground mixture was placed in a glass test tube immersed in a boiling water bath, allowed to melt, and stirred occasionally for 20 minutes. The crude product was dissolved in 5% aqueous ethanol, washed twice in diethyl ether and dried overnight under vacuum, resulting in 3.08 g 1-(1-naphthalenylmethylene)-propanedinitrile (15.1 mmol; 49%). No further purification was required. ^{1}H NMR (300 MHz, $CDCl_3$): δ 7.711 (3H, m), 8.104 (1H, t), 8.296 (3H, m), 9.207 (1H, s).

2-(2-naphthalenylmethylene)-propanedinitrile (2-MN, CAS 2972-84-1) was synthesized similarly using 2-naphthalenecarboxaldehyde (2.36 g; 15.11 mmol), propanedinitrile (1.06 g; 16.04 mmol) and zinc chloride (2.15 g; 15.77 mmol). 2.36 g of 2-(2-naphthalenylmethylene)-propanedinitrile (12.87 mmol; 85%) were obtained. ^{1}H NMR (300 MHz, $CDCl_3$): δ 7.701 (2H, m), 8.130 (4H, m), 8.484 (2H, m).

3,4-Dihydro-1(2H)-phenanthrenylidene malononitrile (r2-MN; CAS unknown or unassigned) was synthesized according to Ettenger et al. [46] using 3,4-dihydro-1(2H)-phenanthreone (1.91 g; 9.73 mmol), propanedinitrile (2.10 g; 31.17 mmol), and sodium acetate (1.80 g; 21.94 mmol). Purification was done by column chromatography using 5% ethyl acetate in hexanes three times. 0.24 g of r2-MN (1 mmol; 10%) were obtained. ^{1}H NMR (300 MHz, $CDCl_3$): δ 2.260 (2H, m), 3.114 (2H, t), 3.438 (2H, t) 7.693 (2H, m) 7.930 (1H, d) 8.003 (1H, d) 8.170 (1H, d) 8.257 (1H, d). Unfortunately, even after three purification steps a

fluorescent impurity at the level of 1-2% remained in this sample. The impurity has a nanosecond lifetime and its emission sufficiently dominated the steady-state emission of r2-MN that it was not suitable for steady-state emission experiments.

Solvents: Most solvents used were from Sigma-Aldrich and were of spectroscopic or HPLC grade. They were used as received except for some being dried over molecular sieves and filtered through a 0.45 μm syringe filter prior use.

Spectroscopic Measurements: A Hitachi U-3010 UV/Vis in combination with a SPEX Fluorolog FL212 spectrometer have been used for steady state absorption and emission measurements. Emission spectra were corrected with respect to spectral responsitivity using secondary emission standards. [21] Samples were prepared from a concentrated 1,4-dioxane stock solution ($\sim$0.01M) and diluted at least 300-fold with the target solvent. At this level of dilution we could not observe any distortion by the dioxane with respect to spectral shapes, positions or lifetimes. Measurements were carried out in 1 cm quartz cuvettes at concentrations providing $\sim$1 OD for absorption spectra and $<$0.1 for emission spectra, quantum yields and single photon counting experiments. Temperature was set at 25°C$\pm$0.1 using a water chiller circulating fluid through sample holders in all experiments except for the Kerr-gated experiments, which were at 21°C$\pm$2. Deoxygenation did not have a noticeable effect and therefore most samples were not deoxygenated. Fluorescence quantum yields were measured relative to quinine sulfate in 0.05 M H_2SO_4 ($\Phi_{em} = 0.508$) and excited at 390 nm [47, 48] and calculated according to

$$\Phi_S = \Phi_R \left(\frac{n_S^2}{n_R^2}\right)\left(\frac{I_S}{I_R}\right)\left(\frac{1-10^{-0.5\cdot A_R}}{1-10^{-0.5\cdot A_S}}\right) \tag{4.1}$$

where n is the solvent refractive index, I the integrated emission intensity, and A the absorbance of the sample (S) and reference (R).

Time-resolved data were acquired using two different instruments. The first is a Kerr-gated emission (KGE) instrument with subpicosecond time resolution, which has been described in detail previously. [16] The KGE system is based on a 250 kHz amplified Ti:sapphire laser system (Coherent Innova 400/Mira 900/RegA 9050) tuned to 775 nm with a power output of 1.5 W. Frequency doubling provided 387 nm light for excitation of the circulating sample in a 0.5 mm flow cell. The fundamental was used to gate the emission in a 0.7 mm thickness benzene cell which served as the Kerr medium. The instrumental response from this system was ∼350 fs (FWHM) based on solvent Raman signal. Data sets were time corrected for group velocity dispersion and intensity corrected for CCD responsitivity and gating efficiency. A deconvolution procedure was also applied in some cases to increase confidence in the kinetics observed at early times.

The time correlated single photon counting (TCSPC) technique employed here utilizes a cavity dumped Ti:sapphire oscillator (Coherent Mira 900 + PulseSwitch) pumped by a CW laser (Coherent Verdi V-5) at 532 nm. Output pulses have a width of <300 fs at a variable repetition rate of 5.43 MHz or lower and a tunable wavelength range of 760 - 900 nm. The mode-locked output of the laser is frequency doubled in a 2 mm BBO crystal. Beam intensity is attenuated by an adjustable $\lambda/2$ plate in front of a Glan-Thompson polarizer to provide vertical polarization with restricted excitation energy to ensure single photon collection. The system allows alignment of the excitation beam for either right angle or front face detection. Emission from the sample passes through an optical filter to remove scattered excitation light and an analyzing Glan-Thompson polarizer for either magic angle (54.7°) other angles relative to the excitation. Finally, the emission is spectrally resolved using a 100 mm single grating monochromator (Instruments SA, Inc. H-10) with a 4 nm band pass prior detection with a 6 μm microchannel plate photomultiplier (MCP-PMT, Hamamatsu, R3809U). The MCP-PMT signal is amplified (Becker & Hickl HFAC-26) and sent to a photon counting module (Becker & Hickl SPC-130) on which

the constant fraction discriminator, time-to-amplitude converter (TAC), analog-to-digital converter, data processing logic, and the data memory are integrated. Photon counting acquisition is operated in a reversed start-stop mode in which an emission photon triggers the TAC and a delayed reference pulse from a photodiode (Opto-Electronics PD-30) is used to synchronize a termination signal. The instrument response function determined by a scattering solution is typically 25 ps FWHM. The experiments performed here utilized 380-390 nm excitation light, right angle collection from a 1 cm square cuvette, a GG-400 optical filter to reject scattered excitation light, and magic angle detection.

Computational Methods: Several quantum chemical methods were used to study the molecular structures and photophysical properties relevant to the excited-state dynamics. Most calculations involved time-dependent density functional theory (TDDFT) with the B3LYP and CAM-B3LYP functionals and a 6-31G(d,p) basis set. Møller-Plesset perturbation theory (MP2) was also used to obtain an S_0 molecular geometry for comparison to X-ray structures and the B3LYP results. Solvent effects were explored using implicit solvent calculations with the polarizable continuum model. [49] Most calculations were performed using Gaussian 09. [50] For exploring the nature of the excited-state potential upon rotation about the double bond, a few spin-flip TDDFT calculations [51–53] were also performed using the GAMESS [54] electronic structure program. We adopted Minezawas method [52] and used the BHHLYP hybrid functional with the Dunning-Hay double-ζ plus polarization DH(d,p) in GAMESS) basis set. [55]

4.4 Results

4.4.1 Electronic Structure Calculations

1-MN and 2-MN can exist as two conformers which differ by rotation around the malononitrile single bond, defined by torsion angle τ. As shown in Figure 4.2, we label the more

extended conformer "**a**" ($\tau \sim 0°$) and the other conformer "**b**" ($\tau \sim 180°$). Results of ground-state optimizations originating from initial $\tau = 0°$ and 180° geometries are compiled in Table 4.1.

We first consider 2-MN. For this isomer, DFT (B3LYP/6-31G(d,p)) calculations predict both conformers **a** and **b** to be planar and to have virtually identical energies and dipole moments. MP2/6-31G(d,p) calculations predict either a very small (2-MN(a), 6°) or moderate (2-MN(b), 25°) degree of nonplanarity caused by repulsion between one CN group and a ring H atom. This repulsion is partly alleviated by an opening of the vinyl angle θ (Figure 4.2). No crystal structure of 2-MN is available for comparison, but experimental data are available for the related molecules benzylidene malononitrile (BzMN) and 2-vinylnapthalene (2-VN). Spectroscopic studies of 2-VN suggest that the **a** conformer is planar, but are indecisive concerning the **b** conformer. [56] Similarly to 2-MN, B3LYP calculations predict both conformers of BzCN to be planar whereas MP2 calculations predict nonplanar forms, $\tau(\mathbf{a}) = 15°$ and $\tau(\mathbf{b}) = 150°$. In the crystal, BzMN is nonplanar, $\tau = 11°$, [57, 58] and the B3LYP ($\tau = 0°$) and MP2 ($\tau = 23°$) predictions bracket this value. (Other comparisons to BzMN X-ray data are provided in Table 4.3) Based on these comparisons we conclude that 2-MN(a) is likely to be planar or nearly so in the ground state, whereas 2-MN(b) probably twisted by a moderate angle, comparable to the 11° twist measured for BzMN. Both model chemistries predict only a slightly lower energy for the **a** conformer and nearly equal dipole moments for both conformers. On this basis we expect both the **a** and **b** conformers of 2-MN to be significantly populated in the room-temperature experiments conducted here.[1]

The ground-state potential energy profile of 2-MN as a function of the torsion angle

[1]The 5.7 kJ/mol difference between the MP2 calculated Gibbs energies from the MP2 calculations results from a very low frequency (3 cm^{-1}) torsional vibration about the τ angle in the case of the **a** conformer. The entropic benefit of this vibration may be exaggerated by the harmonic free energy calculations employed here.

τ is shown in Figure 4.3(a) Because of the possibility of TICT state formation in S_1, we performed torsional scans using both the B3LYP functional (black circles) and its Coulomb attenuated version, [59] CAM-B3LYP (red triangles). In the ground state, similar results are obtained using these two functionals. Both show barriers to interconversion of **a** and **b** conformers to be $\sim$30 kJ mol^{-1} in 2-MN, which is considerably larger than the barrier in 2-VN (10-20 kJ mol^{-1}) [56].

r2-MN was synthesized as a torsionally restricted analogue of 2-MN(a). While we will show that it does share many spectroscopic features in common with 2-MN (**a** or **b**), joining the naphthalene ring and malononitrile groups in this way renders r2-MN significantly nonplanar, $\tau \sim 30^\circ$ (Table 4.1). This nonplanarity relieves some of the strain on vinyl angle allowing θ to decrease, but it also causes some twisting of the C=C bond, denoted by ω (see Figure 4.2).

In the case of 1-MN, steric repulsion leads to both **a** and **b** conformers being significantly nonplanar (Table 4.1, see also Figure 4.6). The **a** conformer is calculated to be preferred in the gas phase and it is the form found in the crystalline state, [60] where $\tau = 38^\circ$. In light of the calculated energy differences and its larger dipole moment (see below) it seems likely that 1-MN(a) is the dominant ground-state conformer in solution. In this conformer there is also a modest twist about the double bond, calculated to be $\omega \sim 3^\circ$ by DFT and MP2 and measured to be $\omega \sim 5^\circ$ in the crystal. [60] The calculated torsional potential of 1-MN (Figure 4.3(b)) shows a slightly smaller barrier separating the **a** and **b** conformers than in 2-MN, but the overall barrier to 180° rotation is comparable. Comparisons to available X-ray data on 1-MN [60] and r2-MN [46] (Tables 4.4 and 4.5) indicate slightly greater accuracy for the DFT predictions of S_0 properties, and we will primarily focus on these calculations in the remainder of the discussion.

	B3LYP/6-31G(d,p)					MP2/6-31G(d,p)				
	ΔE (kJ mol^{-1})	ΔG (kJ mol^{-1})	τ	θ	$\mu(D)$	ΔE (kJ mol^{-1})	ΔG (kJ mol^{-1})	τ	θ	$\mu(D)$
2-MN(a)	(0)	(0)	0°	131.6°	7.7	(0)	(0)	6°	130.6°	6.6
2-MN(b)	1.4	0.8	180°	131.7°	7.2	0.5	5.7	156°	128.4°	6.0
r2-MN	–	–	−26°	124.4°	7.7	–	–	−34°	122.8°	6.5
1-MN(a)	(0)	(0)	27°	129.9°	7.1	(0)	(0)	43°	125.8°	5.8
1-MN(b)	12.9	13.3	138°	130.6°	6.5	5.8	5.5	131°	126.4°	5.3

Table 4.1: Calculated Ground State Properties. ΔE is the difference in electronic energy and ΔG is the Gibbs free energy (298 K) relative to the lowest energy conformer. τ, θ and ω are the angles defined in Scheme 4.1 and μ is the dipole moment.

		S_0	S_1					S_2				
		μ_0 (D)	μ_1 (D)	$\Delta\mu_{01}$ (D)	ν_{01} ($10^3 cm^{-1}$)	M_{01} (D)	f_{01}	μ_2 (D)	$\Delta\mu_{02}$ (D)	ν_{02} ($10^3 cm^{-1}$)	M_{02} (D)	f_{02}
2-MN(a)	B3LYP	7.7	15.0	7.5	26.5	3.3	0.13	10.8	3.2	30.9	6.5	0.62
	CAM-B3LYP	7.4	13.5	6.2	31.3	4.4	0.29	10.5	3.2	34.1	5.8	0.55
2-MN(b)	B3LYP	7.2	14.6	7.5	25.3	2.9	0.10	9.8	2.7	30.3	5.8	0.48
	CAM-B3LYP	6.9	13.0	6.3	30.1	4.0	0.23	9.9	3.0	33.5	5.0	0.39
r2-MN	B3LYP	7.7	14.5	7.4	26.1	3.1	0.12	10.3	3.0	30.6	5.6	0.44
	CAM-B3LYP	7.5	12.8	5.9	30.9	4.1	0.25	9.9	3.0	34.2	4.8	0.36
1-MN(a)	B3LYP	7.1	13.2	6.2	26.0	4.8	0.29	13.4	6.3	30.7	1.4	0.03
	CAM-B3LYP	6.8	12.2	5.5	30.3	5.3	0.40	10.8	4.1	35.2	1.3	0.03
1-MN(b)	B3LYP	6.5	11.8	6.1	25.8	4.1	0.21	12.1	6.2	30.8	1.2	0.02
	CAM-B3LYP	6.1	11.6	6.1	30.4	4.4	0.28	9.4	3.7	35.4	1.0	0.02

Table 4.2: Excited-State and Transition Properties from TD Calculations at S_0 Geometries. μ_i is the permanent electric dipole moment of state $S_i, i = 0, 1, 2$ and $\Delta\mu_{0i}$, ν_{0i}, M_{0i}, and f_{0i} are the change in dipole moment, the transition energy, transition dipole moment, and the oscillator strength of the $0 \rightarrow i$ transition.

Characteristics of the lowest energy electronic transitions and electric dipole moments based on gas-phase TDDFT calculations are summarized in Table 4.2. Additional calculations including implicit solvent are provided in Table 4.6. In all molecules/conformers both functionals predict S_1 to be separated from S_2 by 2900-5000 cm^{-1}. Vertical transition energies (ν_{01}, ν_{02}) calculated with the CAM-B3LYP functional are all 3200-4800 cm^{-1} larger than the B3LYP calculations. As far as these transition energies are concerned, the B3LYP calculations are the more realistic. Figure 4.4 compares experimental absorption spectra in n-hexane to gas-phase B3LYP calculations. As illustrated here, the B3LYP calculations are in reasonable agreement with experiment as regards the frequencies and relative oscillator strengths of the low-energy transitions. The same is true in the case of r2-MN, whose transition properties are close to those of 2-MN(a). Self-consistent reaction field calculations in cyclohexane (Table 4.6) are similar to those shown in Figure 4.4, but with the S_1 and S_2 transitions red-shifted by about 800 cm^{-1}. The comparison between experiment and CAM-B3LYP calculations (Figure 4.5 and Table 4.2) is much poorer; all transition frequencies are calculated higher than observed. As will be seen later, the transition strengths calculated using CAM-B3LYP are also in poorer agreement with experiment than those calculated with B3LYP. Thus, the Coulomb attenuation correction is not helpful for describing these transitions, despite their partial charge-transfer character. We will therefore focus on the B3LYP calculations henceforth. A final observation to be made on the basis of Figure 4.4 (and Table 4.2) is that these calculations predict that it would be difficult to distinguish between the **a** and **b** conformers of either 2-MN or 1-MN in the experimental spectra.[2]

[2]We note that the prediction of only a modest blue-shift of the S_1 absorption of 1-MN(b) compared to 1-MN(a) is consistent with the low-temperature isomerization data of Krishnamoorthy et al. [41]

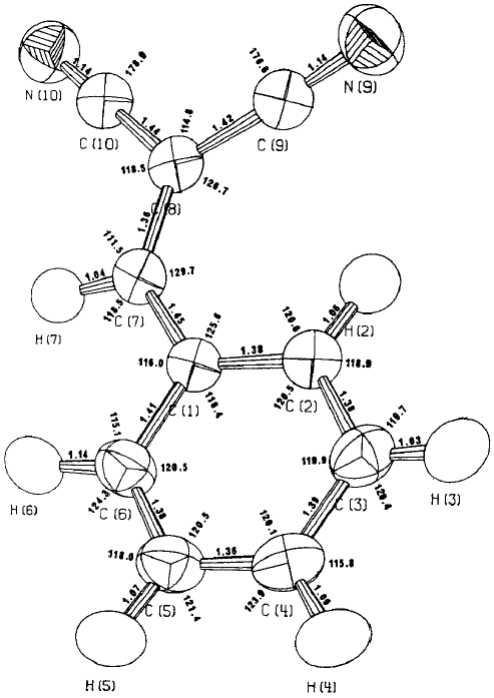

Method	R_{avg}^{ring}	R_{range}^{ring}	$R_{C0-C\alpha}$ (1-7)	$R_{C\alpha=C\beta}$ (7-8)	$R_{C\beta-C\chi}$ (8-9,8-10)	$R_{C\chi\equiv N}$ (9-9,10-10)
X-Ray	1.38	1.36-1.41	1.446	1.360	1.430	1.140
MP2	1.399	1.4392-1.408	1.457	1.360	1.436	1.184
B3LYP	1.400	1.390-1.412	1.453	1.367	1.434	1.164

Method	Bond Angle θ C(1-7-8)	Torsion angle τ C(2-1-7-8)
X-Ray	129.7	11.0
MP2	128.9	23.1
B3LYP	131.6	0.0

Table 4.3: Comparison of calculated and X-ray structures of benzylidene malononitrile. All bond lengths (R) in Å and angles in degrees. R_{avg}^{ring} and R_{range}^{ring} are the average and range of bond lengths in the benzene ring. $R_{C0-C\alpha}$, $R_{C\alpha=C\beta}$, $R_{C\beta-C\chi}$, $R_{C\chi\equiv N}$ are the bond lengths proceeding out from the ring system (0 = ring, then α, β, χ). Figure and X-Ray data from D. A. Wright and D. A. Williams, *J. Cryst. Mol. Struct.* **2**, 31 (1972). [58]

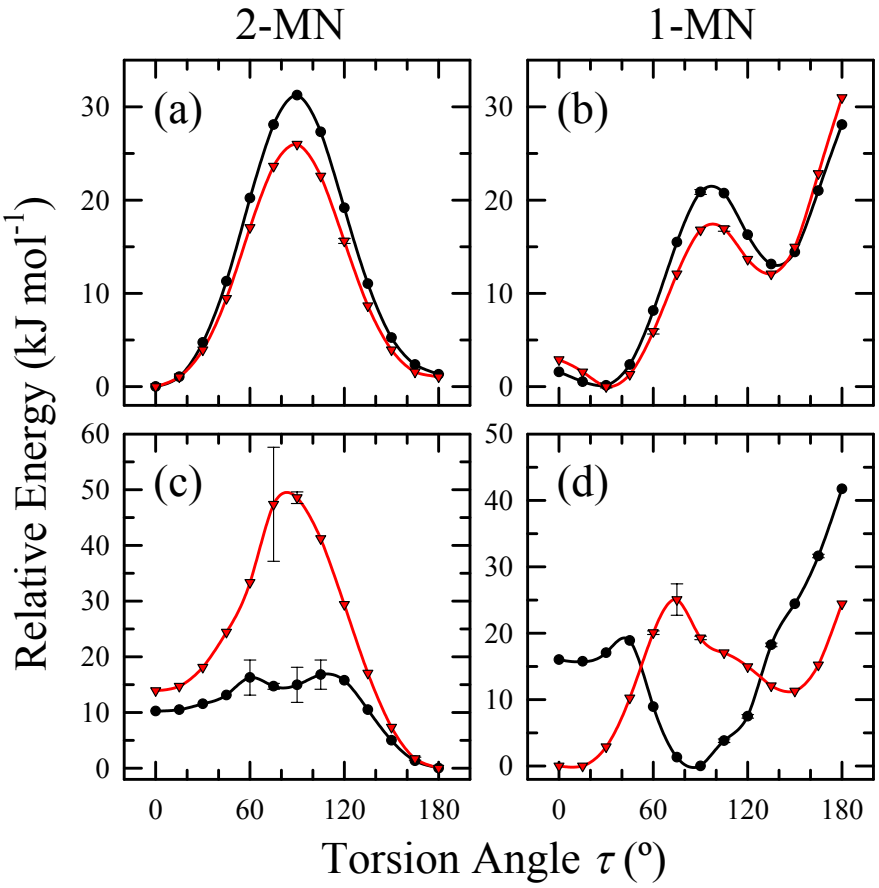

Figure 4.3: Relative potential energies as functions of the single bond torsion angle τ calculated at the levels B3LYP/6-31G(d,p) (black circles) and CAM-B3LYP/6-31G(d,p) (red triangles): (a) 2-MN in S_0, (b) 1-MN in S_0, (c) 2-MN in S_1, and (d) 1-MN in S_1. These profiles were made by fixing the dihedral angle shown in bold in Figure 4.2 and optimizing all other coordinates. S_1 profiles are TDDFT calculations. Energies were calculated over the entire range 0-360° and symmetry related values τ and 360°-τ averaged. Error bars indicate twice the difference between these two energies.

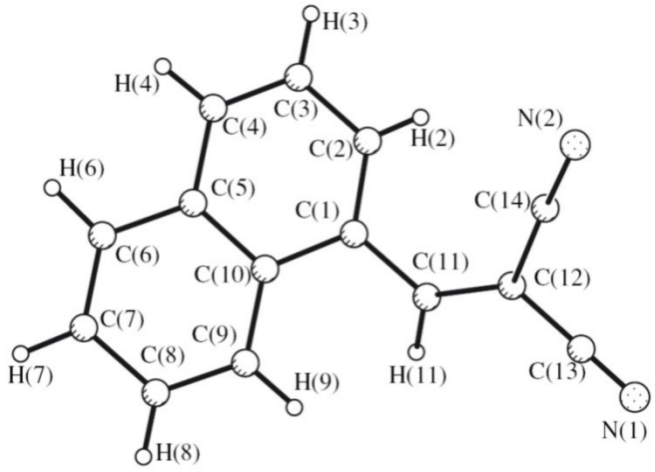

Method	R_{avg}^{ring}	R_{range}^{ring}	$R_{C0-C\alpha}$ (1-11)	$R_{C\alpha=C\beta}$ (11-12)	$R_{C\beta-C\chi}$ (12-13,12-14)	$R_{C\chi\equiv N}$ (13-1,14-2)
X-Ray	1.396	1.359-1.436	1.449	1.353	1.436	1.136
MP2	1.406	1.378-1.433	1.460	1.359	1.436	1.184
B3LYP	1.408	1.375-1.446	1.454	1.367	1.434	1.164

Method	Bond Angle θ C(1-11-12)	Torsion angle τ C(2-1-11-12)	Torsion angle C(10-1-11-12)	Torsion angle C(1-11-12-13)	Torsion angle C(1-11-12-14)
X-Ray	125.9	-38.3	144.1	-6.8	175.4
MP2	125.8	-42.9	142.2	-2.5	176.1
B3LYP	129.9	-26.7	156.6	-2.4	176.2

Table 4.4: Comparison of calculated and X-ray structures of 1-MN. All bond lengths (R) in Å and angles in degrees. R_{avg}^{ring} and R_{range}^{ring} are the average and range of bond lengths in the benzene ring. $R_{C0-C\alpha}$, $R_{C\alpha=C\beta}$, $R_{C\beta-C\chi}$, $R_{C\chi\equiv N}$ are the bond lengths proceeding out from the ring system (0 = ring, then α, β, χ). Figure and X-ray data from V. N. Nesterov, L. N. Kuleshova, and M. Y. Antipin, *Kristallografiya* **46**, 1041-1044 (2001). [60]

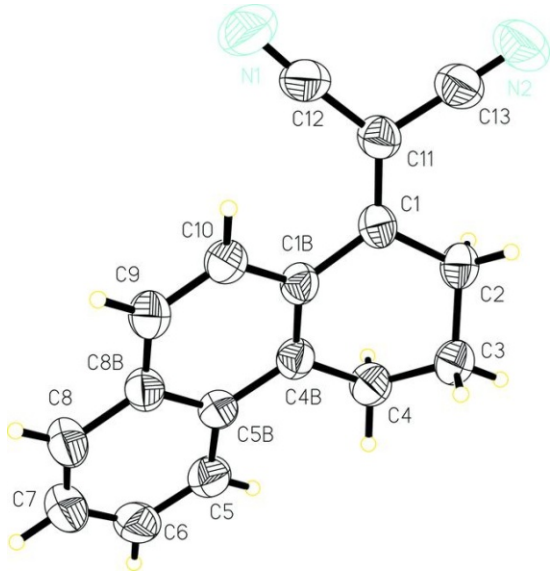

Method	R_{avg}^{ring}	R_{range}^{ring}	$R_{C0-C\alpha}$ (1-11)	$R_{C\alpha=C\beta}$ (11-12)	$R_{C\beta-C\chi}$ (12-13,12-14)	$R_{C\chi\equiv N}$ (13-1,14-2)
X-Ray	1.395	1.350-1.443	1.472	1.353	1.439	1.142
MP2	1.408	1.373-1.435	1.465	1.367	1.434	1.184
B3LYP	1.406	1.367-1.432	1.468	1.378	1.433	1.164

Method	Bond Angle θ (1B-1-11)	Torsion angle τ (10-1B-1-11)	Torsion angle (4B-1B-1-11)	Torsion angle (1B-1-11-12)	Torsion angle (1B-1-11-13)
X-Ray	124.4	-24.7	156.0	-0.8	179.0
MP2	122.8	-34.5	146.7	-3.3	179.6
B3LYP	124.4	-26.2	153.5	-4.7	179.0

Table 4.5: Comparison of calculated and X-ray structures of r2-MN. All bond lengths (R) in Å and angles in degrees. R_{avg}^{ring} and R_{range}^{ring} are the average and range of bond lengths in the benzene ring. $R_{C0-C\alpha}$, $R_{C\alpha=C\beta}$, $R_{C\beta-C\chi}$, $R_{C\chi\equiv N}$ are the bond lengths proceeding out from the ring system (0 = ring, then α, β, χ). Figure and X-ray data from G. B. Ettenger, B. W. Williams, D. Brillhart and M. E. Kastner, *Acta Crystallographica* **E65**, 1711 (2009). [46]

Molecule	Calc.	Solvent	Opt.	τ /deg	θ /deg	$R_{C=C}$ Å	μ_0 /D	μ_1 /D	$\Delta\mu$ /D	λ_{01} /nm	ν_{01} 10^3 cm^{-1}	M_{01} /D	f_{01}
2-MN(a)	B3LYP	gas	S_0	0.0	131.6	1.368	7.73	15.04	7.46	378	26.46	3.28	0.13
	B3LYP	gas	S_1	0.0	130.1	1.444		15.27	7.67	430	23.27	2.63	0.08
	B3LYP	chx	S_0	0.0	131.6	1.370	8.74			391	25.59	4.40	0.23
	B3LYP	acn	S_0	0.0	131.5	1.372	10.12			400	25.01	4.24	0.21
	B3LYP	acn	S_1	0.0	130.4	1.417		20.53		462	21.63	2.27	0.34
	CAM	gas	S_0	0.0	131.5	1.356	7.42	13.46	6.16	320	31.26	4.42	0.29
	CAM	gas	S_1	0.0	130.5	1.396		13.60		357	27.98	1.72	0.25
2-MN(b)	B3LYP	gas	S_0	180.0	131.7	1.368	7.18	14.56	7.54	395	25.30	2.88	0.10
	B3LYP	gas	S_1	180.0	128.2	1.408		14.69	7.66	445	22.48	2.45	0.06
	B3LYP	chx	S_0	180.0	131.8	1.370	8.06		409		24.46	3.58	0.15
	B3LYP	acn	S_0	180.0	131.7	1.371	9.25		419		23.87	3.34	0.12
	B3LYP	acn	$S_1$1	180.0	129.1	1.415		19.56		481	20.79	1.74	0.19
	CAM	gas	S_0	180.0	131.5	1.356	6.88	12.98	6.28	333	30.05	4.00	0.23
	CAM	gas	S_1	180.0	128.9	1.399		12.52		374	26.75	1.73	0.24
r2-MN	B3LYP	gas	S_0	-26.0	124.4	1.378	7.74	14.48	7.37	384	26.05	3.12	0.12
	B3LYP	gas	S_1	-27.3	123.6	1.420		14.53	7.42	438	22.84	1.07	0.08
	B3LYP	chx	S_0	-26.4	124.2	1.380	8.78			396	25.27	4.05	0.19
	B3LYP	acn	S_0	-26.8	123.9	1.382	10.25			405	24.69	3.95	0.18
	B3LYP	acn	S_1	-26.8	121.1	1.382		19.35	10.01				
	CAM	gas	S_0	-28.2	124.1	1.365	7.50	12.85	5.86	324	30.86	4.13	0.25
	CAM	gas	S_1										
1-MN(a)	B3LYP	gas	S_0	26.5	129.9	1.367	7.13	13.21	6.17	385	26.01	4.84	0.29
	B3LYP	gas	S_1	13.0	128.5	1.406		13.02	6.04	426	23.46	4.95	0.27
	B3LYP	chx	S_0	26.8	129.8	1.368	8.01			402	24.90	5.56	0.36
	B3LYP	acn	S_0	27.7	129.5	1.370	9.16			410	24.40	5.39	0.33
	B3LYP	acn	S_1	9.3	129.1	1.418		16.94		480	20.82	2.90	0.53
	CAM	gas	S_0	32.2	128.8	1.354	6.77	12.18	5.47	330	30.33	5.29	0.40
	CAM	gas	S_1	9.8	129.0	1.406				383	26.14	2.48	0.49
1-MN(b)	B3LYP	gas	S_0	138.3	130.6	1.366	6.48	11.82	6.09	388	25.77	4.14	0.21
	B3LYP	gas	S_1	85.8	118.3	1.437		15.70	9.66	594	16.84	0.76	0.00
	B3LYP	chx	S_0	139.3	130.6	1.367	7.34			401	24.92	4.86	0.28
	B3LYP	acn	S_0	140.1	130.4	1.369	8.54			405	24.69	4.86	0.27
	B3LYP	acn	S_1	92.3	121.0	1.434		20.06		571	17.52	0.59	0.02
	CAM	gas	S_0	136.6	129.2	1.352	6.11	11.61	6.11	329	30.40	4.40	0.28
	CAM	gas	S_1	145.7	128.9	1.425		10.13		390	25.67	2.04	0.33

Table 4.6: Calculations are use either B3LYP/6-31G(d,p) or CAM-B3LYP/6-31G(d,p) method without ("gas") or in the presence of an implicit solvent ("chx" = cyclohexane, "acn" = acetonitrile). "Opt." indicates whether the geometry was that optimized for the S_0 or S_1 state. τ and θ are the angles indicated in Figure 4.2 and $R_{C=C}$ the length of the vinyl double bond. μ_0, μ_1 and $\Delta\mu$ are the magnitudes of the dipole moments in S_0 and S_1 and their difference. λ_{01}, ν_{01}, M_{01} and f_{01} are the wavelength, frequency, transition dipole moment, and oscillator strength of the $S_0 \leftrightarrow S_1$ transition.

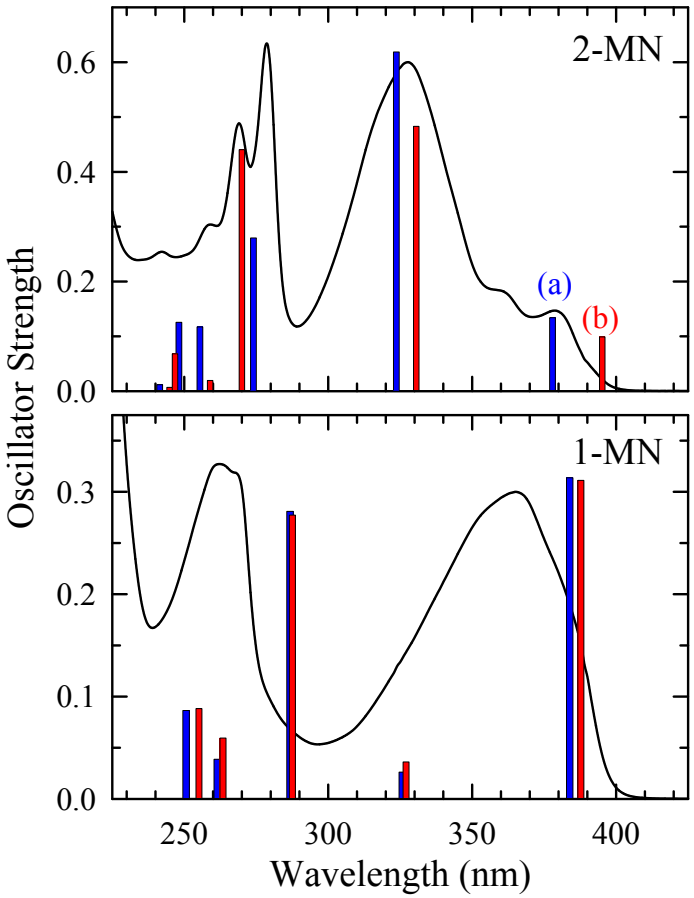

Figure 4.4: Experimental absorption spectra in n-hexane (smooth curves) compared to gas-phase TD-B3LYP-calculated vertical excitation energies and oscillator strengths (bars) of 2-MN and 1-MN. The first $6 S_0 \rightarrow S_n$ transitions are shown. **a** and **b** conformer calculations are shown in blue and red respectively. The vertical scales of the experimental spectra are arbitrarily.

The dipole moments listed in Table 4.2 indicate all molecules/conformers to be significantly more polar in S_1 than in S_0. The increase in polarity results from transfer of electron density from the naphthalene ring to the vinyl malononitrile group. Ground-state dipole moments are all 7-8 D, and, as illustrated in Figure 4.6, they are in all cases oriented from the malononitrile group to the naphthalene ring. These dipole moments suggest significant

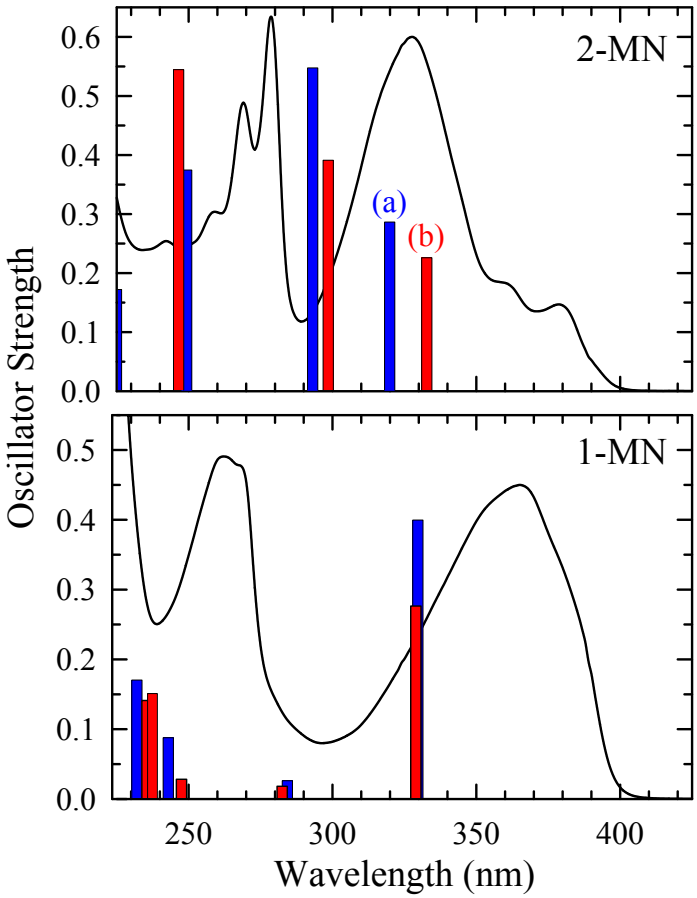

Figure 4.5: Experimental absorption spectra in n-hexane (smooth curves) compared to gas-phase TD-CAM-B3LYP-calculated vertical excitation energies and oscillator strengths (bars) of 2-MN and 1-MN. The first $6 S_0 \rightarrow S_n$ transitions are shown. **a** and **b** conformer calculations are shown in blue and red respectively. The vertical scales of the experimental spectra are arbitrarily.

charge transfer is present in the ground state. Mulliken and ESP-fit atomic charges [61] both indicate the naphthalene ring to be positive by 0.17-.21e in all cases. The S_1-S_0 differences, $\Delta\mu_{01}$, entail loss of an additional $\sim 0.3e$ from the naphthalene ring, so that there is approximately a net charge separation of $0.5e$ in the S_1 state. In the case of 2-MN the S_2 state is of intermediate polarity compared to S_0 and S_1, whereas in 1-MN the S_1 and

S_2 states are of similar polarity.

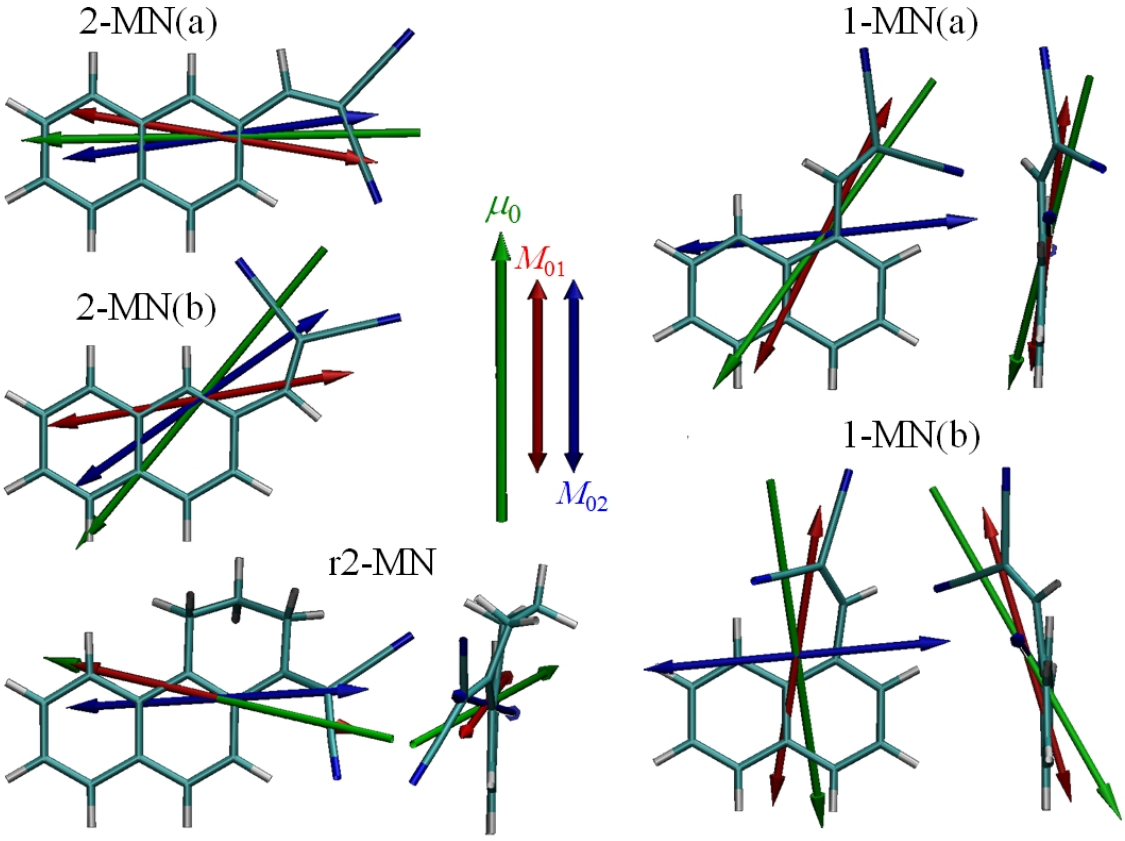

Figure 4.6: Directions of the S_0 state permanent electric dipole (μ_0, green) and transition dipole moments of the transitions $S_0 \rightarrow S_1$ (M_{01}, red) and $S_0 \rightarrow S_2$ (M_{02}, blue). Geometries and μ_0 are from B3LYP/6-31G(d,p) calculations of S_0 and transition moments are from TD-B3LYP calculations at the S_0 geometry.

Figure 4.6 also indicates the directions of the electric transition dipole moments between S_0 and S_1 and S_2 (B3LYP calculations at the S_0-optimized geometries). In 2-MN the $S_0 \rightarrow S_1$ and $S_0 \rightarrow S_2$ transition moment ($\vec{M}_{01}$ and $\vec{M}_{02}$) directions are within 25° of one another, with the stronger S_2 transition lying closer to the ring malononitrile direction (close to $\vec{\mu_0}$) but in this case the $S_0 \rightarrow S_1$ transition is also aligned with the ring mal-

ononitrile direction (close to $\vec{\mu}_0$) but in this case the $S_0 \rightarrow S_1$ transition is closer to being orthogonal to this direction, lying along the long naphthalene axis.

The molecular orbitals and main configurations comprising the S_1 and S_2 states are summarized in Figure 4.7 and Table 4.7. As noted by Pfanstiel and Pratt concerning 2-VN, the π orbitals of 1-MN (**a** or **b**) resemble those of naphthalene much more than do those of 2-MN (**a** or **b**) or r2-MN, which are more like those of a linear polyene including the malononitrile group. In all cases the S_1 state is comprised mainly of the HOMO $\rightarrow$ LUMO excitation, which is not purely charge-transfer in character.

We finally consider the relaxed S_1 torsional potentials displayed on the bottom panels of Figure 4.3. In contrast to the S_0 potentials, the predictions of the B3LYP (black) and CAM-B3LYP (red) calculations differ significantly. In 2-MN the primary minima in S_1 still lie near $\tau = 0$ and 180° but the barrier separating these minima is much larger in the CAM calculations: > 35 kJ mol^{-1} vs. ~ 5 kJ mol^{-1}. Whereas the B3LYP calculations suggest that conformer interconversion might be possible during the lifetime of S_1 the CAM-B3LYP predictions preclude such interconversion. In the case of 1-MN the B3LYP calculations predict a global minimum near 90°, and a state significantly different in character from the Franck Condon (FC) states of 1-MN(a) or 1-MN(b) (see Table 4.6). Whereas all of the other S_1-optimized geometries have dipole moments and transition properties close to those at their respective FC geometries, this $\sim 90°$ state is predicted to have a dipole moment ~ 4 D larger, and much weaker and largely red-shifted emission, hallmarks of a twisted intramolecular charge transfer (TICT) state. The B3LYP torsional profile in S_1 is such that Frank-Condon excitation of 1-MN(**a** or **b**) would lead to a rapid conformational change to this TICT state. In contrast, no TICT state or important torsional relaxation is predicted by the CAM calculations. As discussed later, we believe the CAM calculations are more consistent with experiment as regards the S_1 potential surface.

		H→L	H-1→L	H→L+1	H-2→L	H→L+2
2-MN(a)	S_1	0.61	-0.32			
	S_2	0.33	0.59	0.18	-0.10	
2-MN(b)	S_1	0.66	0.24			
	S_2	-0.25	0.62	-0.20		
r2-MN	S_1	0.64	-0.26			
	S_2	0.27	0.61	0.18	-0.11	
1-MN(a)	S_1	0.69			0.13	
	S_2		0.67			0.21
1-MN(b)	S_1	0.69	0.11			
	S_2		0.67			0.19

Table 4.7: Tabulated values are the largest coefficients of the configurations contributing to the first two singlet excited states based on TD-B3LYP/6-31G(d,p) calculations. "H"=highest occupied molecular orbital (HOMO), "L"= lowest occupied molecular orbital (LUMO), and "H-1→L" indicates a 1-electron excitation from the second highest occupied molecular orbital to the LUMO, etc. Geometries are S_0 optimized.

4.4.2 Steady-State Spectra and Solvatochromism

Steady-state absorption and emission spectra were recorded in a series of 11 solvents. Representative data are shown in Figure 4.8. The spectra of r2-MN closely resemble those of 2-MN (Figure 4.9). As already seen in Figure 4.4, the absorption spectra of 2-MN above 300 nm (34,000 cm^{-1}) appear to consist of two overlapping bands whereas those of 1-MN appear as a single peak. Based on the calculations of the previous section we interpret the absorption of 2-MN in terms of a slightly structured S_1 band centered near 27,000 cm^{-1} and a stronger, less structured band near 30,000 cm^{-1}. Both of these bands are likely to contain contributions from closely spaced 2-MN(a) and 2-MN(b) conformers. The calculations of the previous section suggest that the properties of the two conformers are similar and in the present section we treat them as an effective average species. The lowest energy absorption band of 1-MN is attributed to a single electronic transition from the single conformer 1-MN(a). As illustrated in Figure 4.8 the absorption bands of both

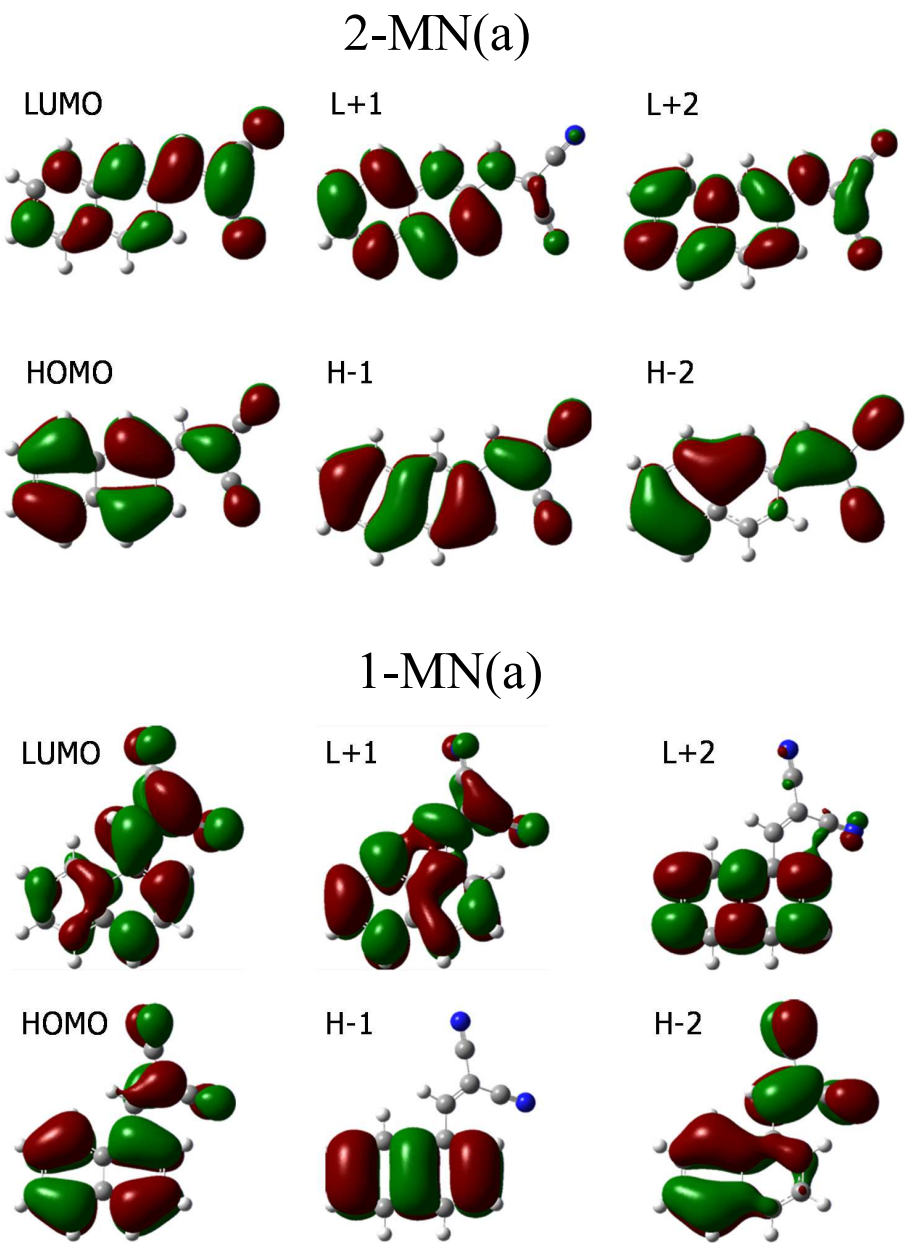

Figure 4.7: Frontier orbitals of 2-MN(a) and 1-MN(a) from B3LYP/6-31G(d,p) calculations. "H-1" denotes the first orbital below the highest occupied molecular orbital, i.e. HOMO-1, etc.

compounds shift to the red with increasing solvent polarity. The emission spectra of 1-MN and 2-MN are similar in shape. In weakly polar solvents vibronic structure is observed but this structure is largely obscured in solvents of even moderate polarity. The emission bands shift considerably more with solvent polarity than do the absorption bands and the shift is larger in 2-MN compared to 1-MN.

In order to quantitatively analyze solvent-induced shifts and other spectral parameters of the absorption of 2-MN and r2-MN, it is necessary to effect an approximate separation of their overlapping S_1 and S_2 absorption bands. As illustrated in Figure 4.10 for the case of 2-MN, this separation is performed by assuming that the overlapping bands can be fit by a sum of two lognormal lineshape functions: [62]

$$L(\nu) = \begin{cases} h \exp\left\{ -\ln(2) \left[\frac{ln(1+\alpha)}{\gamma} \right]^2 \right\} & \text{for } \alpha \geq -1 \\ 0 & \text{for } \alpha < -1 \end{cases} \tag{4.2}$$

where $\alpha = 2\gamma\left(\nu - \nu_0\right)/\Delta$. The parameter γ defines the asymmetry of the band, ν_0 is the peak frequency, and Δ is a width parameter related to the full width at half maximum Γ by $\Gamma = \Delta sinh\left(\gamma\right)/\gamma$. In highly polar solvents like acetonitrile, all 8 parameters $\{h_i, \nu_{i,0}, \Gamma_i, \gamma_i \text{ for } i = 1, 2\}$ are reasonably determined. In less polar solvents and especially in non-polar solvents like *n*-hexane, the structure present in the S_1 absorption cannot be captured by a lognormal function and, as a result, the parameters of the fit cannot all be determined with confidence. To achieve a consistent and sensible representations for all solvents studied we fixed the following parameters to average values observed in polar solvents: $\Gamma_1 = 4000$ cm^{-1}, $\gamma_1 = 0.38$, and $\gamma_2 = 0.26$. We believe that such fits afford relative absorbances accurate to $\pm 10\%$ and first-moment frequencies

$$\langle \nu \rangle \quad = \quad \nu_{pk} + \frac{\Delta}{2\gamma} \left[\exp\left(\frac{3\gamma^2}{4 \ln 2} \right) - 1 \right] \tag{4.3}$$

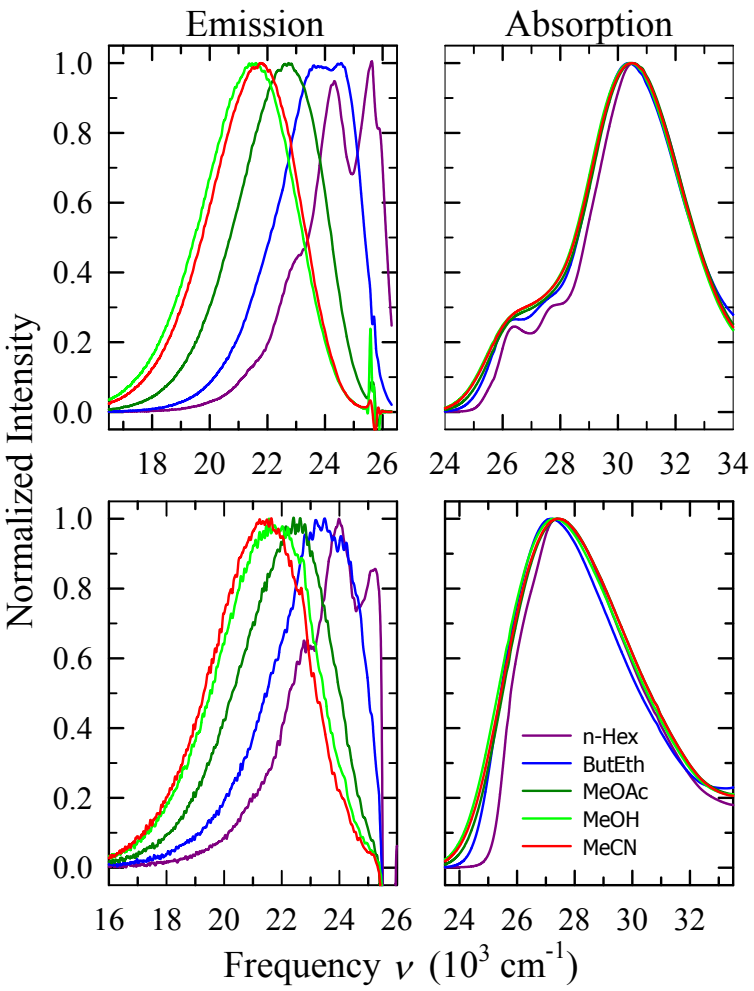

Figure 4.8: Directions of the S_0 state permanent electric dipole (μ_0, green) and transition dipole moments of the transitions $S_0 \rightarrow S_1$ (M_{01}, red) and $S_0 \rightarrow S_2$ (M_{02}, blue). Geometries and μ_0 are from B3LYP/6-31G(d,p) calculations of S_0 and transition moments are from TD-B3LYP calculations at the S_0 geometry.

accurate to 300 cm^{-1} (S_1) or 50 cm^{-1} (S_2).

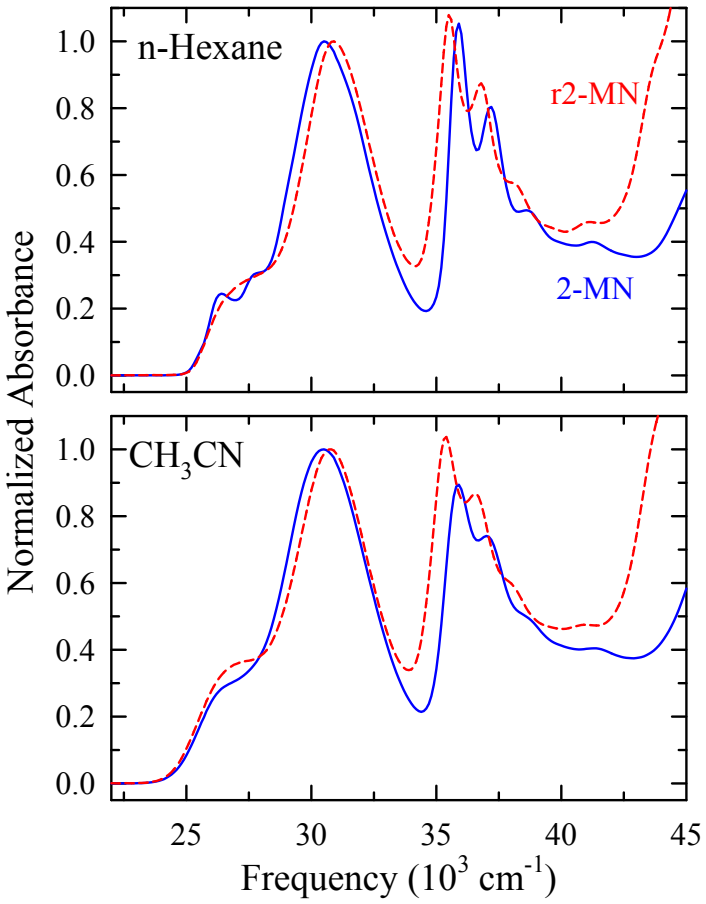

Figure 4.9: Comparison of the absorption spectra of 2-MN (blue solid curves) and r2-MN (red, dashed) in n-hexane and acetonitrile. Absorbance values are normalized to the S_1 + S_2 peak.

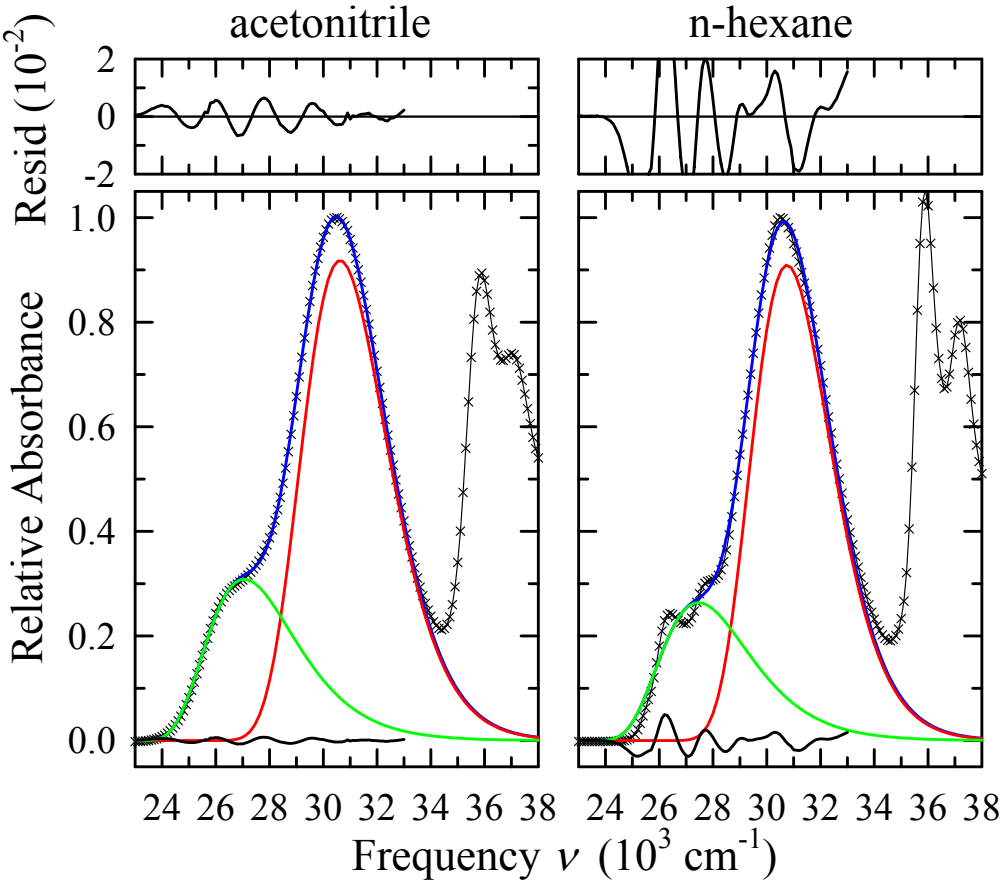

Figure 4.10: Illustration of the decomposition of the lowest-frequency band of 2-MN (black crosses) into approximate S_1 (green) and S_2 (red) contributions. The heavier black curves at the bottom of the lower panels are the residuals, differences between the observed and fit relative absorbance. These residuals are shown on expanded scales in the top panels ($\pm 2\%$).

		ν_{pk}^{abs} ($10^3 cm^{-1}$)	ϵ_{mx} (10^3)	$\left\langle \nu_{abs}^{(1)} \right\rangle$ ($10^3 cm^{-1}$)	M_{01} (D)	$\left\langle \nu_{abs}^{(2)} \right\rangle$ ($10^3 cm^{-1}$)	M_{02} (D)	$\langle \nu_{em} \rangle$ (10^3)	Φ_{em} (10^{-3})	$\langle \tau_{em} \rangle$ (ps)	k_{rad} ($10^7 s^{-1}$)	M_{10} (D)	τ_a (ps)	τ_b (ps)
1	1-hexane	30.53	27.0	28.33	2.7	31.26	4.5	24.05	4.8	154	3.12	1.7	257	21
2	1-heptane	30.47	27.3	28.29	2.7	31.22	4.5	24.04	5.3	150	3.51	1.8	248	22
3	cyclohexane	30.36	27.2	28.20	2.8	31.12	4.4	23.95	5.3	118	4.51	1.9	184	18
4	di-n-butyl ether	30.37	26.1	28.06	2.8	31.08	4.4	23.25	7.0	149	4.69	2.1	146	39
5	diethyl ether	30.46	27.1	28.07	2.9	31.16	4.6	22.86	8.3	149	5.55	2.5	147	39
6	methyl acetate	30.49	26.1	28.02	2.9	31.20	4.6	21.99	7.3	143	5.08	2.5	136	
7	1-pentanol	30.22	27.1	27.78	3.0	30.95	4.6	21.87	7.0	120	5.81	2.6	164	
8	propylene carbonate	30.30	24.5	27.76	2.9	31.02	4.4	20.97	9.4	180	5.22	2.6	166	
9	acetonitrile	30.48	25.7	27.93	2.9	31.17	4.6	21.09	7.7	153	5.02	2.7	154	
10	methanol	30.43	26.7	27.88	3.0	31.13	4.7	20.90	7.8	160	4.86	2.7	154	
11	toluene	29.88	22.5	27.72	2.7	30.76	4.1	22.36	5.4	111	4.90	2.1	154	

Table 4.8: Solvent-Dependent Photophysical Properties of 2-MN at 25°C. ν_{pk}^{abs}, $\left\langle \nu_{abs}^{(1)} \right\rangle$, $\left\langle \nu_{abs}^{(2)} \right\rangle$, $\langle \nu_{em} \rangle$ are the frequencies of the peak of the S_1+S_2 absorption band and the first moment frequencies of the S_1 and S_2 bands and the emission, respectively, all in units of 10^3 cm^{-1}. ϵ_{mx} is the decadic molar absorption coefficient of the S_1+S_2 band at the maximum in units of 10^3 M^{-1} cm^{-1}, the M_{IJ} are the transition dipole moments of the I→J transition in D, and Φ_{em} is the emission quantum yield. $\langle \tau_{em} \rangle$ is the average decay time and τ_a and τ_b the component decay times observed in biexponential fits in units of ps and k_{rad} is the (average) radiative rate in units of 10^7 s^{-1}.

		ν_{pk}^{abs} $(10^3 cm^{-1})$	ϵ_{mx} (10^3)	$\left\langle \nu_{abs}^{(1)} \right\rangle$ $(10^3 cm^{-1})$	M_{01} (D)	$\langle \nu_{em} \rangle$ (10^3)	Φ_{em} (10^{-3})	$\langle \tau_{em} \rangle$ (ps)	k_{rad} $(10^7 s^{-1})$	M_{10} (D)	$\langle \tau_v \rangle$ (ps)
1	1-hexane	27.40	13.2	28.63	3.8	23.10	1.9	0.52	3.67	6.2	
2	1-heptane	27.35	13.3	28.56	3.8	22.98	1.9	0.64	2.96	5.5	
3	cyclohexane	27.25	13.2	28.49	3.8	22.93	2.1	0.84	2.52	4.9	
4	di-n-butyl ether	27.18	12.4	28.38	3.8	22.52	1.1	0.87	1.31	3.7	
5	diethyl ether	27.28	12.6	28.49	4.0	22.28	2.3	0.91	2.57	5.6	
6	methyl acetate	27.46	11.6	28.71	3.9	21.55	2.2	1.7	1.24	4.1	0.41
7	1-pentanol	26.99	12.1	28.22	3.9	21.70	1.9	1.7	1.11	3.6	3.0
8	propylene carbonate	27.23	11.1	28.51	3.8	20.75	3.3	2.7	1.22	4.0	1.7
9	acetonitrile	27.44	11.6	28.70	4.0	20.79	2.2	1.9	1.15	4.2	0.13
10	methanol	27.32	10.8	28.59	3.8	20.97	2.7	1.41	1.90	5.4	6.1
11	toluene	26.73	11.4	27.93	3.6	21.82	2.2	0.84	2.62	5.0	

Table 4.9: Solvent-Dependent Photophysical Properties of 1-MN at 25°C*. ν_{pk}^{abs}, $\left\langle \nu_{abs}^{(1)} \right\rangle$ are the peak and first moment frequencies of the S_1 absorption band and $\langle \nu_{em} \rangle$ are the first moment frequency of the emission band in units of 10^3 cm^{-1}. ϵ_{mx} is the decadic molar absorption coefficient of the S_1 band at the maximum in units of 10^3 M^{-1} cm^{-1}, the M_{IJ} are the transition dipole moments of the I→J transition in D, and Φ_{em} is the emission quantum yield. $\langle \tau_{em} \rangle$ is the emission intensity decay time and $\langle \tau_v \rangle$ the time associated with the frequency shift of the emission spectrum in units of ps. k_{rad} is the radiative rate in units of 10^8 s^{-1}. (*Lifetime data are at 21±2°C rather than 25°C.)

Summaries of solvent-dependent data for 2-MN and 1-MN are provided in Tables 4.8 and 4.9, and analogous results for r2-MN in Table 4.10. Peak frequencies ν_{pk}^{abs} and extinction coefficients ϵ_{mx} are those directly measured in the spectra, i.e. without separating S_1 and S_2. In 2-MN and r2-MN, first moment frequencies in absorption $\left\langle \nu_{abs}^{(1)} \right\rangle$ and $\left\langle \nu_{abs}^{(2)} \right\rangle$ are from the lognormal fits (Eq. 4.3) whereas those for 1-MN and those reported for the emission of all solutes are numerically integrated values.

To quantify and partially interpret the solvent dependence of the solvatochromic shifts we employ a simple polarizable point dipole solute + dielectric continuum solvent model described previously in Refs. [18,63] Within this model absorption and emission frequencies are related to the refractive indices n_D and relative permittivities ϵ_r of solvents according to

$$\nu_{abs,em} = \nu_{abs,em}^{0} + A_{abs,em} d_c\left(n_D^2\right) + C_{abs,em}\left[d_c\left(\epsilon_r\right) - d_c\left(n_D^2\right)\right] \tag{4.4}$$

with

$$d_c\left(x\right) = \left(x-1\right) / \left\{2\left(1-c\right)x + \left(1+2c\right)\right\} \tag{4.5}$$

The factors $d_c\left(n_D^2\right)$ and $\left[d_c\left(\epsilon_r\right) - d_c\left(n_D^2\right)\right]$ characterize the electronic and nuclear (total minus electronic) polarizabilities of the solvent and ν^0, A, and C are related to solute properties, as is the constant c, which is proportional to its electronic polarizability. [18,63] Here we choose $c = 0.25$ and use the factors d_c to correlate observed shifts. (Solvent properties, including these d_c, are provided in Table 4.11.)

Fits of $\left\langle \nu_{abs}^{(1)} \right\rangle$ to Eq. 4.4 are shown in Figure 4.11 and all regression equations are summarized in Table 4.12. Note that toluene has been omitted from these fits because the permittivity of this primarily quadrupolar solvent poorly represents its total polariz-

#	Solvent	$\left\langle \nu_{pk}^{abs} \right\rangle$	ϵ_{mx}	$\left\langle \nu_{abs}^{(1)} \right\rangle$	M_{01}	$\left\langle \nu_{abs}^{(2)} \right\rangle$	M_{02}	τ_{em}
1	n-hexane	30.88	23.8	28.56	2.7	31.09	4.1	8
2	n-heptane	30.86	24.0	28.52	2.7	31.05	4.1	8
3	cyclohexane	30.77	23.6	28.45	2.7	30.98	4.0	8
4	di-n-butyl ether	30.70	22.9	28.22	2.8	30.87	4.0	7
5	diethyl ether	30.77	22.1	28.19	2.8	30.90	4.0	9
6	methyl acetate	30.77	21.6	28.06	2.8	30.89	4.0	9
7	1-pentanol	30.48	22.8	27.78	2.9	30.62	4.1	13
8	propylene carbonate	30.59	21.2	27.80	2.9	30.73	4.0	16
9	acetonitrile	30.76	21.5	27.98	2.9	30.88	4.1	8
10	methanol	30.66	21.9	27.85	2.9	30.76	4.2	12
11	toluene	30.33	20.0	27.84	2.7	30.52	3.7	8

Table 4.10: $\left\langle \nu_{pk}^{abs} \right\rangle$ is the peak frequency of the S_1+S_2 absorption band and $\left\langle \nu_{abs}^{(1)} \right\rangle$ and $\left\langle \nu_{abs}^{(2)} \right\rangle$ are the first moment frequencies of the S_1 and S_2 bands in units of 10^3 cm^{-1}. ϵ_{mx} is the decadic molar absorption coefficient of the S_1+S_2 band at the maximum in units of 10^3 cm^{-1}, the M_{IJ} are the transition dipole moments of the $I \rightarrow J$ transition in D, and τem is the emission decay time in units of ps.

ability in relation to molecular solvation. [64, 65] As illustrated by the spread of points in the top panel of Figure 4.11, the solvent sensitivity of the S_1 absorption bands to solvent increases in the order 1-MN < 2-MN < r2-MN. The difference between 1-MN and 2-MN is anticipated based on the larger S_0 and S_1 dipole moments calculated for 2-MN (Table 4.2), but the even larger solvent sensitivity of r2-MN is contrary to the similar dipole moments of 2-MN and r2-MN and the larger size of r2-MN. The much smaller solvent sensitivity of the S_2 absorption bands of 2-MN and r2-MN compared to S_1 is as expected based on the smaller calculated S_2 dipole moments (Table 4.2), but the greater sensitivity of r2-MN compared to 2-MN is again unexpected.

Using the solvatochromic model above, rough estimates of the change in the (gas-phase) dipole moments between S_1 and S_0, $\Delta\mu = |\vec{\mu_1} - \vec{\mu_0}|$, can be determined from the observed

#	Solvent	ϵ_r	n_D	$d_c(\epsilon_r)$	$d_c(n_D^2)$	$F(\epsilon_r, n_D)$	η (mPa s)	τ_{BzCN} (ps)
1	n-hexane	1.88	1.372	0.204	0.204	0	0.294	3.4
2	n-heptane	1.92	1.385	0.210	0.210	0	0.397	2.5
3	cyclohexane	2.02	1.424	0.225	0.226	0	0.898	1.1
4	di-n-butyl ether	3.08	1.397	0.340	0.215	0.125	0.645	1.6*
5	diethyl ether	4.20	1.349	0.410	0.194	0.216	0.242	4.1*
6	methyl acetate	6.68	1.359	0.493	0.198	0.295	0.364	2.8*
7	1-pentanol	13.90	1.409	0.577	0.220	0.357	3.51	0.28
8	propylene carbonate	64.92	1.419	0.646	0.224	0.422	2.53	0.40
9	acetonitrile	35.94	1.341	0.631	0.190	0.440	0.341	2.9
10	methanol	32.66	1.329	0.627	0.185	0.442	0.551	1.8
11	toluene	2.38	1.494	0.272	0.254	0.018	0.553	1.8*
12	ethyl acetate	6.02	1.370	0.477	0.203	0.274	0.426	2.4
13	CH_2Cl_2	8.93	1.421	0.532	0.225	0.307	0.411	2.4*

Table 4.11: ϵ_r, n_D, and η are the relative permittivity, refractive index, and viscosity of the solvent from Y. Marcus, *The Properties of Solvents* (Wiley, New York, 1998). $d_c(x)$ is the reaction field factor described by Equation 4.5 with c = 0.25. $F(\epsilon_r, n_D) = d_c(\epsilon_r) - d_c(n_D^2$. τ_{BzCN} is the average of the fluorescence lifetimes of DMN and JDMN derived from a combination of quantum yield and lifetime data in H. Jin, M. Liang, S. Arzhantsev, X. Li, and M. Maroncelli, *J. Phys. Chem. B* **114**, 7565 (2010). Values with asterisks indicate estimates based on comparable solvents.

Stokes shifts via [18, 63]

$$\nu_{abs} - \nu_{em} \quad = \quad \left(\nu_{abs}^0 - \nu_{em}^0\right) + \frac{2\left(\Delta\mu\right)^2}{a^3}\left[d_c\left(\epsilon_r\right) - d_c\left(n_D^2\right)\right] \tag{4.6}$$

where a is the radius of the effective spherical cavity representing the solute. In Figure 4.12 plots of the Stokes shifts in 2-MN and 1-MN are provided. (Corresponding data on r2-MN could not be obtained due to interference from impurity emission.) As illustrated in Figure 4.12, good linear correlations are found between $\nu_{abs} - \nu_{em}$ and the solvent nuclear polarizability $d_c(\epsilon_r) - d_c(n_D^2)$; values of r^2 are 0.99 (2-MN) and 0.90 (1-MN). The poorer fit in the case of 1-MN is due to the 1-pentanol datum (asterisk in Figure 4.12). As will be seen later, 1-MN lifetimes are short (∼1 ps) and because 1-pentanol solvates much more slowly (∼100 ps [66]) than the remaining solvents, the steady-state emission of 1-MN is not

	ν_0	A	C	R^2	*StErr.*	F	P
2-MN S_1 ν_{abs}	28.25		-0.97	0.83	0.08	44	0.0002
	29.33	**-5.03**	**-1.11**	**0.96**	**0.04**	**105**	**0.0000**
2-MN S_2 ν_{abs}	31.84	-3.45		0.19	0.09	3	0.1182
	32.31	**-5.27**	**-0.39**	**0.73**	**0.05**	**13**	**0.0042**
2-MN ν_{em}	**24.07**		**-6.85**	**0.98**	**0.16**	**549**	**0.0000**
	24.47	-1.86	-6.90	0.98	0.17	247	0.0000
2-MN $\Delta\nu$	**4.18**		**5.88**	**0.97**	**0.19**	**295**	**0.0000**
	4.86	-3.17	5.79	0.97	0.20	137	0.0000
r2-MN S_1 ν_{abs}	28.49		-1.51	0.90	0.09	80	0.0000
	29.56	**-5.02**	**-1.65**	**0.95**	**0.06**	**91**	**0.0000**
r2-MN S_2 ν_{abs}	31.50		-0.52	0.52	0.09	11	0.0112
	32.43	**-4.35**	**-0.64**	**0.73**	**0.07**	**13**	**0.0045**
1-MN ν_{abs}	**29.79**	**-6.12**		**0.29**	**0.12**	**5**	**0.0621**
	29.96	-6.78	-0.14	0.23	0.13	2	0.1684
1-MN ν_{em}	**23.07**		**-4.83**	**0.95**	**0.20**	**176**	**0.0000**
	23.55	-2.27	-4.90	0.95	0.22	79	0.0000
1-MN $\Delta\nu$	**5.45**		**4.88**	**0.89**	**0.32**	**72**	**0.0000**
	6.41	-4.51	4.75	0.88	0.34	33	0.0003

Table 4.12: $\Delta\nu$ denotes the Stokes shift. ν_0, A, and C are the regression coefficients in Eq. 4.4 all in units of 10^3 cm^{-1}. R^2 is the adjusted r-squared statistic, *StErr.* the standard error of the regression, F the overall F test for the null hypothesis, and P the probability of the null hypothesis. For each observable, regressions both one and two reaction field factors were performed. The preferred regression is shown in bold face. All regressions were performed on the data from the 10 solvents # 1-10 in Table 4.11, which excludes toluene.

equilibrated, an assumption implicit in Eq. 4.6. The slopes derived from fitting these data are 5900 cm^{-1} (2-MN) and 4900 cm^{-1} (1-MN). The value of $\Delta\mu$ derived from these slopes is highly dependent on the choice of cavity radius a. Plausible values for a range between, 3.6 Å, the radius of a sphere equal to the van der Waals volume of the solute (188.8 $Å^3$ based on van der Waals increments [9]) and this value augmented by the radius of a typical solvent molecule (∼2.5 Å). These values, a = 3.6 - 5.1 Å yield values of $\Delta\mu$ = 11.4 - 5.1 D for 2-MN and $\Delta\mu$ = 10.4 4.7 D for 1-MN. The TD-B3LYP/6-31G(d,p) calculated values are $\Delta\mu$ = 6.7 D for 2-MN and 6.0 D for 1-MN. Thus, the calculated values are consistent with the observed solvatochromism of these molecules.

Katritzky et al. [39] previously measured the solvatochromism of 1-MN, but in a smaller collection of solvents (only 6 omitting the quadrupolar solvents toluene and dioxane). Using $a = 3.7$ Å and neglecting any dependence of ν_{abs} with solvent, these authors estimated $\Delta\mu = 3.2$ D. A slightly different analysis of these same data by Ravi et al., [67] using the same value of a later produced a slightly larger value $\Delta\mu = 3.9$ D. Both values fall significantly below the already large range of values $\Delta\mu = 10.4$ 4.7 D derived here for 1-MN derived here. The difference is partly due to assumptions made in the analysis but it is also due to differences in the spectroscopic data. Obtaining reliable emission data for 1-MN is difficult because of its low emission quantum yield and the differences may reflect the effect of impurities in the emission data.[3]

4.4.3 Transition Dipole Moments

Quantities related to the strength of the $S_0 \rightleftarrows S_1$ transitions of these molecules are provided in Tables 4.8, 4.9, and 4.10. Maximal absorption coefficients ϵ_{mx} for the S_1/S_2 composite bands of 2-MN and r2-MN average 2.6×10^4 and 2.2×10^4 M^{-1} cm^{-1}, respectively, whereas the S_1 band of 1-MN is roughly half of these values, 1.2×10^4 M^{-1} cm^{-1}. Previously reported values of ϵ_{mx} are 2.81×10^4 M^{-1} cm^{-1} (2-MN) and 1.42×10^4 M^{-1} cm^{-1} (1-MN) in chloroform [38] and 1.4×10^4 M^{-1} cm^{-1} for 1-MN in tetrahydrofuran. [39]

For quantitative comparison to calculated transition strengths we compute transition

[3]The only emission quantum yield data available in the literature for any of these compounds is from the work of Katritzky et al. [39] These authors reported the quantum yield of 1-MN in dimethylformamide and acetonitrile to be 0.001 and less than this value in less polar solvents. The fact that we find quantum yields to be closer to 10^{-4} than to 10^{-3} in all solvents including acetonitrile might suggest the influence of impurity emission in their data.

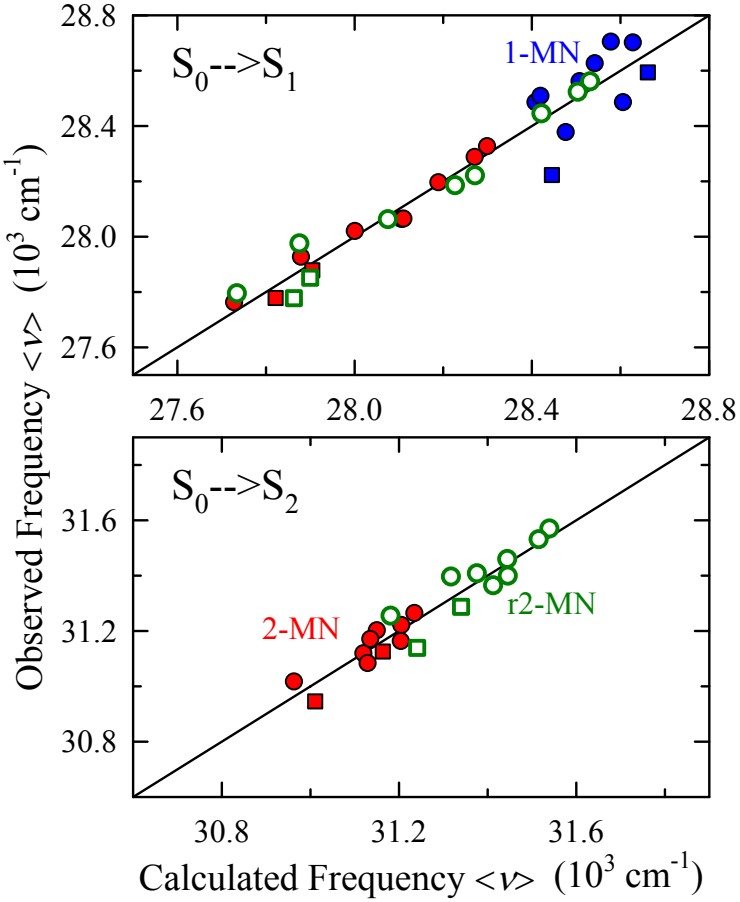

Figure 4.11: Correlations of first-moment absorption band frequencies according to Eqs. 4.4-4.5. Filled red symbols denote 2-MN, open green r2-MN, and filled blue symbols 1-MN. Circles denote aprotic and squares alcohol solvents. Toluene data are omitted. These regressions are the best linear or bi-linear regressions.

dipole moments via [68, 69]

$$\left|\vec{M}_{01}\right|^2 = \frac{1}{n_D}\left[\frac{2303}{8\Pi^3}\frac{3hc}{N_A}\right]\int_{S_1}\frac{\epsilon(\nu)}{\nu}d\nu \tag{4.7}$$

where h, c, and N_A are Planck's constant, the speed of light, and Avogadro's number. For separating the S_1 and S_2 absorption bands we use the lognormal fits described in the previous section. Solvent data for 2-MN and r2-MN are plotted as a function of the total solvent

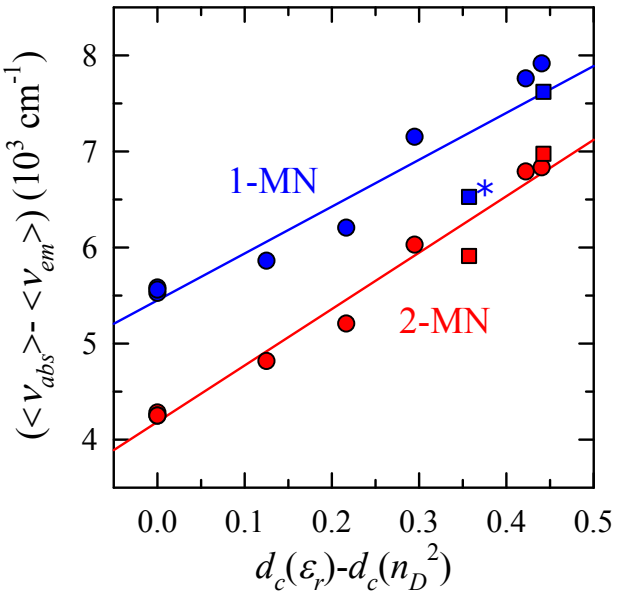

Figure 4.12: Stokes shifts in 2-MN (red) and 1-MN (blue) versus solvent nuclear polarizability factor $d_c(\epsilon_r) - d_c(n_D^2)$. Circles denote aprotic and squares alcohol solvents. The asterisk marks 1-MN in 1-pentanol.

polarity function $d_c(\epsilon_r)$ in Figure 4.13. Experimental values of M_{01} average 2.8, 2.8, and 3.8 D in 2-MN, r2-MN, and 1-MN, respectively. These values are in reasonable agreement with gas-phase TD-B3LYP/6-31G(d,p) calculations, which provide 3.1, 3.1, and 4.8 D (Table 4.2). Average values of the $S_0 \rightarrow S_2$ transition moments are 4.5 D in 2-MN and 4.0 D in r2-MN. These quantities are significantly overestimated by the TDDFT calculations, which predict 6.2 D and 5.6 D, respectively). The absorption transition moments of 2-MN and r2-MN appear to increase slightly with increasing solvent polarity. The change is in all cases less than 10% over the full range of $d_c(\epsilon_r)$. In the case of 1-MN the change is negligible.

We have also determined transition moments for the emission transitions (M_{10}) of 2-MN

and 1-MN using [68, 69]

$$\left|\vec{M}_{10}\right|^2 = \frac{1}{n_D^3}\left[\frac{3hc}{64\Pi^4}\right]\frac{k_{rad}}{\tilde{\nu}_{em}^3} \tag{4.8}$$

In this expression k_{rad} is the radiative rate, calculated from the emission quantum yield ϕ_{em}, and average emission decay time $\langle\tau_{em}\rangle$ via $k_{rad} = \Phi_{em}/\langle\tau_{em}\rangle$ and $\tilde{\nu}_{em}^3 = \left\{\int F(\nu)\,d\nu/\int F(\nu)\,\nu^3 d\nu\right\}$ with $F(\nu)$ the emission spectrum. Values of M_{10} for 2-MN and 1-MN are shown in Figure 4.13 (open symbols). The large error bars here reflect the difficulty associated with accurately measuring quantum yields in the range of 10^{-4} 10^{-3} as well as uncertainties in the lifetime measurements. In the case of 1-MN the emission transition moments average 4.7 ± 0.9 D, compared to 3.8 ± 0.1 D in absorption. Typically, emission transition moments are slightly smaller than absorption moments for well-isolated transitions. We suspect that the apparently larger average value of M_{10} here as well as the scatter may reflect the presence of long-lived impurities. In the case of 2-MN, the average values are more in keeping with expectations: $M_{10} = 2.4 \pm 0.4$ D versus $M_{01} = 2.8 \pm 0.1$ D. There is, however, an unexpectedly large variation of M_{10} with solvent, 40% over the range of solvents considered. The time-resolved data discussed in the next section indicate that the two conformers of 2-MN have markedly different lifetimes and their relative populations vary substantially with solvent polarity. It may be that this variation in conformer populations is somehow responsible for the variations in M_{10} observed here.

4.4.4 Time-Resolved Emission

As indicted by the $\sim$ 30-fold difference in quantum yields of 2-MN and 1-MN (Tables 4.8 and 4.9), the lifetimes of these molecules differ substantially. For this reason different techniques were used to measure time-resolved emission.

In the case of 2-MN, lifetimes are on the order of 100 ps, sufficiently slow that time-correlated single photon counting (TCSPC) is able to faithfully record the emission dy-

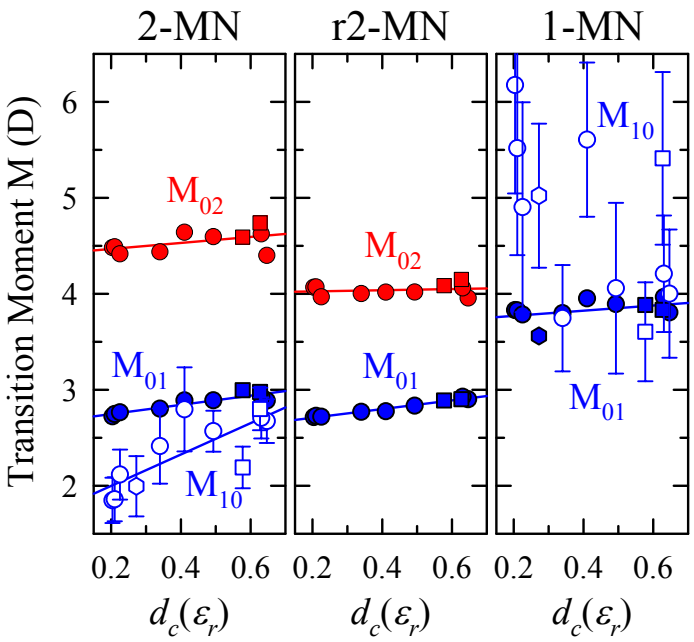

Figure 4.13: Absorption (filled symbols) and emission (open) transition dipole moments plotted as functions of the total solvent polarizability factor $d_c\,(\epsilon_r)$. Circles denote aprotic solvents, squares alcohols, and the hexagon toluene.

namics. In most solvents studied the decay kinetics observed using TCSPC were independent of emission wavelength. The main exception was 2-MN in 1-pentanol, where multi-exponential wavelength-dependent decay kinetics where observed. We attribute this behavior to dynamic Stokes shifting of the emission due to solvation dynamics slow enough to be registered by the 25 ps time resolution of TCSPC. (The average solvation time in 1-pentanol is ∼100 ps. [66]) A ∼5 ps lifetime component was detected on the blue side of the emission spectrum in methanol, which we also ascribe to solvation dynamics. In other solvents we observed either single-exponential emission decays with time constants in the 100-300 ps range or biexponential decays with one component in this same range and another component between 20-50 ps. The latter behavior is observed in the least polar solvents, the alkanes and ethers (#1-5). The amplitude of the short component decreases with increasing solvent polarity, from ∼50% in n-hexane to ∼25% in diethylether.

We attribute the bi-exponential decay kinetics of 2-MN observed in low-polarity solvents to the coexistence of two conformers (**a** and **b**) with distinct lifetimes in these solvents. Evidence for this hypothesis is provided in Figure 4.14, where we show emission of 2-MN in n-hexane monitored at 420 nm as a function of excitation wavelength. On the left panel we show a blow-up of the red edge of the absorption spectrum with the excitation wavelengths indicated. Between 390 and 400 nm, a subtle change in the slope of the absorption edge suggests the possible presence of a weaker transition underlying the primary absorption. Excitation at 390 nm (used for most TCSPC experiments) or redder wavelengths greatly enhances the amplitude of the short (22 ps) component relative to the long (280 ps) component. The latter dominates the emission (70-80%) when excitation is at wavelengths shorter than 385 nm. Based on the TDDFT calculations (Figure 4.4) we tentatively assign the short lifetime component to emission from the **b** conformer, and the long component to emission from the **a** conformer. Assuming approximately equal oscillator strengths, as suggested by calculation, these data indicate ∼25% of the 2-MN adopts the **b** conformer in *n*-hexane at 25°C. This relative population is consistent with TDDFT energy calculations in cyclohexane (Table 4.6). In solvents more polar than the alkanes, the absorption band shifts to the red such that 390 nm excitation is no longer on the edge of the absorption where it emphasizes **b** emission. Nevertheless, we would expect to be able to observe a ∼25% amplitude fast component in the TCSPC decays if one were present. The fact that we fail to observe a shorter component in solvents more polar that diethyl ether suggests that the **a** conformer becomes increasingly favored with increasing solvent polarity, such that in methyl acetate and more polar solvents it contributes negligibly to the emission of 2-MN. Such a change with solvent is also supported by the DFT calculations in Table 4.6.

The emission lifetimes of 1-MN are all considerably shorter than those of 2-MN and Kerr-gated emission (KGE) was therefore used to monitor emission dynamics. Represen-

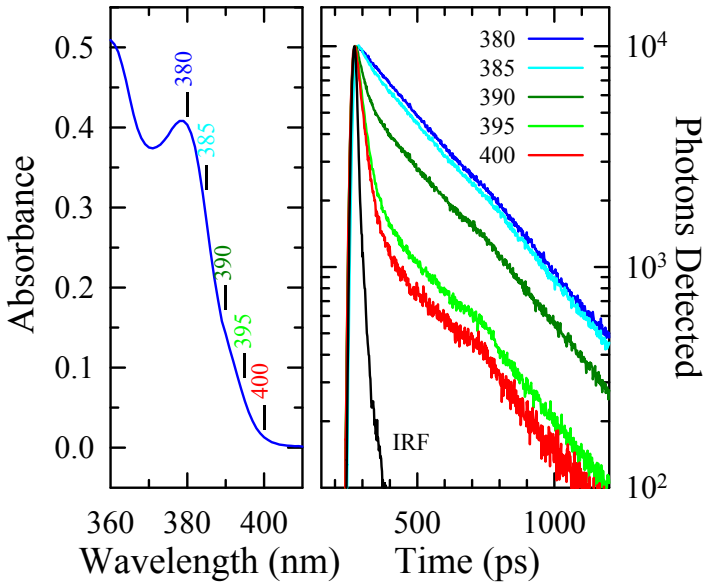

Figure 4.14: Excitation wavelength-dependent emission of 2-MN in n-hexane. The left panel shows the absorption spectrum with excitation wavelengths indicated. The right panel shows emission decays collected at 420 nm. Decays were collected to 10^4 counts in the peak channel except for the 400 nm decay, which was collected to 5000 counts and rescaled for comparison. "IRF" labels the instrument response function

tative spectra of 1-MN in acetonitrile are shown in Figure 4.15 to illustrate the analysis employed. Figure 4.15(a) shows "raw" spectra after correction for temporal dispersion and detection sensitivity. The sharp features at times comparable to the instrument resolution (350-400 fs FWHM) are solvent Raman bands. The raw spectra exhibit both a rapid intensity decay and a frequency shift over the course of a few picoseconds. To partially remove the effects of instrumental broadening from the results, these raw spectra were thinned and fit to a 4-exponential model, resulting in the deconvoluted spectra shown in panel (b). The latter spectra (points) were fit to lognormal functions (time-dependent versions of Eq. 4.5) excluding the Raman region, which are shown as the smooth curves in Figure 4.15(b). These fits are used to provide simple metrics of the spectral evolution. Two spectral characteristics obtained in this manner, the integral intensities and peak frequencies of 1-MN

in three solvents are shown in Figure 4.16. In all three solvents the intensity decays are significantly non-exponential. In highly polar solvents such as those illustrated, peak frequencies shift by 1500-2000 cm^{-1}. This shift is also non-exponential in time and occurs on a time scale comparable to the intensity decay. The widths of the spectra (not shown) also decrease from $\sim$ 5000 cm^{-1} to $\sim$ 4000 cm^{-1} over this same time range. We fit both the intensity and frequency decays to bi-exponential functions of time to extract the integral times listed in Table 4.9. No obvious correlation exists between the times associated with the loss of emission intensity $\langle\tau_{em}\rangle$ and the peak shift $\langle\tau_{nu}\rangle$. Rather, in four of the five solvents where comparisons are possible, the peak shift time is close to the Stokes shift times measured with the coumarin 153 (C153) probe. [66] These observations suggest that the spectral shift is due to polar solvation and is not closely tied to the process leading to loss of emission. In 1-pentanol the value of $\langle\tau_{nu}\rangle$ obtained here ($\sim$ 3 ps) appears unrelated to the time associated with C153 solvation ($\sim$ 100 ps). But this discrepancy is likely the result of the short lifetime of 1-MN (2 ps) obscuring the dominant slow solvation time constants ($\tau > 20$ ps [66]) present in 1-pentanol.

The lifetimes of r2-MN fall in the range 5-20 ps, intermediate between those of 2-MN and 1-MN. Due to the very limited amount of r2-MN available, we only measured its dynamics using TCSPC, which requires much less sample than the KGE experiment. Given the fact that the lifetimes of r2-MN are smaller than the 25 ps instrument response function, only an overall time constant associated with the emission decay could be determined. These lifetimes, which are averages over decays measured at 4-5 emission wavelengths, are collected in Table 4.10. It should be noted that the impurities which preclude accurate determination of the steady-state emission of r2-MN do not influence these lifetime data. In the TCSPC data, the impurities are manifest as a 1-2% component with a lifetime of $\sim$ 3 ns. Although the difference in r2-MN and impurity lifetimes means that the impurities dominate the steady-state spectra, the opposite is true of the TCPC data, where the

r2-MN decay constitutes 98% or more of the amplitude.

We finally take an empirical look at the solvent dependence of the lifetimes observed for all three solutes. We consider three quantities potentially relevant to the emission deactivation process: the total solvent polarizability function, $d_c(\epsilon_r)$, the solvent viscosity η, and the average emission lifetime of the benzylidene malononitriles DMN and JDMN, τ_{BzMN}. (Because prior work showed a high degree of correlation between the lifetimes of DMN and JDMN [18] we use the average value here to represent this class of molecule.) The function $d_c(\epsilon_r)$ is expected to be relevant to the decay kinetics if some polarity-dependent barrier controls the deactivation. The viscosity, a coarse measure of solvent friction, is expected to be relevant if deactivation is controlled by some large amplitude motion through solvent. Finally, if the same mechanism of relaxation controls the fluorescence of the naphthalene and benzylidene malononitriles, one might expect τ_{BzMN} to correlate the observed solvent dependence.

Figure 4.17 displays the lifetimes of 2-MN and 1-MN as functions of these three quantities. Consider first 2-MN. The decay time τ_a, attributed to the dominant **a** conformer of 2-MN, is approximately constant for most solvents except the alkanes, where it is significantly larger. As indicated by the small values of the coefficients of determination ("r^2") provided in Figure 4.17 (top values), none of the three quantities examined here explains most of the variance in τ_a with solvent. In the case of τ_b, attributed to 2-MN(b), times are most strongly correlated to $d_c(\epsilon_r)$, they exhibit a slightly weaker correlation to τ_{BzMN}, and appear unrelated to viscosity. The same pattern is observed in the case of the integral decay times of 1-MN. The strongest correlation is found with $d_c(\epsilon_r)$, and weakest correlation with η. As shown by the dashed line of equality ("1:1") in Figure 4.17, in 7 out of the 11 solvents studied, the intensity decay times of 1-MN are nearly equal to τ_{BzMN}, but in the 4 other solvents the 1-MN lifetimes are significantly shorter than those of the benzylidene

malononitriles. Finally, in the case of r2-MN, the decay times correlate moderately well with all three of these quantities ($r^2 = 0.5 - 0.6$).

4.4.5 Potential Energy Surface and its Reaction Coordinate

Steady state measurements show simple $S_0 \leftrightarrow S_1$ transitions. There is no evidence of an emissive TICT state in these spectra. If TICT would be the dominating deactivation process than the finding that 1-MN fluorescence is depleting within a picosecond while 2-MN has a longer lifetime in combination with the predicted non-TICT state for latter in quantum chemical calculation would be consistent. However, the fact that r2-MN cannot undergo a TICT rotation but still shows similar lifetimes suggests that there might be another underlying process. We addressed previously [18, 26] the mechanism and likelihood of double bond torsion in the excited states of related fluorophores rather than a TICT state formation. Shown in Figure 4.18 are resonance structures relevant to CT. This CT would allow the double bond to rotate in the excited state due to its single bond character.

Different to classical TDDFT the SPIN-FLIP method enumerates the states at each optimization step according to their energy level and will change the target state when states change in their relative energy order. Also, due to unrestricted Hartree-Fock calculation it is difficult to assign singlet or triplet characters to states. Last but not least no oscillator strengths are available for these calculations which would allow a comparison with our spectroscopic data like we did earlier when we addressed the equivalence of the **a** and **b** conformers. By optimizing with respect to the ground state and calculating the single point energies then revealed similar rotations profiles compared to TDDFT calculations which allowed us to assign which ones were likely to be singlet states. Figure 4.17 shows a model representation of the significant feature noticeable: A conical intersection is apparent at 90° twist between the ground and the second excited state which we assume to be the first excited singlet state. The barrier height is in the order of a few k_BT. The barrier peak is

around 45° and falls steeply at higher angles. Here is where the similarities between 1-MN and r2-MN come in and the discrepancy to 2-MN: the ground state geometries for both show a strong out-of-plane angle of the malononitrile moiety. For r2-MN the dihedral angle around α in Figure 4.1 is about 25° and for 1-MN even 40° while 2-MN is planar with 0°. In Figure 4.19 the torsion or dihedral angle, respectively, is around β though. The initial non-planarity might to be a precursor to the double bond torsion that supports a 90° twist into the conical intersection geometry.

4.5 Summary & Conclusion

We conclude by discussing the nature of the emitting states and origins of the short lifetimes of these naphthalene malononitriles in light of the results collected here as well as those available in the literature. The two studies to previously investigate emission in any of these molecules described the emission of 1-MN (and several other Ar-CH=C$(CN)_2$ systems) as reflecting the presence two distinct excited states, a locally excited (LE) state and an ICT state having much greater intramolecular charge transfer character. [39, 40] The time-resolved spectra of 1-MN and the other solutes recorded here indicate that excitation into S_1 leads to emission from only a single excited state. Comparisons between absorption and emission transition dipole moments (Figure 4.13) indicate that the absorbing and emitting states do not differ markedly. Although the solvent dependence of the emission moments of 2-MN are puzzling (and those of 1-MN scattered), these data are inconsistent with the idea that emission arises from a TICT state, as was originally suggested. [39]

Calculations predict the ground-state dipole moments of all three solutes to be large, in the range 6-8 D. The solvent dependence of the Stokes shifts observed here (Figure 4.12) suggest that their S_1 state dipole moments are substantially higher, $\Delta\mu > 5$ D. These estimates are consistent with values of $\Delta\mu$ from TDDFT calculations, which are all in the

range 5-8 D (Table 4.2). Thus the S_1 state can be reasonably described as an ICT state as previously suggested. But calculations indicate that the charge transfer is only partial – the naphthalene ring is already positive by $\sim 0.2e$ in S_0 and this charge only increases to $\sim 0.5e$ in S_1.

2-MN and 1-MN can exist as two ground state conformers which differ in the torsional angle τ between the naphthalene ring and the vinylmalononitrile units. In both cases the more extended **a** form (Figure 4.2) is preferred. Calculations suggest that in 2-MN the conformers are sufficiently close in energy that both forms would be expected to be present in room-temperature samples, whereas in 1-MN the energy difference is sufficiently great that the **a** conformer is expected to dominate (Table 4.1). In both 2-MN and 1-MN the electronic properties of the two forms are calculated to be sufficiently similar (Figure 4.4, Table 4.2) that it would be difficult to distinguish them on the basis of their absorption or emission spectra. Time-resolved emission of 2-MN does, however, reveal the presence of two emitting species with distinct lifetimes in low polarity solvents. We interpret this behavior as indicative of a ground-state equilibrium in which the slightly more polar **a** form begins to dominate as solvent polarity increases.

Like the benzylidene malononitriles, the lifetimes of all three of these naphthalene malononitriles is short and indicative of some fast excited-state process leading to a non-fluorescent state. In 2-MN and 1-MN one cannot rule out the possibility that this process involves a TICT mechanism, i.e. twisting about τ to a virtually dark state at $\tau \sim 90°$. B3LYP calculations suggest that such a state might represent a minimum on the S_1 potential energy surface (PES) of 1-MN but CAM-B3LYP calculations (Figure 4.3), even in the presence of polar solvent (Table 4.6), do not predict a TICT state. As discussed previously in regard to calculations on DMN, [26] it is likely that the presence of this minimum is an artifact. The fact that r2-MN, which cannot undergo a TICT process, behaves similarly

to 2-MN and 1-MN also argues against a TICT mechanism. Instead, it seems more likely that the fluorescence deactivation mechanism operative here is the same as in DMN and JDMN "isomerization" about the double which leads to an intersection between S_1 and S_0 near $\omega = 90°$. We did not pursue multi-configurational calculations of the sort needed to adequately explore the S_1 potential energy surfaces of these molecules with respect to this coordinate. However preliminary spin-flip TDDFT calculations [51–53] did demonstrate the presence of such a conical intersection at large ω.

Assuming this common mechanism, the question remains why significant differences exist among the lifetimes of these molecules: 2-MN(a) ($\sim$ 100 ps) > 2-MN(b) ($\sim$ 30 ps) > r2-MN ($\sim$ 10 ps) > 1-MN ($\sim$ 1 ps). No definitive conclusions are possible at this point, but a few observations can be made. First, if one views these differences as resulting from changes to energy barriers along the reaction coordinate, factors of 10 equate to barrier height variations of or $\sim$ 6 kJ mol^{-1} ($\sim$ 2 k_BT at room temperature). Thus, one might reasonably ascribe these variations in lifetime to rather subtle differences in their S_1 PESs (differences which would be hard to capture in with current electronic structure methods). Second, there are structural differences among the three solutes with respect to the torsion angle τ, which might give rise to such differences in the S_1 PES. Although we believe that the excited-state reaction is directly related to torsion about ω rather than τ, it is reasonable to assume that these two angles are coupled. If the MP2 predictions are taken as the best estimators of ground-state geometries, one finds the torsion angle τ to vary in inverse order to the lifetimes: 2-MN(a) (6°) < 2-MN(b) (25°) < r2-MN (34°) < 1-MN(a) (43°). In some cases relief of the steric interference reflected in these τ angles also results in some nonplanarity of the double bond ($\omega \neq 0$) in the ground-state. MP2 calculations indicate $\omega = 0$ for both conformers of 2-MN whereas in r2-MN and 1-MN this angle has been measured to be $\sim 1°$ and $\sim 6°$, respectively. [46, 60] Thus, there is a correlation between twisting of the τ angle, which is perhaps accompanied by some slight nonplanarity of the

double bond in the ground state, and the rate of the excited-state reaction. A similar correlation between the ground-state τ angle and the barriers to excited-state isomerization in styrene derivatives was previously noted by Lewis and Zuo. [70]

With the exception of 2-MN(a), these naphthalene malononitrile reactions display a solvent dependence not unlike that previously found for the benzylidene malononitriles DMN and JDMN. [18] For the collection of 11 solvents considered here, we find that the lifetimes of 2-MN(b), r2-MN, and 1-MN all show significant correlations ($r^2 > 0.5$) with the average lifetimes of DMN and JDMN (Figure 4.17), which are themselves strongly correlated. It therefore seems reasonable to conclude that the origins of the solvent dependence are similar. Despite the poor correlations with viscosity in Figure 4.17, we expect solvent friction to be one important factor controlling the lifetimes and emission yields of these molecules, as it is in the benzylidene malononitriles. Evidence comes from the ability to greatly enhance the emission yields upon environmental rigidification by either temperature[4] or pressure [40] variation. The poor correlation with solvent viscosity observed here is likely a manifestation of the fact that solvent viscosity is a poor indicator of the friction operative on these reactions, at least when one considers an assortment of different solvents as was done here. In addition, solvent polarity, which provides some of the best correlations observed here (Figure 4.17), also appears to play a role in determining the solvent dependence of both of these classes of fluorophores, making them imperfect as simple reporters of fluidity. Disentangling frictional and energetic effects on these reactions is a challenging task, one which must await further investigation.

[4]We have made preliminary temperature-dependent measurements of 2-MN and 1-MN emission spectra in toluene from room temperature down to 77 K which show that their emission quantum yield increase by ~ 100 and ~ 400 fold, respectively.

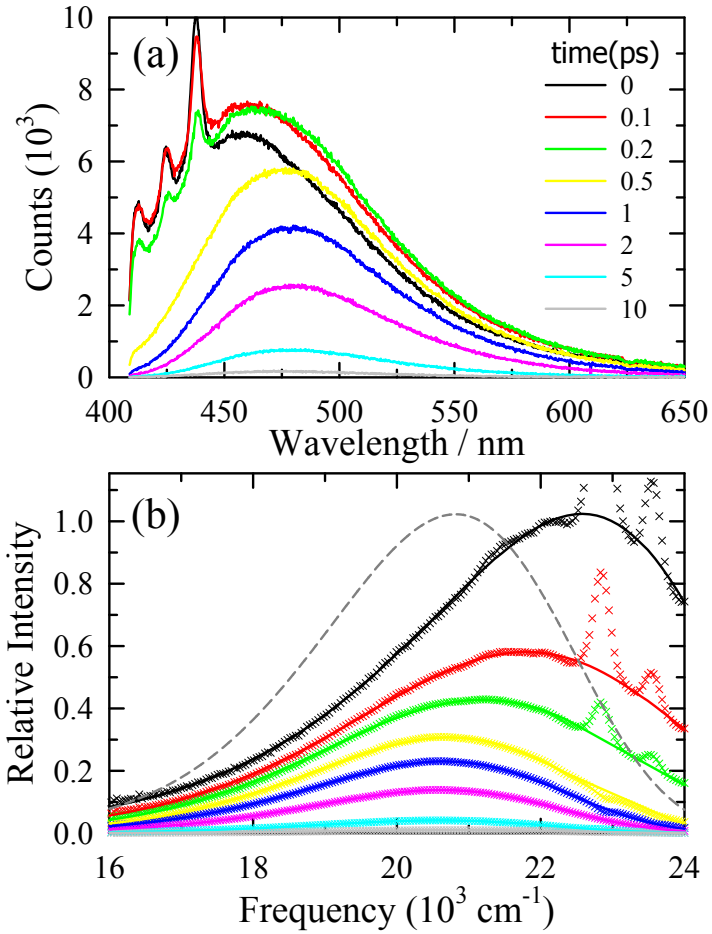

Figure 4.15: KGE spectra of 1-MN in acetonitrile showing (a) "raw" data (prior to deconvolution), (b) spectra after thinning, conversion to frequency, and multi-exponential fitting to remove instrumental broadening (points). The solid curves in (b) are lognormal fits to the data. The dashed curve is the 10 ps spectrum renormalized to highlight the spectral shift.

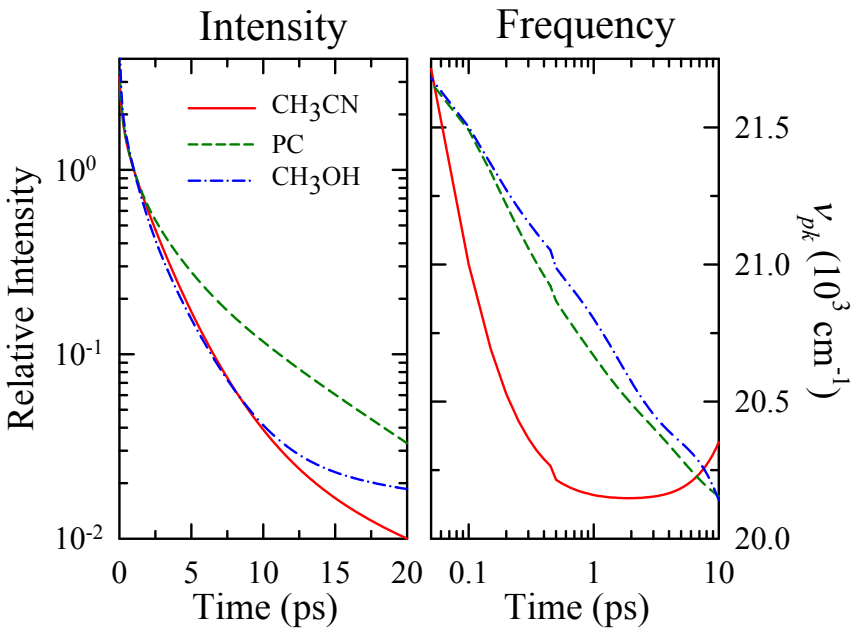

Figure 4.16: Characteristics of the spectral evolution of 1-MN emission in acetonitrile, propylene carbonate (PC) and methanol. The left panel shows the decay of integral emission intensity and the right panel the peak frequency.

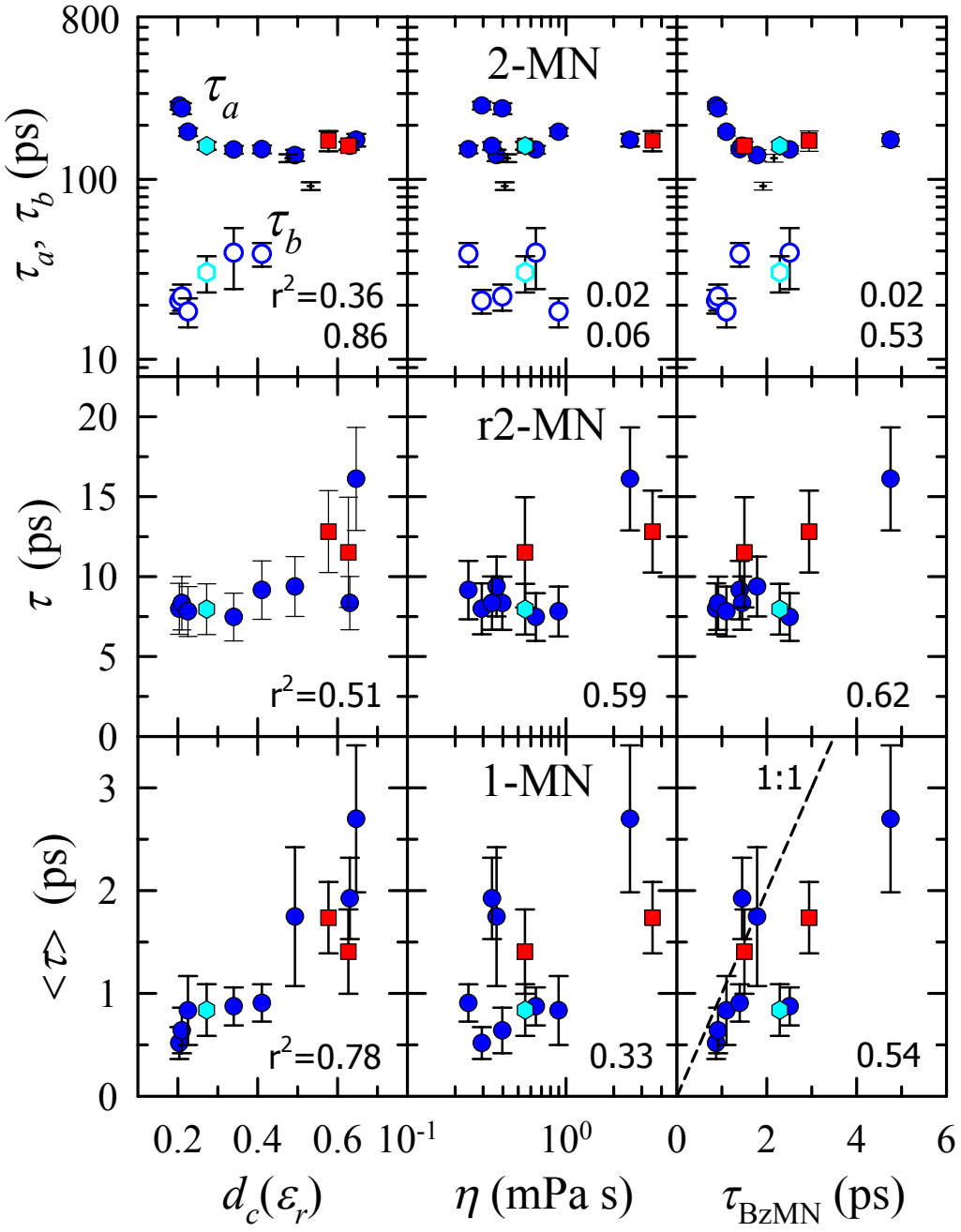

Figure 4.17: Decay times plotted as functions of the total polarizability factor $d_c(\epsilon_r)$, the solvent viscosity η, and the average decay time estimated for benzylidene malononitriles τ_{BzCN} (see text). Circles denote aprotic solvents, squares alcohols, and the hexagon toluene. Inset numbers are the coefficients of determination of linear fits to the data. In the case of 2-MN the top values are for τ_a (filled points) and bottom values τ_b (open symbols) regressions. The two small points in the top panel are 2-MN (τ_a) data for the additional solvents CH_2Cl_2 ($\tau_a \sim 100$ ps) and ethyl acetate. These points are not included in the correlations.

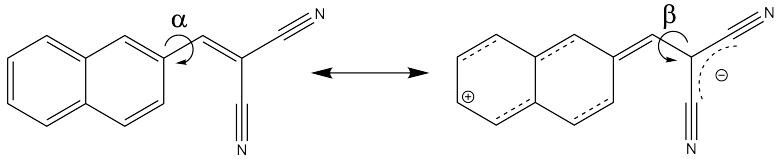

Figure 4.18: Naphthalene malononitrile S_1 resonance structures which can allow for a twist of the ground state double bond.

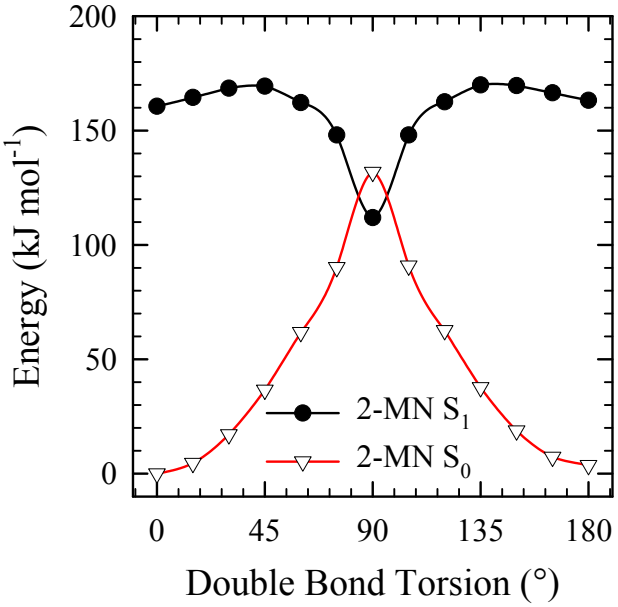

Figure 4.19: Double bond torsion profile in the first excited state. Upon twist into a TICT the possibilty of a conical intersection arises. Triangles show the ground state optimized SPIN-FLIP energies at a given dihedral angle. The first excited state was omitted because we identified it as a triplet state T_1 which we see no indicators it would be actually populated. The second excited state shown here represents the first excited singlet state S_1.

Chapter 5

Thioflavin T

5.1 Abstract

Thioflavin T (ThT) has been employed for decades as a fluorescence marker of amyloid fibril formation and has proven its value in many biological applications. However, its actual excited state dynamics remained unclear for many years. Early work showed a simple viscosity dependence of the fluorescence quantum yield which resulted in its use as a fluidity probe. Experimental and computational studies over the last decade indicate that upon photoexcitation ThT undergoes a twist between the benzothiazole and the aniline groups which quenches its fluorescence. In the present work the excited-state dynamics of ThT has been studied in a series of selected solvents to characterize the quenching mechanism in more detail. Because recent work by Hsu and coworkers shows evidence of auto-degradation of ThT we have performed extensive purification of the probe itself. We find that the fluorescence quenching is strongly correlated to both solvent viscosity and solvation time. There is a clear distinction between protic (alcohols) and aprotic solvents with respect to both of these correlations.

5.2 Introduction

2-[4-(Dimethylamino)phenyl]-3,6-dimethyl-1,3-benzothiazol-3-ium chloride, commonly known as Thioflavin T (ThT), was discovered in the 1960s as a potent sensor for amyloid-related diseases. [71–79] Amyloid fibrils are aggregates of proteins which possess a rigid and filamentary structure. Their accumulation in living cells is associated with a number of diseases like Alzheimers and Parkinsons diseases and type II diabetes. [80–82] Gaining a better understanding of the dynamics of the fibrillation is an imperative in the pursuit to find a cure.

In a non-restrictive environment, e.g. a low viscosity conventional solvent, ThT fluorescence is quenched on a few picosecond timescale, resulting in a low quantum yield ($10^{-3} - 10^{-4}$). [83,84] ThT was found to be non-interacting with either folded or unfolded proteins but to bind highly selectively to amyloids. [85] Upon binding its fluorescence quantum yield increases by 2 to 3 orders of magnitude [72, 74, 85] indicating a significant rigidification of its surroundings. This increase of quantum yield allows one to follow the fibrillization process by monitoring fluorescence intensities.

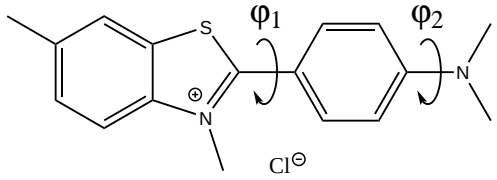

Figure 5.1: ThT with two rotational degrees of freedom possibly responsible for fluorescence quenching.

Despite the fact ThT has proved valuable as a fibrillization sensor for decades, the actual photophysics responsible for its quenching is not fully understood. In recent years several groups have tried to gain a better understanding of the quenching mechanism and the environmental parameters affecting its emission by conducting computational and

experimental studies. [85–95] There is a common assumption in virtually all of these studies that the underlying fluorescence deactivation mechanism is a twisted intramolecular charge transfer (TICT) process involving relative twisting of the benzothiazol and aniline groups (φ_1 in Figure 5.1). Quantum mechanical calculations using TDDFT theory show an energy minimum near $\varphi_1 = 90^\circ$ twist of φ_1 in the S_1 potential energy surface (PES). [85, 88, 89, 92, 95, 96] In the ground state, the energy minimum is predicted to be at $\varphi_1 = 37^\circ$ rather than $\varphi_1 = 0^\circ$ due to the steric interference between the benzothiazole methyl group and the benzene ortho hydrogen atoms, in agreement with X-ray data. [97] These calculations also show the oscillator strength reaching zero at φ_1=90°. An oscillator strength of zero would mean that there would be no radiative transition occurring between the excited and ground states and thus a strictly 90° TICT state would be dark and transition to this one possible explanation of the quenching.

Experimental research by the groups of Maskevich and Turoverov [83, 87–90, 98, 99], Huppert [86, 93–95, 100, 101] and Nath [85, 91, 92, 102] have contributed significantly to a better understanding of the photophysics of ThT. In 2003 Voropai et al. were the first to study qualitatively the effect of the solvent environment on ThT. [83] Using steady state absorption and emission techniques they found two emission maxima with different absorption band correlation, suggesting the presence of an impurity which can be excited at ∼350 nm and emits to the blue of the actual ThT emission. They also found the quantum yield was not only a function of viscosity but also showed a polarity dependence. Unfortunately, little quantitative data was provided with this report. However, they were (one of) the first groups to use quantum chemical calculations to recognize the possibility of twisting about the two single bonds to a TICT state as being responsible for the rapid deactivation in fluid solution.

Maskevich and coworkers in collaboration with Turoverov and coworkers subsequently

performed a more detailed analysis of the steady state spectra of ThT. [87–90, 98] The absorption spectrum blue shifts by ∼600 cm^{-1} with increasing polarity indicating a modest decrease in dipole moment in the FC S_1 state. [87] Excimer formation was ruled out as a source of increased fluorescence intensity which is a concern because of the ionic nature of ThT. [98] Gas phase spectra and properties were calculated with low level basis sets. [88, 89] Across several employed theories (functionals) a non-planar nature of ThT in the S_0 state was revealed and compared to BTA-2 (2-(4'-(dimethylamino)phenyl)-6-methylbenzothiazole, the non-methylated derivative on the thiazol-nitrogen) which does show a planar geometry, suggesting the methyl group on the nitrogen causing a steric interference with the aniline group. The existence of a TICT state was confirmed via torsional scans of φ_1. Broadband transient absorption measurements of ThT in water by Stsiapura et al. [90] showed that loss of the stimulated emission signal takes place in about $\sim$ 1 ps whereas the ground-state bleach recovers on a 10-15 ps timescale. The slower recovery of the ground state signal could be due to vibrational relaxation on the ground state PES after internal conversion. In addition, complete recovery of the bleach was not observed; 3-5% of the sample did not recover at times longer than 3 ps which might be explained by photolysis upon excitation.

Huppert and coworkers used the TCSPC and fluorescence upconversion techniques in several studies in which they observed both the pressure dependence of ThT lifetimes in alcohol solvents and as a function of temperature over wide temperature ranges. [93–95] In their high pressure experiments a reasonably good linear correlation was found between the nonradiative rate k_{nr} and viscosity η over a range of three orders of magnitude of η. However, more interestingly, Amdursky et al. showed in their cryostat experiments that the nonradiative rate of ThT follows the dielectric relaxation times in 1-propanol over 4 orders of magnitude. [94]

In addition to their efforts acquiring experimental data, they describe the reaction in their analysis as a diffusion on a 1-dimensional PES according to the analysis of van der Meer [103], allowing them to simulate a spectral shift. The time dependent population distribution along the reaction coordinate (twist angle φ_1) is propagated with some overall diffusion constant on a torsional potential obtained from TDDFT calculations. The model accounts for the dynamic red shift of the emission and the time dependent decrease in the time-resolved intensity of the emission spectra at intermediate and long times ($t \geq 5$ ps), but it does not account for solvation, which limits its ability to accurately describe the time evolving spectra.

Nath and coworkers used fluorescence upconversion to reconstruct time-resolved emission spectra and area normalized emission spectra in several solvents. [85,92] They reported spectra undergo a significant red-shift and exhibit an isoemissive point in water within 2 ps following photoexcitation. Based on the presence of an isoemissive point, they concluded the TICT state must be emissive. The observed spectral shift and the drop in emission intensity by ~90% both occur within 2 ps. The same behaviour was observed in acetonitrile. They interpreted this similarity in time scale as indicating that the spectral shift is not due to solvation, but instead due to evolution of the twisting coordinate. We do not find these two observations mutually exclusive and their statement would require further explanation. In a separate publication they substituted the dimethyl amino group for a julolidine group to eliminate φ_2 as a rotational degree of freedom, leaving effectively only φ_1. [102] No major differences in lifetime or spectral shifts could be reported, leading to the conclusion that φ_1 twisting is the time limiting factor for the quenching.

The experimental disagreement about an emissive or non-emissive TICT state could be explained as being due to another factor. To the best of our knowledge commercially available ThT is offered most commonly in purities of only 60-80% and not at all in spec-

troscopic grade. Purity, however, is an imperative when studying fluorescence as weak as that of ThT. Very recently Hsu and coworkers conducted LC-MS and NMR studies on the stability of ThT. [104] They observed both photodegradation and a surprisingly fast auto-degradation in the dark. The LC spectrum showed 3 additional peaks besides ThT which they labeled dThT-1, dThT-2 and dThT-3. Combined LC-MS and NMR analysis revealed the following nature of the decomposition products: dThT-3 contains one carbon and two hydrogen atoms fewer than ThT, and dThT-2 contains two carbon and four hydrogen atoms fewer than ThT. ^{1}D-NMR spectra show a single and double de-methylation, respectively, of the aminobenzene moiety in these two degradation products. dThT-1 contains one oxygen more and two hydrogens fewer than ThT, suggesting an oxidation reaction. It is difficult to guess what effects impurities and photodegradation may have played in past work. For example, Stsiapura et al. are missing the recovery of 3-5% of the sample in their transient absorption experiment, which could very well be due to the photodegradation of the sample.

Despite the effort of several groups for a better understanding of the TICT mechanism, just what environmental factors affect the twisting remain unclear. The lifetime of ThT depends on solvent viscosity. But Huppert and coworkers have also shown that there is also a correlation to the dielectric relaxation times in alcohol solvents. Some of the conclusions present in the literature could be misinterpreted due to the presence of impurities. Regarding the quantum mechanical achievements there seems qualitatively an agreement across employed computational methods but some show a broken symmetry around a $\varphi = 90°$ twist which might not be real.

To help address some of these outstanding issues we have investigated the effect of impurities, conducted quantum mechanical calculations to compare rotation around the two possible TICT axis φ_1 and φ_2, and measured the solvent dependent fluorescence quenching

dynamics of ThT in a series of aprotic solvents and n-alcohols.

5.3 Experimental

Thioflavin T (CAS 2390-54-7), 95+% purity was purchased from Matrix Scientific (Columbia, SC). The received material was recrystallized 7 times in different hexane / ethanol mixtures as listed in Table 5.1. (Other solvent mixtures have also been used [78, 105, 106]) All solvents used for spectroscopic measurements were either of spectroscopic or HPLC grade (Sigma-Aldrich CHROMASOLV or Merck Omnisolv) and were used as received.

Recrystallization #	Solvents	Volume Ratio
1 - 2	Hexanes : Ethanol	3 : 1
3 - 7	Hexanes : Ethanol	9 : 1

Table 5.1: ThT recrystallization from solvent mixtures

Absorption spectra were measured using a Hitachi UV-3010 spectrometer and emission spectra a Horiba FL-3 Fluorolog fluorimeter. The latter were photometrically corrected for the responsivity of the PMT detector. Samples for steady state measurements were prepared in 1 cm quartz cuvettes using solute concentrations with OD <0.2 at the absorption wavelength for emission data and <1.5 for absorption data. Samples for extinction coefficient measurements were prepared using a stock solution of ThT in acetonitrile of known concentration and diluted 300-fold into the target solvent. At this level of dilution previous studies by our group showed no differences in spectral shapes or position when compared to solutions made by direct addition of solid solute to the solvent. [18] Quantum yields were determined relative to coumarin 153 (C153) in acetonitrile ($\phi_f = 0.64$) [69] and excited at $\lambda_{ex} = 415$ nm. Time resolved fluorescence spectra were recorded using the Kerr-gated emission technique (KGE), described in Section 3.2.1. The second harmonic of the laser at $\lambda_{SHG} = 387$ nm is used for pumping and the overall system provides an

instrument response function (IRF) having a full width at half maximum (fwhm) of ∼400 fs before deconvolution. Time-correlated single photon counting (TCSPC), described in Section 3.2.2, was also used to explore the effects of the long-lived impurities.

Electronic structure calculations were performed using the Gaussian 09 program. [50] Ground state geometry optimization was accomplished using density functional theory (DFT) in conjunction with the B3LYP functional [107,108] and the 6-311G(d,p) basis set. Time dependent DFT [109] using the same functional and basis set was used to determine excited state properties.

5.4 Results

5.4.1 Quantum Mechanical Calculations

Ground state optimization shows a nonplanar geometry ($\varphi_1 = 37°$) which is in good agreement with previous publications [85,88,89,92,95–97] and X-ray structure. [97] To check for an appropriate employment of a density functional and basis set, we used a ground state optimized structure and performed a single point (SP) TDDFT calculation. The obtained excited states with their transition energies and relative oscillator strengths are consistent with the observed absorption spectrum, as shown in Figure 5.2. The first transition, $S_0 \leftrightarrow S_1$, is well isolated from higher states transitions ($S_0 \leftrightarrow S_n$, $n \geq 2$). The agreement between theory and experiment is reasonable, considering we do not employ additional PCM theory where we would expect a redshift and the experimental spectrum has been taken in a polar solvent (we avoid less polar solvents for potential ion pairing distortion as addressed in Section 5.4.3).

A torsional scan of φ_1 in the ground state in 15° steps has been performed by freezing the dihedral angle (coordinates # 4-10-17-19 in Figure 5.4) and optimizing all other coor-

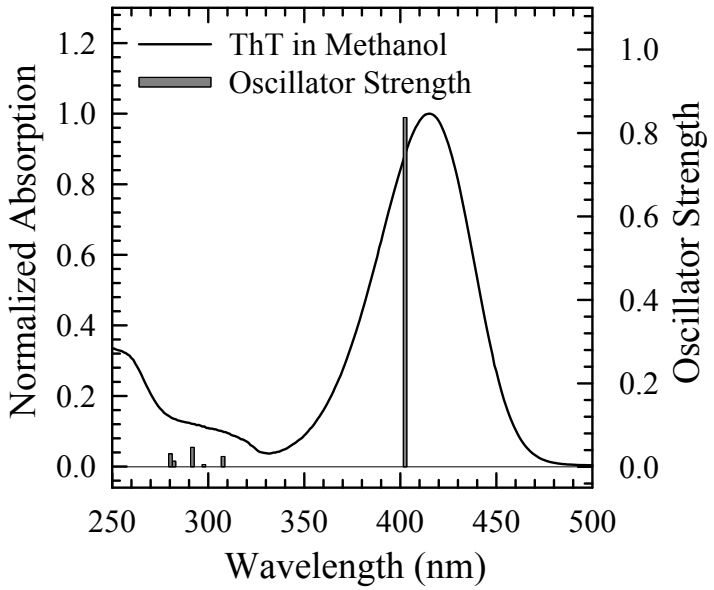

Figure 5.2: ThT absorption spectrum in methanol compared to the transition wavelengths gas phase oscillator strengths calculated using B3LYP/6-311G(d,p).

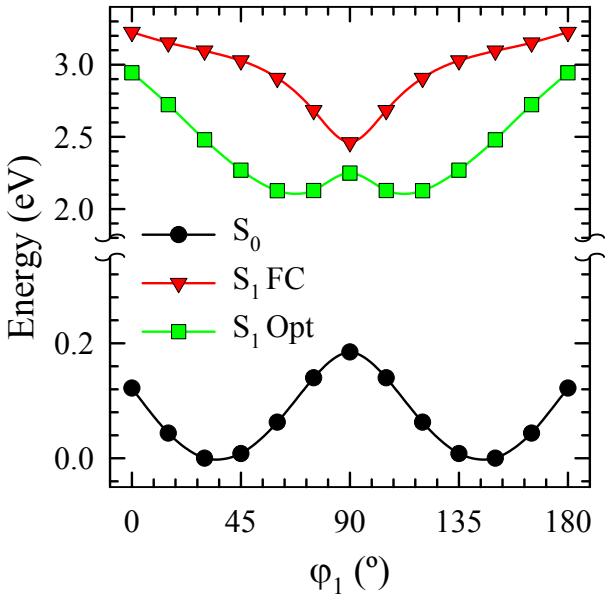

Figure 5.3: ThT torsion profile versus φ_1 in ground state (optimized, S_0), excited state (optimized, S_1(Opt)) and excited state from ground state optimized geometry in single point calculations (S_1(SP)). The discrepancy between the energy trajectories around 90° shows that the effective reaction path is propbably insufficiently described by φ_1 alone.

dinates. Along the ground state potential energy surface (PES) a rotation barrier of 0.2 eV ($\sim 10\ k_BT$) with a maximum at 90° is observed (S_0 in Figure 5.3). To obtain the same information about the first excited state we pursue two methods: a) taking the torsion geometries just discussed and performing SP TDDFT calculations (S_1(SP) in Figure 5.3) and b) freezing the dihedral angle but performing excited state optimizations (S_1(Opt) in Figure 5.3). In the first case a barrier-free relaxation into a 90° twist is observed. In the second case the slope at the FC state is larger but the minimum is at $\varphi_1 = 68°$ rather than 90°. The difference is related to a second important coordinate. The bottom structure in Figure 5.4 shows a fully relaxed (optimized) geometry in the excited state. While the dihedral angle φ_1 describes the twist of the two planes (benzothiazol and aniline ring structures) along the bond axis, in the excited state these ring planes also bend with an angle $\theta \approx 21°$ relative to one another. We assume this is due to a partial tetrahedral sp^3-hybridization in the excited state after charge transfer vs. its planar sp^2-hybridization in the ground state. Consequently, the reaction coordinate for twisting would need to be described by a two dimensional PES along the dihedral angle φ_1 and the bend angle θ. This observation is consistent with what Ren and coworkers had also recently reported. [96]

Based on this finding we revisited the definition of the dihedral angle φ_1 and consider how to best define the bend angle θ. As stated above, torsional scans were performed by defining frozen dihedral angles among the atom coordinates # 4-10-17-19 (see top Figure 5.4). However, the opposite dihedral angle # 6-10-17-20 provides a different measure of the torsion angle as a result of a nonplanar geometry of the 5-membered thiazol ring. This deviation already exists in the ground state but becomes much larger in the excited state. Consequently, we define the dihedral angle as the average of both opposing angles. For

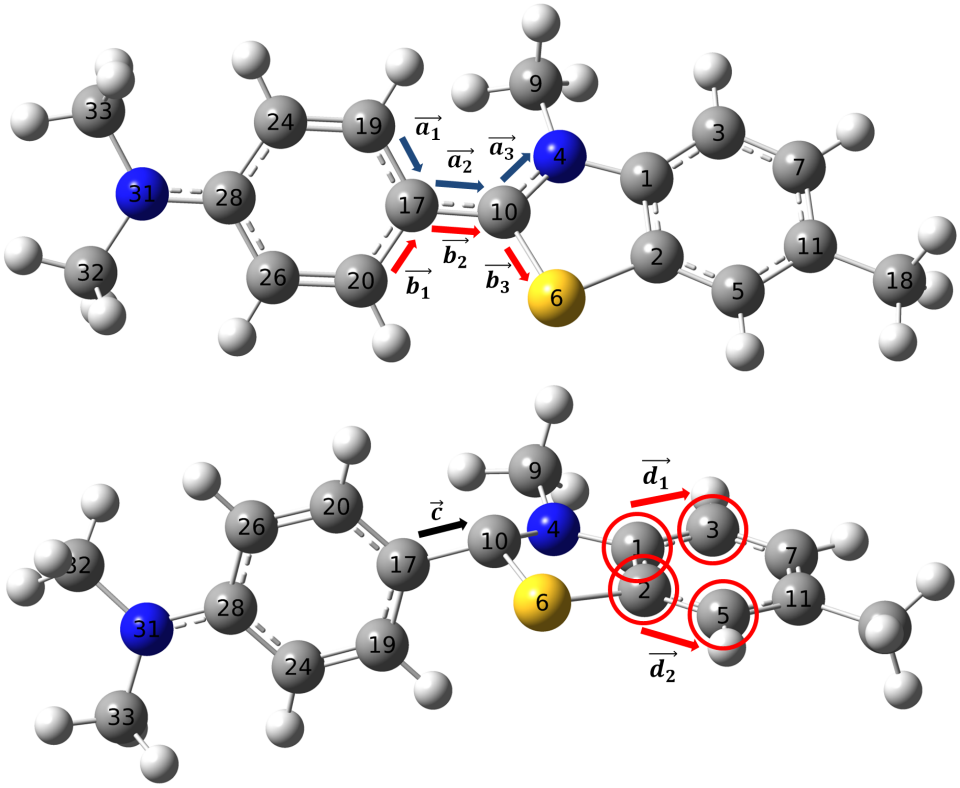

Figure 5.4: ThT optimized ground state (top) and excited state (bottom) structure. Figure created using GaussView Version 5 [110]

clarity and distinction we call the resulting angle τ_1 instead of φ_1:

$$\tau_a = cos^{-1}\left\{\frac{(\vec{a_1}\times\vec{a_2})\cdot(\vec{a_2}\times\vec{a_3})}{|(\vec{a_1}\times\vec{a_2})|\cdot|(\vec{a_2}\times\vec{a_3})|}\right\}(=\varphi_1) \tag{5.1}$$

$$\tau_b = cos^{-1}\left\{\frac{\left(\vec{b_1}\times\vec{b_2}\right)\cdot\left(\vec{b_2}\times\vec{b_3}\right)}{\left|\left(\vec{b_1}\times\vec{b_2}\right)\right|\cdot\left|\left(\vec{b_2}\times\vec{b_3}\right)\right|}\right\} \tag{5.2}$$

$$\tau_1 = \frac{\tau_a+\tau_b}{2} \tag{5.3}$$

We explored several coordinate combinations for a better description of the bend angle. Since the thiazol ring is twisted we utilize the rigidity of the benzyl rings and define θ via

the orthogonal normal between the benzothiazol-aniline bond vector and the benzyl plane in the benzothiazol group (see bottom Figure 5.4):

$$\theta \quad = \quad cos^{-1} \left\{ \frac{\vec{c} \cdot \left(\vec{d_1} \times \vec{d_2} \right)}{|\vec{c}| \cdot \left| \left(\vec{d_1} \times \vec{d_2} \right) \right|} \right\} - 90^{\circ} \tag{5.4}$$

The dependence between the bend angle θ and the twist angle τ_1 is shown in Figure 5.5.

Our quantum mechanical findings support the fluorescence deactivation via TICT mechanism by φ_1 or τ_1, respectively. Independently, the question about the dimethylamino group rotation needs to be addressed. Conducting a ground state torsion profile calculation for φ_2 (Figure 5.1), similar to φ_1, Figure 5.10 shows a barrier of 0.8 eV at 90° in the ground state. The SP energies indicate a slight barrier of $\sim$ 0.1 eV at 45° before relaxing also into a fully twisted geometry as well. Under the circumstance that τ_1 twists barrier free into a TICT state within sub-ps we conclude the dimethylamino group is likely not responsible for the very fast fluorescence quenching which is in agreement with the experimental result of Srivastava et al. using the julolidine substituted derivative. [102]

5.4.2 Thioflavin T Purity

Upon request we received a certified purity of 97.52% from Matrix Scientific for the particular batch of ThT used by us. This analysis was based on integrated peak intensity of an LC spectrum which showed at least two additional peaks, similar to what Hsu and coworkers reported. [104] A publication by Zhang in 2009 is the only synthesis published that reports a $\geq$96% yield. [111] (Their purity evaluation is also based on solely LC spectrum peak area integration.)

The sample received was recrystallized 7 times. Shown in Figure 5.11A is a series of

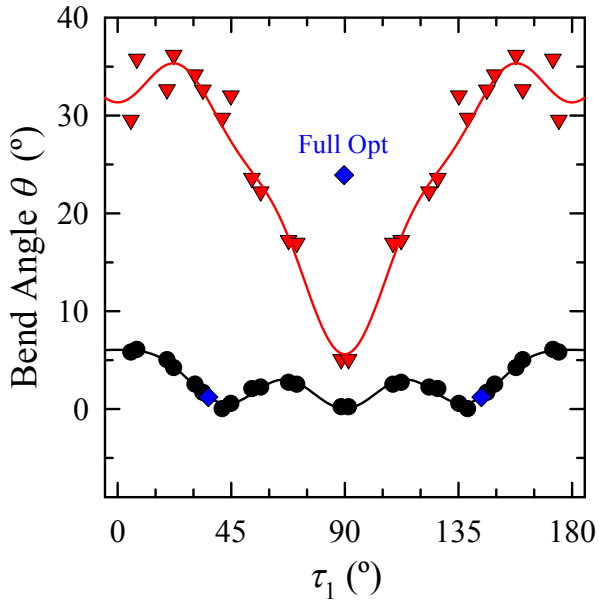

Figure 5.5: Bend angle θ versus twist angle τ_1.

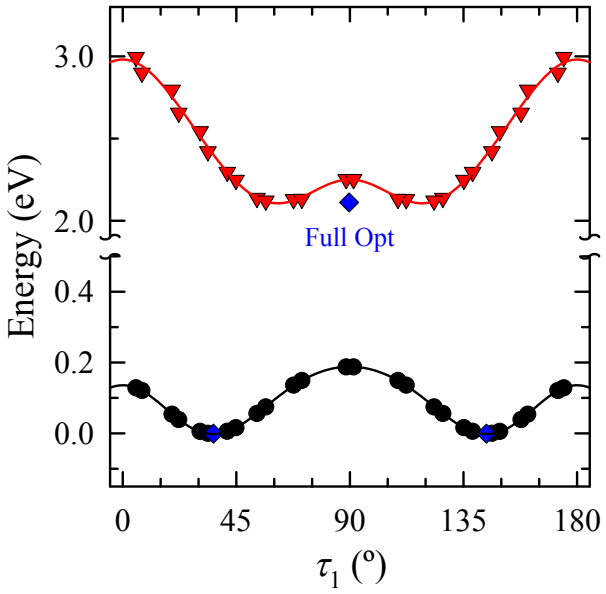

Figure 5.6: ThT torsion profile versus τ_1 in optimized ground state (black) and excited state (red)

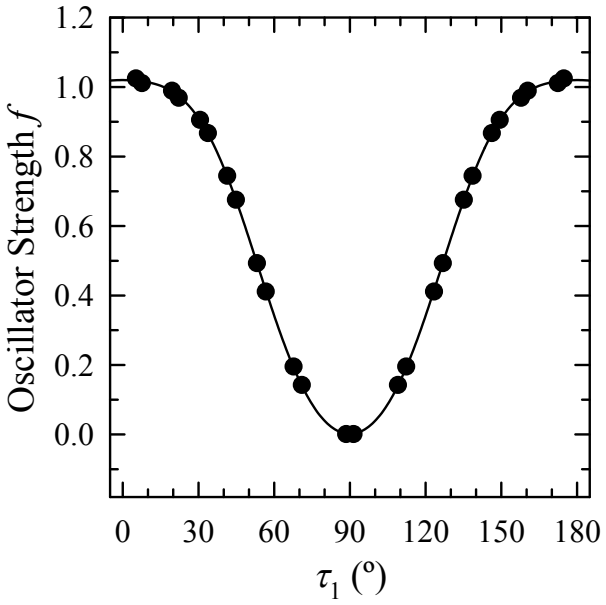

Figure 5.7: $S_0 \rightarrow S_1$ oscillator strengths versus torsion τ_1.

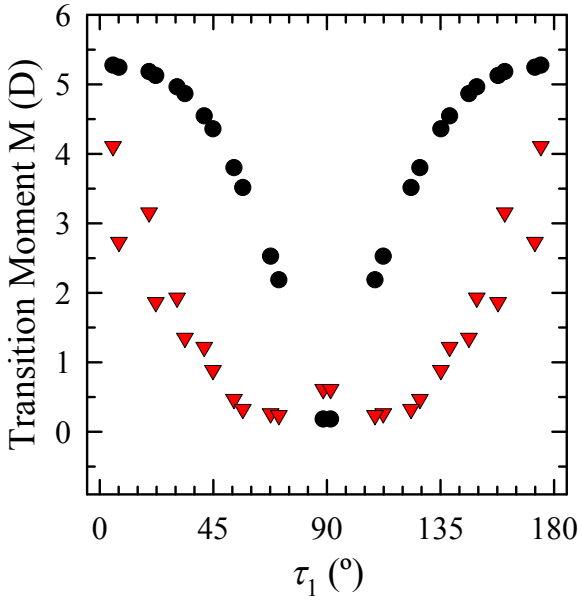

Figure 5.8: FC $S_0 \rightarrow S_1$ transition moments versus torsion τ_1.

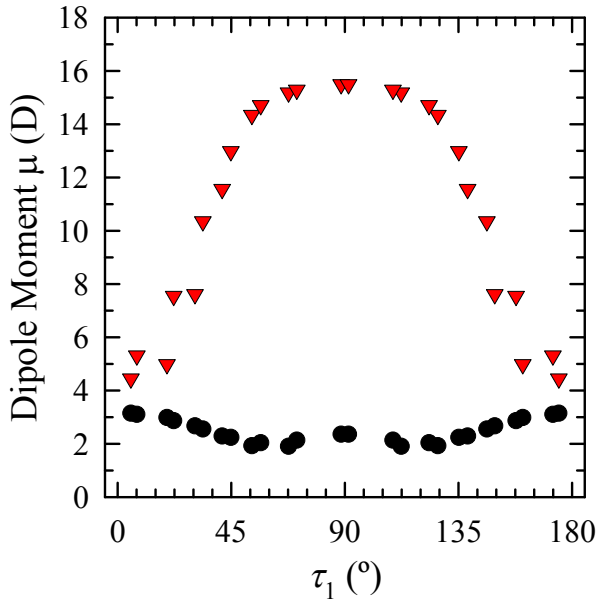

Figure 5.9: ThT dipole moments along torsion τ_1 in ground (S_0, black) and first excited state (S_1, red).

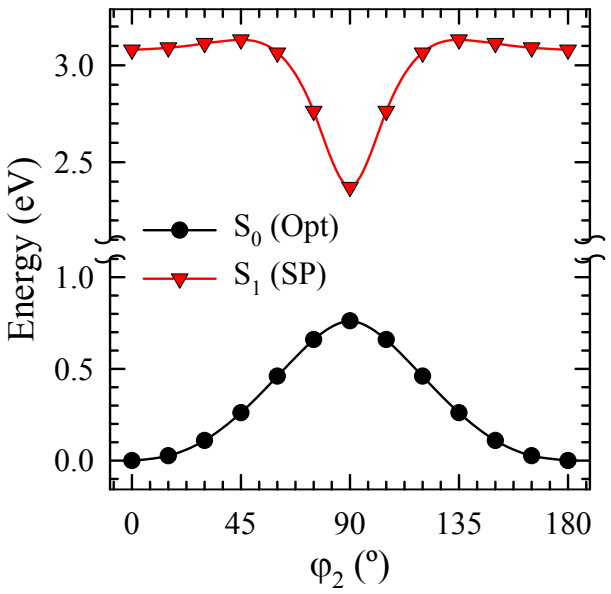

Figure 5.10: ThT dimethylamino group rotation along φ_2.

ThT excitation spectra in acetonitrile taken after each recrystallization step. The emission is recorded at 500 nm. It shows an initially dominating emission from a state not in agreement with the absorption spectrum. Along with each purification step this emission intensity decreases, identifying it as an impurity. However, this emission reaches a steady state after 3-4 recrystallizations and never fully vanishes. This residual impurity seems to be in agreement with Hsu's observation of a fast decomposition upon irradiation or even cold storage in the dark. It also seems noteworthy a fairly large amount of insoluble white salt was removed during the 1^{st} recrystallization which we have not further analyzed.

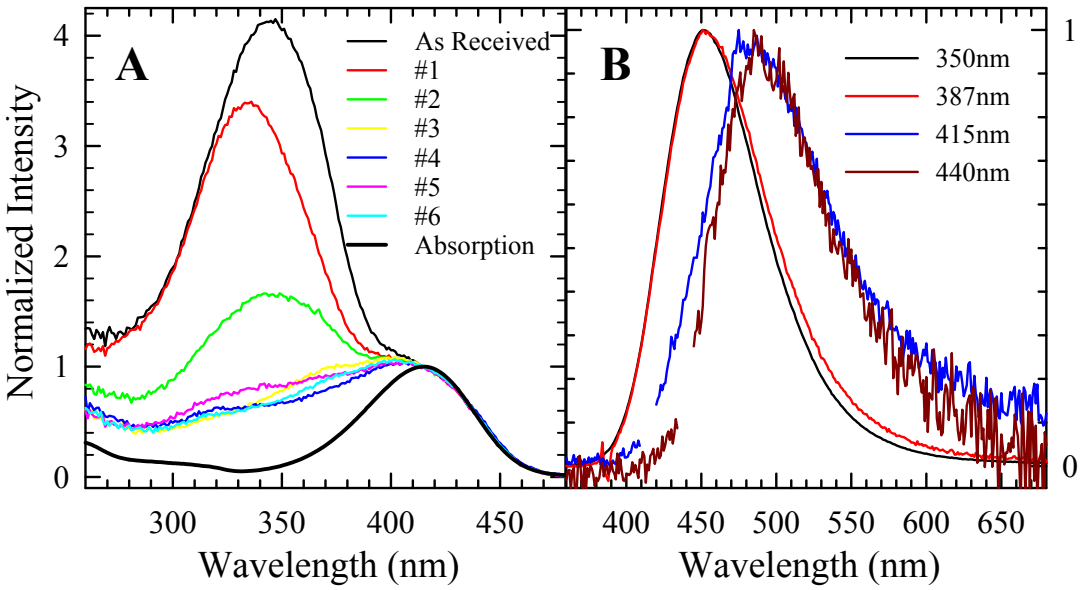

Figure 5.11: A. Fluorescence excitation spectra of ThT during purification. Emission was recorded at 500 nm. Spectra were normalized to a value of 1 at 415 nm (absorption peak maximum). B. Emission spectra of final purified ThT in acetonitrile, excited at different wavelengths and peak normalized.

The residual impurity has its absorption maximum around 350 nm (Figure 5.11A). The shift of this peak across the recrystallization seen are probably within this series is prob-

ably due to insufficient drying or solvent removal, respectively, between recrystallizations and before preparing the sample cuvette. Measuring the fluorescence emission of the final purity in acetonitrile at different excitation wavelengths reveals the emissive nature of the impurity (Figure 5.11B): Similar in shape and Stokes shift with respect to its absorption, the impurity has a 50 nm hypsochromic shift and a much higher quantum yield compared to ThT. Checking the emission from excitation at 387 nm was required since the laser system for the KGE is tuned to 775 nm, consequently exciting with its second harmonic at 387 nm. The results show under steady state conditions the obtained emission is primarily from the impurity if excited below $\sim$415 nm. Consequently, for representative quantum yield measurements ThT needs to be excited $\geq$415 nm.

Assuming the traces of decomposed ThT must have a long lifetime in order to contribute to the steady state emission, samples in pentanol and water were measured using TCSPC to obtain lifetime information, exciting again at 387 nm for a quantitative comparison with KGE data. Numerical deconvolution with the instrument response function and fitting of the decays reveals 99% of a lifetime component well below the time resolution of the TCSPC instrument ($\ll$25ps), assigned to ThT, and $<$1% component of 1.6 ns which we assign to the impurity. For our Kerr-gated experiment, these results imply that we should expect a 1% contribution of a long lifetime species in the spectra. A component of this small amplitude is within the uncertainty of the measurements and we conclude it will not effect our time resolved measurements.

5.4.3 Ion Pairing

The KGE experiments require a relatively high sample concentrations, up to 10^{-4} M (1 OD in 1 mm cuvette with $\epsilon \approx 30,000$). In order to measure the properties of the ThT cation in a series of solvents across the polarity scale, we need to consider the possibility of ion pairing in less polar solvents. [112] Figure 5.12 shows a dilution series of ThT in acetone

as one of the least polar solvents we employ. No noticeable spectral change is observed with increasing concentration except for a clipping on the blue edge of the emission. This clipping is due to re-absorption, expected at higher solute concentrations. We therefore conclude that no ion pairing distortion should be present in our measurements.

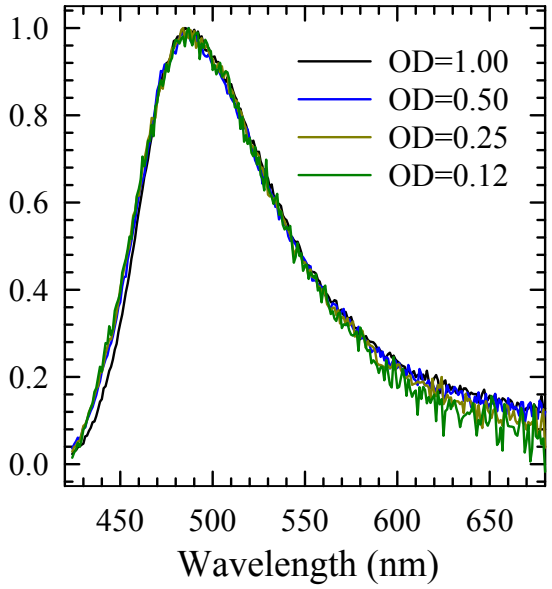

Figure 5.12: ThT in acetone in a dilution series to determine spectral changes which would indicate ion pairing. Measurements were performed in a 1 mm cuvette in a front face geometry and excited at $\lambda_{ex} = 415$ nm.

5.4.4 Steady State Spectra

The acquired absorption and emission spectra show little differences in spectral shift and shape across the solvents used in this study. Figure 5.13 and 5.14 are presented in selected solvents and separately plotted in the homologous n-alcohol series. The only significant difference can be noted for the emission which shows a varying red tail. Both absorption and emission spectra have been fit using a lognormal function (Eq. 4.2) to extract information about peak frequency, width, asymmetry, intensity and 1^{st} moment frequency

analytically as well as calculating the extinction coefficient ϵ_{max} and quantum yield (listed in Table 5.2). Selected correlations of these emission fits with solvent properties are shown in Figure 5.15, 5.16, 5.17 and 5.18.

Over the moderate polarity scale we felt safe measuring, the absorption and emission frequencies vary by only $\sim$500 cm^{-1} compared to widths of $\sim$3500 cm^{-1} (absorption, Figure 5.13) and $\sim$4100 cm^{-1} (emission, Figure 5.14). The absorption frequencies show a clear trend only within the homologous series of n-alcohols with respect to their dielectric properties. However, it is hard to deduce the origin of this dependence because everything varies systematically in a homologous series. With respect to the emission frequencies there is no trend noticeable at all and there may not be one. However, it should be kept in mind that the lifetimes of ThT are short enough that the steady state emission does not reflect the equilibrium solvation of the S_1 and that therefore dynamics are relevant here.

The truly distinct observation is the emission FWHM in the spectra which we can discern clear correlation amongst the non-alcohols which has also been reported by Nath and coworkers. [92] To avoid possible misrepresentation by a single lognormal function for the red tail we plot the FWHM directly from the experimental data (i.e. not the lognormal fit parameter). To our surprise we did find an interesting correlation when the FWHM is plotted against the solvation time of the respective solvent it is in and and its lifetime (Figure 5.18), with a differentiation between protic and aprotic solvents. This dynamical behavior will be discussed later.

Quantum yields (Φ_f, Table 5.2) were measured against C153 in acetonitrile and are in good agreement within $\sim$30% or better of previously published values. [87, 89, 113]

Calculating the transition moments M_{01} from the ground to the excited state we use

Birks' approach [68] (Equation 4.7). The average value of ∼5.5 D is in good agreement with the calculated value of ∼5 D in the FC state (compare to Figure 5.8 at $\tau_1 = 37°$). Anticipating already the measured average lifetimes, which will be discussed in greater detail in the following Section 5.4.5, it allows to calculate the reverse transition moments from the excited back to the ground state:

$$M_{1\to 0} = 1.786 \times 10^3 \left(\frac{k_{rad}}{n_D^3 \tilde{\nu}_{em}^3} \right)^{\frac{1}{2}} \tag{5.5}$$

$$k_{rad} = \frac{\Phi_f}{\langle \tau_f \rangle} \tag{5.6}$$

All transition moments, both M_{01} and M_{10}, are listed in Table 5.2 and plotted in Figure 5.19. It appears that there is a systematic increase of M_{01} with $F(\epsilon, n_D)$. Unclear remain the systematically higher transition moments M_{10} compared to M_{01} since they are expected to be lower. The uncertainties have not been determined yet because quantum yield measurements have not been repeated. Despite the reasonable agreement of quantum yields compared to other groups we may have calculated too high numbers which would result in higher transition moments.

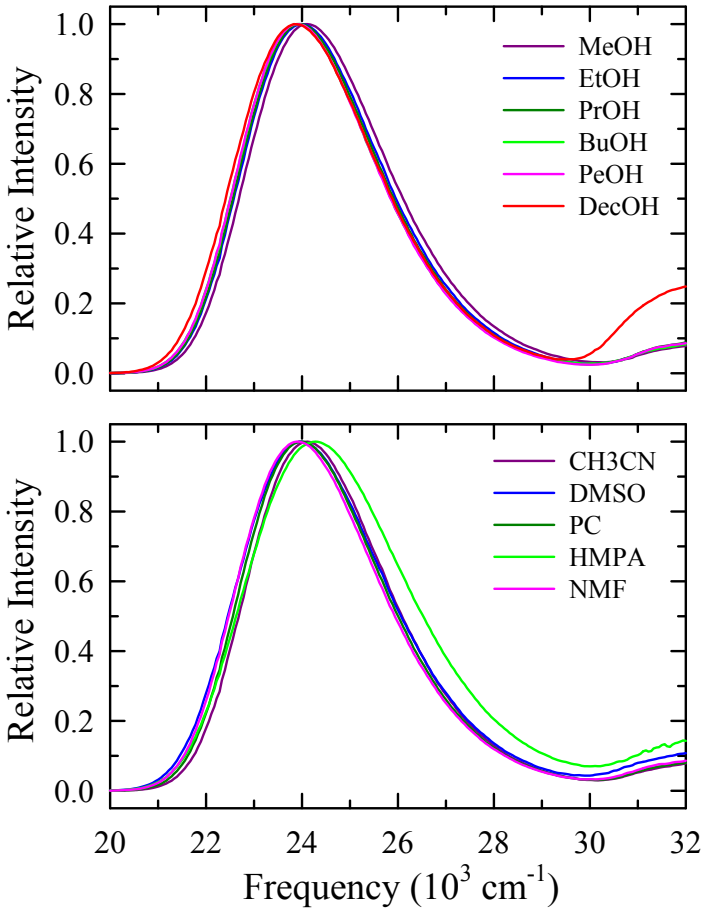

Figure 5.13: ThT steady state absorption spectra in selected solvents.

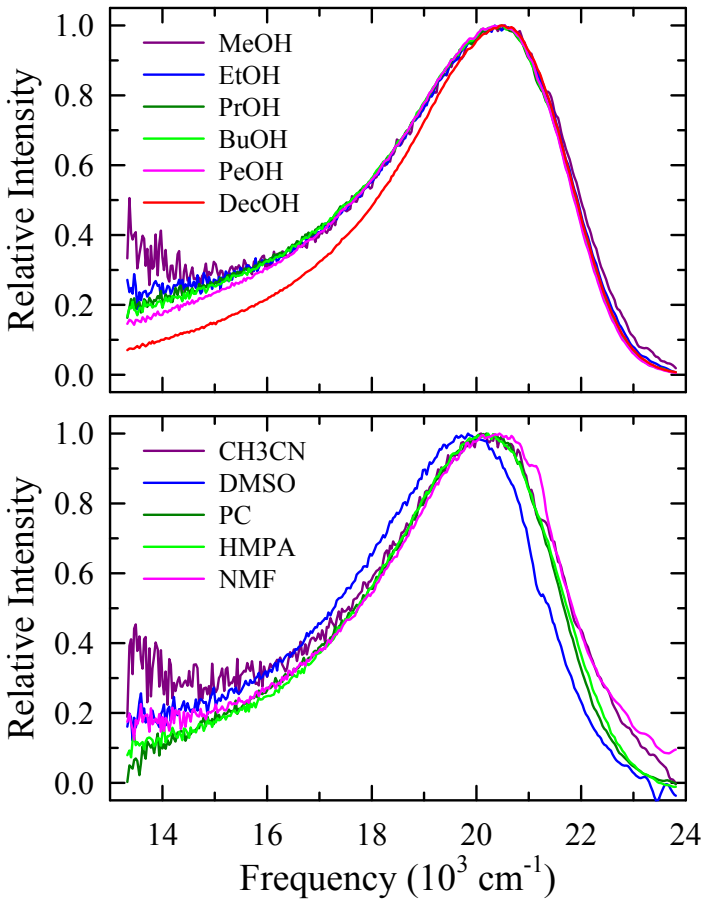

Figure 5.14: ThT steady state emission spectra in selected solvents.

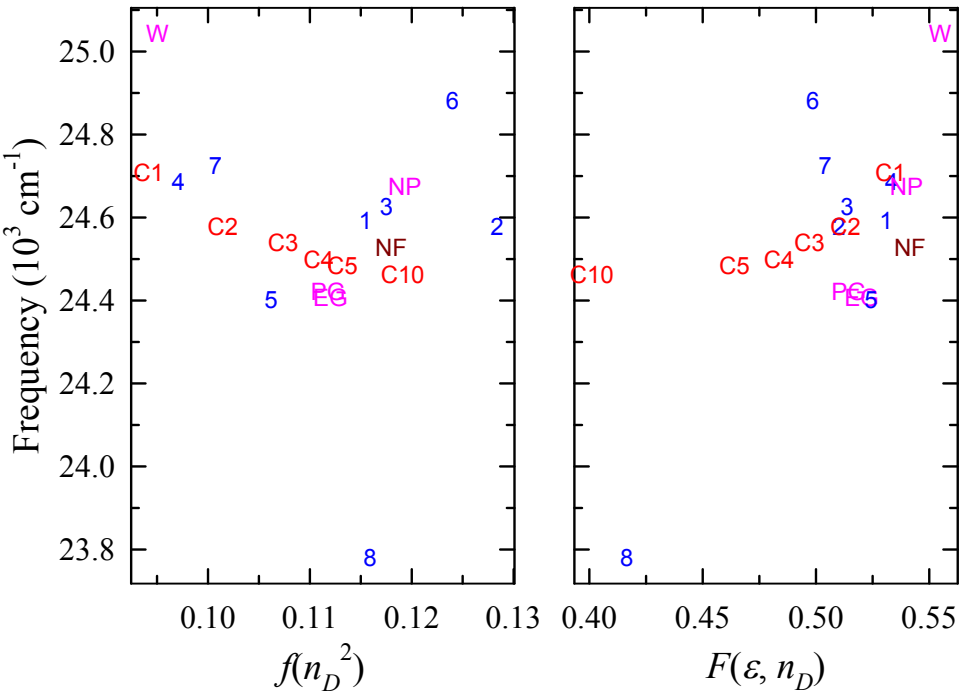

Figure 5.15: ThT absorption 1^{st} moment frequency versus dielectric parameters. Symbols are according to Table 5.2; red: n-alcohols; magenta: diols; blue: aprotic solvents.

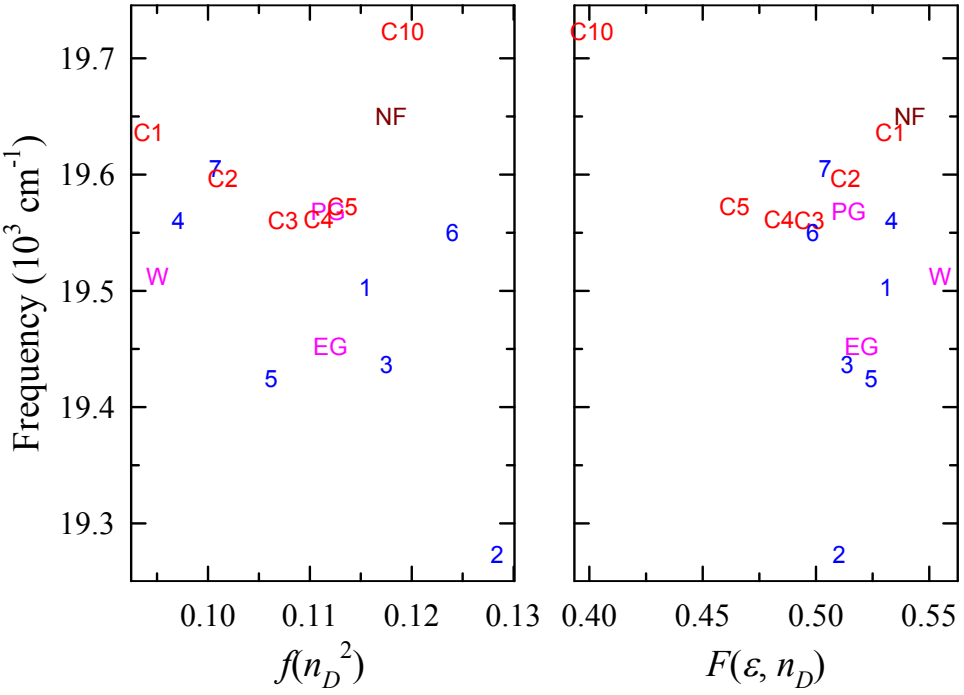

Figure 5.16: ThT emission 1^{st} moment frequency versus dielectric parameters. Symbols are according to Table 5.2; red: n-alcohols; magenta: diols; blue: aprotic solvents.

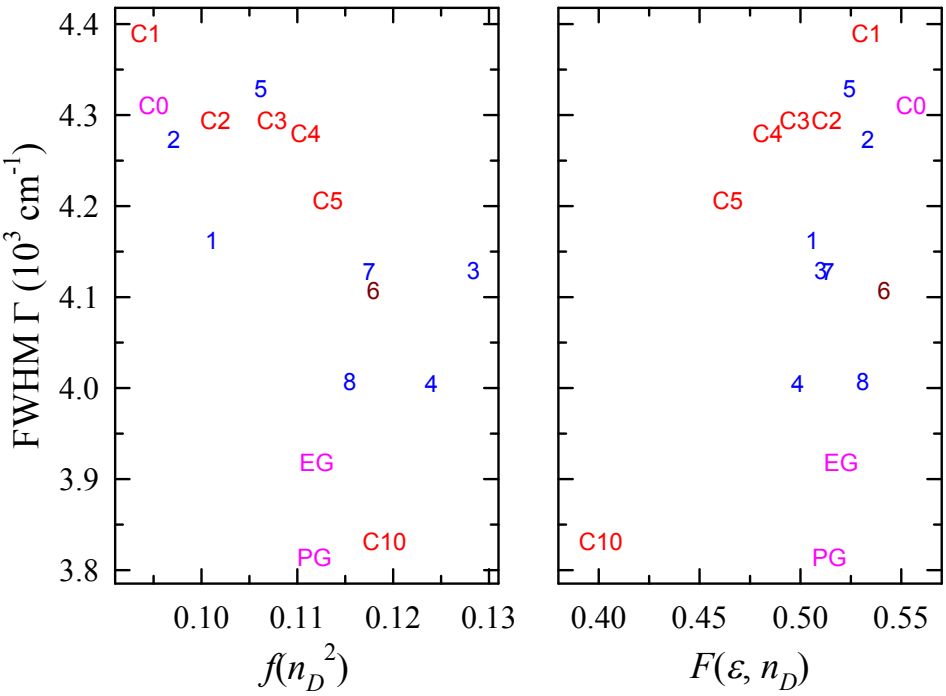

Figure 5.17: ThT steady state emission FWHM versus dielectric parameters. Symbols are according to Table 5.2; red: n-alcohols; magenta: diols; blue: aprotic solvents.

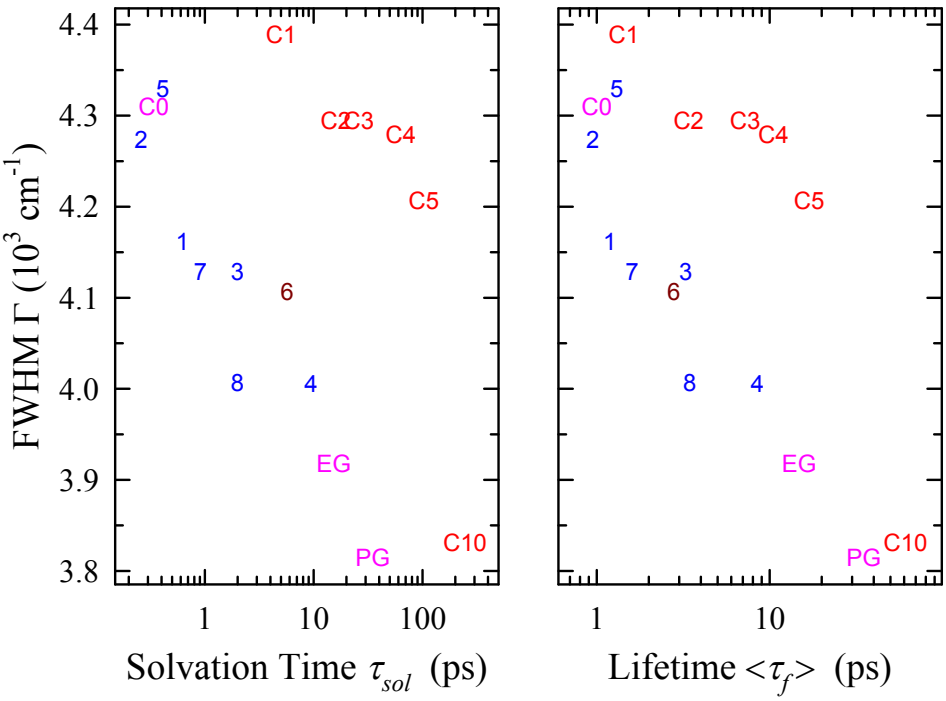

Figure 5.18: ThT steady state emission FWHM versus solvation time $\langle\tau_{solv}\rangle$ and fluorescence lifetime $\langle\tau_f\rangle$. Symbols are according to Table 5.2; red: n-alcohols; magenta: diols; blue: aprotic solvents.

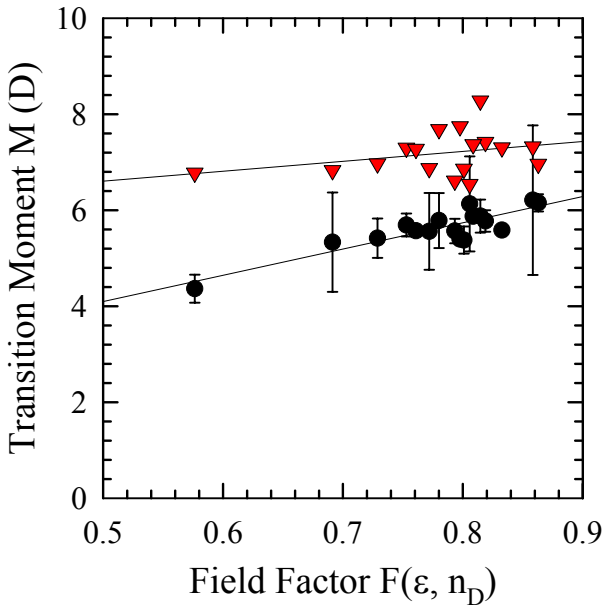

Figure 5.19: ThT transition moments. • M_{01}; ▼ M_{10}

#	Solvent	η cP	τ_{sol} ps	ϵ_0	n_D	$\mathrm{F}(\epsilon, n_D)$	$\langle\nu_{abs}\rangle$ cm^{-1}	$\epsilon(\max)$ $M^{-1}cm^{-1}$	M_{01} D	Φ_f	$\langle\nu_{em}\rangle$ cm^{-1}	$\langle\tau_f\rangle$ ps	k_{rad} ps^{-1}	M_{10} D
1	Propylene Carbonate	2.530	2.0	64.92	1.419	0.833	24,610	31,440	5.59	1.2×10^{-3}	19,470	3.45	0.339	7.31
2	DMSO	1.991	2.0	46.45	1.477	0.801	24,590	27,910	5.38	1.0×10^{-3}	19,250	3.28	0.326	6.86
3	NN-Dimethylformamide	0.802	0.91	36.71	1.428	0.798	24,650	28,950	5.40	6.1×10^{-4}	19,400	1.6	0.384	7.75
4	Acetonitrile	0.348	0.26	35.94	1.341	0.819	24,700	33,150	5.78	2.8×10^{-4}	19,490	0.95	0.295	7.42
5	Nitromethane	0.614	0.41	35.87	1.379	0.809	24,400	34,860	5.87	4.1×10^{-4}	19,390	1.31	0.312	7.37
6	Hexamethylphosphoramide	3.10	9.90	29.3	1.457	0.772	24,920	28,820	5.56	2.8×10^{-3}	19,510	8.5	0.327	6.87
7	Acetone	0.303	0.58	20.56	1.356	0.761	24,740	29,680	5.57	3.4×10^{-4}	19,540	1.14	0.296	7.28
8	Dichloromethane	0.411	0.56	8.93	1.421	0.603	23,790	39,000		1.1×10^{-2}				
C1	Methanol	0.551	5	32.66	1.329	0.815	24,730	34,430	5.88	5.2×10^{-4}	19,570	1.43	0.362	8.28
C2	Ethanol	1.083	16	24.55	1.359	0.780	24,600	35,220	5.79	1.1×10^{-3}	19,540	3.4	0.332	7.69
C3	1-Propanol	1.94	26	20.45	1.384	0.753	24,560	31,690	5.69	2.3×10^{-3}	19,510	7.2	0.315	7.30
C4	1-Butanol	2.593	63	17.51	1.399	0.729	24,500	31,500	5.42	3.1×10^{-3}	19,500	10.5	0.297	6.97
C5	1-Pentanol	3.548	103	13.9	1.400	0.691	24,500	33,400	5.34	4.9×10^{-3}	19,530	16.9	0.292	6.83
C10	1-Decanol	11.32	245	8.1	1.435	0.576	24,460	18,300	4.37	1.9×10^{-2}	19,670	61.1	0.311	6.78
EG	Ethylene Glycol	16.0	15.3	37.7	1.404	0.806	24,420	33,640	6.13	3.9×10^{-3}	19,420	14.8	0.262	6.54
PG	1,2-Propylene Glycol	42.2	30	32	1.403	0.793	24,440	32,650	5.57	9.5×10^{-3}	19,550	35.1	0.272	6.61
W	Water	0.890	0.47	78.36	1.330	0.863	25,130	31,630	6.15	2.7×10^{-4}	19,460	1.05	0.254	6.96
NF	N-Methylformamide	1.65	5.7	182.4	1.43	0.858	24,550	32,240	6.21	9.9×10^{-4}	19,570	2.79	0.354	7.33

Table 5.2: Properties of the S_1 absorption and emission bands of ThT in selected solvents. Measurements were performed at $25°C \pm 0.2°C$. η is the solvent viscosity from ref [114]. ϵ_0 is the solvent dielectric constant, n_D is the solvent refractive index (both Ref. [114]), and $\mathrm{F}(\epsilon, n_D)$ is the reaction field factor. $\langle\nu_{abs}\rangle$ is the first moment absorption frequency, $\epsilon(\max)$ the maximum value of the molar extinction coefficient, M_{01} the transition moment from the ground to the first excited state (eq. 4.7). Φ_f is the fluorescence quantum yield. $\langle\nu_{em}\rangle$ the first moment of the steady state emission spectrum, $\langle\tau_f\rangle$ is the average fluorescence lifetime, k_{rad} is the estimated radiative rate (Eq. 5.6), and M_{10} the transition moment from the excited state back to the ground state (Eq. 4.8).

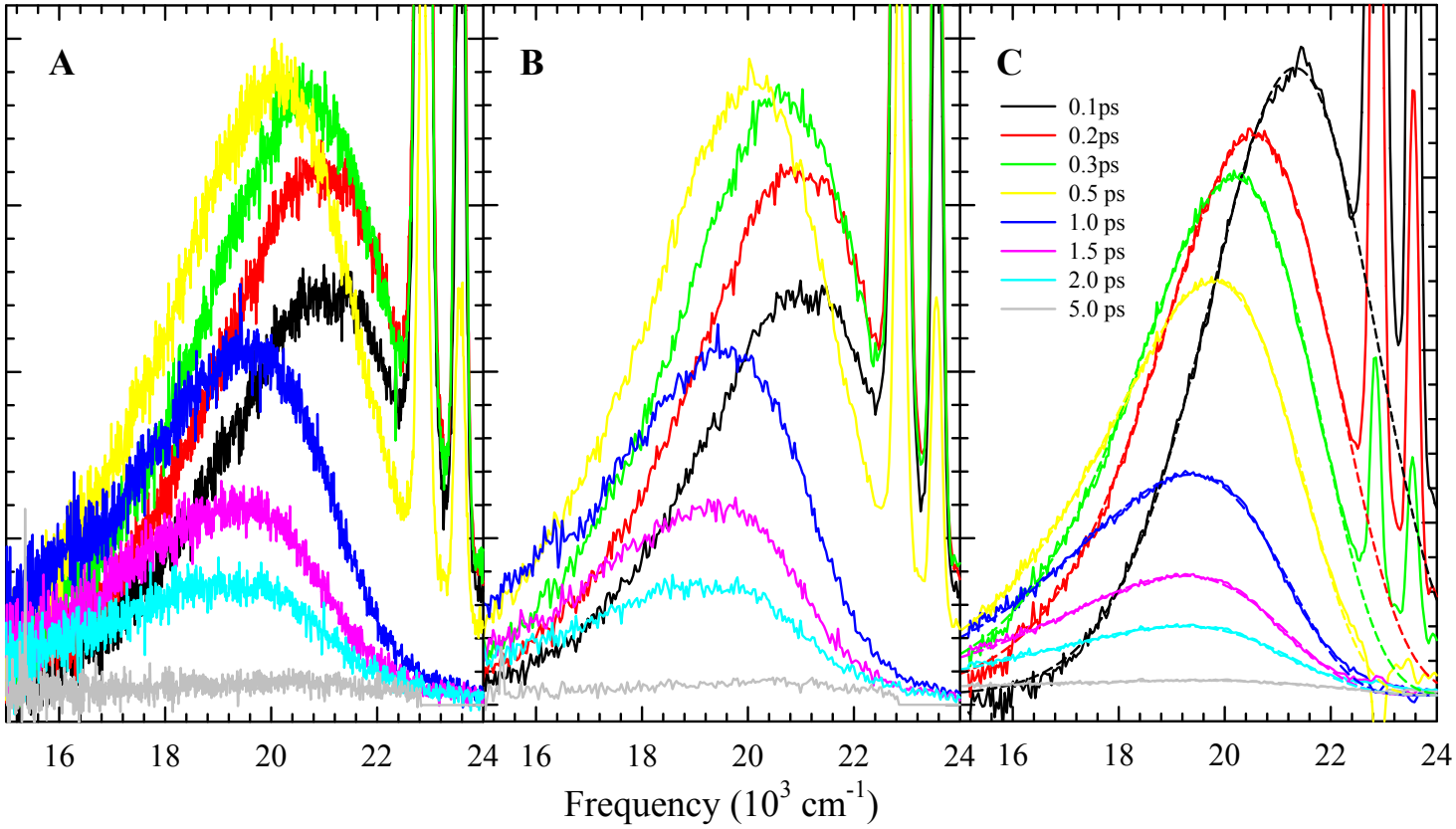

Figure 5.20: Illustration of KGE data analysis of ThT in acetonitrile. A. Spectral and time corrected raw data from KGE experiment. B. Thinned data set by a factor of 5 using boxcar method. C. Deconvoluted data with lognormal fit which provides final parameters like e.g. intensity decay and spectral shift over time. Due to a partial spectrum fitting at early times we are able to exclude the solvent Raman bands.

5.4.5 Time Resolved Emission

Time resolved KGE data was corrected for GVD and photometric, thinned and deconvoluted as shown in Figure 5.20A-C. Time dependent lognormal fitting allows to parametrize the emission shape with respect to peak frequency, width, asymmetry and intensity just like for steady state but with time dependent information. In addition, by fitting the spectra only partially around time zero allows to remove the intrinsic solvent Raman bands as can be seen by the dashed lognormal fit shape at early times (< 0.5ps) in Figure 5.20C.

Figures 5.21 and 5.22 show representative examples of the evolution of the ThT emission lognormal parameters over time. Several features require detailed explanation: Our IRF has a FWHM of over 300 fs and even after processing the time resolution limitation is no better than 200 fs. That said, strong deviations < 200 fs in some data sets are deconvolution artifacts and shall not be considered. At 0.5 ps a little step function is noticeable which is due to the switch between a partial to a full spectrum fitting to avoid Raman band fitting at early times. Those two mentioned features are of systematic nature and have no actual physical meaning. The important observation is the evolution of the FWHM and consequently the 1^{st} moment frequency undergo a significant change after several picoseconds which seems to be in agreement with the steady state red tail we already reported in the previous section. However, due to the very short lifetime of ThT the increasing second character at later times (> 2 ps for acetonitrile, > 10 ps for 1,2-propylene glycol) remains at low absolute intensity.

The observed dynamic Stokes shift is between 1200 cm^{-1} to about 3000 cm^{-1} across the solvents used in this study. These shifts are surprisingly large compared to C153 as a well studied probe with dynamic shifts of only up to 2000 cm^{-1} [66] and considering we don't observed a significant shift in the steady state peak frequency in the first place. Therefore the question arises what the origin of the observed dynamic spectral shift is. It

could be solvation of the FC state or an evolution in φ_1 (or τ_1, respectively). Based on what we have learned already from the quantum chemical calculations we expect the φ_1 evolution to be closely linked to the loss of emission intensity due to decreasing oscillator strength. Therefore, the comparison between the intensity decay time and the Stokes shift time is relevant. Figure 5.23 shows these correlations. Within our determined experimental certainties we can definitively say that the dynamic Stokes shift is solely due to the usual solvation dynamics but as is can been seen in the figure it may as well be. The only unusual aspect of the spectral evolution is the marked broadening on the red tail which is noticeable in the steady state emission and increasingly predominant in the time resolved emission over time. This tail could indeed be an indication that the spectral shapes are picking up some information about the twisting φ_1 evolution.

Unfortunately, there are not many lifetimes published in solution at room temperature. Huppert and coworkers have performed pressure and temperature measurements to vary the viscosity in a series of n-alcohols. [93, 101] We can confirm this linearity but one has to assume they would have found different behaviors for aprotic solvents. In a correlation between the fluorescence lifetime $\langle\tau_f\rangle$ and the solvation time τ_{sol} the trend continuous, differentiating aprotic solvents and n-alcohols (Figure 5.24). More importantly, it shows even better how solvation plays an important role explaining underlying TICT mechanism dependencies.

Singh et al. have measured ThT in acetonitrile and ethylene glycol. Their average lifetimes of 0.61 ps and 17.64 ps agree well with our times of 0.95 ps and 14.80 ps, respectively. However, they reported the formation of the TICT state from the LE within ∼570 fs through an intramolecular process and that this TICT is then also emissive in nature due to an isoemissive point they found in they reconstructed spectra. [92] Shown in Figure 5.25 is our area normalized emission spectra of the broadband acquired data. For a complete

area normalization the integrated area of the lognormal fit has been employed rather than by a partial spectrum. No isoemissive point can be found but a dynamics Stokes shift and a red-tailing of the emission over time.

Since ThT has been used as a viscosity sensor we consider the radiative rate $k_{rad} \propto \langle \tau_f \rangle$ (Eq. 5.6) by plotting the average fluorescence lifetime $\langle \tau_f \rangle$ over viscosity η in Figure 5.24(right). What we have already observed in steady state measurements is observed also in the time resolved experiments. A distinguished trend between aprotic solvents and n-alcohols.

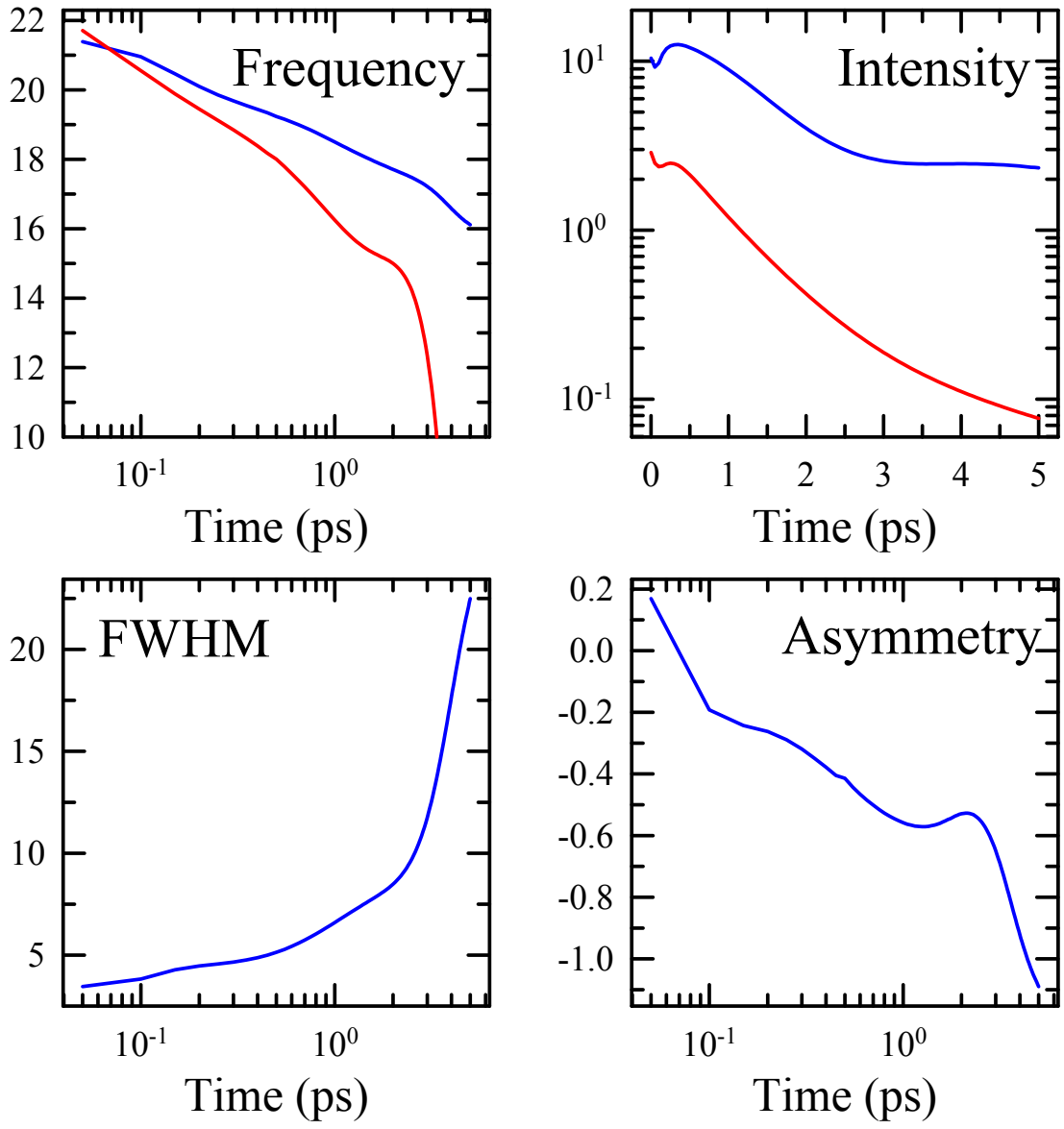

Figure 5.21: ThT time dependent lognormal fit parameters in acetonitrile. For frequency and intensity blue represents the peak frequency and peak intensity while red is the 1^{st} moment frequency and integrated intensity decay, respectively.

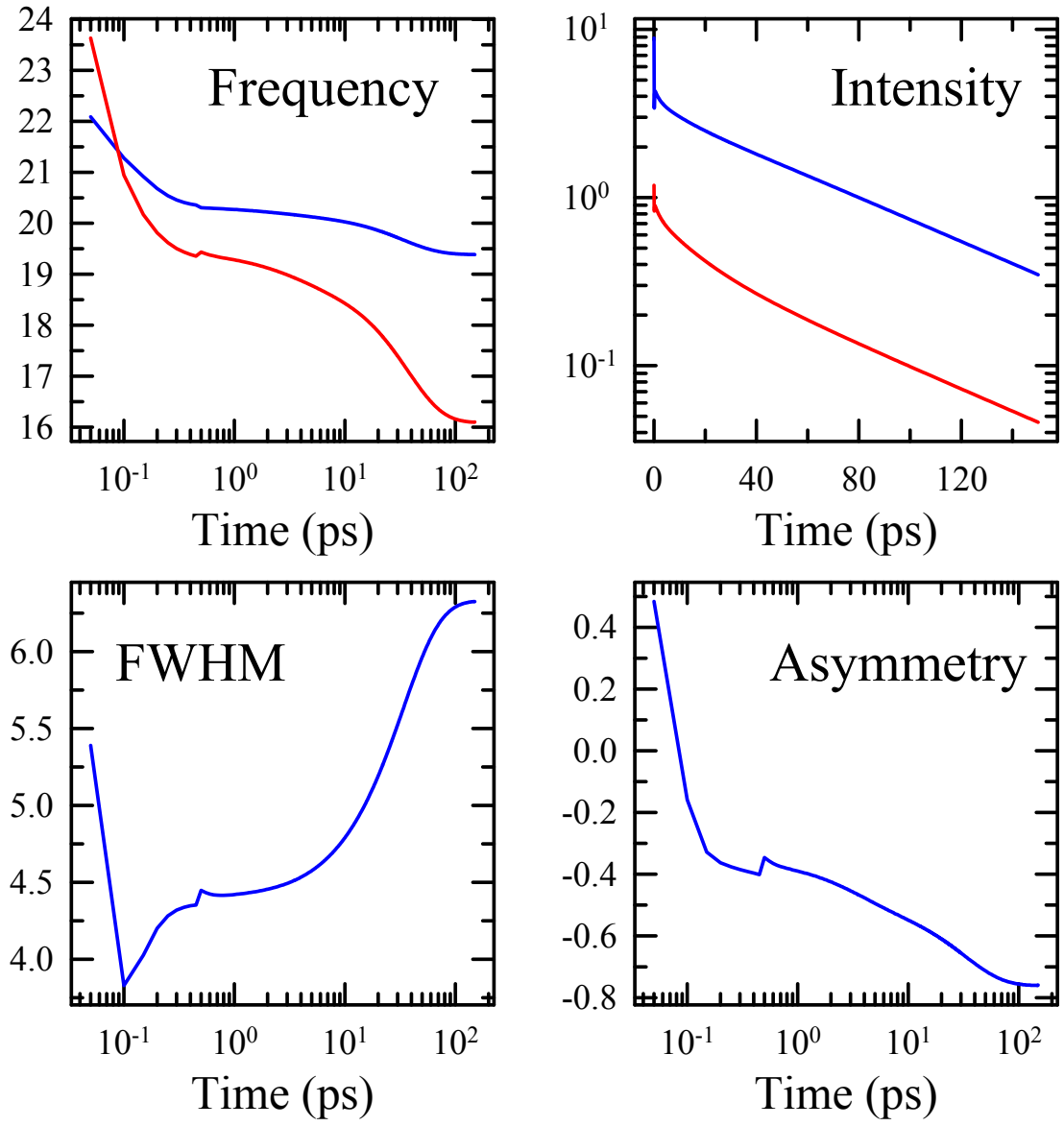

Figure 5.22: ThT time dependent lognormal fit parameters in 1,2-propylene glycol. For frequency and intensity blue represents the peak frequency and peak intensity while red is the 1^{st} moment frequency and integrated intensity decay, respectively.

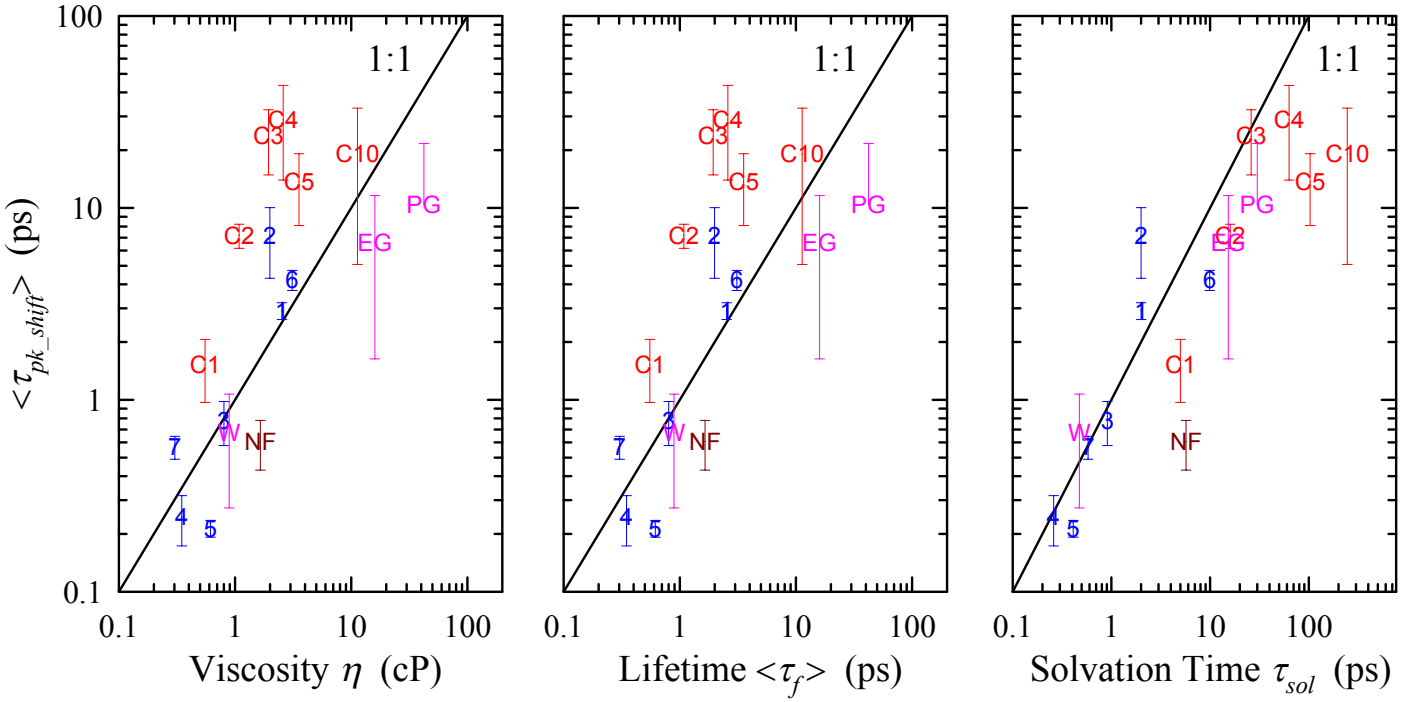

Figure 5.23: ThT dynamic Stokes shift versus viscosity η (left), emission lifetime $\langle\tau_f\rangle$ (center) and solvation time τ_{sol} (right). All correlation lines represent unity.

5.5 Summary

ThT has been used in biological application for decades. However, a fundamental understanding of its photophysical properties is only beginning to emerge. Simple fluorescence excitation spectra accompanying a purification procedure and a LC-MS chromatogram revealed the rapid decomposition, even in the cold dark. Naiki and coworkers published a protocol in 1989 for the use of ThT as an amyloid fibril sensor, providing the instruction to excite an aqueous solution of ThT at 350 nm and detect the fluorescence at 438 nm. We have shown that these conditions exactly probe the impurity or decomposition product. Upon binding to amyloid fibrils the instruction says to excite at 450nm which is outside the absorption range in water, consequently we cannot say anything about which molecule gets excited but we have reason for suspicion if it really is ThT that is the actual sensor probed in amyloid fibrils.

The arguments if the TICT state is dark or weakly emissive might be a matter of inaccurate spectral reconstruction or impurity. Both our computational and time resolved data indicate the TICT state is present but dark and that fluorescence occurs directly from the LE state with picosecond lifetime in low viscosity environment. Nevertheless, we believe the TICT dynamic to be true, located at the bond twist between the benzothiazol and the aniline group. Our data shows viscosity alone is insufficient to describe the quenching reaction. The question is if this reaction follows solvation, does it follow the viscosity, or is it a combination of both. We have presented new data showing how ThT emission behaves in a series of protic and aprotic solvents. We cannot explicitly rule out the viscosity dependence. However, we were successfully able to emphasize the importance of solvation dynamics upon photoexcitation and the twist into its TICT state.

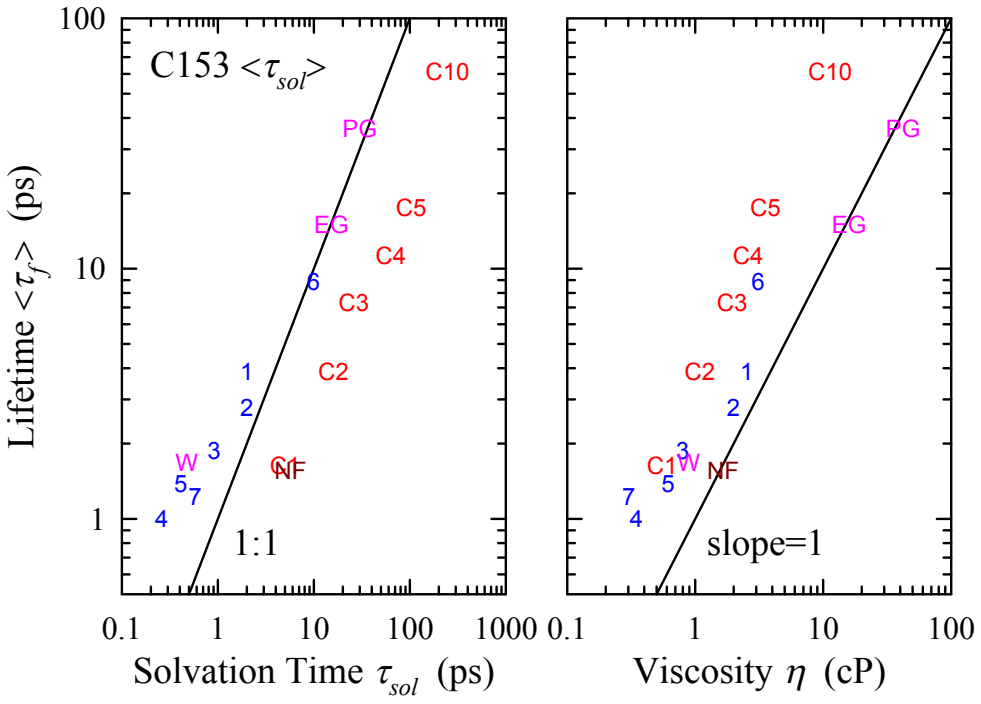

Figure 5.24: ThT emission lifetime $\langle\tau_f\rangle$ versus solvation time τ_{sol} (left) and viscosity η (right).

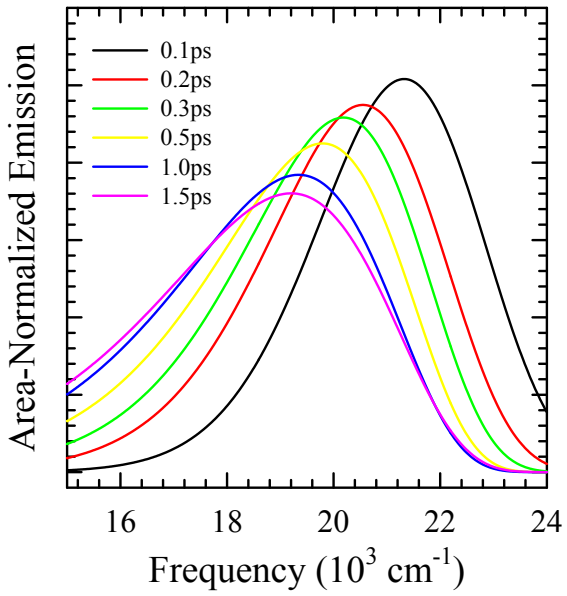

Figure 5.25: Area normalized ThT emission in acetonitrile from 0.1 - 1.5 ps of lognormal fitted KGE data. The absence of an isoemissive point is observed in all solvents studied here.

Chapter 6

Solvation Dynamics and Proton Transfer in DEAHF

6.1 Abstract

The molecule 4'-N,N-diethylamino-3-hydroxyflavone (DEAHF) has been studied for more than two decades as a model proton transfer system. Upon photo-excitation, DEAHF undergoes an intramolecular proton transfer into its tautomer form. Both forms exhibit well separated fluorescence bands which allow convenient access to kinetic information and population analysis. Time resolved and computational studies by Chou and coworkers [115] indicated the reaction barrier for this tautomerization in conventional solvents depends upon solvation dynamics. However, recent Kerr-gated fluorescence measurements by Kimura and coworkers [116] yielded constant ESIPT rates in ionic liquids and acetonitrile. This is surprising because ionic liquids are known to have much slower solvatio times compared to conventional solvents. These comparable ESIPT rates apparently contradict the model proposed by Chou and coworkers. It remains unclear whether Kimura's recent results are due to unusual features of ionic liquids or if there is really no dependence of the DEAHF reaction on solvation dynamics. We propose to test for the presence of a

dynamical solvent effect by utilizing binary mixtures of conventional solvents (acetonitrile and propylene carbonate) with constant polarity but variable solvation times.

We find that in the excited state, both the normal and the tautomer forms exhibit fluorescence which allows to analyze the lifetimes and the individual populations separately. A change of dipole moment in the Frank-Condon state from $\mu \approx 5$ D to 10 D triggers a solvent response. Upon intramolecular proton transfer in the excited state the tautomer form has a dipole moment of $\mu \approx 5$ D, which leads to the possibility of a barrier-free reaction at early times before solvent reorganization would induce a reaction barrier. Insufficient time or spectral resolution by both Chou and Kimura inhibited complete understanding. In our experiment we chose a binary mixture of acetonitrile and propylene carbonate which have similar dielectric properties which presented no change in the excited state equilibrium. Our two solvents of choice are distinguished by their solvation times which differ by almost one order of magnitude. [117] Our data shows clearly a decreasing tautomer formation rate with increasing solvation time, suggesting an increase of a reaction barrier over time induced by solvent dynamics.

6.2 Introduction

Proton (or hydrogen) transfer is one of the major mechanisms in living nature. Among numerous studies of proton transfer (PT) reactions [118] excited-state proton transfer (ESIPT) has received considerable attention. In living nature it is sunlight which triggers these types of photochemical reactions and makes life possible. [119] In condensed phases PT strongly depends upon solvent-solute interactions. A proton transferred, either inter- or intramolecularly, causes a change in the dipole moment of the solute and this change will affect its solvation energy in a polar solvent. In addition to generic polarity effects, hydrogen bonding between solute and solvent can have a large influence on the solvation energy and PT. Such interactions influence the energy of both the reactant and product

states as well as the energy of the reaction barrier and thereby influence the equilibrium constant and reaction rate. Dynamical solvent effects can also control reaction rates in some cases. [1] For a better understanding of such solvent effects we are studying one particular reaction, excited-state intramolecular PT in 4'-N,N-diethylamino-3-hydroxyflavone (DEAHF).

4'-N,N-dialkylamino-3-hydroxyflavones (see figure 6.1) are probes with remarkable solvent-polarization-dependent ESIPT reaction dynamics. Upon excitation they show emission from both excited "normal" (N*) and "tautomer" (T*) forms (see figure 6.2). This dual fluorescence allows for tracking the populations of both states and enables a definitive analysis of reaction rates.

One of the earliest studies of the DEAHF reaction was done by Kelly and coworkers [120] who used steady state emission spectroscopy and picosecond time resolved emission in a binary mixture of a polar (acetonitrile) and a nonpolar (benzene) solvent. They found that the frequency of the N^* emission depends on solvent composition (polarity) but that of T^* does not. They also obtained the equilibrium constant K_{eq} for the excited-state reaction. Both the frequency of the N^* emission and K_{eq} correlated linearly with the dielectric parameter $[(\epsilon_0 - 1)/(2\epsilon_0 + 1)]$ of the solvent, consistent with a dielectric continuum description of solvation. Time resolved measurements yielded reaction rates of a few tens of picoseconds (time resolution $\sim$5 ps). Kelly and coworkers showed that these rates could be understood in terms of a Marcus-like theory without any influence of solvation dynamics. [1]

In 2005, Chou and coworkers revisited this reaction using the fluorescence upconversion technique, which provided much higher time resolution ($\sim$200 fs). [115] They found two distinctly different times for the $N^* \rightarrow T^*$ reaction: (i) a very fast rise in the tautomer region (fast ESIPT), (ii) a second gradual growth of the same (slow ESIPT), accompanied

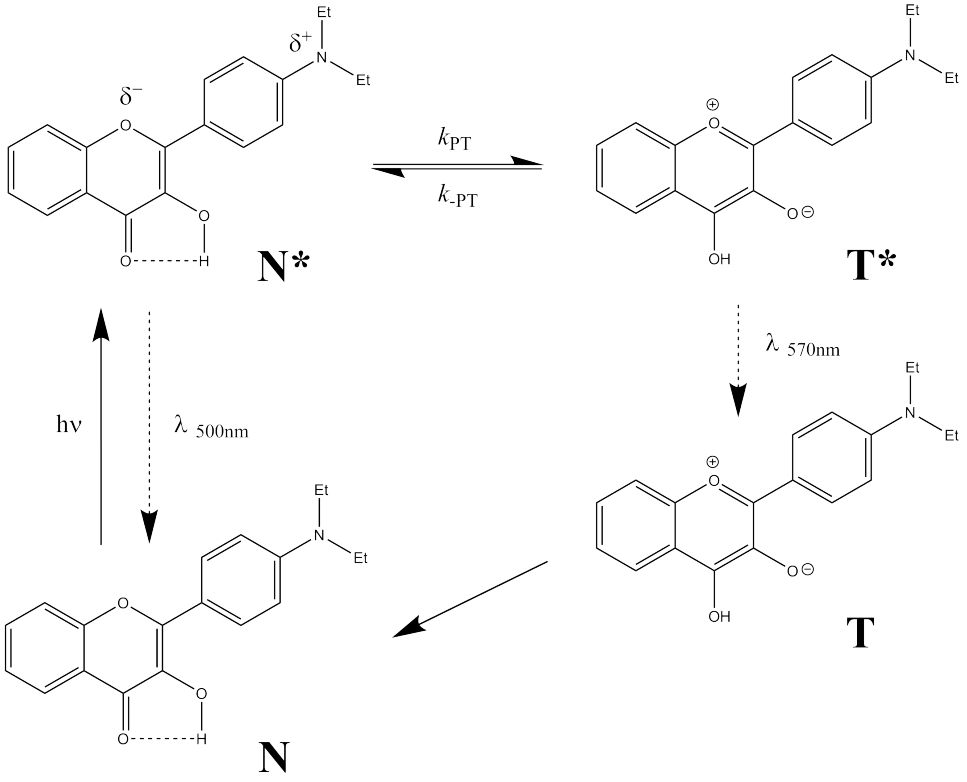

Figure 6.1: 4'-N,N-diethylamino-3-hydroxyflavone (DEAHF) and its proton transfer cycle. The asterisk (*) indicates the form in its excited state

by (*iii*) a decrease of the normal fluorescence. They concluded that ESIPT occurs partially in the sub-ps region and partially in the tens of picoseconds range. To distinguish between solvation and ESIPT effects on the time-resolved spectra Chou and coworkers measured a blocked analogue of DEAHF, the methoxy substituted derivative, 4'-N,N-diethylamino-3-methoxyflavone (DEAMF). The methoxy group prevents PT from the 3-position to the carbonyl group, so that DEAMF shows no tautomer emission, only emission very similar to that of the normal form of DEAHF. By spectral reconstruction of their DEAHF data they found a dynamic Stokes shift of the normal emission but not of the tautomer, consistent with the solvatochromic differences between these two bands. They assumed that the early temporal evolution of N^* observed upon Frank-Condon excitation is due to a large dipolar

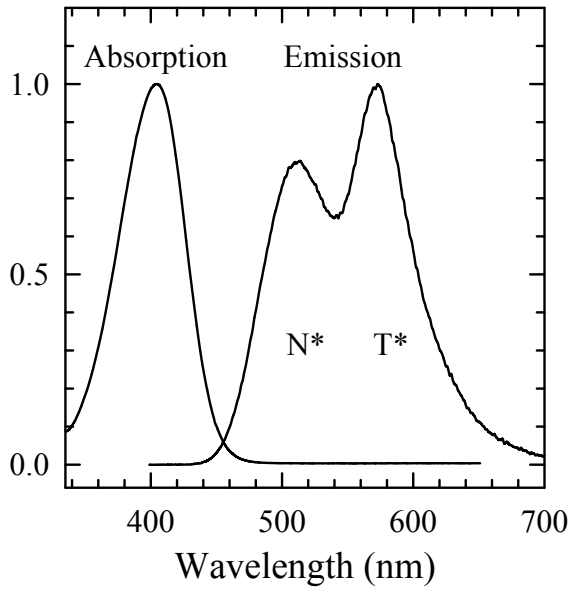

Figure 6.2: Steady state absorption and fluorescence spectra of 4-N,N-diethylamino-3-hydroxyflavone (DEAHF) in acetonitrile, showing normal and tautomer emission bands.

change between N and N^*, which could be treated as a charge-transfer process. To verify this idea Chou and coworkers performed ab initio calculations of the dipole moments of DEAHF. Based on the CIS/6-31G(d,p) method they obtained the following dipole moments: N (5.4 D); N^* (9.2 D); T (5.2 D); T^* (5.5 D). These results are in agreement with experimental observation: The large dipolar change between N and N^* ($\Delta\mu\,(N)$ ~4 D) and the negligible change in the case of the tautomer ($\Delta\mu\,(T)$ ~0.3 D) explains why a dynamic Stokes shift is observed for N but not for T. Even more importantly, these dipole moments suggested why two ESIPT rates are found: Immediately after excitation the solvent configuration is favorable for T^*, and this favorable solvation results in the fast ESIPT. But as time progresses solvation takes place and increases the barrier for the PT, causing a different (slower) ESIPT rate. A schematic potential energy surface illustrating the competition between PT and solvation is provided in figure 6.3.

The question that comes up is if there is a ground state equilibrium. It would imply the presence of a tautomer concentration $[T] \neq 0$ in the ground state which then could be excited as well. The kinetic of the tautomer rise and decay profile would become much more complicated. [116, 120] Previous experiments were not able to answer the question if there is a tautomer emission at time zero ($[T*]_0 \neq 0$).

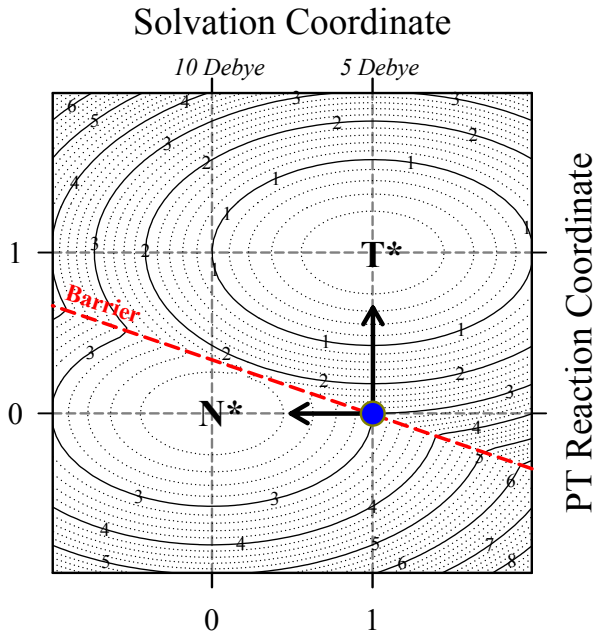

Figure 6.3: Schematic potential energy surface (PES) of DEAHF in its first excited state. The solvation coordinate describes the configuration of solvent molecules in terms of an effective solvent dipole moment. The PT reaction coordinate describes the intramolecular degrees of freedom of the solute that change in the $N^* \rightarrow T^*$ process. The red dashed line indicates the intersection of the individual PES of N^* and T^* and form hence the reaction barrier. In this illustration the Frank-Condon region reached upon excitation is shown as the blue spot with competitive pathways between solvation and PT indicated as arrows.

Most recently, Kimura and coworkers used a broadband Kerr-gating technique to study the DEAHF reaction in room temperature ionic liquids (ILs). [116] ILs are a new class of solvents being explored in a variety of contexts. For purposes of solvation studies the main features of interest are their high polarities and high viscosities. The high viscosities enable

a new look at the solvation-reactant coupling in reactions such as the ESIPT in DEAHF. The use of broadband detection and also comparison to DEAMF allowed for a more rigorous analysis of the solvation and ESIPT by Kimura and coworkers. They were able to show that the solvation of N^* as revealed by the Stokes shift of the N^* emission is simply proportional to viscosity in a series of ILs (Figure 6.4). Like Chou and coworkers, they also found two distinct phases to the reaction, in this case both much faster than solvation. In addition, the average reaction time $\langle\tau\rangle$ was found to be nearly constant over a viscosity range of up to 400 cP, a range over which solvation times vary more than 1000-fold.

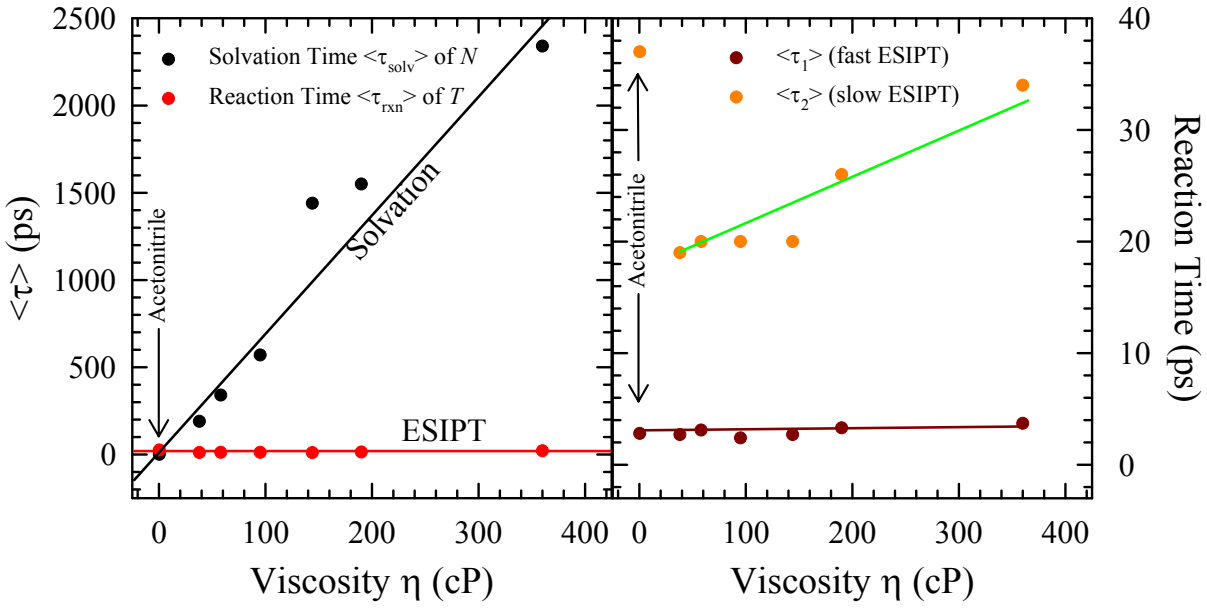

Figure 6.4: Plot of the extracted solvation and reaction times of DEAMF (N) and DEAHF (T) in acetonitrile and different ionic liquids based on data given in Table 2 of reference [116].

These new results appear inconsistent with the model proposed by Chou. If solvation tempered reaction in the manner proposed, slower solvation should produce faster reaction.

Kimura's observation of a basically negligible change of the ESIPT rate by a factor of two over the range of solvents measured is difficult to reconcile with Chou's model. While the ionic liquids show a systematic dependence of the slow reaction rate τ_2 over viscosity η the only conventional solvent acetonitrile has a higher τ_2 overall. This observation may indicate that ionic liquids affect the reaction in manner not accounted for by viscosity or solvation time alone.

Most recently, Hayaki et al. theoretically investigated the ESIPT of the methyl equivalent DMAHF molecule in the very common ionic liquid 1-butyl-3-methylimidazolium hexafluorophosphate ([BMIm][PF6]), using the RISM-SCF-SEDD method. Their results confirm no tautomer presence in the ground state due to a single energy minimum but two minima in the excited state for both N^* and T^*. More importantly, while immediately after the excitation the barrier height of the proton transfer process is relatively small, the barrier becomes larger as the solvation relaxation to the excited normal state proceeds. [121]

At this point the validity of the proposed model of solvent involvement is uncertain. It remains unclear what causes the inconsistency uncovered by Kimura et al. ILs could behave differently from conventional solvents so that the proposed model could still be valid in conventional solvents. In the experiment by Kimura and coworkers the reaction energy is not properly controlled in the series if ILs. The dielectric of the ILs are unknown and approximated by the concentration of the IL. Thus, previous experiments are inconclusive and don't allow for definitive conclusions.

We used a binary mixture consisting of acetonitrile and propylene carbonate to investigate the role of solvation dynamics in the DEAHF reaction. The solvation dynamics of this solvent pair was measured previously in our group. [117] Acetonitrile and propylene carbonate have nearly identical polarities so that in their mixtures solvent polarities and

thus reaction energies will be approximately constant. But the solvation times of the neat solvents differ by a factor of ten. By using such a mixture solvation times can be varied significantly while keeping the potential energy surface (PES) constant. In addition, both solvents are aprotic and do not form hydrogen bonds with the solute which could interfere with the PT reaction.

6.3 Experimental Section

4'-diethylamino-3-hydroxyflavone (DEAHF; CAS 146680-78-6) was synthesized according to Smith [122] and Ormson [123] as illustrated in figure 6.5: A solution of sodium hydroxide (5 g; 0.25 mol) in 7.5 mL water was added with vigorous stirring to a solution of 2'-hydroxyacetophenone (5.01 g; 0.037 mol) and 4-(diethylamino) benzaldehyde (7.09 g; 0.040 mol) in 50 mL ethanol. A heavy green precipitate formed immediately. Gradually the mixture became warm and more fluid, eventually setting (after 10 min stirring) to a firm orange paste that was allowed to stand overnight. The paste was dissolved in a solution of sodium hydroxide (2.5 g), 12.5 ml water and 250 ml ethanol. After cooling to 15 °C, 40 ml of 15 % hydrogen peroxide was added slowly with vigorous stirring. A red precipitate formed immediately and the temperature rose to 30 °C. The reaction mixture was stirred for a further 15 min, neutralized with dilute sulphuric acid and poured into 500 ml of water. Upon standing for 1 h, the yellow solid was filtered by suction, washed with a little ice-cold methanol and recrystallized from methanol to yield pale yellow needles. Final purification was performed using column chromatography (silica gel, 20 % ethyl acetate/hexane) twice to produce a yellow solid. Purity was confirmed by NMR and the fluorescence excitation spectrum checked for fluorescing impurities.

A Hitachi U-3010 UV/Vis in combination with a Horiba FL-3 Fluorolog spectrometer were used for steady state absorption and emission measurements. Emission spectra were corrected with respect to spectral responsitivity using secondary emission standards. [21]

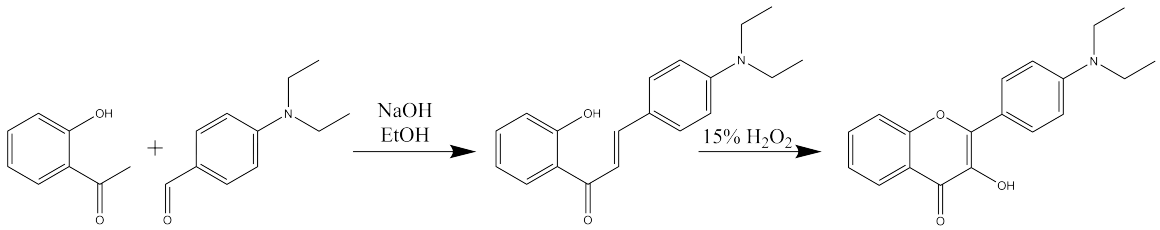

Figure 6.5: DEAHF synthesis scheme.

Steady state measurements were carried out in 1 cm quartz cuvettes at concentrations providing ∼1 OD for absorption spectra and <0.1 for emission spectra. Temperature was set at 25°C±0.1 using a water chiller circulating fluid through sample holders in all experiments. Both solvents used were from Sigma-Aldrich and of spectroscopic grade and used as received. Prepared samples were checked for water content < 100 ppm using a Mettler-Toledo Karl-Fischer coulometer DL-32. For time resolved experiments water content was measured before and after each run. To obtain time resolved data we employed the Kerr-gated emission (KGE) instrument with subpicosecond time resolution described in detail in chapter 3.2.1.

Binary mixtures of acetonitrile and propylene carbonate were prepared and stored in septa-sealed bottles to be used when needed. The compositions by mole fraction were calculated as follows:

$$V_2 = \left[\frac{\frac{x_2}{x_1} \times \frac{MW_2}{MW_1} \times \frac{\rho_1}{\rho_2}}{1 + \frac{x_2}{x_1} \times \frac{MW_2}{MW_1} \times \frac{\rho_1}{\rho_2}} \right] \times V_{total} \tag{6.1}$$

where V_{total} is the total desired volume of the mixture, x_i is the mole fraction of each of the solvents ($\sum x_i = 1$), MW_i is the molecular weight and ρ_i its density. Table 6.1 lists the individual volumes necessary to prepare 100 mL of these solutions.

x_{acn}	$V_{acetonitrile}$	$V_{propylene\ carbonate}$
0.0	0.00 mL	100.00 mL
0.2	13.35 mL	86.65 mL
0.4	29.13 mL	70.87 mL
0.6	48.04 mL	51.96 mL
0.8	71.15 mL	28.85 mL
1.0	100.00 mL	0.00 mL

Table 6.1: Preparation instruction for 100 ml each of the binary mixture series acetonitrile with propylene carbonate.

Quantum chemical calculations were employed to study the molecular structure and photophysical properties relevant to the excited-state dynamics. We used time-dependent density functional theory (TDDFT) with the CAM-B3LYP functional and a 6-31G(d,p) basis set, using Gaussian 09. [50]

6.4 Results and Discussion

6.4.1 Computational Section

We computed dipole moments of the normal and tautomer in both ground and first excited state to verify the results of Chou and coworkers. We used the CAM-B3LYP method [59] for ground and excited state calculations, which should be better than the CIS approach of Chou and coworkers. Our calculations with the basis set 6-31G(d,p) yielded dipole moments similar to those calculated by Chou and coworkers: N (4.8 D); N^* (10.6 D); T (4.8 D); T^* (5.0 D). These results are in good agreement and emphasize the favorable ESIPT at early time by the even larger change in dipole moment ($\Delta\mu\,(N) \sim$6 D).

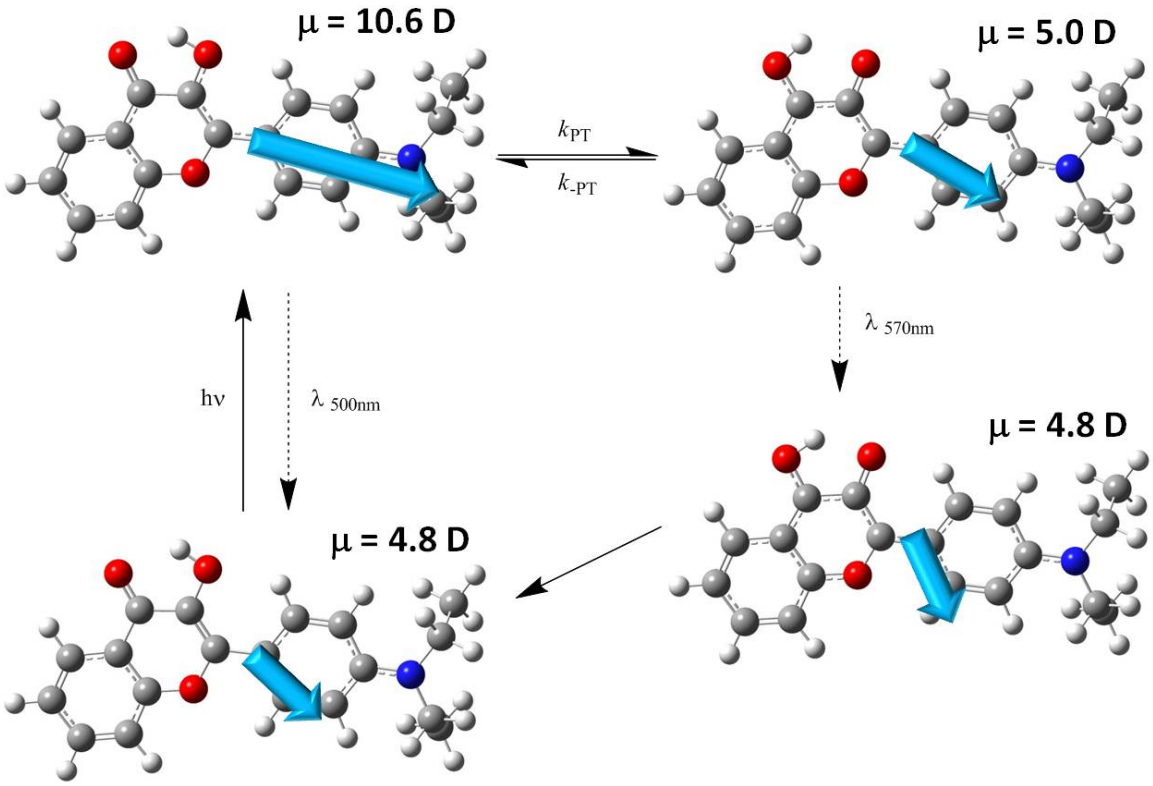

Figure 6.6: Calculated dipole moments and their vectors of all four states in the DEAHF excitation cycle using CAM-B3LYP/6-31G(d,p).

6.4.2 Steady State Results

Both absorption and emission spectra, shown in Figure 6.7, express only small peak shifts of < 300 cm^{-1}. This is expected since the binary mixture is designed to have an almost constant polarity. The absorption spectra show identical width and asymmetry but minor peak shifts, shown in Figure 6.8. The emission spectrum consist of overlapping normal and tautomer emission bands, requiring a spectral dissection in order to analyze each state separately. By fitting the emission envelope to two lognormal functions (Eq. 4.2) as shown in Figure 6.9 we can determine the properties of each band separately. In order to account for the frequency dependence of the radiative rate we convert to lineshape representation by

multiplying the observed emission intensities by ν^{-3}. To illustrate the importance of this consideration, Figure 6.10 shows the difference of DEAHF spectra in propylene carbonate in both representations. All emission analyses here were conducted using the lineshape representation.

In Table 6.2 and Figure 6.11 the lognormal parameters describing the steady-state emissions are provided. The peak frequencies of both emission bands shift by only ~ 250 cm^{-1}, and the width doesn't change at all. This shift is in very good agreement with an observed ~ 200 cm^{-1} shift observed for C153. [117] Most important to this steady state analysis is the calculation of the equilibrium constant:

$$K_{eq}(x) = \frac{[T^*]}{[N^*]} = \frac{k_{rad}^N}{k_{rad}^T}\frac{A_T(x)}{A_N(x)} \quad \propto \quad \frac{A_T(x)}{A_N(x)} \tag{6.2}$$

where A is the integrated area of the two emission bands in the lineshape representation form. The change in reaction free energy across the series is given by:

$$\Delta\Delta G \quad = \quad -RTln\left(\frac{A_T(1)/A_N(1)}{A_T(0)/A_N(0)}\right) \tag{6.3}$$

With the numerator $A_T(1)/A_N(1) = 0.483$ and denominator $A_T(0)/A_N(0) = 0.518$ we obtain $\Delta\Delta$ G = 0.221 kJ mol^{-1} or 0.002 eV, a negligible difference at room temperature. We conclude the $N* \rightleftharpoons T*$ equilibrium is virtually unchanged as a function of composition in this particular mixture. This is a significant difference when compared to Swinney et al. who used a binary mixture of acetonitrile and benzene where K_{eq} varied from 1 to $\sim$100 with $\Delta\Delta$ G $\approx$ 11.9 kJ mol^{-1} or 0.12 eV. [120] We can therefore assume that any change in the kinetics of the proton transfer reaction as a function of composition here will not occur due to a change of the reactive PES.

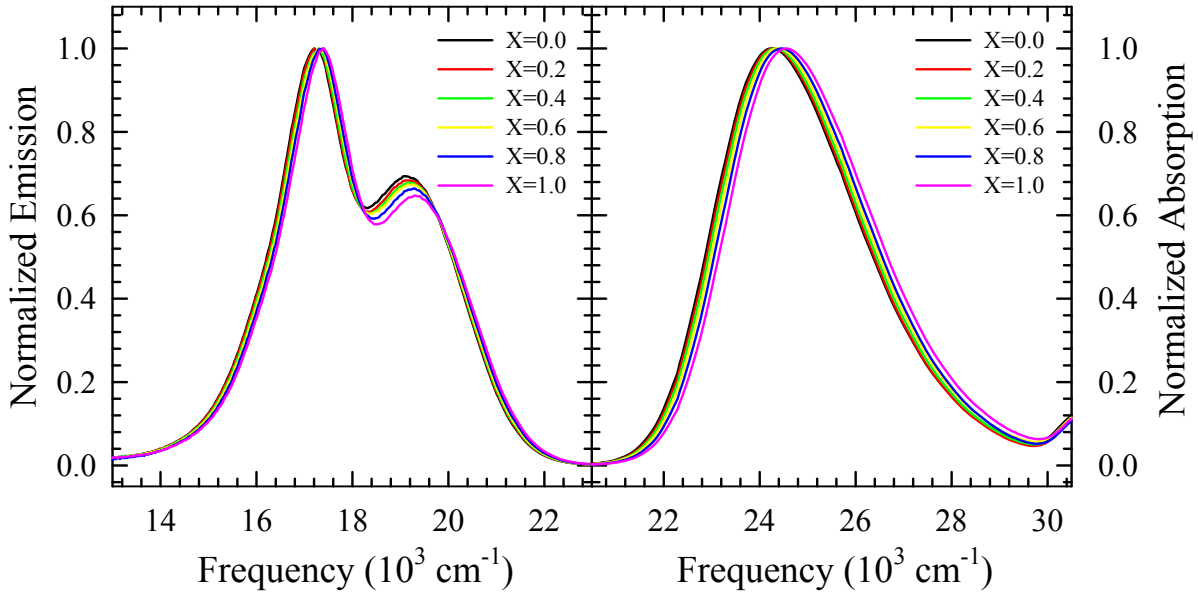

Figure 6.7: DEAHF steady state absorption (right) and emission (left) spectra in the binary mixture series.

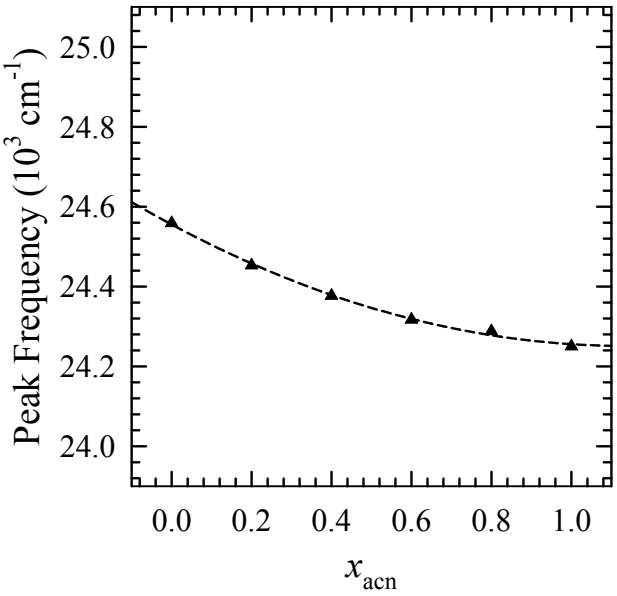

Figure 6.8: DEAHF absorption peak frequency in the binary mixture series.

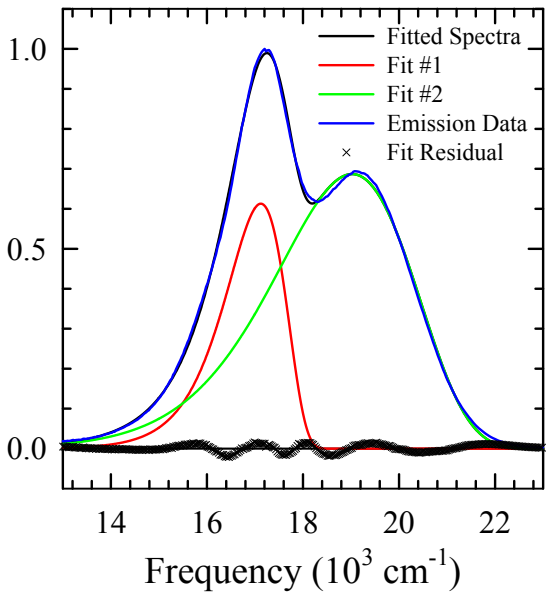

Figure 6.9: Dissection of DEAHF emission spectra into their respective normal and tautomer spectra using two lognormal functions.

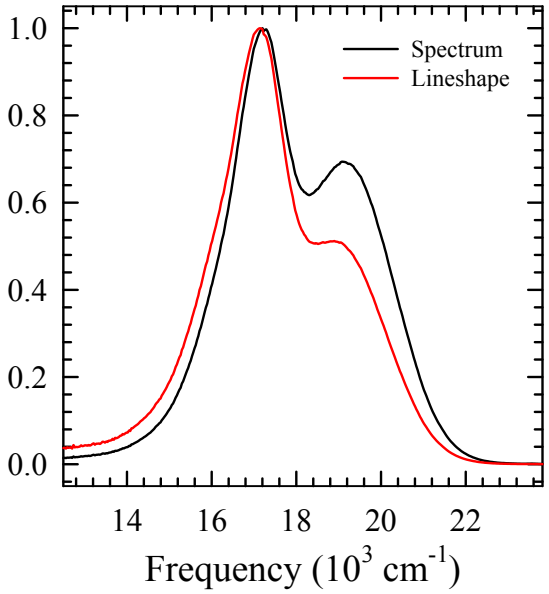

Figure 6.10: Conversion from the observed emission spectrum (black) to lineshape (red) representation for DEAHF in propylene carbonate.

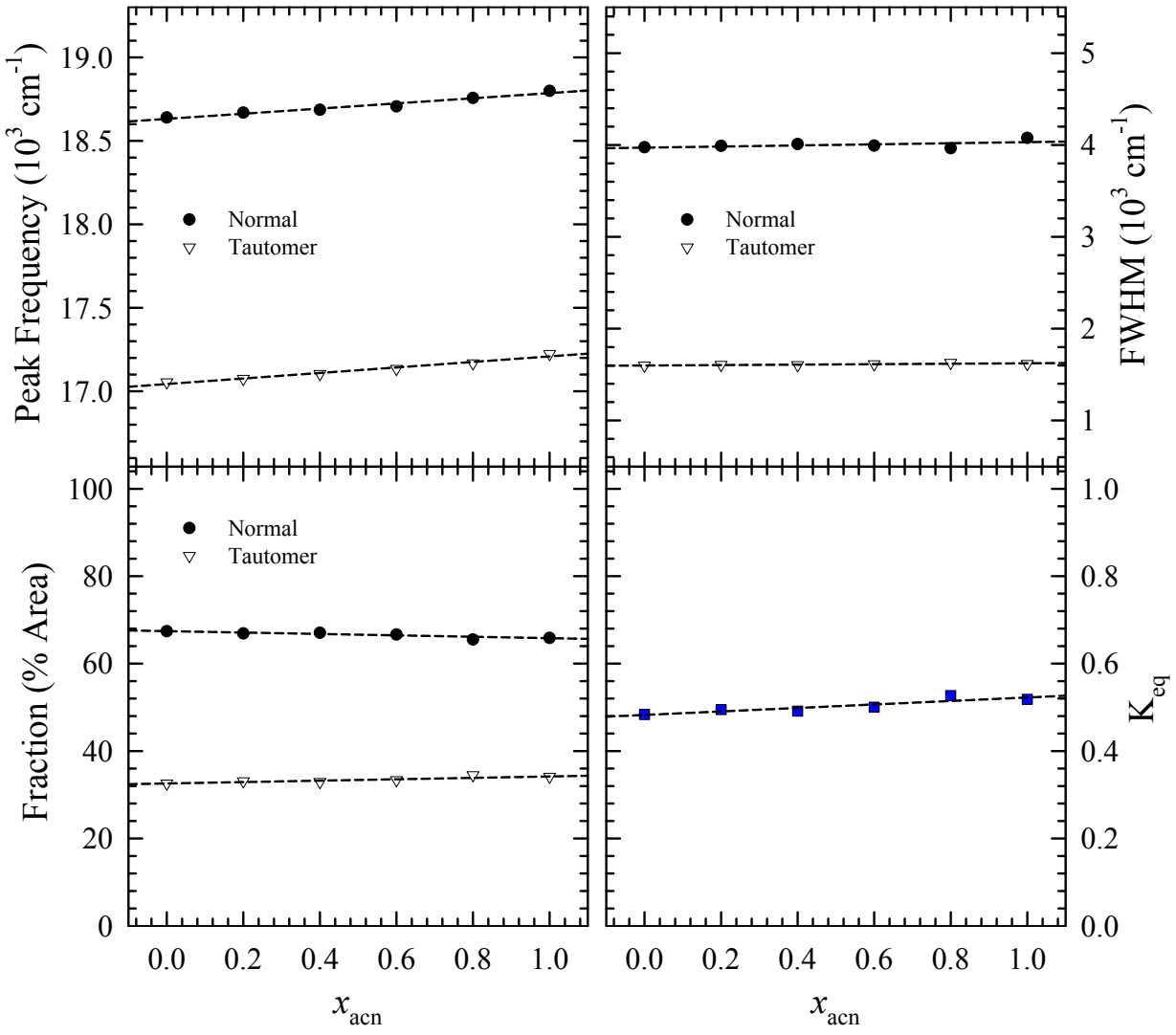

Figure 6.11: Steady state emission parameters for the normal isomer (•) and the tautomer (▽) obtained from lognormal fits.

χ_{acn}	$\nu_{0,N}$ $(10^3 cm^{-1})$	h_N	FWHM$_N$ $(10^3 cm^{-1})$	γ_N	$\langle\nu_{avg,N}\rangle$ $(10^3 cm^{-1})$	%Area(N)	$\nu_{0,T}$ $(10^3 cm^{-1})$	h_T	FWHM$_T$ $(10^3 cm^{-1})$	γ_T	$\langle\nu_{avg,T}\rangle$ $(10^3 cm^{-1})$	%Area(T)	K_{eq}
0.0	18,640	0.520	3,980	-0.34	17,880	67.4	17,050	0.617	1,600	-0.43	16,650	32.6	0.483
0.2	18,670	0.512	3,990	-0.35	17,880	66.9	17,070	0.621	1,600	-0.44	16,670	33.1	0.495
0.4	18,690	0.511	4,010	-0.35	17,890	67.1	17,100	0.621	1,600	-0.44	16,700	32.9	0.491
0.6	18,710	0.509	3,990	-0.34	17,930	66.7	17,130	0.621	1,610	-0.44	16,720	33.3	0.500
0.8	18,760	0.499	3,970	-0.34	18,000	65.5	17,170	0.629	1,630	-0.45	16,740	34.5	0.527
1.0	18,800	0.485	4,080	-0.36	17,960	65.9	17,220	0.628	1,620	-0.43	16,820	34.1	0.518

Table 6.2: Lognormal parameters according to Eq. 3.19 for DEAHF normal and tautomer emission in binary mixture and the resulting equilibrium constant K_{eq} as defined in Eq. 6.2. The parameter h defines the height of the band, γ is the asymmetry, ν_0 is the peak frequency.

6.4.3 Time Resolved Results

Time resolved KGE data were corrected for wavelength dependent temporal dispersion and detection sensitivity and thinned and deconvoluted as shown in Figure 6.12A-C. Each solvent mixture was measured multiple times and processed individually. After deconvolution the spectra were transformed into a lineshape representation. Time dependent lognormal fits then allow us to parametrize the frequency, shape and relative areas of the two emission bands. Figure 6.13 shows an example of the contour plot of a broadband spectral evolution of DEAHF in propylene carbonate. A significant dynamic Stokes shift of $\sim 1,200\ \mathrm{cm}^{-1}$ can be noticed for the N^* emission and also a modest change in width and asymmetry. The tautomer emission, however, shows a very little shift and no noticeable change in width or asymmetry. We therefore follow Kimura's analysis [116] and fix the tautomer peak frequency $\nu_{0,T}$, width FWHM_T and asymmetry γ_T, according to the corresponding steady state spectra, as given in Table 6.2. The resulting lognormal fits from 2-4 data sets were then combined (averaged) before the N and T areas were fit to a 3-exponential function:

$$I(t) \quad = \quad A_1 \exp\{t/\tau_1\} + A_2 \exp\{t/\tau_2\} + A_3 \exp\{t/\tau_3\} \tag{6.4}$$

An example of the uncertainties within one series of three measurements (solid lines) and their average (cross points) is shown in Figure 6.14. The fitted rise times of the tautomer are summarized in Table 6.3. For comparison the measured rise times by Kimura [116], Chou [115] and Kelley [120] are listed for DEAHF in acetonitrile. Our number agree reasonably well with Kimura who has the only broadband measured and fitted data. In comparison with Chou and Kelley the numbers agree within a factor of 2-3.

The dynamic Stokes shift times of the normal emission agrees very well with the measured times of C153 in the same solvent mixture series originally proposed by Gardecki et al. [117], given in Table 6.4 and shown in Figure 6.15. We can therefore conclude with con-

x_{acn}	A_1	τ_1	A_2	τ_2	$\langle\tau\rangle$	Comment
0.0	0.40	1.44	0.60	28.57	17.6 ± 3.0	
0.2	0.29	1.62	0.71	33.33	24.1 ± 1.5	
0.4	0.27	1.35	0.73	25.00	18.7 ± 4.0	
0.6	0.18	1.27	0.82	32.26	26.8 ± 4.8	
0.8	0.22	1.96	0.78	43.48	34.4 ± 10.5	
1.0	0.07	3.72	0.93	45.45	42.3 ± 7.0	
1.0		2.8		37	25.3 ± 2.3	Kimura et al. [116]
1.0		0.8		20.9		Chou et al. [115] (averaged from 3 single channels)
1.0					113	Swinney et al. [120] (IRF >10 ps)

Table 6.3: Tautomer rise times in the binary mixture series based on the first two exponential components in Eq. 6.4 with renormalized pre-exponential factors. The third component describes the lifetime decay. The uncertainties of $\langle\tau\rangle$ were determined by the variations within a series as shown for $x_{acn} = 0.0$ and $x_{acn} = 1.0$ in Figure 6.16.

fidence that the spectral shift of DEAHF in its normal form results directly from solvation.

Eq. 6.4 describes $N(t)$ and $T(t)$ with 3 exponential where 2 are for the rise time and 1 is for the mutual decay time. For a comparative population analysis between N and T it is more convenient to calculate the fractional population between the two of them. For the tautomer is means $T(t)/[N(t)+T(t)]$ and the obtained curve can be described by only a 2-exponential rise (compare right side graphs in Figure 6.14). By doing so it allows us to focus on the population transfer between N^* and T^* and removes the overall decay part.

If we assume that the reaction and overall S_1 population decay are well separated, then we can simply assume that the kinetics of the PT reaction and reverse PT reaction are reflected in the rise of the fractional area of the tautomer. Within the uncertainty of our experiments and the data we extracted we find it unlikely that there is a tautomer population at time zero in the Frank-Condon state, therefore we conclude $[T*]_0 = 0$.

In Figure 6.16 is shown the fractional tautomer rise compared between the two neat solvents, acetonitrile and propylene carbonate. Within the uncertainties we determined

based on our repeated experiments we can declare a significant difference of the reaction rate. As expected based on the model depicted in Figure 6.3, the more rapidly the solvent relaxes the slower the PT rate gets. The uncertainties were estimated based on the width of standard deviation at half point of the rise function. Shown in Figure 6.17 is the average rise time $\langle\tau\rangle$ of the tautomer in dependence of the binary mixture composition and consequently the solvation time which reflects the distinguished difference between the two solvents. Despite the inconsistent agreement within their uncertainties, we are confident to state that in this final result the reaction clearly slows down with increasing acetonitrile composition x_{acn}.

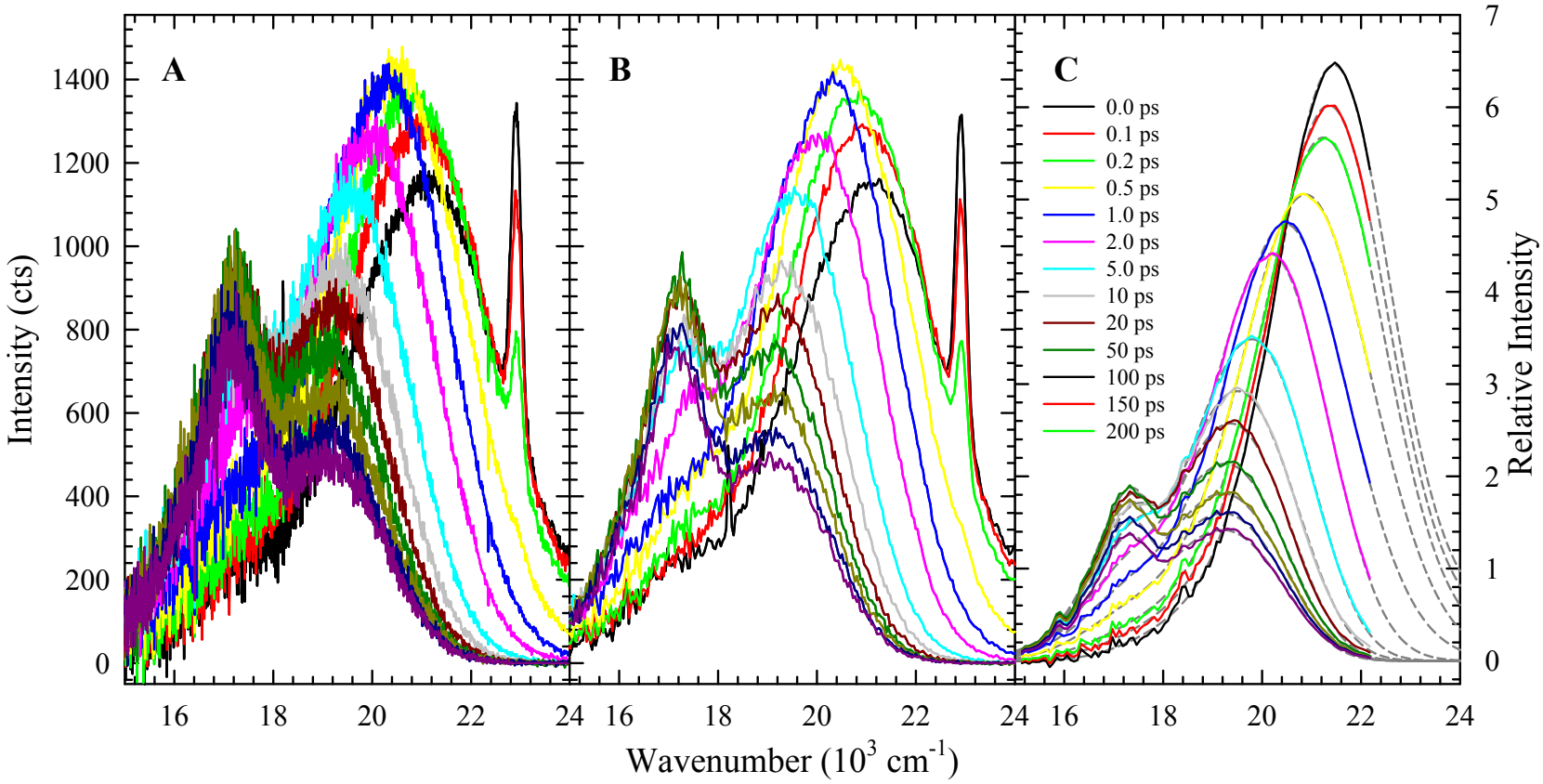

Figure 6.12: Illustration of KGE data analysis. A. Spectral and time-corrected raw data from the KGE experiment. B. The same data set thinned by a factor of 5 using the boxcar method. C. Deconvoluted data (solid lines) and time dependent lognormal fits (dashed lines) which provide final parameters for analysis.

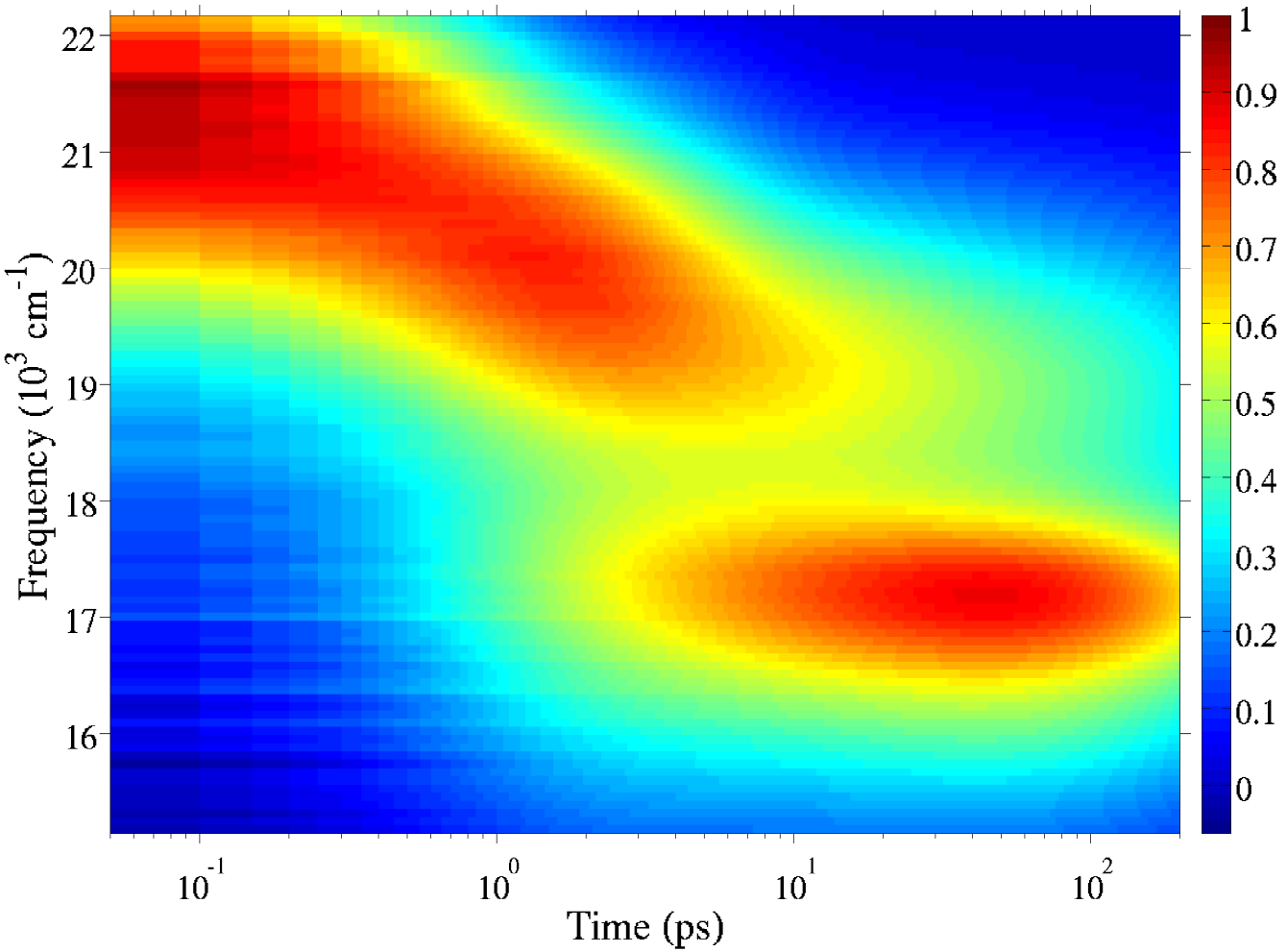

Figure 6.13: 2-Dimensional representation of the KGE spectral evolution of DEAHF in propylene carbonate.

6.5 Summary

DEAHF undergoes an intramolecular proton transfer upon photo excitation. In the excited state, both the normal and the tautomer form exhibit a fluorescence which allows one to trace the proton transfer. A change of dipole moment in the Frank Condon State from $\mu \approx$ 5 D to 10 D triggers a solvent response. Chou's model proposed the possibility of a barrier-free reaction at early times before solvent reorganization would induce a reaction barrier. Insufficient time or spectral resolution of prior experiments prohibited definitive testing of this idea. In the present experiments a binary mixture of acetonitrile and propylene carbonate, which have similar dielectric properties, was chosen to ensure that the effects being observed were not due to changes in the PES. Our data shows clearly a decreasing tautomer formation rate with increasing solvation time, suggesting an increase of a reaction barrier over time with induced by solvent dynamics. Thus, Chou's hypothesis is supported.

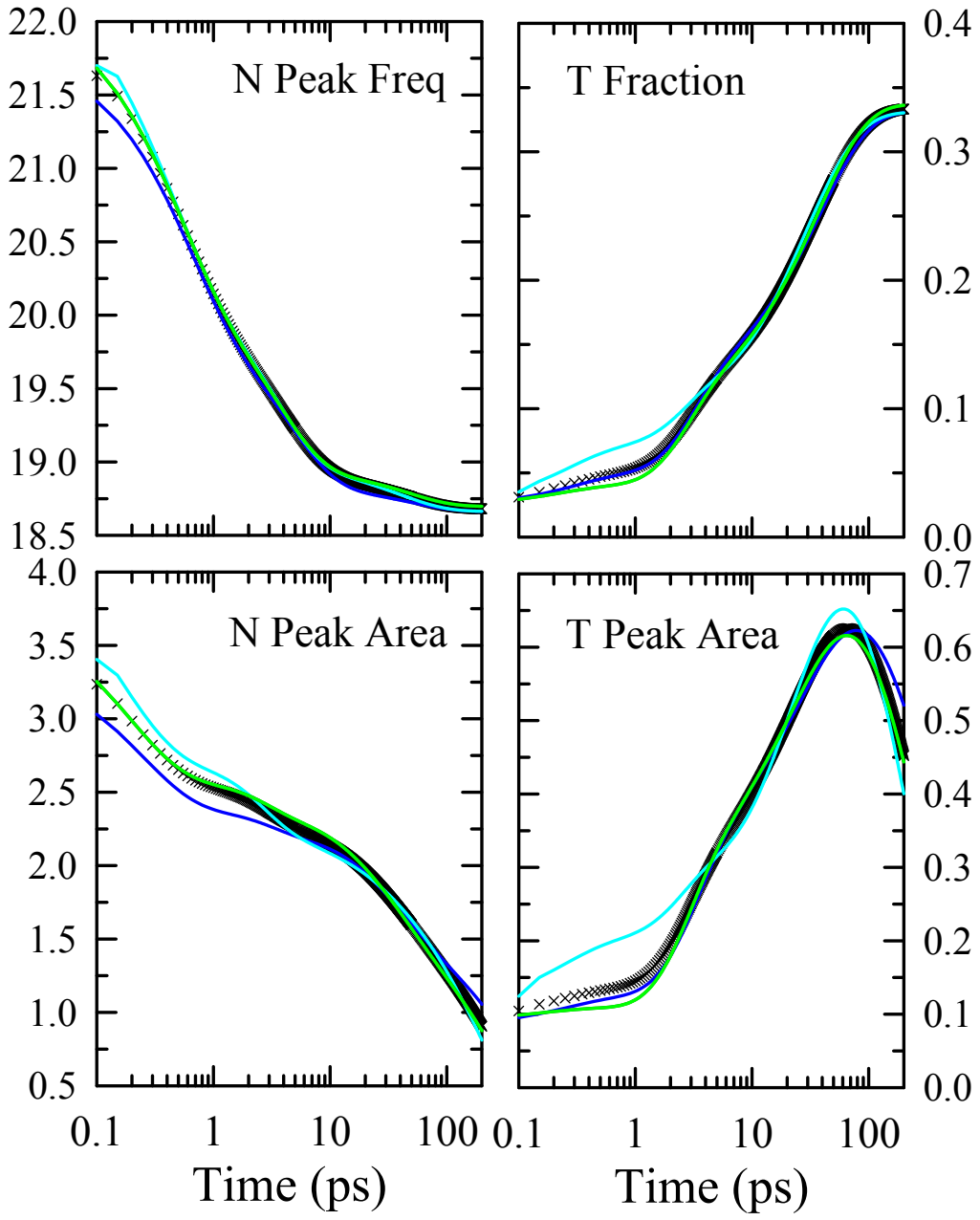

Figure 6.14: Example of N and T area data used for kinetic analysis set examples of time resolved lognormal parameters of DEAHF in $x_{acn} = 0.2$. In here, the three solid lines represent the individual measurements and the averaged value at each time is shown as $\times$.

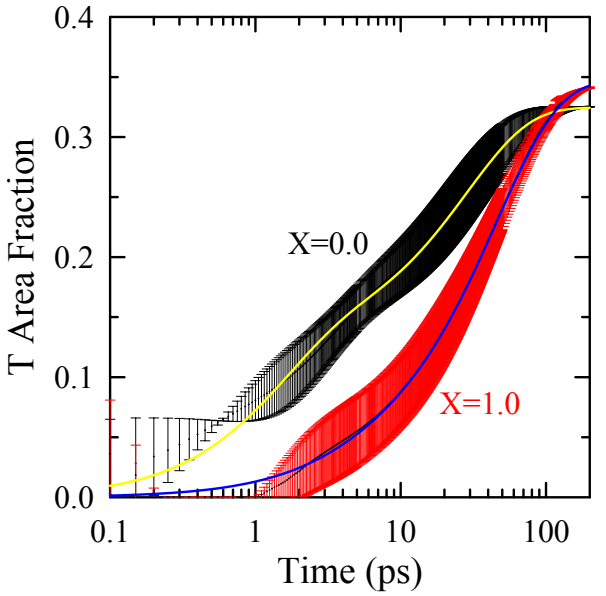

Figure 6.16: Extracted tautomer rise in acetonitrile and propylene carbonate. The error bars are based on the uncertainties resulting from $N = 4$ repeated measurements. The curves represent the biexponential fit as listed in Table 6.3.

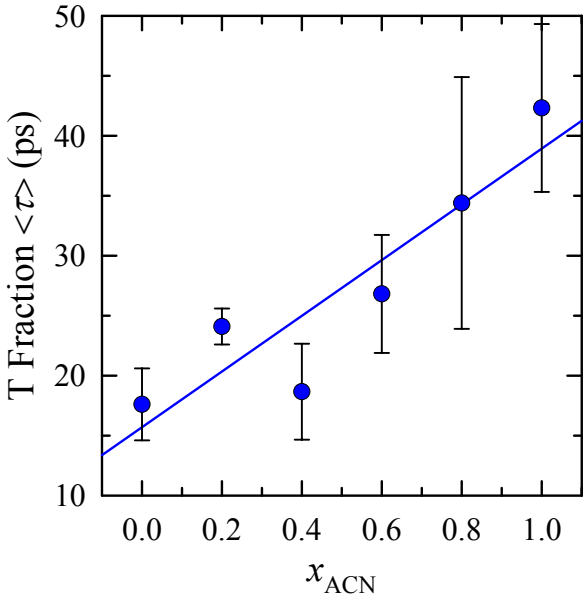

Figure 6.17: Averaged tautomer rise times $\langle\tau\rangle$ (Table 6.3) in binary mixture series.

x_{acn}	$\langle\tau_{Stokes}\rangle$(DEAHF)	$\langle\tau_{Stokes}\rangle$(C153)
0.0	2.15	2.35
0.2	1.73	1.40
0.4	1.11	1.11
0.6	0.77	0.85
0.8	0.66	0.46
1.0	0.44	0.25

Table 6.4: Dynamic Stokes shift times for DEAHF and C153 in the binary mixture of acetonitrile and propylene carbonate. DEAHF times are based on a two-exponential fit of the emission peak shift over time. C153 times were taken from Gardecki et al. [117].

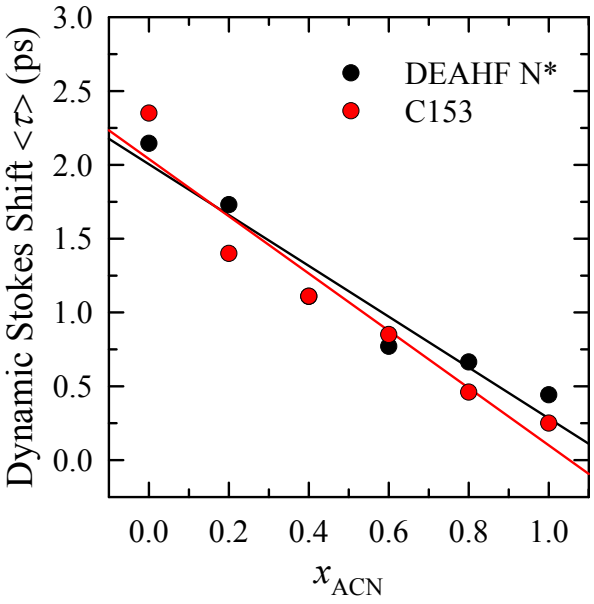

Figure 6.15: Dynamic Stokes shift times of N^* (black) and C153 by Gardecki et al. [117] as listed in Table 6.4.

Bibliography

[1] Heitele, H. *Angew. Chem. Int. Ed.* **32**(3), 359–377 (1993).

[2] Lustres, J. L. P., Kovalenko, S. A., Mosquera, M., Senyushkina, T., Flasche, W., and Ernsting, N. P. *Angew. Chem. Int. Ed.* **44**(35), 5635–5639 (2005).

[3] Haidekker, M. A. and Theodorakis, E. A. *Org. Biomol. Chem.* **5**, 1669–1678 (2007).

[4] Haidekker, M. and Theodorakis, E. *J. Biol. Eng.* **4**(1), 11 (2010).

[5] Laurent, T. *Ultraschnelle Dynamik in Flüssigkeiten: Zeitaufgelöste Untersuchungen zum Optischen Kerr-Effekt / Raman-Induzierten Kerr-Effekt.* PhD thesis, Humboldt-Universität zu Berlin, (2000).

[6] Breffke, J. Master's thesis, Humboldt-Universität zu Berlin, (2009).

[7] Böttcher, C. *Theory Of Electric Polarization, Volume I: Dielectrics in static fields.* Elsevier, Amsterdam, 2nd edition edition, (1973).

[8] Onsager, L. *J. Am. Chem. Soc.* **58**(8), 1486–1493 (1936).

[9] Edward, J. T. *J. Chem. Educ.* **47**(4), 261 (1970).

[10] Liptay, W. *Angew. Chem.* **81**(6), 195–206 (1969).

[11] Lippert, E. *Z. Naturforschg.* **10a**, 541–546 (1955).

[12] Van der Zwan, G. and Hynes, J. T. *J. Phys. Chem.* **89**(20), 4181–4188 (1985).

[13] Bingemann, D. *Untersuchung der molekularen Solvatationsdynamik in dielektrischen Flüssigkeiten mittels Femtosekunden-Absorptions- und Verstärkungsspektroskopie.* PhD thesis, Georg-August-Universität Göttingen, (1994).

[14] Schwarzschild, K. *Abh. Goettinger Akad.* **4**(2), 1 (1905).

[15] Zhao, L., Lustres, J. L. P., Farztdinov, V., and Ernsting, N. P. *Phys. Chem. Chem. Phys.* **7**(8), 1716–1725 (2005).

[16] Arzhantsev, S. and Maroncelli, M. *Appl. Spectrosc.* **59**(2), 206–220 February (2005).

[17] Neelakandan, M., Pant, D., and Quitevis, E. L. *Chem. Phys. Lett.* **265**(12), 283–292 January (1997).

[18] Jin, H., Liang, M., Arzhantsev, S., Li, X., and Maroncelli, M. *J. Phys. Chem. B* **114**(22), 7565–7578 (2010). PMID: 20476729.

[19] Lambert, J. H. *Photometria sive de mensura et gradibus luminis, colorum et umbrae.* Eberhardt Klett, (1760).

[20] Beer, A. *Annalen der Physik und Chemie* **86**, 78–88 (1852).

[21] Gardecki, J. A. and Maroncelli, M. *Appl. Spectrosc.* **52**(9), 1179–1189 September (1998).

[22] Sellmeier, W. *Annalen der Physik und Chemie* **219**, 272–282 (1871).

[23] Jones, G. R. N. *Nature* **235**(5336), 257–261 February (1972).

[24] Freeman, F. *Chem. Rev.* **80**(4), 329–350 (1980).

[25] Haidekker, M. A., Nipper, M., Mustafic, A., Lichlyter, D., and Dakanali, M. *Dyes with Segmental Mobility: Molecular Rotors*, volume 8. Springer, (2010).

[26] Swalina, C. and Maroncelli, M. *J. Phys. Chem. C* **114**(12), 5602–5610 (2010).

[27] Rumble, C., Rich, K., He, G., and Maroncelli, M. *J. Phys. Chem. A* **116**(44), 10786–10792 (2012).

[28] Loutfy, R. O. and Law, K. Y. *J. Phys. Chem.* **84**(21), 2803–2808 (1980).

[29] Loutfy, R. O. and Arnold, B. A. *J. Phys. Chem.* **86**(21), 4205–4211 (1982).

[30] Paul, A. and Samanta, A. *J. Phys. Chem. B* **112**(51), 16626–16632 (2008).

[31] Jee, A.-Y., Bae, E., and Lee, M. *J. Phys. Chem. B* **113**(52), 16508–16512 (2009). PMID: 19968266.

[32] Grabowski, Z. R., Rotkiewicz, K., and Rettig, W. *Chem. Rev.* **103**(10), 3899–4032 (2003). PMID: 14531716.

[33] Allen, B. D., Benniston, A. C., Harriman, A., Rostron, S. A., and Yu, C. *Phys. Chem. Chem. Phys.* **7**, 3035–3040 (2005).

[34] Lan, Z., Lu, Y., Weingart, O., and Thiel, W. *J. Phys. Chem. A* **116**(6), 1510–1518 (2012).

[35] Sawada, S., Iio, T., Hayashi, Y., and Takahashi, S. *Anal. Biochem.* **204**(1), 110–117 July (1992).

[36] Zhang, W., Lan, Z., Sun, Z., and Gaffney, K. J. *J. Phys. Chem. B* **116**(37), 11527–11536 (2012). PMID: 22934677.

[37] Levitt, J. A., Chung, P.-H., Kuimova, M. K., Yahioglu, G., Wang, Y., Qu, J., and Suhling, K. *ChemPhysChem* **12**(3), 662–672 (2011).

[38] Aihara, J., Araya, K., Chiba, K., and Matsunaga, Y. *Adv. Mol. Relax. Interact. Processes* **18**, 199–210 (1980).

[39] Katritzky, A. R., Zhu, D. W., and Schanze, K. S. *J. Phys. Chem.* **95**(15), 5737–5742 (1991).

[40] Wang, Q., Li, S., He, L., Qian, Y., Li, X., Sun, W., Liu, M., Li, J., Li, Y., and Yang, G. *ChemPhysChem* **9**(8), 1146–1152 (2008).

[41] Krishnamoorthy, G., Asato, A. E., and Liu, R. S. H. *Chem. Commun.* **17**(17), 2170–2171 (2003).

[42] Liu, R. S. H. and Hammond, G. S. *PNAS* **97**(21), 11153–11158 (2000).

[43] Donovan, D. R. Master's thesis, Bucknell University, (2012).

[44] Bello, K. A., Cheng, L., and Griffiths, J. *J. Chem. Soc., Perkin Trans. 2* **6**(6), 815–818 (1987).

[45] Shanthan Rao, P. and Venkataratnam, R. V. *Tetrahedron Lett.* **32**(41), 5821–5822 October (1991).

[46] Ettenger, G. B., Williams, B. W., Brillhart, D., and Kastner, M. E. *Acta Crystallographica Section E* **65**(7), o1711 (2009).

[47] Velapoldi, R. and Mielenz, K. *National Bureau of Standards: Washington, DC,* **1**, 1–122 (1980).

[48] Melhuish, W. H. *J. Phys. Chem.* **65**(2), 229–235 (1961).

[49] Tomasi, J., Mennucci, B., and Cammi, R. *Chem. Rev.* **105**(8), 2999–3094 August (2005).

[50] Frisch, M. J., Trucks, G. W., Schlegel, H. B., Scuseria, G. E., Robb, M. A., Cheeseman, J. R., Scalmani, G., Barone, V., Mennucci, B., Petersson, G. A., Nakatsuji, H., Caricato, M., Li, X., Hratchian, H. P., Izmaylov, A. F., Bloino, J., Zheng, G., Sonnenberg, J. L., Hada, M., Ehara, M., Toyota, K., Fukuda, R., Hasegawa, J., Ishida,

M., Nakajima, T., Honda, Y., Kitao, O., Nakai, H., Vreven, T., Montgomery, Jr., J. A., Peralta, J. E., Ogliaro, F., Bearpark, M., Heyd, J. J., Brothers, E., Kudin, K. N., Staroverov, V. N., Kobayashi, R., Normand, J., Raghavachari, K., Rendell, A., Burant, J. C., Iyengar, S. S., Tomasi, J., Cossi, M., Rega, N., Millam, J. M., Klene, M., Knox, J. E., Cross, J. B., Bakken, V., Adamo, C., Jaramillo, J., Gomperts, R., Stratmann, R. E., Yazyev, O., Austin, A. J., Cammi, R., Pomelli, C., Ochterski, J. W., Martin, R. L., Morokuma, K., Zakrzewski, V. G., Voth, G. A., Salvador, P., Dannenberg, J. J., Dapprich, S., Daniels, A. D., Farkas, Ö., Foresman, J. B., Ortiz, J. V., Cioslowski, J., and Fox, D. J. Gaussian Inc. Wallingford CT 2009.

[51] Huix-Rotllant, M., Natarajan, B., Ipatov, A., Muhavini Wawire, C., Deutsch, T., and Casida, M. E. *Phys. Chem. Chem. Phys.* **12**(39), 12811–12825 (2010).

[52] Minezawa, N. and Gordon, M. S. *J. Phys. Chem. A* **115**(27), 7901–7911 (2011).

[53] Bernard, Y. A., Shao, Y., and Krylov, A. I. *J. Chem. Phys.* **136**(20), 204103 (2012).

[54] Schmidt, M. W., Baldridge, K. K., Boatz, J. A., Elbert, S. T., Gordon, M. S., Jensen, J. H., Koseki, S., Matsunaga, N., Nguyen, K. A., Su, S., Windus, T. L., Dupuis, M., and Montgomery, J. A. *J. Comput. Chem.* **14**(11), 1347–1363 (1993).

[55] Dunning, Thom.H., J. and Hay, P. In *Methods of Electronic Structure Theory,* Schaefer, HenryF., I., editor, volume 3 of *Modern Theoretical Chemistry*, 1–27. Springer US (1977).

[56] Pfanstiel, J. F. and Pratt, D. W. *J. Phys. Chem.* **99**(19), 7258–7266 (1995).

[57] Auvray, P. and Genet, F. *Acta Crystallographica Section B* **27**(12), 2424–2429 (1971).

[58] Wright, D. and Williams, D. *J. Cryst. Mol. Struct.* **2**, 31–40 (1972).

[59] Yanai, T., Tew, D. P., and Handy, N. C. *Chem. Phys. Lett.* **393**(1-3), 51–57 July (2004).

[60] Nesterov, V. *Crystallogr. Rep.* **46**(6), 959–962 (2001).

[61] Besler, B. H., Merz, K. M., and Kollman, P. A. *J. Comput. Chem.* **11**(4), 431–439 (1990).

[62] Fraser, R. and Suzuki, E. *Spectral Analysis*. Pitman Publishing, London, UK, (1970).

[63] Arzhantsev, S., Jin, H., Ito, N., and Maroncelli, M. *Chem. Phys. Lett.* **417**(4-6), 524–529 January (2006).

[64] Reynolds, L., Gardecki, J. A., Frankland, S. J. V., Horng, M. L., and Maroncelli, M. *J. Phys. Chem.* **100**(24), 10337–10354 (1996).

[65] Jeon, J. and Kim, H. J. *J. Chem. Phys.* **119**(16), 8606–8625 (2003).

[66] Horng, M. L., Gardecki, J. A., Papazyan, A., and Maroncelli, M. *J. Phys. Chem.* **99**(48), 17311–17337 (1995).

[67] Ravi, M., Samanta, A., and Radhakrishnan, T. P. *J. Phys. Chem.* **98**(37), 9133–9136 (1994).

[68] Birks, J. *Photophysics of Aromatic Molecules.* Wiley Monographs in Chemical Physics. Wiley-Interscience, (1970).

[69] Lewis, J. E. and Maroncelli, M. *Chem. Phys. Lett.* **282**(2), 197–203 January (1998).

[70] Lewis, F. D. and Zuo, X. *J. Am. Chem. Soc.* **125**(8), 2046–2047 (2003).

[71] Vassar, P. and Culling, C. *Arch. Pathol.* **68**(4), 487–494 (1959).

[72] Rogers, D. R. *Am. J. Clin. Pathol.* **44**, 59–61 (1965).

[73] Kelenyi, G. *J. Histochem. Cytochem.* **15**(3), 172–180 (1967).

[74] Saeed, S. M. and Fine, G. *Am. J. Clin. Pathol.* **47**(5), 588–593 (1967).

[75] Cundall, R. B., Davies, A., Morris, P. G., and Williams, J. *J. Photochem.* **17**(2), 369–376 (1981).

[76] Naiki, H., Higuchi, K., Hosokawa, M., and Takeda, T. *Analytical Biochemistry* **177**(2), 244 – 249 (1989).

[77] Khurana, R., Coleman, C., Ionescu-Zanetti, C., Carter, S. A., Krishna, V., Grover, R. K., Roy, R., and Singh, S. *J. Struct. Biol.* **151**(3), 229 – 238 (2005).

[78] Groenning, M., Olsen, L., van de Weert, M., Flink, J. M., Frokjaer, S., and Jorgensen, F. S. *J. Struct. Biol.* **158**(3), 358–369 June (2007).

[79] Alavez, S., Vantipalli, M. C., Zucker, D. J. S., Klang, I. M., and Lithgow, G. J. *Nature* **472**(7342), 226–229 April (2011).

[80] Chiti, F. and Dobson, C. M. *Annu. Rev. Biochem.* **75**(1), 333–366 (2006). PMID: 16756495.

[81] Caughey, B. and Lansbury, P. T. *Annu. Rev. Neurosci.* **26**(1), 267–298 (2003). PMID: 12704221.

[82] Rishton, G. M. *Nat. Chem. Biol.* **4**(3), 159–160 March (2008).

[83] Voropai, E., Samtsov, M., Kaplevskii, K., Maskevich, A., Stepuro, V., Povarova, O., Kuznetsova, I., Turoverov, K., Fink, A., and Uverskii, V. *J. Appl. Spectrosc.* **70**(6), 868–874 (2003).

[84] Sulatskaya, A. I., Maskevich, A. A., Kuznetsova, I. M., Uversky, V. N., and Turoverov, K. K. *PLoS ONE* **5**(10), e15385 10 (2010).

[85] Singh, P. K., Kumbhakar, M., Pal, H., and Nath, S. *J. Phys. Chem. B* **114**(7), 2541–2546 (2010). PMID: 20095597.

[86] Amdursky, N., Erez, Y., and Huppert, D. *Acc. Chem. Res.* **45**(9), 1548–1557 (2012).

[87] Maskevich, A. A., Stsiapura, V. I., Kuzmitsky, V. A., Kuznetsova, I. M., Povarova, O. I., Uversky, V. N., and Turoverov, K. K. *J. Proteome Res.* **6**(4), 1392–1401 (2007).

[88] Stsiapura, V. I., Maskevich, A. A., Kuzmitsky, V. A., Turoverov, K. K., and Kuznetsova, I. M. *J. Phys. Chem. A* **111**(22), 4829–4835 (2007).

[89] Stsiapura, V. I., Maskevich, A. A., Kuzmitsky, V. A., Uversky, V. N., Kuznetsova, I. M., and Turoverov, K. K. *J. Phys. Chem. B* **112**(49), 15893–15902 (2008).

[90] Stsiapura, V. I., Maskevich, A. A., Tikhomirov, S. A., and Buganov, O. V. *J. Phys. Chem. A* **114**(32), 8345–8350 (2010).

[91] Singh, P. K., Kumbhakar, M., Pal, H., and Nath, S. *J. Phys. Chem. B* **113**(25), 8532–8538 (2009). PMID: 19485371.

[92] Singh, P. K., Kumbhakar, M., Pal, H., and Nath, S. *J. Phys. Chem. B* **114**(17), 5920–5927 (2010).

[93] Amdursky, N., Gepshtein, R., Erez, Y., Koifman, N., and Huppert, D. *J. Phys. Chem. A* **115**(24), 6481–6487 (2011).

[94] Amdursky, N., Gepshtein, R., Erez, Y., and Huppert, D. *J. Phys. Chem. A* **115**(12), 2540–2548 (2011).

[95] Erez, Y., Liu, Y.-H., Amdursky, N., and Huppert, D. *J. Phys. Chem. A* **115**(30), 8479–8487 (2011).

[96] Ren, H., Fingerhut, B. P., and Mukamel, S. *J. Phys. Chem. A* **117**(29), 6096–6104 (2013).

[97] Rodriguez-Rodriguez, C., Rimola, A., Rodriguez-Santiago, L., Ugliengo, P., Alvarez-Larena, A., Gutierrez-de Teran, H., Sodupe, M., and Gonzalez-Duarte, P. *Chem. Commun.* **46**, 1156–1158 (2010).

[98] Sulatskaya, A. I., Turoverov, K. K., and Kuznetsova, I. M. *Spectroscopy* **24**, 169–172 (2010).

[99] Sulatskaya, A. I., Kuznetsova, I. M., and Turoverov, K. K. *J. Phys. Chem. B* **116**(8), 2538–2544 (2012).

[100] Hutter, T., Amdursky, N., Gepshtein, R., Elliott, S. R., and Huppert, D. *Langmuir* **27**(12), 7587–7594 (2011).

[101] Erez, Y., Amdursky, N., Gepshtein, R., and Huppert, D. *J. Phys. Chem. A* **116**(49), 12056–12064 (2012).

[102] Srivastava, A., Singh, P., Kumbhakar, M., Mukherjee, T., Chattopadyay, S., Pal, H., and Nath, S. *Chem. Eur. J.* **16**(30), 9257–9263 (2010).

[103] van der Meer, M. J., Zhang, H., and Glasbeek, M. *J. Chem. Phys.* **112**(6), 2878–2887 (2000).

[104] Hsu, J. C.-C., Chen, E. H.-L., Snoeberger, R. C., Luh, F. Y., Lim, T.-S., Hsu, C.-P., and Chen, R. P.-Y. *J. Phys. Chem. B* **117**(13), 3459–3468 (2013).

[105] De Ferrari, G. V., Mallender, W. D., Inestrosa, N. C., and Rosenberry, T. L. *J. Biol. Chem.* **276**(26), 23282–23287 (2001).

[106] Johnson, J. L., Cusack, B., Davies, M. P., Fauq, A., and Rosenberry, T. L. *Biochemistry* **42**(18), 5438–5452 (2003). PMID: 12731886.

[107] Becke, A. D. *J. Chem. Phys.* **98**(2), 1372–1377 (1993).

[108] Lee, C., Yang, W., and Parr, R. G. *Phys. Rev. B* **37**, 785–789 Jan (1988).

[109] Hohenberg, P. and Kohn, W. *Phys. Rev.* **136**(3B), B864–B871 November (1964).

[110] Dennington, R., Keith, T., and Millam, J. Semichem Inc., Shawnee Mission, KS, 2009.

[111] Zhang, L.-j., Cui, J.-m., Hui, Pei-huaand Liu, H., Ji, M.-l., and Zhang, C.-j. *Applied Chemical Industry* **38**(6), 919–920 June (2009).

[112] Horng, M., Dahl, K., II, G. J., and Maroncelli, M. *Chem. Phys. Lett.* **315**(56), 363 – 370 (1999).

[113] Naik, L., Naik, A. B., and Pal, H. *J. Photochem. Photobiol. A* **204**(23), 161 – 167 (2009).

[114] Marcus, Y. *The Properties of Solvents.* John Wiley & Sons, Inc., November (1998).

[115] Chou, P.-T., Pu, S.-C., Cheng, Y.-M., Yu, W.-S., Yu, Y.-C., Hung, F.-T., and Hu, W.-P. *J. Phys. Chem. A* **109**(17), 3777–3787 (2005).

[116] Kimura, Y., Fukuda, M., Suda, K., and Terazima, M. *J. Phys. Chem. B* **114**(36), 11847–11858 (2010).

[117] Gardecki, J. A. and Maroncelli, M. *Chem. Phys. Lett.* **301**(5-6), 571–578 March (1999).

[118] Müller, A. amd Ratajack, H., Junge, W., and Diemann, E. *Electron and Proton Transfer in Chemistry and Biology*, volume 78. Elsevier: Amsterdam, The Netherlands, (1992).

[119] Waluk, J. *Conformational Aspects of Intra- and Intermolecular Excited-State Proton Transfer*. Wiley-VCH: New York, (2000).

[120] Swinney, T. C. and Kelley, D. F. *J. Chem. Phys.* **99**(1), 211–221 (1993).

[121] Hayaki, S., Kimura, Y., and Sato, H. *J. Phys. Chem. B* **117**(22), 6759–6767 (2013).

[122] Smith, M. A., Neumann, R. M., and Webb, R. A. *J. Heterocycl. Chem.* **5**(3), 425–426 (1968).

[123] Ormson, S. M., Brown, R. G., Vollmer, F., and Rettig, W. *J. Photochem. Photobiol. A* **81**(2), 65–72 July (1994).

[124] Hopf, F. A. *Applied Classical Electrodynamics: Nonlinear Optics*. Krieger Publishing Company, (1992).

[125] Maker, P. D. and Terhune, R. W. *Phys. Rev.* **137**(3A), A801–A818 February (1965).

[126] Shen, Y. R. *The Principles of Nonlinear Optics*. Wiley-Interscience, New York, (1984).

[127] Born, M. and Wolf, E. *Principles of Optics: Electromagnetic Theory of Propagation, Interference and Diffraction of Light*. Cambridge University Press, New York, 7th edition edition, (1999).

[128] Hellwarth, R. *Prog. Quant. Electr.* **5**, 1–68 (1979).

Appendix A

Theory of Light

A.1 Polarization of Light: Linear and Nonlinear [5, 6]

In the following part we shall derive several properties of light which will provide a better understanding of important aspects when working with lasers and *Kerr*-gated emission in particular.

A.1.1 Polarization as a Wave

A complete description of the propagation of electromagnetic fields requires use of the *Maxwell* equations, which in the SI system are [124]

$$\begin{aligned} \nabla \times \vec{E}(\vec{r},t) &= -\frac{\partial}{\partial t}\vec{B}(\vec{r},t) && \text{(A.1)} \\ &= -\mu_0 \frac{\partial}{\partial t}\left(\vec{H}(\vec{r},t) + \vec{M}(\vec{r},t)\right) && \text{(A.2)} \\ \nabla \times \left(\nabla \times \vec{E}(\vec{r},t)\right) &= -\mu_0 \frac{\partial}{\partial t}\left(\frac{\partial}{\partial t}\vec{D}(\vec{r},t) + j(\vec{r},t)\right) && \text{(A.3)} \\ &= -\mu_0 \frac{\partial}{\partial t}\left(\epsilon_0 \frac{\partial}{\partial t}\vec{E}(\vec{r},t) + \frac{\partial}{\partial t}\vec{P}(\vec{r},t) + j(\vec{r},t)\right) && \text{(A.4)} \end{aligned}$$

with $\nabla \times (\nabla \times \vec{z}) = -\nabla^2 \vec{z} + \nabla (\nabla \cdot \vec{z})$. Neglecting the current density $j(\vec{r},t)$ Eq. A.4 becomes:

$$-\nabla^2 \vec{E}(\vec{r},t) + \nabla \left(\nabla \cdot \vec{E}(\vec{r},t) \right) + \epsilon_0 \mu_0 \frac{\partial^2}{\partial t^2} \vec{E}(\vec{r},t) = -\mu_0 \frac{\partial^2}{\partial t^2} \vec{P}(\vec{r},t) \tag{A.5}$$

In vacuum we can set $\nabla \left(\nabla \cdot \vec{E}(\vec{r},t) \right) = 0$. Recognizing $c = 1/\sqrt{\epsilon_0 \mu_0}$ we obtain the simple wave equation:

$$-\nabla^2 \vec{E}(\vec{r},t) + \frac{1}{c^2} \frac{\partial^2}{\partial t^2} \vec{E}(\vec{r},t) = -\frac{1}{\epsilon_0 c^2} \frac{\partial^2}{\partial t^2} \vec{P}(\vec{r},t) \tag{A.6}$$

Eq. A.6 is the basis for the treatment of Gaussian beam propagation. When radiation interacts with matter the primary medium effects occur through dielectric interactions embodied by the displacement field $\vec{D}(\vec{r},t)$. In this case the wave equation of primary interest is

$$-\nabla^2 \vec{D}(\vec{r},t) + \frac{n^2}{c^2} \frac{\partial^2}{\partial t^2} \vec{D}(\vec{r},t) = \nabla \times \left(\nabla \times \vec{P}(\vec{r},t) \right) \tag{A.7}$$

If we set planar monochromatic waves for the electric field $\vec{E}$ (or $\vec{D}$, respectively) the polarization $\vec{P}$ can be considered as a superposition of monochromatic waves. We therefore decompose all $\left\{ \vec{E}, \vec{D}, \vec{P} \right\}(\vec{r},t)$ into the frequency domain $\left\{ \vec{E}, \vec{D}, \vec{P} \right\} \left(\vec{k}, \omega \right)$ for a simplified representation:

$$\vec{E}(\vec{r},t) \longleftrightarrow \vec{E}\left(\vec{k},\omega\right) = \frac{1}{2} \vec{\mathbf{E}}\left(\vec{k},\omega\right) exp\left[i \left(\vec{k}\vec{r} - \omega t \right) \right] \tag{A.8}$$

$$\vec{D}(\vec{r},t) \longleftrightarrow \vec{D}\left(\vec{k},\omega\right) = \frac{1}{2} \vec{\mathbf{D}}\left(\vec{k},\omega\right) exp\left[i \left(\vec{k}\vec{r} - \omega t \right) \right] \tag{A.9}$$

$$\vec{P}(\vec{r},t) \longleftrightarrow \vec{P}\left(\vec{k},\omega\right) = \frac{1}{2} \vec{\mathbf{P}}\left(\vec{k},\omega\right) exp\left[i \left(\vec{k}\vec{r} - \omega t \right) \right] \tag{A.10}$$

Here we denote $\vec{k}$ the wave vector and ω the angular frequency. In the isotropic media of interest $\vec{P} \perp \vec{k}$ and we write $\vec{\mathbf{P}} = \hat{p} \cdot \left| \vec{\mathbf{P}} \right|$, where $\hat{p}$ is a unit vector with $\hat{p} \perp \vec{k}$. Any

phase shift can be described by a phase factor ϕ, such that the polarization wave can be expressed:

$$\vec{P}\left(\vec{r},t\right)=\frac{1}{2}\hat{p}\left|\vec{\mathbf{P}}\left(\vec{k},\omega\right)\right|exp\left[i\left(\vec{k}_p\vec{r}-\omega t+\phi\right)\right]+cc \tag{A.11}$$

In this context the concept the slowly varying envelope approximation is of importance. It says the change of the complex field amplitudes in Eq. A.8, Eq. A.9 and Eq. A.10 vary much more slowly in comparison to the optical carrier frequency. Thus an observer in the z-direction notices:

$$\frac{\partial\vec{\mathbf{E}}\left(z,\vec{k},\omega\right)}{\partial z}\ll\vec{k}\vec{\mathbf{E}}\left(z,\vec{k},\omega\right) \tag{A.12}$$

Applying this approximation to Eq. A.5 or Eq. A.6, respectively, we obtain:

$$\frac{\partial\vec{\mathbf{E}}\left(z,\vec{k},\omega\right)}{\partial z}=\frac{i\omega}{n\epsilon_0 c}\vec{\mathbf{P}}\left(z,\vec{k},\omega\right)exp\left[i\left(\vec{k}_P+\vec{k}\right)z\right] \tag{A.13}$$

were n is the complex refractive index of the medium and $\vec{k}_P$ is the wave vector.

A.1.2 Higher Order Polarization

In case of not too large fields $\vec{E}\left(\vec{r},t\right)$ a series expansion of the polarization field $\vec{P}\left(\vec{r},t\right)$ is reasonable:

$$\begin{aligned}\vec{P}\left(\vec{r},t\right) &= \vec{P}^{(0)}\left(\vec{r},t\right)+\vec{P}^{(1)}\left(\vec{r},t\right)+\vec{P}^{(2)}\left(\vec{r},t\right)+\vec{P}^{(3)}\left(\vec{r},t\right)+\ldots+\vec{P}^{(n)}\left(\vec{r},t\right) &\text{(A.14)}\\ &= \vec{P}^{(0)}\left(\vec{r},t\right)+\vec{P}^{(1)}\left(\vec{r},t\right)+\vec{P}^{(NL)}\left(\vec{r},t\right) &\text{(A.15)}\end{aligned}$$

wherein

$$\vec{P}^{(n)}\left(\vec{r},t\right)\propto\left(\vec{E}\left(\vec{r},t\right)\right)^n \tag{A.16}$$

$\vec{P}^{(0)}(\vec{r},t)$ stands for the static polarization, $\vec{P}^{(1)}(\vec{r},t)$ for the linear polarization, $\vec{P}^{(2)}(\vec{r},t)$ and $\vec{P}^{(3)}(\vec{r},t)$ for the quadratic and cubic polarizations, etc. Of interest is the nth order macroscopic polarization response of a medium to n applied electric fields. The required proportionalities can be described via suitable linear and nonlinear response functions χ analogous to Eq. A.9. These functions are now complex tensors of order n. For the first n elements in Eq. A.14 considered in the time domain:

$$\vec{P}_i^{(1)}(\vec{r},t) = \epsilon_0 \int dt_1\, \chi_{ij}^{(1)}(t;t_1)\cdot\vec{E}_j(\vec{r}_1,t_1) \tag{A.17}$$

$$\vec{P}_i^{(2)}(\vec{r},t) = \epsilon_0 \int dt_1 \int dt_2\, \chi_{ijk}^{(2)}(t;t_1,t_2) : \vec{E}_j(\vec{r}_1,t_1)\,\vec{E}_k(\vec{r}_2,t_2) \tag{A.18}$$

$$\vec{P}_i^{(3)}(\vec{r},t) = \epsilon_0 \int dt_1 \int dt_2 \int dt_3\, \chi_{ijkl}^{(3)}(t;t_1,t_2,t_3) \vdots\vec{E}_j(\vec{r}_1,t_1)\,\vec{E}_k(\vec{r}_2,t_2)\,\vec{E}_l(\vec{r}_3,t_3) \tag{A.19}$$

$$\vec{P}_i^{(n)}(\vec{r},t) = \epsilon_0 \int dt_1 \ldots \int dt_n\, \chi_{ii_1\ldots i_n}^{(n)}(t;t_1\ldots t_n) |\vec{E}_{i_1}(\vec{r}_1,t_1)\ldots\vec{E}_{i_n}(\vec{r}_n,t_n) \tag{A.20}$$

Eq. A.17 to Eq. A.20 turn out to be convolutions over each integration variables indicated by the notation ($\cdot\vec{E}_j$, $:\vec{E}_j$ and $\vdots\vec{E}_j$). In the frequency domain the convolution operation is simplified to a product and we can write[1]:

$$\vec{P}_i^{(1)}\left(\vec{k},\omega\right) = \epsilon_0\,\chi_{ij}^{(1)}(\omega;\omega_j)\cdot\vec{E}_j\left(\vec{k}_j,\omega_j\right) \tag{A.21}$$

$$\vec{P}_i^{(2)}\left(\vec{k},\omega\right) = \epsilon_0\,\chi_{ijk}^{(2)}(\omega;\omega_j,\omega_k)\cdot\vec{E}_j\left(\vec{k}_j,\omega_j\right)\cdot\vec{E}_k\left(\vec{k}_k,\omega_k\right) \tag{A.22}$$

$$\vec{P}_i^{(3)}\left(\vec{k},\omega\right) = \epsilon_0\,\chi_{ijkl}^{(3)}(\omega;\omega_j,\omega_k,\omega_l)\cdot\vec{E}_j\left(\vec{k}_j,\omega_j\right)\cdot\vec{E}_k\left(\vec{k}_k,\omega_k\right)\cdot\vec{E}_l\left(\vec{k}_l,\omega_l\right) \tag{A.23}$$

$$\vec{P}_i^{(n)}\left(\vec{k},\omega\right) = \epsilon_0\,\chi_{ii_1\ldots i_n}^{(n)}(\omega;\omega_i\ldots\omega_n)\cdot\vec{E}_{i_1}\left(\vec{k}_1,\omega_1\right)\cdot\ldots\cdot\vec{E}_{i_n}\left(\vec{k}_n,\omega_n\right) \tag{A.24}$$

[1]Here the notation by Maker and Terhune is used, whereby $\omega = \omega_1 + \ldots + \omega_n$. [125] The order of the $\vec{E}$-fields regarding the χ-indices are handled differently by different authors. Occasionally there are additional nonlinear coefficients and degeneracy factors necessary to properly connect the amplitudes of $\vec{E}$ and $\vec{P}$. [126]

According to these equations $\chi^{(n)}$ interlinks n plane, monochromatic $\vec{E}$-fields to create a new polarization wave $P^{(n)}$.

A.1.3 The *Kerr*-Effect as χ^3-Process

The Kerr-effect is a nonlinear optical effect because it violates the fundamental principles of linear optics (superposition and frequency maintenance) [127]. It can be observed only in the high field intensities of laser radiation. The description of the generated polarization field requires comprehension of higher, nonlinear terms in Eq. A.14. Because liquids possess inversion symmetry $\chi^{(2)} = 0$. According to Eq. A.19 and Eq. A.23 three electromagnetic fields generate a new fourth (potential) field by $\chi^{(3)}$. Within a two-laser-beam experiment two fields are associated with the pump pulse, and the third with the time delayed probe pulse. The required second pump field is here the complex conjugated of the first one. For this reason the respective fields in Eq. A.23 can denoted as:

$$\begin{aligned} \vec{\mathbf{P}}_i^{(3)}\left(\vec{k},\omega\right) &= \epsilon_0\,\chi^{(3)}\left(\omega_2;\omega_2,\omega_1,-\omega_l\right) \\ &\quad \cdot\vec{\mathbf{E}}_{probe}\left(\vec{k}_2,\omega_2\right)\cdot\vec{\mathbf{E}}_{pump}\left(\vec{k}_1,\omega_1\right)\cdot\vec{\mathbf{E}}^*_{pump}\left(\vec{k}_1,-\omega_1\right) \end{aligned} \tag{A.25}$$

For simplicity here we regard only the complex field amplitudes. Eq. A.25 shows that the *Kerr*-effect is quadratic in the pump field and linear in the probe field.

A.1.4 Local Coordinate System

A number of symmetry restrictions apply to the expansion order n for the susceptibility tensors $\chi^{(n)}$. Depending on the symmetry of the medium, some tensor elements can disappear and some elements become identical. Consequently the total number of independent tensor elements can be reduced.

The inner (here denoted "local") coordinate system shall be defined by the polarization

direction of the optical fields. By regarding the normalized complex field vectors and the reduced $\chi^{(3)}$-tensor we obtain from Eq. A.23 for the vector of the polarization response $\vec{\mathbf{P}}^{(3)}(\omega)$:

$$\begin{aligned}
\vec{\mathbf{P}} &= \epsilon_0 \, \chi^{(3)} \cdot \vec{\mathbf{E}}_{probe} \cdot \vec{\mathbf{E}}_{pump} \cdot \vec{\mathbf{E}}^{*}_{pump} \\
&\propto \begin{pmatrix} \begin{pmatrix} \vdots\vdots \\ \vdots\vdots \end{pmatrix} & \begin{pmatrix} \vdots\vdots \\ \vdots\vdots \end{pmatrix} & \begin{pmatrix} \vdots\vdots \\ \vdots\vdots \end{pmatrix} \\ \begin{pmatrix} \vdots\vdots \\ \vdots\vdots \end{pmatrix} & \begin{pmatrix} \vdots\vdots \\ \vdots\vdots \end{pmatrix} & \begin{pmatrix} \vdots\vdots \\ \vdots\vdots \end{pmatrix} \\ \begin{pmatrix} \vdots\vdots \\ \vdots\vdots \end{pmatrix} & \begin{pmatrix} \vdots\vdots \\ \vdots\vdots \end{pmatrix} & \begin{pmatrix} \vdots\vdots \\ \vdots\vdots \end{pmatrix} \end{pmatrix} \cdot \begin{pmatrix} 1 \\ -1 \\ 0 \end{pmatrix} \cdot \begin{pmatrix} 1 \\ 0 \\ 0 \end{pmatrix} \cdot \begin{pmatrix} 1 \\ 0 \\ 0 \end{pmatrix} \\
&\propto \begin{pmatrix} \chi^{(3)}_{1111} \\ \chi^{(3)}_{1122} \\ 0 \end{pmatrix}
\end{aligned} \tag{A.26}$$

The radiated signal field $\vec{\mathbf{E}}_S$ will be detected perpendicular to the probe field in the xy-plane under $-45°$ and is:

$$\vec{\mathbf{E}}_S \equiv \vec{\mathbf{P}}^{(3)}_{x+y} \propto \chi^{(3)}_{1111} - \chi^{(3)}_{1122} \tag{A.27}$$

The implication for the Kerr-gated pump-probe experiment is, the probe pulse (perpendicular to the pump field which we set at $-45°$) will have to have a $+45°$ polarization of our gate pulse relative to the fluorescence polarization (=radiated signal field).

A.1.5 Birefringence as a χ^3-Process

The treatment of the Kerr-effect can now be reduced to first expansion order. The first two tensor operations in Eq. A.26 are merged to one effective tensor - now first order:

$$\chi^{(1)}_{eff} \equiv \begin{pmatrix} \chi^{(1)}_{xx} & 0 & 0 \\ 0 & \chi^{(1)}_{yy} & 0 \\ 0 & 0 & \chi^{(1)}_{zz} \end{pmatrix} \tag{A.28}$$

$$\equiv \begin{pmatrix} \chi^{(3)}_{1111} & 0 & 0 \\ 0 & \chi^{(3)}_{1122} & 0 \\ 0 & 0 & \chi^{(3)}_{1122} \end{pmatrix} \cdot \left|\vec{\mathbf{E}}_{pump}\right| \cdot \left|\vec{\mathbf{E}}_{pump}\right| \tag{A.29}$$

The χ tensor here is similar to the $\chi^{(1)}$ tensor of a birefringent uniaxial crystal. Thus birefringence - at least for the duration of interaction with the electric pump field - is observed even in some liquids, i.e. benzene. Birefringence is detected as a phase difference $\Delta n = n_x - n_y$ between the refractive indices in the representative directions x and y [124]:

$$n_x = n - \frac{n^3}{2}\chi^{(3)}_{1111}\left|\vec{\mathbf{E}}_{pump}\right|^2 \tag{A.30}$$

$$n_y = n - \frac{n^3}{2}\chi^{(3)}_{1122}\left|\vec{\mathbf{E}}_{pump}\right|^2 \tag{A.31}$$

So far we have taken the pump field like all other electric fields as a basis of planar waves (Eq. A.8). In this case we speak in general about of the a.c. Kerr-effect. The d.c. Kerr-effect is the limiting case $\omega \to 0$ where $\vec{\mathbf{E}}_{pump} = const$ [128], which you find applied e.g. in laser systems.

A.1.6 Orientation Distribution Functions

The effective tensor $\chi^{(1)}_{eff}$ is the result of all contributions from polarizable molecules in the interaction volume. These molecules have an orientation distribution. First of all we look at a single particle: $\alpha_{\parallel}$ and $\alpha_{\perp}$ are the polarizabilities parallel and perpendicular to its molecular axes. The angle θ indicates a twist of the molecular axis compared to the x-axis. A linear electric field $\vec{E}$ induces a dipole $\vec{\mathbf{p}}$ in the molecule with $p_x = \alpha_{xx}\vec{E}$ and

$$\alpha_{xx} = \alpha_{\parallel} cos^2(\theta) + \alpha_{\perp} sin^2(\theta) \tag{A.32}$$

$$= \bar{\alpha} + \Delta\alpha \left(cos^2(\theta) - \frac{1}{3} \right) \tag{A.33}$$

with $\bar{\alpha} = \frac{1}{3}\left(\alpha_{\parallel} + 2\alpha_{\perp}\right)$ and $\Delta\alpha = \alpha_{\parallel} - \alpha_{\perp}$.

The induced dipole interacts with the applied electric field to cause preferential orientation along the x-axis. For a collection of N non-interacting particles orientations will be distributed according to some distribution functions. For the first tensor element of the effective susceptibility:

$$\chi^{(1)}_{xx} = \bar{\chi} + N\Delta\alpha \left\langle cos^2(\theta) - \frac{1}{3} \right\rangle \tag{A.34}$$

$$= N\bar{\alpha} + N\Delta\alpha \left\langle cos^2(\theta) - \frac{1}{3} \right\rangle \tag{A.35}$$

and for the remainder of the main diagonal:

$$\chi^{(1)}_{yy} = \chi^{(1)}_{zz} = N\bar{\alpha} - N\Delta\alpha\frac{1}{2} \left\langle cos^2(\theta) - \frac{1}{3} \right\rangle \tag{A.36}$$

where $\langle\rangle$ represents an average over the orientation distribution of θ. [126]

Implications of the theory only briefly addressed in here which are of relevance to Kerr-gated emission spectroscopy are:

1. The gate pulse energy $\vec{\mathbf{E}}_{pump}$ has a quadratic influence on the tilting polarization,
2. the gate pulse polarization must be $-45°$ oriented to the fluorescence polarization,
3. the number N of molecules (= concentration of the dye) are directly proportional to the signal intensity,
4. the susceptibility $\chi^{(3)}$ of the *Kerr* medium.

Appendix B

Deconvolution Function

The instrument response function (IRF) dictates the time resolution of an instrument for time-resolved measurements. It can be obtained directly by measuring the Raman signal of a solvent blank. In Figure 3.14 the Raman transient observed in ethanol is shown. Benzene as Kerr medium has a ∼15 % broad nuclear relaxation component (vs. ∼85 % electronic) due to the contribution of orientational polarizability to its nonlinear refractive index (birefringence). [16, 17]. Because of this asymmetric IRF a deconvolution of our Kerr-gated emission is necessary to achieve accurate time information, especially at early time (<1 ps).

Any measured fluorescence signal represents a convoluted response of the sample emission and the instrument response. A general convolution of two functions is defined by

$$(f * g)(t) = \int_{-\infty}^{+\infty} f(t')g(t-t')dt' \tag{B.1}$$

$$= \int_{-\infty}^{+\infty} f(t-t')g(t')dt' \tag{B.2}$$

Our experimental data is a convolution of an ideal lifetime decay, assumed to be repre-

sentable as a sum of exponentials and an IRF represented as a sum of Gaussian functions.

$$I(t) = \int_0^\infty \overbrace{R(t-t')}^{IRF} \overbrace{D(t')}^{Decay} dt' \tag{B.3}$$

I(t) will be composed of a sum of terms of the form

$$\therefore R(t) = \sum_{i=1}^{M} R_i(t) = \sum_{i=1}^{M} a_i \times e^{-\frac{(t-t_i)^2}{2\sigma_i^2}} \tag{B.4}$$

$$\therefore D(t) = \sum_{j=1}^{N} D_j(t) = \sum_{j=1}^{N} b_j \times e^{-\frac{t'}{\tau_j}} \tag{B.5}$$

$$\Longrightarrow I(t) = \sum_{i=1}^{M}\sum_{j=1}^{N} a_i b_j \int_0^\infty e^{-\frac{(t-t_i-t')^2}{2\sigma_i^2}} e^{-\frac{t'}{\tau_j}} dt' \tag{B.6}$$

where M is the number of Gaussians used to describe the instrument response function (IRF) and N is the number of exponentials to describe the fluorescence lifetime decay. t_i is an wavelength-dependent time shift which allows one to correct for a displacement of time zero since the experiment might not be exactly set to zero.

We substitute

$$\alpha_i = \frac{1}{2\sigma_i^2} \tag{B.7}$$

$$\beta_j = \frac{1}{\tau_j} \tag{B.8}$$

$$\Longrightarrow I(t) = \sum_{i=1}^{M}\sum_{j=1}^{N} a_i b_j \int_0^\infty e^{-\alpha_i(t-t_i-t')^2} e^{-\beta_j t'} dt' \tag{B.9}$$

To solve this integral we transform the exponent to

$$\begin{aligned}
\left(t - t_i - t'\right)^2 &= t'^2 - 2t't + t^2 + 2t't_i - 2tt_i + t_i^2 && \text{(B.10)}\\
&= t'^2 - t'\left(2t - 2t_i\right) + \left(t^2 - 2tt_i + t_i^2\right) && \text{(B.11)}\\
&= t'^2 - t'\left(2t - 2t_i\right) + \left(t - t_i\right)^2 && \text{(B.12)}
\end{aligned}$$

$$\begin{aligned}
\Rightarrow -\alpha_i\left(t - t_i - t'\right)^2 - \beta_j t' &= -\alpha_i t'^2 + \alpha_i t'\left(2t - 2t_i\right) - \alpha_i\left(t - t_i\right)^2 - \beta_j t' && \text{(B.13)}\\
&= -\alpha_i t'^2 + t'\left(2\alpha_i t - 2\alpha_i t_i - \beta_j\right) - \alpha_i\left(t - t_i\right)^2 && \text{(B.14)}\\
&= -\alpha_i t'^2 + t'\left(2\alpha_i\left(t - t_i\right) - \beta_j\right) - \alpha_i\left(t - t_i\right)^2 && \text{(B.15)}
\end{aligned}$$

substitute with

$$\begin{aligned}
A_i &= \alpha_i && \text{(B.16)}\\
B_{ij} &= \beta_j - 2\alpha_i\left(t - t_i\right) && \text{(B.17)}\\
C_i &= \alpha_i\left(t - t_i\right)^2 && \text{(B.18)}
\end{aligned}$$

and obtain

$$= -\left[A_i t'^2 + B_{ij} t' + C_i\right] \qquad \text{(B.19)}$$

$$\therefore A_i t'^2 + B_{ij} t' + C_i = A_i \left(t'^2 + \frac{B_{ij}}{A_i} t' \right) + C_i \tag{B.20}$$

$$= A_i \left(t'^2 + \frac{B_{ij}}{A_i} t' + \overbrace{\frac{B_{ij}^2}{4A_i^2} - \frac{B_{ij}^2}{4A_i^2}}^{=0} \right) + C_i \tag{B.21}$$

$$= A_i \left(t' + \frac{B_{ij}}{2A_i} \right)^2 - \frac{B_{ij}^2}{4A_i^2} + C_i \tag{B.22}$$

$$\Rightarrow e^{-\left[A_i t'^2 + B_{ij} t' + C_i\right]} = e^{-\left[A_i \left(t' + \frac{B_{ij}}{2A_i}\right)^2 - \left(\frac{B_{ij}^2}{4A_i} - C_i\right)\right]} \tag{B.23}$$

$$= e^{-A_i \left(t' + \frac{B_{ij}}{2A_i}\right)^2} \overbrace{e^{\left(\frac{B_{ij}^2 - 4A_i C_i}{4A_i}\right)}}^{=const} \tag{B.24}$$

To integrate the dependent term

$$\int_0^\infty e^{-A_i \left(t' + \frac{B_{ij}}{2A_i}\right)^2} dt' \tag{B.25}$$

we substitute

$$u = t' + \frac{B_{ij}}{2A_i} \longrightarrow du = dt' \tag{B.26}$$

$$\therefore \quad u(t' = 0) = \frac{B_{ij}}{2A_i} \tag{B.27}$$

$$\therefore \quad u(t' = \infty) \to \infty \tag{B.28}$$

and obtain

$$\int_{\frac{B_{ij}}{2A_i}}^{\infty} e^{-A_i u^2} du = \frac{\sqrt{\pi}}{2\sqrt{A_i}} \left[\mathrm{Erf}\left(\sqrt{A_i} u\right) \right]_{\frac{B_{ij}}{2A_i}}^{\infty} \tag{B.29}$$

$$= \frac{\sqrt{\pi}}{2\sqrt{A_i}} \left[\lim_{u\to\infty} \mathrm{Erf}\left(\sqrt{A_i} u\right) - \lim_{u\to\frac{B_{ij}}{2A_i}} \mathrm{Erf}\left(\sqrt{A_i} u\right) \right] \tag{B.30}$$

$$= \frac{\sqrt{\pi}}{2\sqrt{A_i}} \left[\lim_{u\to\infty} \mathrm{Erf}\left(\sqrt{A_i} u\right) - \mathrm{Erf}\left(\sqrt{A_i} \frac{B_{ij}}{2A_i}\right) \right] \tag{B.31}$$

$$= \frac{1}{2}\sqrt{\frac{\pi}{A_i}} \left[1 - \mathrm{Erf}\left(\frac{B_{ij}}{2\sqrt{A_i}}\right) \right] \tag{B.32}$$

$$= \frac{1}{2}\sqrt{\frac{\pi}{A_i}} \mathrm{Erfc}\left(\frac{B_{ij}}{2\sqrt{A_i}}\right) \tag{B.33}$$

We re-substitute to get the full expression

$$\int_0^{\infty} e^{-\left[A_i t'^2 + B_{ij} t' + C_i\right]} dt' = \int_0^{\infty} e^{-A_i \left(t' + \frac{B_{ij}}{2A_i}\right)^2} e^{\left(\frac{B_{ij}^2 - 4A_i C_i}{4A_i}\right)} dt' \tag{B.34}$$

$$= \frac{1}{2}\sqrt{\frac{\pi}{A_i}} \mathrm{Erfc}\left(\frac{B_{ij}}{2\sqrt{A_i}}\right) e^{\left(\frac{B_{ij}^2 - 4A_i C_i}{4A_i}\right)} \tag{B.35}$$

and the sum over all parameters is finally

$$I(t) = \sum_{i=1}^{M}\sum_{j=1}^{N} a_i b_j \int_0^{\infty} e^{-\left[A_i t'^2 + B_{ij} t' + C_i\right]} dt' \tag{B.36}$$

$$= \sum_{i=1}^{M}\sum_{j=1}^{N} a_i b_j \frac{1}{2} \left(\frac{\pi}{A_i}\right)^{\frac{1}{2}} e^{\left(\frac{B_{ij}^2 - 4A_i C_i}{4A_i}\right)} \mathrm{Erfc}\left(\frac{B_{\mathrm{ij}}}{2\sqrt{A_i}}\right) \tag{B.37}$$

In particular, the IRF in our data shall be represented as a sum of three Gaussians as explained in section 3.3.3.

$$R(t) = \sum_{i=1}^{3} a_i \times e^{-\alpha_i (t - t_i)^2} \tag{B.38}$$

which is independent of the wavelength and will be treated as a global function.
The ideal intensity decay for each wavelength λ will be a sum of N exponentials:

$$D(\lambda,t) = \sum_{j=1}^{N} b_j(\lambda) \times e^{-\beta_j t} \tag{B.39}$$

where the pre-exponential factors $b_j(\lambda)$ are wavelength specified but not the lifetimes.
The observed intensity is then

$$I(\lambda,t) = \sum_{j=1}^{N} b_j(\lambda) \sum_{i=1}^{3} a_i \times T_{i,j}(t) \tag{B.40}$$

$$\therefore T_{i,j}(t) = \int_0^{\infty} e^{-\beta_j t'} e^{-\alpha_i (t-t_i-t')^2} dt' \tag{B.41}$$

$$= \frac{1}{2}\left(\frac{\pi}{A_i}\right)^{\frac{1}{2}} e^{\left(\frac{B_{ij}^2 - 4A_iC_i}{4A_i}\right)} \mathrm{Erfc}\left(\frac{B_{ij}}{2\sqrt{A_i}}\right) \tag{B.42}$$

For fitting purposes the i portion of $T_{i,j}(t)$ terms can be summed

$$T_j(t) = \sum_{i=1}^{3} a_i T_{i,j}(t) \tag{B.43}$$

Then the observed intensity becomes

$$I(\lambda,t) = \sum_{j=1}^{N} b_j(\lambda) T_j(t) \tag{B.44}$$

This fit function allows us to fit the data with respect to the IRF described by 3 Gaussian functions, a selectable number of exponentials describing the fluorescence lifetimes and a time shift correction. We are using MathWorks™MatLab® nonlinear least-squares data fitting routine for processing. The Gaussian functions are allowed to vary by $\sim$ 15-20 % in width and time relative to each other to account for varying daily performance. As an additional boundary condition we restrict the time shifts t_i across the spectra to match

a second polynomial function to account for minor deviations between the absolute time shift and the correction function measured as describes in section 3.3.1. As a result we obtain an idealized data matrix the effects of the IRF and time shift are removed.

Appendix C

Standard Operational Procedure (SOP) for Kerr-Gated Emission Spectroscopy

C.1 Introduction

1. Spectroscopy system location: The Pennsylvania State University, Department of Chemistry, 411 Chemistry Building, University Park, PA 16802
2. Diagram of room with location of the spectroscopy system, see Figure C.1:
3. Description of spectroscopy system, see Figure C.2
4. Application of the spectroscopy system: Ultrafast time resolved fluorescence spectroscopy

C.2 Hazards

1. Beam and non-beam hazards - optical, electrical and chemical hazards

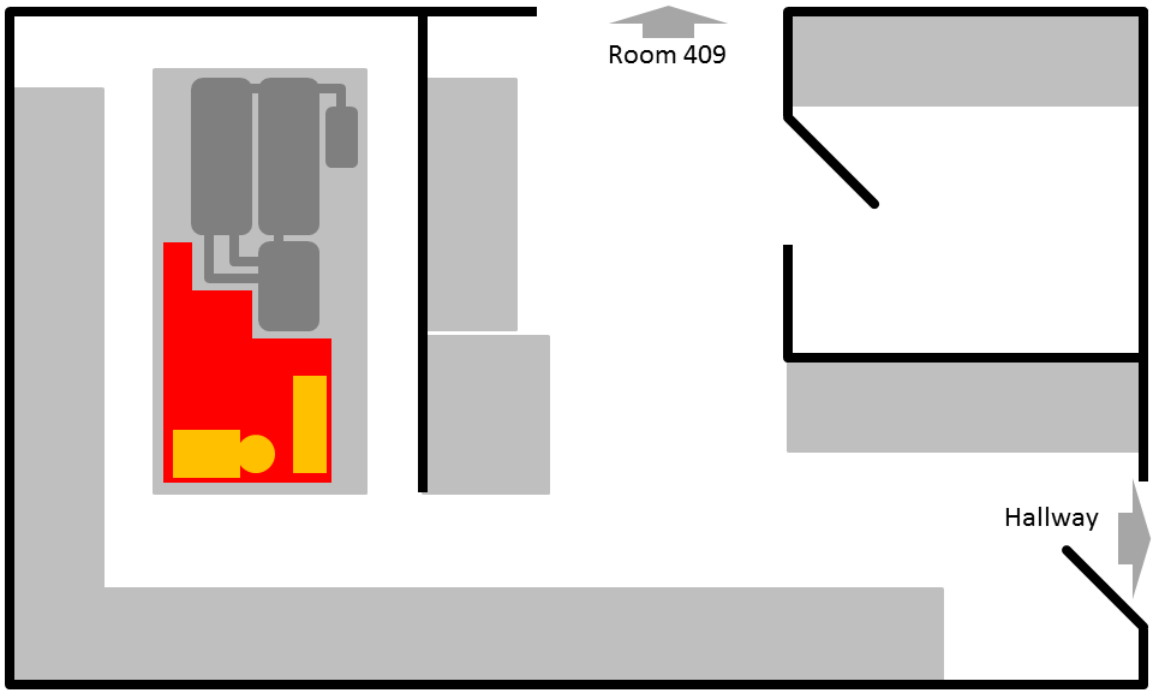

Figure C.1: Diagram of laser laboratory in room 411 Chemistry Building. In dark gray illustrated is the commercial laser system from Coherent. In red the principle location of the spectroscopy setup

2. Analysis and control safety goggles must be worn to prevent optical hazards and a single isolated circuit with breaker for electrical hazard. Gloves must be worn when dealing with the benzene as Kerr media and sample vials upon loading and unloading sample cell through peristaltic pump

C.3 Controls

1. Access controls - Access to the lab restricted to personal

2. Beam controls - Power supply is key locked, emergency interlock, beam shutter on pump laser head and panel and software controlled beam shutters in Kerr-shutter setup

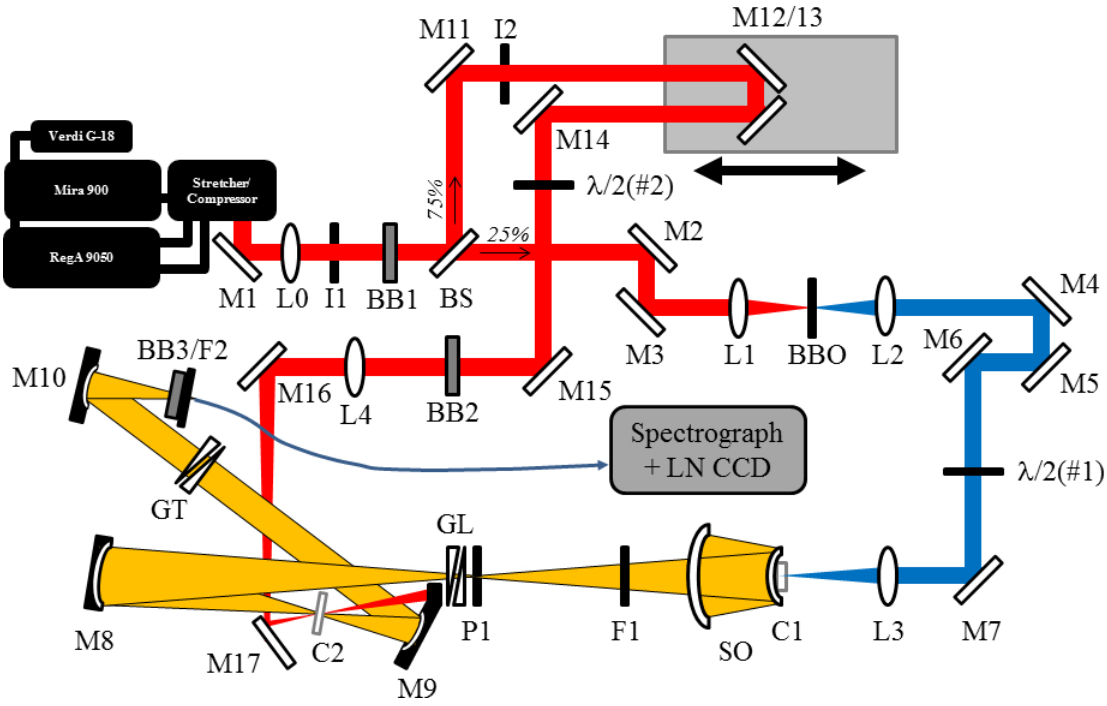

Figure C.2: Kerr shutter setup: The black boxes represents the amplified Ti:Sapphire laser system. *M1* 45° high reflectivity (*HR*) mirror; *L0* 3000 mm focal length lens to collimate the laser; *I1,I2* irises for alignment purposes; *BB1* solenoid beam blocker #1; *BS* beam splitter (75 % reflectivity; 25% transmittance).
25% transmittance path: *L1,L2* 50 mm focal length lenses; *BBO* 0.2 mm BBO (*Inrad*, Type I); $\lambda/2$*(#1)* $\lambda/2$ retarder for magic angle excitation; *L3* 100 mm focal length lens; *C1* 0.5 mm sample flow cell, 0.2 mm / 1 mm suprasil window; *S0* on-axis Schwarzschild objective with 1:10 magnification; *F1* GG400 optical filter to remove excitation scattering; *P1* 300μm pinhole; *GL* Glan-Laser calcite polarizer (Halle); *M8* 250 mm focal length mirror; *C2* 0.65 mm *Kerr* flow cell (benzene), 0.2 mm / 0.2 mm suprasil window; *M9* 100 mm concave mirror to collimate beam; *GT* Glan-Taylor polarizer (1.5 in aperture); *M10* -100 mm focal length mirror; *BB3* UniBlitz® beam blocker; *F2* 0° dichroic mirror for 775nm to filter gate beam scattering; multimode optical fiber coupling directly into spectrograph (Acton SpectraPro-300i) with attached liquid nitrogen cooled CCD detector (Princeton Instrument, LN/CCD-1340/100-EB/1).
75 % transmittance path: *M12/M13* translation/delay stage (Newport ILS250PP), $\lambda/2$*(#2)* $\lambda/2$ plate for 45° polarization; *BB2* solenoid beam blocker #2; *L4* 500 mm focal length lens; *C2* 0.65 mm *Kerr* flow cell (benzene), 0.2 mm/0.2 mm suprasil window; *M9* holder serves as beam blocker.

3. Electrical controls - UPS battery and circuit breaker
4. Eye protection types - goggles OD 6 775 nm - 800 nm and regular safety goggles when handling liquid nitrogen
5. Hand protection types - cryogenic gloves when handling liquid nitrogen, disposable laboratory gloves (nitrile, latex) when handling solvent vials and dealing with benzene Kerr cell
6. Any medical surveillance requirements - none required
7. Other controls needed - none needed

C.4 Operating Procedures - Startup

1. Initial preparation of laboratory
   (a) Close door to hallway
   (b) Close curtain to avoid lab exposure
   (c) Identification of all personnel present
   (d) Personnel protection requirement acknowledged by persons present
   (e) Target area - Enclosed
2. Turn on Coherent laser system according to its SOP
   (a) Tektronix 11302 oscilloscope shall show:
      - *C1* (references photodiode from oscillator pulse train)
      - *L1* (cavity dumper sequence)
   (b) Signals need to be triggered against *L1*. If triggered against external trigger dumping sequence will appear very late and you will have to decrease horizontal size (time scale)

(c) *Trouble shooting*: If nothing reasonable appears on the screen but you know laser seems to operate fine press "*Autoset*". Most likely you will have to change trigger to *L1* but should see the dumping sequence when slightly increasing the signal threshold.

3. Fill Princeton Instruments CCD camera with liquid nitrogen. If CCD is at room temperature it will take up to 1.5 h to cool down to the desired set temperature of $-120°C$.

4. Turn on power supply for Princeton Instrument CCD camera and Acton spectrograph.

5. Wait 1-2 minutes until spectrograph initializes and then start WinSpec software.

6. Turn on the shutter control and the Newport translation stage controller. The shutter control will beep once when communication is established and beep several times if not. The translation stage will beep loudly if not communicating, otherwise it won't beep at all. After its initialization you have to manually turn on the motor by pushing the button next to the display that says "MTR OFF" $\rightarrow$ "MTR ON". Then push "HOME $\rightarrow$ Axis 1". This will reset the internal position with respect to time zero.

7. Start the measurement control software in WinSpec. It is the white macro icon #1.

8. Turn on Kerr cell gear pump and sample cell peristaltic pump.

9. Turn on heat bath. Note: $27.3°C$ will result in $25°C$ at flow cell.

Trouble shooting:

- Failing to follow the exact order of [5-7] will cause miscommunication and measurement software will not start successfully. However, it will remain in the background and needs to be terminated manually by pressing *Ctrl + Alt + Del* simultaneously to end process.

- The spectrograph sometimes resets itself after power fluctuations. What happens is the acquired spectrum is centered at 0 nm. In WinSpec go to "Spectrograph" → "Move" and choose grating "300 BLZ= 500 nm"; "Move to: 550 nm" and "Speed: 100 nm/min"

C.5 Operating Procedure Daily Tuning

There are only three parts you should need to adjust for daily signal tuning: the excitation / fluorescence light coupling, the gate beam coupling and the pulse stretcher / compressor. It is very important that only the optics mentioned here are used to gain signal. It is possible to move only a few in order to correct for others too.

DO NOT MOVE ANY OTHER OPTICS BUT THE ONES MENTIONED BELOW!!

1. Excitation / fluorescence light coupling
   (a) open only the detector shutter and acquire a background
   (b) open the main shutter but keep gate closed
   (c) run the focus (continuous acquisition)
   (d) move M7 to maximize the signal background
   (e) move M10 to maximize the signal background
   (f) repeat 1d & 1e as necessary
   (g) rotate the GT rotation knob until signal (background) is minimized
2. Gate beam coupling
   (a) with main shutter open and gate shutter closed acquire a background
   (b) move the motion stage to 0 ps

(c) open the gate shutter

(d) adjust M17 to maximize signal

(e) adjust the carrier micrometer screw on motion stage to maximize the Raman signal. DO NOT adjust the actual mirrors!

(f) repeat [2d - 2e] as necessary

3. Pulse stretcher / compressor

(a) adjust the micrometer screws for the stretcher and compressor gratings to gain Raman signal. Unfortunately, the internal alignments may not be perfect and the beam may be walking while moving the gratings. Tweaking through repeating all steps above might be necessary.

Trouble shooting:

- If you cannot get any fluorescence or Raman signal use DCS in methanol provided as a stock bottle which should provide good fluorescence intensity. Move the motion stage to later times (e.g. 10 ps) to make sure you are at later times relative to time zero. Repeat all steps above.

C.6 Operating Procedure Shutdown

1. close all shutters
2. write down all laser parameters in the laser logbook
3. turn off the laser as instructed in its SOP
4. remove the sample from flow cell and flush with methanol
5. move the motion stage to hardware home by pushing "HOME → Axis 1"

6. turn off both pumps (Kerr & peristaltic) and the water bath

7. close software

8. turn off the motion stage controller, shutter controller, CCD controller and spectrograph

C.7 Training

1. Environmental Health & Safety Training - Prior to beginning work with any lasers supervisor and users of lasers shall complete the fundamental laser safety training class offered by EHS online. The training will consist of the following general topics: Laser Fundamentals, Laser Hazards, Non-beam Hazards, Laser Accidents, Control Measures, and Elements of PSU's Laser Safety Program.

2. Specific training for laser use - The Supervisor shall provide training to users in the operating and safety procedures of individual laser systems.

3. Maintenance and repair training if applicable - N/A (manufacturer will do any maintenance or repairs)

C.8 Responsibilities

1. Supervisor for normal operations - supervisors are responsible for the safe operation and maintenance of the lasers and shall provide training to users in the operating and safety procedures of individual laser systems.

2. Emergency coordinator - following up on reports of unsafe conditions, ensuring work with the laser is suspended until the unsafe conditions are rectified, and completing and documenting the required inspections, that include but are not limited to, laser specific information, administrative controls, and engineering controls.

3. Operators and other personnel - are required to complete the laser safety training provided by EHS before beginning work with lasers, to follow written operating procedures, to perform all work in a safe manner and use approved personal protective equipment. Users are also responsible for reporting to the supervisor any unusual or unsafe condition they discover with the laser, and for suspending work with that laser until the unsafe condition is rectified. The user is responsible for immediately informing the supervisor in the event of any exposure to the laser.

C.9 Miscellaneous

1. Visitor regulations at site No unsupervised visitors permitted

Vita

Jens Breffke

Education

12/2014 Ph.D. in Chemistry
Pennsylvania State University, University Park, PA, USA
Advisor: Mark Maroncelli
"Ultrafast Molecular Rotor and Proton Transfer Dynamics in Solution"

01/2009 Diplom in Chemistry
Humboldt-Universität zu Berlin, Germany
Advisor: Nikolaus P. Ernsting
"Sub-Picosecond Fluorescence Evolution by Kerr-Shutter Experiments"

Scholarships & Awards

- American Chemical Society (ACS) Leadership Development Award, 2013
- Global Innovation Award, ACS Office of International Activities, 2012
- Harry and Catherine Dalalian Travel Award 2008, 2009 & 2011
- Friends and Sponsors of the JungChemikerForum Travel Award
  to 2nd EuCheMS Chemistry Congress 2008, Torino, Italy
- Evonik Industries Thesis Research Scholarship, 2008
  Diplom thesis research in USA. Awarded by Prof. Michael Dröscher
- Leonardo da Vinci II 2007 Scholarship by German Academic Exchange Service (DAAD)
  Visiting Research Student, Universidad de Santiago de Compostela, Spain